CHARACTERIZATION OF THE MENISCAL ATTACHMENTS AND THE EXTENSION OF THIS KNOWLEDGE TO TISSUE ENGINEERING AND OTHER BIOLOGICAL SYSTEMS

A Dissertation

Presented to the Faculty of the Graduate School

of Cornell University

in Partial Fulfillment of the Requirements for the Degree of

Doctor of Philosophy by

Alexander Jacob Boys

May 2019

CHARACTERIZATION OF THE MENISCAL ATTACHMENTS AND THE EXTENSION OF THIS KNOWLEDGE TO TISSUE ENGINEERING AND OTHER BIOLOGICAL SYSTEMS

Alexander Jacob Boys, Ph. D.

Cornell University 2019

Soft tissue-to-bone interfaces, also called entheses, are found throughout the human body, typically linking structures like tendons, ligaments, and the meniscus to bone. These structures are of great interest to both the materials and biomedical engineering communities due to their unique properties and clinical relevance. The enthesis links highly dissimilar materials, often mediating a multiple order of magnitude change in stiffness, over only a few hundred microns. Such a feat has not yet been created in synthetic structures. Clinically, these tissues are often replaced during the repair of the meniscus, ligaments, and tendons. While the enthesis does not often tear, the reconstruction of the enthesis by the body is difficult due to the minimal vascularity and innervation in this region. As such, when adjacent soft tissue structures (ligaments, the meniscus, etc.) are damaged, clinicians will often include the enthesis from a cadaveric replacement tissue to avoid a need for recapitulating this structure. These examples highlight the importance of this tissue and the need to understand the mechanisms by which it functions.

This dissertation begins with a review of the soft tissue-to-bone interfaces and previous methods utilized by researchers to engineer these structures. After this discussion, a study analyzing the development of a structure-function relationship for the meniscal enthesis is detailed. This study utilizes Raman imaging and confocal elastography for the spatial correlation of composition, structure, and mechanics, finding new mechanical mechanisms within the soft tissue of the enthesis, as well as an overall picture of the enthesis at the microscale. The techniques

developed in this study are then extended to other systems for the development of high resolution, non-destructive imaging of the exact concentration of different biochemical components found in articular cartilage. This technique has the clinical potential for analyzing local cartilage composition on living tissue. Information learned from the analysis of the enthesis is then applied for the development of interfacial scaffolds for tissue engineering the enthesis. These scaffolds possess an interface between mineralized and unmineralized tissue that has application for interfacial engineering. Lastly, a study focusing on the development of a laboratory for introducing engineering to early-stage students is discussed. This laboratory is directed establishing critical thinking skills revolving around engineering and design in up-and-coming scientists. Supplemental information for this dissertation includes Movies 2.1 – 2.12 and Movie 4.1, which can be accessed online.

BIOGRAPHICAL SKETCH

Alexander Boys was born in Pottstown, PA. Alex attended high school at the Hill School, where his interests shifted across numerous subjects. He ultimately applied to Lehigh University as a humanities major. Prior to matriculating at Lehigh, Alex took Physics with Tom Hutchinson, a Lehigh Alumnus. Alex loved physics and changed his major to engineering prior to his arrival at Lehigh. Alex graduated from the Hill School in 2009.

At Lehigh University, Alex chose to major in Materials Science and Engineering. He received his education from numerous excellent professors, including Dr. Wojciech Misiolek, Dr. Richard Vinci, and Dr. John DuPont. After his sophomore year, Alex received an internship at Stryker Orthobiologics, operating under Antony Koblish and Dr. Maarten Persenaire, in the Clinical Department, working under Joe Popowicz. Alex's work at Stryker began his foray into the biomedical sciences. Arriving back at Lehigh, Alex began research under Dr. Himanshu Jain on the formation of dual-porous bioglass. Alex's work focused on applying the pore-forming techniques developed by the Jain Lab to an FDA-approved composition of bioglass. Alex graduated from Lehigh University in 2013 with High Honors having received the Bradley Stoughton Student Award for outstanding achievement in Materials Science and Engineering.

Alex began his Ph.D. at Cornell University in Materials Science, working jointly under Dr. Lara Estroff and Dr. Lawrence Bonassar. Alex has been very successful at Cornell, receiving numerous fellowships, including a NIH F31 Fellowship and a NSF EAPSI Fellowship. Alex has published two first-author papers, with three more in progress. Alex has also given six talks at international conferences over the course of his Ph.D., in addition to multiple other presentations.

Upon finishing his Ph.D. at Cornell, Alex will begin postdoctoral work at the University of Cambridge under Dr. George Malliaras and Dr. Róisín Owens. Following his postdoctoral work, Alex plans to begin an academic lab focusing on interfacing materials with the human body.

I would like to dedicate my dissertation to my parents, who have done so much to help me throughout my life. Thank you for always being there for me. I wouldn't be where I am today without your love and support.

ACKNOWLEDGEMENTS

I have had the honor and the pleasure of working with numerous amazing people during my time at Cornell, many of whom have been invaluable to my success. I first want to thank my two excellent advisors, Lara Estroff and Larry Bonassar. Thank you for providing me with help, feedback, and advice throughout my time in graduate school. Also thank you for putting up with me wandering into your offices at random times over the years and still providing me with a word of advice or even a lengthy conversation. I also want to thank all the other faculty and doctors I've interacted with at Cornell and elsewhere, especially Lisa Fortier, Itai Cohen, Shefford Baker, Michelle Delco, Peter Doerschuk, Eve Donnelly, Delphine Gourdon, Justin Jiang, and Scott Rodeo.

I want to acknowledge my groupmates who were always around over the years for some help or a conversation. To the members of the Estroff and Bonassar Groups, especially Coit Hendley, Mary Clare McCorry, Ethan Susca, Jennie Kunitake, Reum Scott, Abby Goldman, Chris DiDomenico, Ben Cohen, Kasia Oleske, Jill Middendorf, Nicole Diamantides, Damian Palin, Corinne Henak, Brandon Borde, Jenny Puetzer, Zihao Zheng, Amnon Ortoll-Bloch, and Emily Asenath-Smith, thank you for not only being my colleagues but also my friends.

I also want to thank my other friends scattered around campus and now the world, specifically Ben Richards, Peter Beaucage, Ryan Harris, Tom Gardinier, Heather Hunt, Ben Mac Murray, Brian Schutter, Lena Bartell, Erik Taylor, Pablo Palomino, Shreyas Honrao, John Eom, and Ben Treml.

I especially want to acknowledge all the wonderful undergraduate and masters students I had the privilege of working with at Cornell: Leanne Iannucci, Hao Zhou, Tianyu Gao, Gavisha Waidyaratne, Rachel Boedecker, Jordan Harrod, Kiara Chan, Natalie Goh, Ebuka Onwuchekwa, Tyler Khilnani, Crystal Zhao, and Roland Babmatee.

I of course also need to thank the funding organizations which supported my work throughout my Ph.D. research. I would like to acknowledge the National Institute of Arthritis and Musculoskeletal and Skin Diseases (NIAMS) of the National Institutes of Health (NIH) under award (F31AR070009). I also would like to acknowledge the NSF EAPSI program for sending me to China to work at the National Center for Nanoscience and Technology in Beijing, as well as NYSTAR, the Dow Scholarship, the John McMullen Fellowship, and the Morel Graduate Fellowship for supporting my research. I also want to acknowledge the Cornell Center for Materials Research (CCMR) for my making my work at Cornell possible. I especially want to thank Mark Walsh and John Grazul for their part in my work.

Lastly, I want to thank my family and friends for supporting me throughout my life. To my mom and dad, to Jody, Shawn, and Declan, to Uncle Ernie and Aunt Sandy, to the Carles, and lastly to my wonderful fiancée and soon-to-be wife, Stephanie Mack, thank you all so much. I couldn't have done this without you.

TABLE OF CONTENTS

LIST OF FIGURES

LIST OF TABLES

LIST OF SCHEMATICS

PROLOGUE

This dissertation focuses on the characterization and construction of tissues found in orthopedic systems. These tissues have unique spatial patterns in structure and composition that allow them to function under high loads. Particularly, interfacial systems, such as the enthesis, hold a broad interest in the engineering community, as current synthetic materials cannot mimic the properties of these biological interfaces. Therefore, characterization of these structures to understand the mechanisms by which nature binds highly dissimilar materials is an important area of study.

Chapter 1 is a review of mechanical interfaces found in biology and the tissue engineering of such systems. The mechanical interfaces discussed herein typically link soft to hard tissues, namely the meniscus, ligaments, and tendons to bone. These interfaces, termed entheses, are important in musculoskeletal function, allowing for actuation and stabilization in joints. Further, they are interesting systems, as they mediate large order of magnitude changes in properties over small areas, a feat that has not been replicated in engineered systems. The structure of these interfaces is a typically a graded series of regions that are continuously connected. This chapter outlines the structure of these tissues and the attempts by various research groups to engineer such systems. Engineered systems often consist of joined regions that are designed to mimic the properties of the native tissue regions. However, these engineered tissues have generally proven insufficient to accurately recreate the enthesis, calling for a further examination of native tissue composition, structure, and the resulting mechanics.

Chapter 2 focuses on the characterization of the native meniscal enthesis. As highlighted in Chapter 1, the exact mechanisms by which the enthesis functions are still unknown, therefore requiring an in depth analysis of enthesis composition, structure, and mechanics. This study uses spatially resolved Raman microscopy to assess regional changes in composition and structure across the enthesis. These data are combined with a spatially resolved mechanical analysis through

confocal elastography. Overall, the analysis shows two major compositional regions that map to five structural regions, resulting in three mechanical regions. This analysis of the enthesis reveals the major mechanisms that lead to enthesis function under physiological loading conditions, providing a series of structural and compositional features that are required for the creation of a synthetic enthesis. Overall, this study dictates a spatially resolved structure-function relationship, providing the necessary information for engineering an enthesis.

Chapter 3 extends the techniques developed in Chapter 2 from Raman microscopy to other tissues. Namely, this chapter provides a non-destructive spatially resolved analysis of living articular cartilage, with the potential for clinical application. Compositional changes in articular cartilage are associated with changes in local mechanical properties as well as certain disease states. The current field standards for identifying relative and absolute local composition rely on destructive means, typically histological or biochemical analyses of explanted tissues. Raman microscopy provides an alternative methodology for analyzing living systems without damaging the tissue. Here, relative local compositions are generated using a statistical analysis of Raman spectra that closely matches data collected through field standard analysis. We also show that tissues remain alive and undamaged throughout analysis. Overall, this technique may prove a useful diagnostic tool for analyzing cartilage and other tissues *in vivo*.

Chapter 4 discusses the extension of data collected in Chapter 2 to the development of an interfacial tissue scaffold. This scaffold is generated by explanting trabecular bone biopsies and spatially removing mineral content from these structures, thus creating an interfacial scaffold with spatially varying mineral content. The mineral removal process is performed by hanging the biopsies in a demineralizing solution that was shown to remove mineral content without affecting the underlying collagen structure. The exact progression by which the mineral was removed was examined, generating a repeatable process for creating these scaffolds. Further, the scaffolds were

tested for their ability to support a population of stem cells, showing high cell viability and differences in cell behavior with respect to local mineral content. Overall, these scaffolds can be applied to a variety of systems for regenerating or recreating interfacial tissue systems.

Chapter 5 describes the development of an educational laboratory for introducing engineering and design concepts to students earlier in their academic careers. This study identifies a dearth of engineering concepts at early stages in academic curriculae, specifically those targeting elementary- to middle school-aged children. The laboratory described seeks to teach these concepts in an approachable manner for younger students to introduce scientific concepts that they can use to judge designs they generated. This laboratory utilizes casting, a common industrial process, to generate a series of objects that have varying properties based on the initial viscosity of the fluid used to generate the object. Students are asked to evaluate the resulting objects based on a series of criteria and produce a recommendation for production. A study was performed to evaluate the success of this laboratory for teaching these concepts to children finding overall success. This laboratory will ideally aid students in learning important critical thinking skills earlier in their careers.

Overall, this dissertation focuses on biological interfaces, tissue characterization and engineering, and scientific outreach. This work identifies a series of areas in orthopedics that have not yet been fully explored but are necessary for treating a variety of conditions and ailments that affect significant portions of the population. The advanced characterization techniques developed in this dissertation can be used to analyze living tissue systems, producing vast amounts of information relating to local mechanics and function. Such information can be used to engineer complex tissue structures for the production of implants. Lastly, this dissertation highlights the generation of a laboratory for teaching up-and-coming scientists and engineers, as these studies and others cannot continue without future generations of researchers.

CHAPTER 1

Next Generation Tissue Engineering of Orthopedic Soft Tissue-to-Bone Interface[1]

Abstract

Soft tissue-to-bone interfaces are complex structures that consist of gradients of extracellular matrix materials, cell phenotypes, and biochemical signals. These interfaces, called entheses for ligaments, tendons, and the meniscus, are crucial to joint function, transferring mechanical loads and stabilizing orthopedic joints. When injuries occur to connected soft tissue, the enthesis must be re-established to restore function, but due to structural complexity, repair has proven challenging. Tissue engineering offers a promising solution for regenerating these tissues. This prospective review discusses methodologies for tissue engineering the enthesis, outlined in three key design inputs: materials processing methods, cellular contributions, and biochemical factors.

Introduction

Soft tissue-to-bone interfaces are present in many tissues, supporting movement in vertebrate animals. These interfaces mediate transitions between materials with highly dissimilar mechanical properties, with a three or more order of magnitude change in stiffness occurring over only a few hundred microns.[1–3] While these interfaces are robust, undergoing wear and tear over the entire lifespan of humans, they fail in instances of extreme joint loading. Tissue engineered replacements can be constructed outside of the body and implanted as living tissue, offering a promising alternative to current repair options. This review discusses the structure and development of some representative orthopedic interfaces in the body (e.g. ligamentous, tendinous, and meniscal

[1] This chapter is published: Boys, A. J., McCorry, M. C., Rodeo, S., Bonassar, L. J., Estroff, L. A. Next generation tissue engineering of orthopedic soft tissue-to-bone interfaces. *MRS Comm*. **7**, 289-308 (2017).

attachments) and how we can use this information to engineer living tissues for the repair and replacement of these mechanically, compositionally, and structurally complex interfaces.

The ligamentous, tendinous, and meniscal attachments, also called entheses, act to anchor soft tissues to bone. Injuries to the enthesis often result in acute disability and may ultimately predispose the affected joint to diseases such as osteoarthritis, a disease estimated to affect over 70% of people aged 55 to 78.[4] Severe injuries of these tissues often require replacement, which is typically accomplished using cadaveric tissue (allograft) or tissue removed from the patient's own body (autograft) (Figure 1.1). Allograft tissue can effectively replace the damaged tissue in its

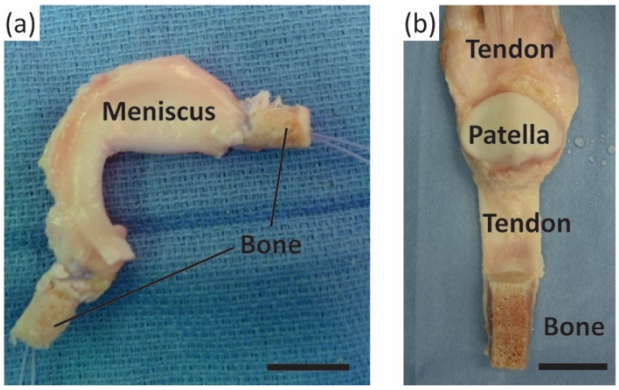

Figure 1.1 Surgical adult human allograft replacements for **a** meniscus and **b** patellar tendon with full bone insertions intact. Sutures are threaded through the insertion points and pulled into bone tunnels to anchor allograft tissues in place. Leaving the entheses intact obviates the need for enthesis healing, increasing the success rate for patient recovery. Scale bars are 20 mm.

entirety. For example, in the case of meniscus replacement, an allograft tissue consists of the entire meniscus, including the entheses.[5] Proper fixation of the implant at the entheses is a necessity for surgical success.[6] Including the entheses also obviates the need to reconstruct this complex interface between soft tissue and bone. Despite the advantages of allografts, limitations related to cost, tissue sizing, availability, and potential for an adverse immune response still exist. Autograft tissue is also frequently used for ligament and tendon repair, where a portion of the patient's native tendon is used. However, autograft tissue replacement can require multiple surgical sites, and harvest of autografts from ligament sites is not feasible. Tissue engineered implants combine the advantages of both the allograft and autograft options in that they offer a customizable, living implant that can be produced without requiring a donor or donor site.

Tissue engineering interfaces requires an interdisciplinary effort among biomedical engineers, materials scientists, and orthopedic surgeons. These tissues are complex in nature, consisting of multi-scale arrangements of multiple tissue types. The mechanical function of these interfaces is derived in part from the hierarchical arrangement of relatively simple building blocks into composite materials. Interfacial tissues are integrated into a continuous gradient populated by a variety of cell types, and these cell types are accompanied by chemical factors and signaling molecules that influence the maturation of these tissues and maintain homeostasis.[7–9] Two types of entheses can be found in the body: direct and indirect. Direct entheses have a fibrocartilaginous region between the bone and the highly organized collagen fibers of the ligament, tendon, etc.[10] Conversely, indirect entheses are usually observed on the shafts of long bones and have fibers that connect directly into bone (Sharpey's fibers) (Figure 1.2). This review will focus on direct entheses.

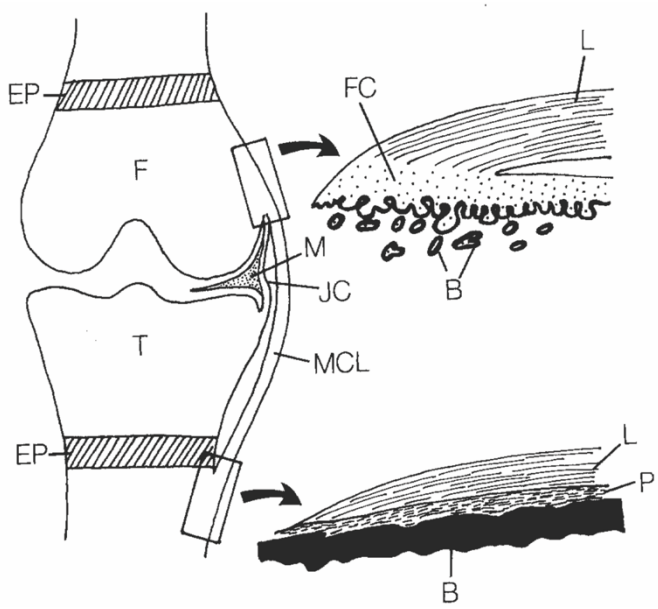

Figure 1.2 Schematic of the direct and indirect entheses for the femoral and tibial insertions of the medial collateral ligament (MCL), respectively. Abbreviations are as follows: femur (F), tibia (T), fibrocartilage (FC), ligament (L), bone (B), periosteum (P), meniscus (M), joint capsule (JC), and epiphyseal plate (EP). Reprinted from Springer Anatomy and Embryology, An immunohistochemical study of enthesis development in the medial collateral ligament of the rat knee joint, Volume 194, Issue 4, 1996, 399 – 406, J. Gao, K. Messner, J. R. Ralphs, M. Benjamin, © Springer-Verlag 1996, with permission of Springer.[11]

All direct entheses have the same general subdivisions based on tissue type, as observed through histological analysis: subchondral bone, calcified fibrocartilage, uncalcified fibrocartilage, and oriented soft tissue.[12–14] Comparative structures of tendon, ligament, and meniscal entheses are highlighted using a tetrachrome stain of sagittal sections of these interfaces (Figure 1.3). The

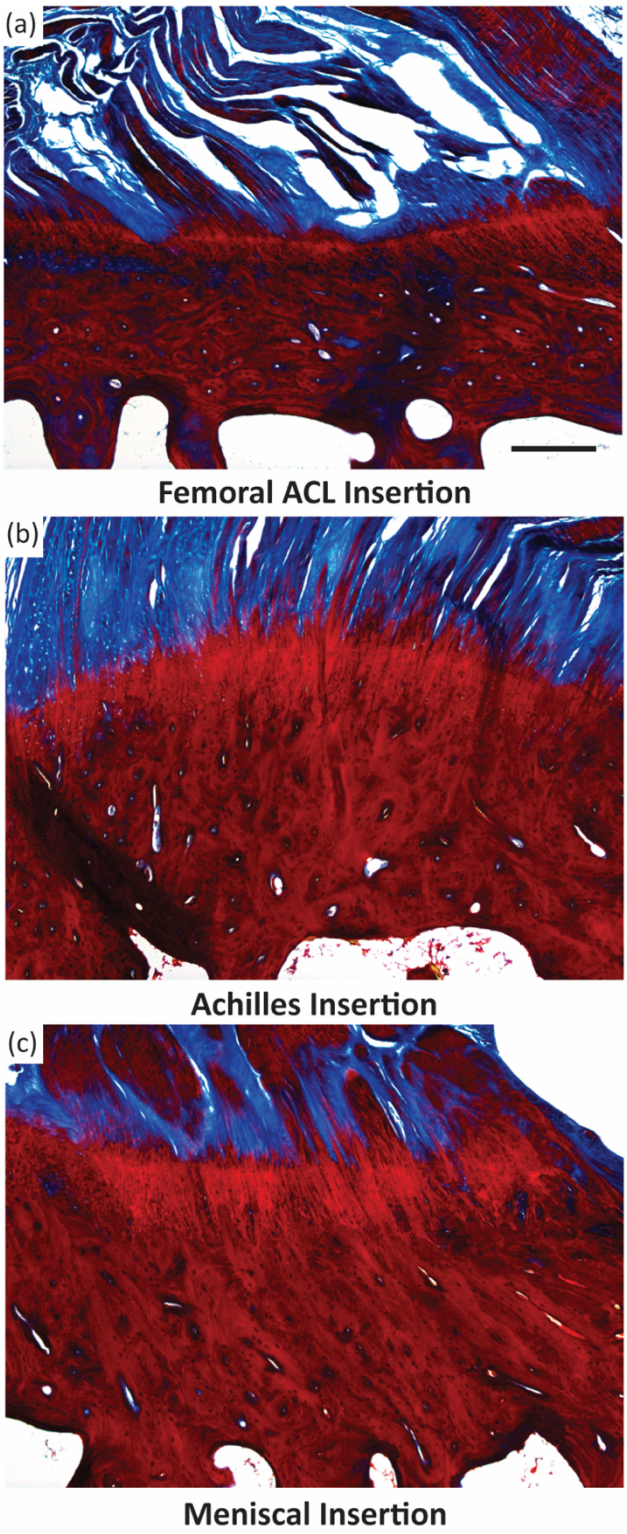

Figure 1.3 Light microscope images of three different osteochondral interfacial tissues, stained with tetrachrome stain. All images show ovine tissue, cut in the sagittal plane of the enthesis: **a** the femoral anterior cruciate ligament (ACL) insertion, **b** insertion point of gastrocnemius tendon with the calcaneal bone, referred to here as the Achilles insertion, and **c**, the meniscal insertion. Trabecular pores are visible on the bottoms of each image, beneath dense calcified bone (deep red). Porous regions transition through to fibers (blue). Note the varying thicknesses of the interfacial regions, and variable morphology of the intermediate bony regions per anatomy. Scale bar is 400 μm.

extracellular matrix (ECM) of these tissues consists primarily of collagen, proteoglycans, and apatite. The interfacial region consists of a spatial distribution of cell types, moving from bone

cells (osteoblasts, osteoclasts, osteocytes) to hypertrophic fibrochondrocytes in the calcified fibrocartilage to fibrochondrocytes in the uncalcified fibrocartilage to fibroblasts in the oriented collagenous region of the enthesis (Figure 1.4). These cell types are accompanied by biochemical and biomechanical cues that also vary by region, often with temporal and spatial gradients in concentration.[15–18] The demarcation between calcified and uncalcified fibrocartilage is called the tidemark, referring to a distinctive transition between tissue regions. However, recent evidence indicates the presence of a mineral gradient at what has been historically referred to as the tidemark, meaning that this shift in composition may be less distinct.[7,12,19]

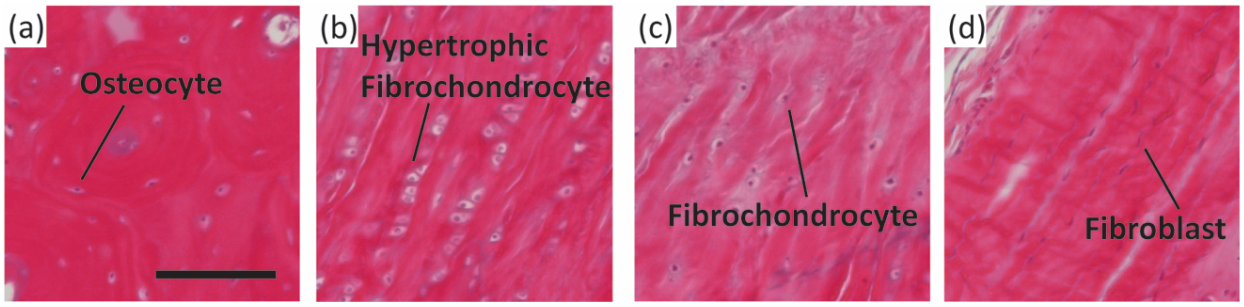

Figure 1.4 Representative histological images of cellular phenotypes from **a** bone, **b** calcified fibrocartilage, **c** fibrocartilage, and **d** ligament from a mature ovine ACL enthesis (hematoxylin and eosin). **a** Osteocyte embedded between lamellae of an osteon. **b** Enlarged hypertrophic fibrochondrocytes organized in columns indicating rapid proliferation. **c** Fibrochondrocyte in disorganized fiber region. **d** Elongated spindle shaped fibroblast between large organized fibers. Scale bar is 200 μm.

As a prospective review, this paper highlights current methods of designing and fabricating a tissue engineered enthesis construct with a view toward future directions. Enthesis engineering is still at an early stage, even when compared with other tissue engineering efforts. While prior studies have examined methods to engineer bulk tendon, ligament, meniscus, and even other orthopedic interfaces,[20,21] such as the osteochondral interface and the periodontal interface,[22,23] few studies have focused on engineering entheseal tissues.[7–9] This review divides the orthopedic interface engineering process into three main design inputs: materials processing methods, cellular contributions, and biochemical factors. These inputs must be developed in parallel for both the

osteogenic and soft tissue-generating portions of a construct, then combined across an interfacial region of the construct to promote continuity and integration. This interface can be formulated into either continuous but opposing gradients of soft tissue and bone inputs or a compartmentalized interface, consisting of multiple regions that reflect the composition of the native tissue. Following tissue assembly, the maturation process is key to promote eventual integration with the local joint tissues (Figure 1.5). The following sections discuss these inputs individually and address how these methods can be utilized in parallel to generate soft tissue-to-bone interfaces.

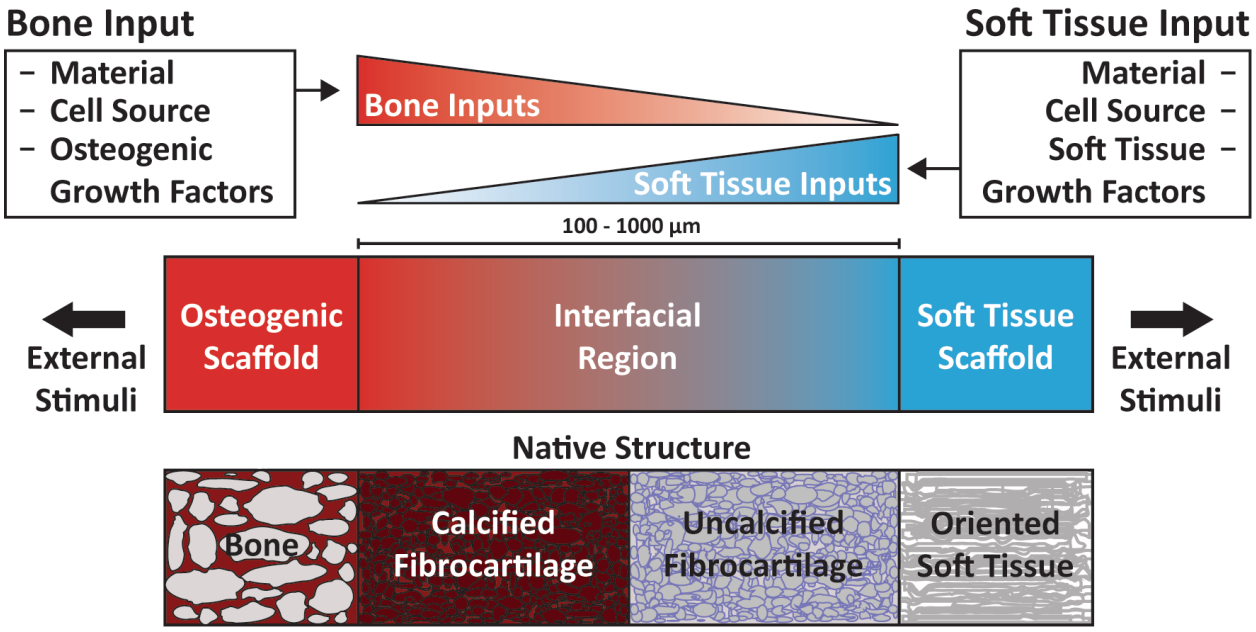

Figure 1.5 Schematic highlighting the process for constructing a tissue engineered interfacial construct. Materials, cell source, and growth factors are the central input considerations for a tissue engineering study design. The interfacial region requires complementary gradients of bone and soft tissue inputs. Following construct assembly, external stimuli such as mechanical loading can be applied to further aid in tissue development.

Materials Processing Methods

The architecture of the enthesis is complex, consisting of hierarchical arrangements of collagen fibrils, proteoglycans, and apatite [$Ca_{10}(PO_4)_6(OH)_2$] crystals. The molecular composition, spatial distribution, and nano- to micro-scale assembly of these components dictate the properties of each tissue region and are critical for defining the mechanical stability of the entire enthesis. The

following sections describe the native enthesis structure and methods for mimicking this structure through tissue engineering.

Native Organization

Collagen is the main component of the enthesis. Three major types of collagen are found across the interface: type I, type II, and type X. Collagens III, V, and VI are also found in these interfaces at much lower concentrations.[24] Types I and II collagen are fibrillar collagens, meaning they self-assemble into organized nanofibers, ~50 to 500 nm in diameter.[25] Type I collagen is deposited in association with tensile forces and is found in bone and ligamentous tissue. Type II collagen is associated with compressive forces and is found primarily in fibrocartilaginous regions.[15,26] The presence of compressive forces has been postulated to aid in the reduction of stress concentrators in the enthesis, possibly indicating the origin of type II collagen.[27] These fibrillar collagens can further assemble into increasingly large fiber-like structures. This type of organization is found within the oriented soft tissue of the entheseal attachments and is typically associated with type I collagen. Collagen fibrils in this region can bundle together into structures called fascicles, ~50 to 300 μm in diameter, which are in turn bundled into large fibers, ~100 to 500 μm in diameter.[25] Type X collagen is found in calcified fibrocartilage regions and is non-fibrillar.[15] Type X collagen is thought to play a role in ossification, but its exact function is unknown. Hypotheses include type X collagen acting to regulate mineralization at the ossifying front, and type X collagen functioning as a matrix protein and facilitating the ingrowth and mineralization of new bone.[28]

The enthesis contains proteoglycans that bind water, provide compressive strength, and contribute to collagen fiber formation. Proteoglycans consist of a central core protein and at least one covalently attached glycosaminoglycan (GAG) chain. GAGs are linear, highly charged polysaccharides that can contain sulfate and carboxylate groups.[29] Aggrecan is the predominant proteoglycan in cartilage and fibrocartilage and is the largest of the proteoglycans. In tendon and

ligament, aggrecan is most prevalent in regions of compression and in the fibrocartilage of the insertion site.[24,30] Similar to ligament and tendon, aggrecan in the meniscus is located in the inner portion of the meniscus, which is subject to more compressive loads, and the entheseal attachments.[31,32] The large "bottle brush" structure and negative charge of aggrecan helps to bind and retain water, which contributes to the ability of the tissue to resist compression.[33] Small leucine-rich proteoglycans (SLRPs) such as fibromodulin, decorin, and biglycan are known to bind to collagen and help to regulate collagen fiber formation and maintenance.[34–36] SLRPs are prevalent in association with highly organized collagen bundles of tendon, ligament, and meniscus.[32,37] Aggrecan is often found in regions of soft tissue-to-bone interfaces under compressive loading, while SLRPs are found in regions with large fibers experiencing tensile loads.[32]

Apatitic mineral is found within the subchondral bone and calcified fibrocartilage regions of the interfacial tissues. The mineral phase is primarily non-stoichiometric hydroxyapatite with carbonate substitutions, as opposed to geologic hydroxyapatite,[38] that is arranged into nanocrystalline platelets. In bone, these platelets are contained within collagen fibrils and are oriented with their c-axis parallel to the direction of the fibril. Non-collagenous proteins are thought to organize the apatite platelets into the intrafibrillar spacing of collagen, but the exact mechanism through which this hierarchical structuring occurs is unknown.[39] Thorough reviews of bone structure are available.[40,41] The mineral phase in calcified fibrocartilage is also mainly carbonate-substituted hydroxyapatite, but the organization of the crystals within the matrix is not as well understood.[12,42]

Aggregating the above information, subchondral bone consists of type I collagen fibrils infiltrated with nanocrystalline, carbonated apatite arranged circumferentially around pores, typically on the order of 1 mm in diameter.[43] This structure transitions into non-porous calcified

fibrocartilage, consisting of type II and type X collagen, apatitic mineral, and proteoglycans. Uncalcified fibrocartilage consists of splayed fibrils of type II collagen with proteoglycans. These splayed fibrils transition from the uncalcified fibrocartilage region into large type I collagen fibers that make up the oriented fiber region of the enthesis.[32,44] Understanding native structure/composition should inform material selection for tissue engineering.

Materials Selection

Appropriate materials for a tissue engineered scaffold must possess adequate mechanical properties, support cellular attachment and differentiation/proliferation, and potentiate cellular remodeling. Since the modulus ranges drastically across soft tissue-to-bone interfaces, a variety of materials have been used for tissue engineered constructs. To match the moduli of the stiff, mineralized regions of the enthesis, various calcium phosphate minerals, such as hydroxyapatite and tricalcium phosphate, and bioglass have been used.[45–51] The compliant portions of the enthesis have been constructed from polymers and copolymers consisting of poly(capralactone) (PCL), poly(lactic acid) (PLA), poly(glycolic acid) (PGA), and/or poly(ethylene glycol) diacrylate (PEGDA),[49,51–56] as well as other biopolymers such as silk, agarose, gelatin, hyaluronic acid, and collagen.[48,57–62] Decellularized or demineralized native matrices have also been used to engineer the enthesis.[49,60,61,63,64]

Materials-based Design & Fabrication

The complex structure of the enthesis is related to its function, providing continuity and integration between multiple tissues with differing properties. The necessity for this integration and continuity arises from the loading of such interfaces in tension;[8] hence, failure modes like delamination become relevant for poorly integrated constructs. To promote continuity, various materials processing techniques have been used. Many of these techniques revolve around the construction of gradients or the binding of multiple “compartmentalized” materials. Controlled crystal growth

on electrospun poly(lactic-*co*-glycolic) acid (PLGA) resulted in a nanofiber scaffold with a mineral gradient.[47] This gradient was formed through syringe pump-mediated injection of a calcium and phosphate salt-containing solution. Upon cell-seeding, the activity of alkaline phosphatase (ALP), an enzyme associated with mineral deposition, the expression of RUNX2, an osteoblast-related transcription factor, and the expression of osteocalcin, an osteoblast-related protein, were correlated with mineral deposition. Cellular density and cell proliferation were negatively correlated with mineral deposition.[47] These results indicate that proper processing and appropriate arrangement of enthesis-related materials result in spatially localized cellular responses that mimic those found in the body. However, implantation of this scaffold for the repair of the murine supraspinatus tendon resulted in scar formation, indicating that further processing is required for optimal enthesis reconstruction.[65]

Regional integration in scaffolds can also be induced through the production of microstructure gradients. For example, freeze-casting coupled with salt-leaching enabled the formation of a multi-region scaffold composed of silk fibroin (Figure 1.6a).[58] The processing conditions were designed to form a continuous scaffold with a porous, trabecular bone-like structure that transitions into a fiber-like morphology. The porous region results from salt-leaching, in which a solution of silk fibroin and NaCl is frozen and freeze-dried. The precipitated salt crystals are subsequently dissolved, creating pores within the silk matrix. This region transitions to a fiber-like morphology, created using freeze-casting, a process in which directional freezing is used to grow elongated ice crystals within a polymer solution. During solidification, the polymer, i.e. silk fibroin, is concentrated into the boundaries between the crystals.[66] Upon sublimation of the ice crystals, oriented fiber-like structures composed of silk fibroin remain. These processing methods result in a continuous silk structure that mimics the morphology of collagen in the native enthesis.[58] Similar

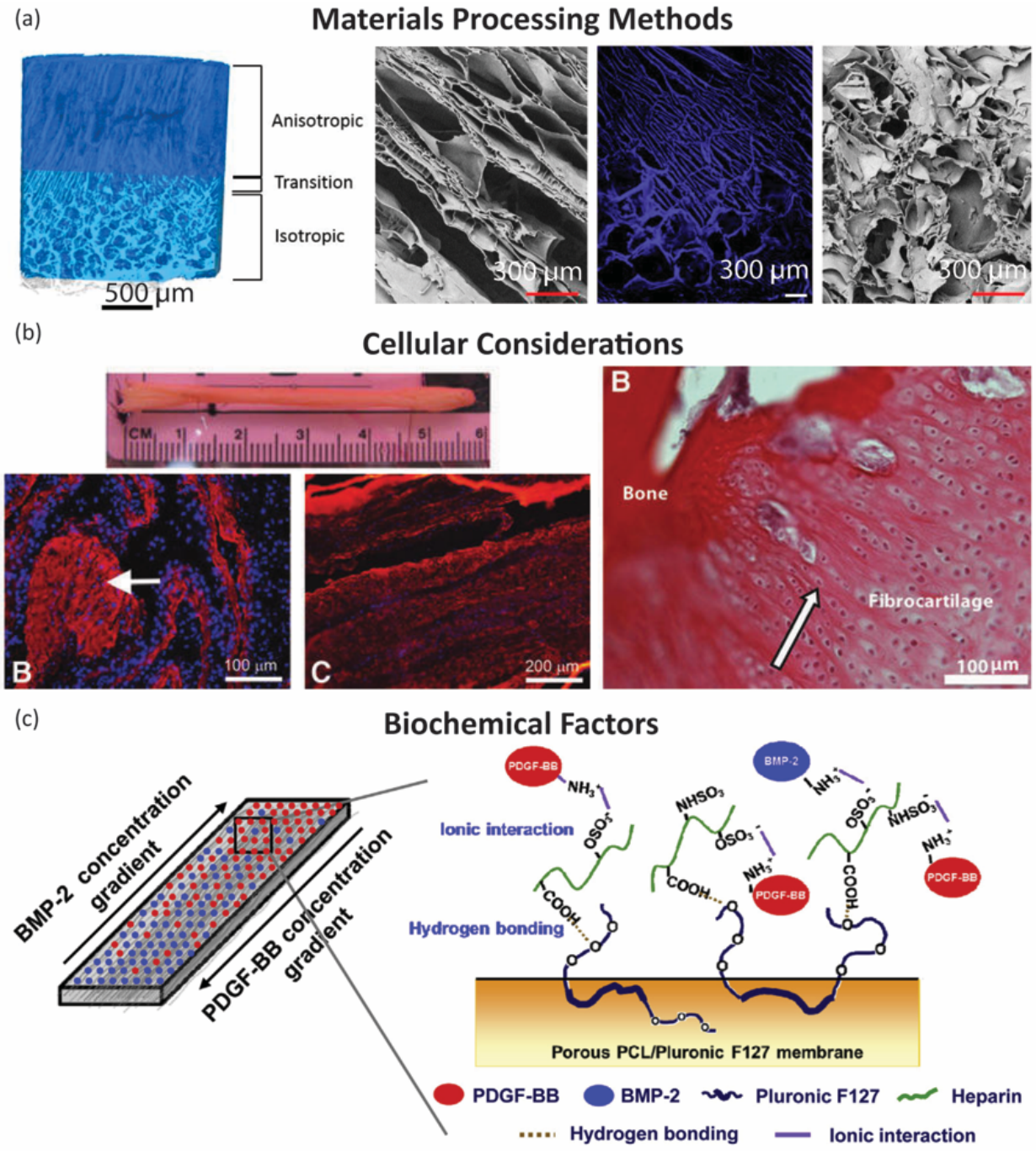

Figure 1.6 Examples of tissue engineered interface constructs for soft tissue to bone. **a** Biphasic anisotropic silk fibroin scaffold with integrated fiber/bone interface. Images from left-to-right: µCT of full construct, field emission scanning electron microscopy (FESEM) image of, anisotropic (fiber) region, fluorescence microscopy image of transition region, and FESEM image of porous "(trabecular) region. Reprinted with permission from TISSUE ENGINEERING, Part A, Volume 23, Issue 15-16, published by Mary Ann Liebert, Inc., New Rochelle, NY.[58] **b** Bone-ligament-bone ACL replacement generated using stem cell self-assembly and targeted differentiation. Images from left-to-right: full tissue engineered construct, immunostained for collagen (red) and

DAPI stained (nuclear stain) section showing bony region prior to implantation, immunostained for collagen (red) and DAPI stained (nuclear stain) section showing ligament region prior to implantation, image of regenerated fibrocartaliginous region with aligned nuclei (arrow) after 2 months implantation. Reprinted with permission from TISSUE ENGINEERING, Part A, Volume 18, Issue 1-2, published by Mary Ann Liebert, Inc., New Rochelle, NY.[68] **c** Porous membrane with inverse gradients of PDGF and BMP-2 for tendon-bone repair. Reprinted from Acta Biomaterialia, Volume 10, Issue 3, Hyun Ki Min, Se Heang Oh, Jonh Min Lee, Gun Il Im, Jin Ho Lee, Porous membrane with reverse gradients of PDGF-BB and BMP-2 for tendon-to-bone repair: In vitro evaluation on adipose-derived stem cell differentiation, 1272 – 1279, Copyright © 2013, with permission from Elsevier.[69]

scaffolds have been produced for the osteochondral interface, demonstrating the customizability of these techniques.[67]

Structural characteristics are important in that they not only affect the mechanical properties of the scaffold but also drive cellular differentiation. Fiber alignment drives matrix deposition rates in meniscal fibrochondrocytes and mesenchymal stem cells (the progenitor cells for bone, cartilage, etc.).[70] Pore size affects the production of cartilage matrix proteins by cells. For example, smaller pore sizes cause cells to produce more GAGs.[22] In addition to structurally-derived cellular effects, the material composition of scaffolds also has an effect on differentiation. The addition of hydroxyapatite to scaffolds improves osteogenic properties and increases cellular attachment,[45,56] and the presence of GAGs in scaffolds drives cells toward a chondrogenic lineage.[71,72]

The use of materials to control cellular responses can also be achieved through biodegradability and remodeling. For example, a compartmentalized triphasic scaffold, created by sintering polyglactin mesh, PLGA microspheres, and bioglass and PLGA microspheres together, shows varying rates and types of tissue ingrowth into the scaffold following subcutaneous implantation.[51] All regions of the scaffold showed collagen deposition, and the bioglass and PLGA microsphere region allowed for mineral deposition. The polyglactin region degraded entirely, producing a fibrocartilage-like area between the polyglactin and PLGA microsphere region.[51,73] In design of scaffolds that utilize multiple materials, structural considerations must be made for the

types of mechanical forces to which the scaffold will be subjected. For example, fused microspheres are resistant to compression and polyglactin mesh is resistant to tension, but neither structure is designed to resist shear. Additionally, the differing structures could result in stress concentrations at the interface between the materials, arising from dissimilarities in their Poisson's ratios. Use of biodegradable materials can promote tissue infiltration, and particularly in this case, can be used to diminish the sharpness of the interface over time. The mechanism of biodegradation should also be considered for tissue engineering. Biodegradable polymers like PLA and PGA can be degraded through hydrolysis, opening up space for tissue to grow into, whereas biopolymers such as collagen must be enzymatically degraded and rearranged by cells, providing a template for remodeling. For example, cells rearranged collagen gels into large, oriented fibers during culture of a meniscus construct, indicating the value of incorporating cellular remodeling capability into a scaffold.[74] Implementation of continuity, integration of structure, and support for cellular remodeling in scaffolds allows for control of mechanical properties, strengthening of interfacial regions, and ability of the scaffold to integrate with native tissue upon *in vivo* implantation.

Cellular Contributions

Cells and cellular interactions drive the maturation of scaffolds before implantation and integration of scaffolds with native tissue after implantation, therefore cellular content is an essential component to the design of any tissue engineered construct. Biocompatibility, cellular integration, and cellular remodeling are key considerations when creating, culturing, and implanting a construct. Cells function in complex 3D environments and respond to a plethora of inputs including materials interactions, substrate stiffness, mechanical conditioning, biochemical signaling, and cell-cell interactions. Tissue engineering approaches utilize such inputs to drive maturation of a functional construct.

Native Cell Types

Soft tissue-to-bone interfaces span four regions with distinct cellular phenotypes (Figure 1.3 and 1.4). Each cellular type found in the enthesis has a distinctive behavior, cell shape, matrix production profile, and genetic expression that defines its phenotype. Osteoblasts, osteoclasts, and osteocytes are the three main cell types that reside in bone. Osteoblasts initiate new bone formation, while osteoclasts resorb and remodel bone. An osteocyte is a terminally differentiated osteoblast that resides in the mineralized matrix to maintain bone homeostasis (Figure 1.4a). Together, these cells regulate bone formation and maintenance. The bone phenotype is typically quantified by expression or accumulation of proteins, such as osteopontin and osteocalcin, type I collagen, markers of mineralization, such as ALP activity, and expression of transcription factors, such as RUNX2.[75] The transition from bone to the calcified fibrocartilage region, is regulated by hypertrophic fibrochondrocytes (Figure 1.4b). Hypertrophy is the process in which chondrocytes increase in size and secrete type X collagen in a mineralized cartilaginous matrix.[76] In contrast, chondrocytes are found in cartilage and exhibit a rounded morphology. These cells reside in a proteoglycan-rich (mostly aggrecan) matrix composed of collagens I and II. Chondrocytes, found in the cartilaginous tissue, have upregulated levels of aggrecan, type II collagen, link protein, Sox9, and COMP genes.[77] Fibrochondrocytes that reside in the uncalcified fibrocartilage region of the enthesis are named as such because they exhibit phenotypic markers of both fibroblasts and chondrocytes (Figure 1.4c).[78] The native cell phenotypes serve as benchmarks for cell behavior and stem cell differentiation in tissue engineered constructs. Ligament cells and tenocytes (tendon cells) are often described as exhibiting a fibroblastic phenotype due to their spindle shape and production of type I collagen (Figure 1.4d).[18] While these two cell types belong to distinctly different tissues, they share many common markers. Key positive markers for this phenotype are

production of type I collagen, tenascin-C, scleraxis, tenomodulin, and proteoglycans such as decorin, biglycan, versican, lumican, and fibromodulin.[79,80]

Tissue Engineering with Cells

A consistent challenge of producing these soft tissue-to-bone interfaces is incorporating cells into the materials processing methods of the scaffold. Cellularizing these constructs can be accomplished by either encapsulating cells directly into the scaffold or by seeding cells onto the material surface and directing migrating cells into the scaffold. Growth factors or other chemoattractants are useful to encourage cellular migration and infiltration into scaffolds.[64,81,82] Processing cells and materials together restricts the conditions in which a scaffold can be processed. Cells require a specific operational window of temperature, pH, pressure, strain, osmolarity, and ion and solute balance in order to maintain viability. Furthermore, the soft tissue-to-bone interface contains an array of cell types. The number of cell types and the cellular locations in the tissue engineered scaffold play a role in soft tissue-to-bone interface assembly, culture, and development.

Given the gradient of cell types present in the enthesis, co-culture is one method to generate a graded interface. Different cell types are constantly interacting during native development and have intertwined signaling feedback mechanisms that are critical to development.[18,76,83] *Ex vivo* co-culture mediates cell-cell contact and paracrine interactions that have been shown to influence cellular phenotype. Co-culturing of chondrocytes and osteoblasts in direct contact using a high cell density 3D micromass reduced GAG deposition in chondrocytes and cell-mediated mineralization in osteoblasts.[84] Furthermore, co-culture can be used as a tactic to guide stem cell differentiation.[85–89] One strategy to create an integrated gradient is to co-culture the desired cell types and generate cell gradients that utilize cell-cell interactions to mature the material into a graded interface. For ligament-bone interfaces, 2D co-culture of fibroblasts and osteoblasts, modeled using a fibroblast region, interface region, and osteoblast region, decreased cell proliferation and increased cell-

mediated mineralization by fibroblasts. In addition, production of type II collagen and aggrecan increased, indicating that co-culture interactions can lead to cell trans-differentiation from one cell phenotype to another.[62] Co-culturing of different cell types is a useful technique to integrate the different tissue regions of the soft tissue-to-bone interface.

An alternative to using multiple cell types is using mesenchymal stem cells (MSCs), which can differentiate into multiple cell types. *In* vivo entheses begin as dense mesenchymal condensates and develop into complex interfaces.[90–92] Since MSCS have the capacity to differentiate into all the cell phenotypes of the enthesis, MSCs are a logical cell source to use for tissue engineering the enthesis.[93,94] MSCs from bone marrow (bmMSCs) are a popular source for tissue engineering, because they are easily obtained and expanded. Adipose-derived stem cells (ASCs) are another common stem cell source. Since ASCs are easily obtained from fat which is considered surgical debris, they are the most readily available stem cell source from human tissue. While ASCs do have multipotent properties, they have been shown to be less effective than bmMSCs at differentiating into cartilage and bone.[95] Stem cells seeded into tissue engineered enthesis constructs rely on mimicking the biomaterial and biochemical inputs that direct differentiation during development. For example, regional changes in pore alignment of a tendon/ligament enthesis silk fibroin scaffold resulted in corresponding ASC differentiation into cartilage and tendon lineages (Figure 1.6a).[58] These examples emphasize the importance of scaffold material and biochemical design in order to inform cell behavior when generating enthesis constructs.

Construct geometry and chemistry have been shown in multiple systems to affect cellular phenotype through cell-material interactions.[96,97] Cellular phenotypes can be dictated by cell-material interactions. A material such as collagen has cellular adhesion sites, allowing cells to bind and spread, encouraging the cells to develop a fibroblastic morphology. Alternatively, a material

lacking in cell adhesion sites, like alginate, prevents cells from binding, encouraging a chondrogenic morphology.[98,99] Cell morphology, such as a fibroblastic or chondrogenic morphology, has been shown to be an indicator for cell behavior and matrix production.[100] Scaffold mechanical properties are known to direct stem cell fate, where materials with stiffer structures promote osteogenic differentiation.[101,102] Lastly, chemical composition dictates cellular response. Cells embedded in a proteoglycan-rich region experience increased strain shielding compared to cells embedded in collagen fibers when a tissue level mechanical deformation is applied to the scaffold.[72] Furthermore, the arrangement and alignment of fibers in a 3D microenvironment affects cellular behavior and the distribution of applied loads. In an aligned poly(ethylene oxide) scaffold, cells attach and elongate in the direction of the fibers. Fiber alignment aided bmMSC differentiation into a fibrous phenotype compared to the same bmMSCs in pellet culture which developed a chondrogenic phenotype.[100] Furthermore, aligned fibers improved ligamentous phenotype, as cells develop characteristic spindle shapes and increase production of collagen when compared to random fiber alignment. The alignment of fibers also affects the cellular response to an applied strain, with longitudinal strains in the fiber direction inducing the largest increase in collagen production.[103,104] These studies emphasize the importance of material mechanical properties and structure when considering cellular interactions and response.

Another approach to tissue engineering soft tissue-to-bone interfaces shifts the focus from materials design to utilizing the cells themselves to create the scaffold. Cells grown in mono-layers have the ability to proliferate to fill the surface area and then self-assemble to form their own matrix. A multi-component bone-ligament-bone tissue engineered ACL graft was created using confluent cell monolayers (Figure 1.6b). The bmMSCs were first pre-differentiated into ligamentous or bone pathways in monolayer and then assembled together into a 3D scaffold. The resulting scaffold showed sufficient properties for ACL replacement and performed well during

long term implantation in an ovine model.[68] Gene transfer is another strategy to spatially regulate genetic modification and differentiation of primary dermal fibroblasts. A retrovirus encoding the factors RUNX2 and cbfa1 was used to induce osteoblastic and fibroblastic differentiation respectively.[105] These techniques demonstrate that cells can be used to produce complex gradients for soft tissue-to-bone interfaces.

Biochemical Factors

A range of biochemical factors can influence production and remodeling of ECM by cells. Growth factors are proteins that are secreted by cells and act as signaling molecules to other cells via cell surface receptors. These molecules play active roles in establishing the complex structure of the enthesis, healing the tissue after injury, and maintaining tissue homeostasis. This section highlights relevant biochemical signals in development and their application to enthesis tissue engineering.

Native Biochemical Signaling

Soft tissue-to-bone interfaces have a wide array of growth factors that influence cellular activities such as differentiation, proliferation, apoptosis, and matrix production. Key growth factor contributors to bone growth, repair, and differentiation are BMPs, transforming growth factor-βs (TGF-βs), and insulin-like growth factors (IGFs) (Table 1).[106–108] The growth plate contains similar regional zones to the enthesis since it is an interface between bone and cartilage. Growth factors secreted in the growth plate are essential to endochondral bone formation and include IGFs, Indian hedgehog (Ihh), parathyroid hormone-related peptide (PTHrP), BMPs, Wnts, fibroblast growth factors (FGFs), and TGF-βs.[76] Key players in bulk tendon and ligament development, healing, and remodeling are IGFs, growth and differentiation factors (GDFs), TGF-βs, vascular endothelial growth factor (VEGF), platelet-derived growth factor (PDGF), and FGFs.[109,110] IGFs, FGFs, TGF-βs, and PDGF are the central growth factors that contribute to developing and maintaining organized collagen structures and high levels of proteoglycans in cartilage and

Native Expression							Tissue Engineering Applications	
Growth Plate	Bone	Tendon	Ligament	Cartilage	Meniscus	Growth Factor	Isoform	Effect
X	X			X		Bone Morphogenic Proteins (**BMP**s)	**BMP-2**	Stem cell proliferation and differentiation into osteoblasts [50,54,69,111,112] Stimulate bone formation and mineralization [50,54,111–114]
							BMP-6	Enhance effect of TGF-β3 [115] Increase collagen production [89]
							BMP-7	Stimulate bone formation and mineralization [116]
X	X	X	X	X	X	Transforming Grown Factor-β **(TGF-β)**	**TGF-β1**	Encourages chondrogenesis [54,117,118] Increased production of collagen and GAGs [54,119–121] Increases proliferation [121–123] Under certain conditions can be osteogenic and associate with hypertrophy [50,122,124]
							TGF-β3	Encourages chondrogenesis [71,81,89,94,125] Increased production of collagen and GAGs [71,81,89,94,115,125] Enhance hypertrophic chondrocyte phenotype [124]
						Growth and Differentiation Factor **(GDF)**	**GDF-5**	Encourages chondrogenesis and tenogensis Increased ECM deposition[126,127]
X	X	X	X	X	?	Insulin-like Growth Factor	**IGF-I**	Stimulates proteoglycan synthesis [119,128,129] Enhance effect of TGF-β3 [115]
X	X	X	X	X	?	Fibroblast Growth Factor (**FGF**)	Basic FGF **bFGF** or **FGF-2**	Enhances proliferation [121,130] Enhance chondrogenesis [121] Increase collagen production [130]
X	X	X	X	X	X	Platelet-derived Growth Factor (**PDGF**)	**PDGF-BB**	Enhances proliferation [130] Enhances tenogenesis [69] Boost ECM deposition for tendon and ligament regeneration [69,130,131]
X	X	X	X		X	Vascular Endothelial Growth factor (**VEGF**)	**VEGF**	Increases vascularization [111] Enhances bone formation [111,114]

Table 1.1 Growth factors commonly used in orthopedic tissue engineering applications. See the following reviews for more on specific growth factors. See the following reviews for more on growth factors.[108–110,132] ? indicates that no native study on these growth factors has been performed; however, tissue engineering applications have been performed using these growth factors and they are believed to play a role.

meniscus.[133] While many of these growth factors are present in all of these tissues (Table 1), the spatial and temporal expression of growth factors are important drivers of tissue development.

TGF-βs, GDFs, BMPs, and IGFs regulate bone and joint development by influencing stem cell differentiation, matrix synthesis and remodeling, and cellular migration and proliferation. The TGF-β superfamily is a group of structurally related proteins including TGF-βs, GDFs, and BMPs that influence a broad range of activities in musculoskeletal development. Members of the BMP family encourage stem cell proliferation and differentiation into osteoblasts.[134,135] Furthermore, BMPs are osteoinductive, encouraging bone formation and maintenance by recruiting bone-forming cells that result in the formation of mineralized bone. BMPs have successfully navigated the FDA approval process for bone healing applications, notably BMP-2(Infuse® Medtronic) and BMP-7 (also called OP-1 by Stryker).[136] GDFs, specifically GDF-5, interact closely with BMPs and act as signaling molecules in the growth and differentiation of cartilage, tendon, and ligament.[126,127,137–139] TGF-βs are prevalent in all of these tissues and are known to play a role in proliferation and stem cell differentiation.[140] In particular, TGF-β is heavily implicated for its role in chondrogenic differentiation and development.[141,142] IGF is a regulator of longitudinal bone growth in that it stimulates osteoblast proliferation and differentiation as well as increasing general cell proliferation and ECM synthesis.[143–146] These growth factors are essential signaling contributors to stem cell differentiation and tissue development in native orthopedic tissues.

Several growth factors prevalent in the inflammatory and healing processes also aid in the production of tissue. Vascularization-related growth factors are important in soft tissue development and healing; common growth factors include PDGF and VEGF.[54,108,110,130,147–149] Basic fibroblastic growth factor (FGF-2) is known to contribute to cell proliferation and is expressed in the developmental and healing phases of these tissues.[130,135] Growth factors have been specifically targeted for tissue engineering applications, because they are exogenously secreted factors that can be dosed into a system with relative ease and can drive stem cell differentiation and tissue maintenance.

Biochemical Applications in Tissue Engineering

Since growth factors are known to play influential roles in cell behavior, they have been frequently applied to tissue engineer bone, cartilage, meniscus, tendon, and ligament (Table 1). BMPs are popular for tissue engineering applications in bone interfaces and have been shown to induce mineralization as well as to stimulate osteoblast proliferation in scaffolds.[114,122,136] Scaffolds doped with IGF-I increased cartilage regeneration in growth plate injuries *in vivo* and increased the collagen and GAG content in tissue engineered cartilage constructs *in vitro.*[129,150,151] VEGF was incorporated into a mineralized degradable polymer scaffold to provide osteoconductive signals for bone growth and angiogenesis.[152] GDFs increased type I collagen production in 3D tissue engineered scaffolds.[126,127] TGF-βs increase GAG and collagen production which improves the quality of tissue engineered cartilage and meniscus.[81,120,123,153] Growth factors provide signaling mechanisms to encourage cellular components to exhibit a specific phenotype.

Prominent growth factors in these developmental processes can also guide stem cell differentiation in tissue engineered constructs. BMP-2 combined with hydroxyapatite in a silk fibroin fiber scaffold supported MSC growth and differentiation towards an osteogenic phenotype, quantified by increased BMP-2 transcription levels and mineral deposition.[112] Delivering BMP-2 and BMP-7 sequentially increased ALP activity while suppressing proliferation of MSCs,[116] highlighting the potential for benefits from temporal application of biochemical factors to cells. Growth factor delivery using a scaffold can increase efficiency of stem cell differentiation into a desired cell phenotype. Localized delivery of IGF in a PLGA scaffold increased MSC chondrogenesis *in vitro,*[150] while FGF-2 and TGF-β1 increased chondrogenesis of periosteum derived cells.[121] GDF-5 supplemented medium as well as GDF-5 induction by adenovirus increased expression of type I collagen and scleraxis, associated with tenogensis, in stem cells seeded on a 3D scaffold.[126,127] TGF-β3 conjugated with chondroitin sulfate increased MSC

chondrogenic differentiation by increasing GAG production and expression of Sox9, COMP, aggrecan, and type II collagen genes.[71] Controlled release of TGF-β3 also promoted chondrogenesis of human infrapatellar fat pad-derived stem cells, measured by increased production of sulfated GAGs and collagen.[125,154]

Growth factors are useful chemical tools for generating complex materials gradients. Since growth factors can be incorporated into a biomaterial, they can be strategically placed or applied to influence cellular behavior in controlled chemical gradients for soft tissue-to-bone tissue engineering. BMP-2, delivered using microspheres in a poly(propylene fumarate) scaffold, increased bone regeneration and ACL graft fixation.[113] An integrated gradient of BMP-2 and TGF-β1 has been shown to create a continuous material and phenotypic transition between cartilage and bone.[50,54] Application of growth factors is especially favorable when using a single progenitor cell type in the scaffold. Rather than seeding multiple cell types, growth factors can be incorporated to initiate the differentiation of stem cells. ASCs, seeded in a porous PCL/Pluronic F127 membrane with gradients of PDGF, specifically PDGF-BB (tendon) and BMP-2, created a continuous interface between tendon and bone, with PDGF promoting tenogenesis and BMP-2 promoting osteogenesis (Figure 1.6c).[69] In combination with materials processing methods and cells, growth factor gradients contribute to the development of integrated and graded regions for engineered soft tissue-to-bone interfaces.

In addition to facilitating cell-biochemical interactions, growth factors can be sequestered by ECM proteins. Proteoglycans function as physiologic regulators by sequestering growth factors and controlling release. SLRPS, such as biglycan, decorin, and fibromodulin, are capable of binding to TGF-β and are likely to regulate the availability of TGF-β to cells.[155] While the exact mechanism is not well understood, increased levels of type II collagen in a scaffold enhance the effect of TGF-β on chondrocytes.[156] FGFs bind to heparan proteoglycans in the ECM. For example

perlecan, a heparan sulfate proteoglycan, co-localizes with FGF thus regulating FGF availability to cell receptors.[157] Availability of BMP-2 is regulated through sequestering with heparin and type IIA procollagen.[158,159] Biomaterials, such as alginate, have been modified with binding peptides that specifically bind a growth factor in order to sustain growth factor availability over longer culture periods.[129] The ability of ECM proteins to regulate growth factor availability contributes to the highly complex interplay of materials, cells, and biochemical signaling in a tissue engineered construct but also allows for the engineered regulation of cellular behavior and scaffold maturation.

Biomaterials combined with growth factors can act as powerful chemoattractants. Growth factors, connective tissue growth factor (CTGF) and TGF-β3, seeded onto a tissue engineered scaffold encouraged cellular recruitment and region specific cell morphology in the meniscus.[81] Decellularization techniques preserve the material structure and resident biochemical components that can be used as a fully functional scaffold.[160] Decellularized and demineralized bone matrix applied to the tendon-to-bone surgical suture site improved tendon-to-bone healing, demonstrated through increased amounts of fibrocartilage and mineralized fibrocartilage in the repair site enthesis and reduced rates of tendon failure.[64] Recent work has successfully decellularized the entire tendon-to-bone insertion,[63] with significant improvements in pullout strength using the decellularized tendon-to-bone insertion over the direct suture technique.[161] Cells were able to repopulate the graft and exhibited a transition from a cartilage-like to tenocyte-like morphology across the interface.[161] Biomaterials and growth factors together serve as promising tissue engineered scaffolds that rely on cell repopulation after *in vivo* implantation.

Construct Maturation

After producing a viable, chemically active, cell-seeded scaffold, the maturation of the scaffold must be driven through external stimuli, either *in vitro* or *in vivo* (Figure 1.5). In the body, chemical and mechanical signals guide development. Mechanical loading of the tissue helps to direct proper

enthesis development, as immobilization during development results in altered enthesis geometry and significantly decreased mechanical properties.[162] As described in the previous section, various biochemical factors affect the differentiation of cells in different regions of the enthesis. These biochemical factors can be engineered into a scaffold with a controlled release over time or can be supplemented into culture media utilizing diffusion to create stimulation gradients. Given these two factors, this section discusses culture methods and bioreactor designs for driving proper maturation using chemical and mechanical stimulation.

Chemically Driven Maturation

Chemical means of driving cell maturation typically occur through media supplementation. In the case of the enthesis, bone media, cartilage media, ligamentous/tendinous media, and meniscal media are typically used individually or in combination. The majority of osteogenic media contains β-glycerophosphate and dexamethasone,[52,55,68,163–165] with some including BMP-2[163,165] and TGF-β.[68] Dexamethasone is also included in some chondrogenic media,[124,164,165] while TGF-β is often used in media for the soft tissue portions of the enthesis.[52,68,124,163–165] Dexamethasone is a glucocorticoid that has been shown to increase ALP activity in MSCs.[166] β-glycerophosphate is an organic phosphate donor classically used to induce MSC differentiation towards bone phenotypes.[52,163,167,168] Application of β-glycerophosphate at the interface of a calcium polyphosphate substrate cultured with chondrocytes formed two zones, a calcified region between a calcium phosphate bony substrate and a hyaline cartilage-like zone.[45] Furthermore, combining β-glycerophosphate and BMP-2 in the bone region of an osteochondral scaffold directed stem cell osteogenesis.[122] Ascorbic acid and L-proline are added to media to promote collagen production. Ascorbic acid or ascorbate-2-phosphate (a format used to stabilize ascorbic acid in solution)[169] has been shown to increase the hydroxylation rate of proline,[170] aiding in collagen production. These chemical stimulants can be incorporated into the scaffold design to enhance a desired cell behavior

either through direct interaction with cells or complementary mechanisms to other growth factors or ECM materials present in the scaffold.

Many of the relevant published systems have been produced for the osteochondral interface, given its similarity to other soft tissue-to-bone interfaces. The majority of systems designed to promote interface formation in culture rely on diffusion-based bioreactors; the general principle being that bone phenotype-promoting media and soft tissue phenotype-promoting media will diffuse through the construct, meet in the middle, and facilitate the formation of an interface.[61,164,165,171] Using this concept, a microfluidic bioreactor directed MSC differentiation along osteogenic and chondrogenic pathways in parallel (Figure 1.7a). The bioreactor consisted of an MSC-seeded agarose gel sandwiched between two other MSC-seeded agarose gels that contained channels. The channel-containing gels are perfused with osteogenic and chondrogenic media, respectively, creating a tri-layered scaffold with an interfacial region. This system produced gradients from the osteogenic to chondrogenic regions: decreasing type I collagen content, increasing type II collagen content, and decreasing Alizarin Red staining, reflecting decreasing matrix-immobilized calcium content. These gradients indicate that interfacial regions can be formed by supplying one cell type with different medias and flow conditions simultaneously (Figure 1.7a).[165,172] Flow of chondrogenic and osteogenic media through the top and bottom of a singular osteochondral scaffold, while maintaining media separation around the scaffold using an O-ring, produced distinctive corresponding regions (Figure 1.7b). Osteochondral scaffolds were produced by pipetting a chondrogenic, photo-crosslinked, cell-seeded gel onto an osteogenic, photo-crosslinked, cell-seeded gel. Chondrogenic gels consisted of MSC-seeded methacrylated gelatin with hyaluronic acid and a photo-crosslinker (lithium phenyl-2,4,6-trimethylbenzoylphosphinate). Osteogenic gels had a similar composition, except with hydroxyapatite rather than hyaluronic acid. After 4 weeks of culture, the

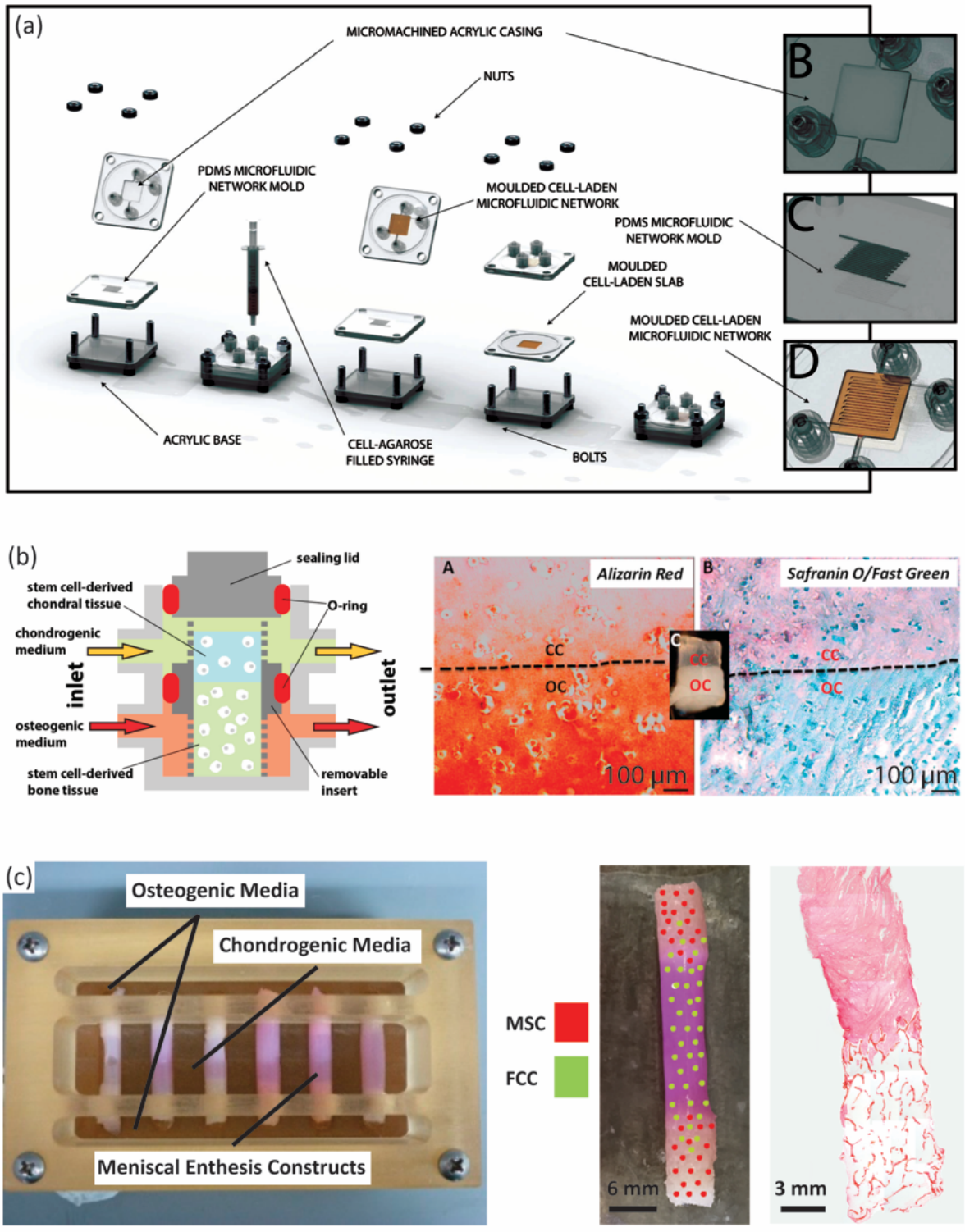

Figure 1.7 Examples of bioreactor designs for maturation of tissue engineering interfacial tissues. **a** Osteochondral microfluidic bioreactor.[172] This bioreactor creates two microchannel arrays in a gel, separated by a non-channel gel slab in the center. Osteogenic and chondrogenic media are flowed through the microchannels allowing for diffusion into surrounding walls and through central slab, creating an interfacial construct. Reprinted with permission from Stephen M.

Goldman, Gilda A. Barabino, Cultivation of agarose-based microfluidic hydrogel promotes the development of large, full-thickness, tissue-engineered articular cartilage constructs, John Wiley and Sons. Copyright © 2014 John Wiley & Sons Ltd.[172] **b** Osteochondral bioreactor.[163] Chondrogenic and osteogenic media are continuously flowed through a scaffold, while maintaining separation of media baths through use of an O-ring. Histology shows interfacial region for construct: chondral component (CC) and osseous component (OC). Alizarin Red stains for calcium, Safranin-O stains for negatively charged molecules (GAGs), and fast green stains for proteins. This schematic was reprinted from <http://pubs.acs.org/doi/abs/10.1021/mp500136b>. Further permissions related to the material excerpted should be directed to the ACS.[163] **c** Combination mechanical, chemical, and co-culture bioreactor for culturing meniscal enthesis constructs. These constructs consist of two bone plugs seeded with mesenchymal stem cells (MSCs) injected and connected with a high density collagen gel embedded with meniscal fibrochondrocytes (FCCs). The bone plugs are anchored down in the bioreactor using the walls, and then osteogenic media and meniscal media can be applied to different portions of the scaffold. Image shows distribution of co-cultured cells on constructs, and histology shows the morphology of the interfacial region of the construct (images courtesy of Leanne Iannucci). Reprinted from Acta Biomaterialia, Volume 56, Mary Clare McCorry, Melissa M. Mansfield, Xiaozhou Sha, Daniel J. Coppola, Jonathan W. Lee, Lawrence J. Bonassar, A model system for developing a tissue engineered meniscal enthesis, 110 – 117, Copyright © 2016, with permission from Elsevier.[60]

corresponding sections of the osteochondral construct showed heightened expression of chondrogenic and osteogenic markers. The construct also contained a junction between the sections of the scaffold, with visible GAG staining in the chondrogenic portion and calcium staining in the osteogenic portion (Figure 1.7b).[163]

Mechanically Driven Maturation

The native enthesis sustains dynamic tensile, compressive, and shear loading that contributes to the development of the integrated regions. The structural transition from soft tissue-to-bone promotes gradual load transfer across the interface, indicating the importance of the structure-function relationship in the enthesis.[1,26,173] The native enthesis contains a dense network of collagen fibers interdigitated into bone that aid in tensile and compressive load transmission.[174–177] The loading environment of the enthesis provides mechanical cues to cells that instruct matrix production and remodeling. Lack of loading during native development results in impaired mineral deposition and disorganized fiber distribution.[178] In the case of healing after tendon injury, immobilization actually increased structural, compositional, and viscoelastic properties compared

to an exercised group.[179] Considering the mechanical influences on tissue development is important when designing methods for tissue engineered enthesis maturation.

During development, anchoring of the meniscus to the tibia produces a static mechanical boundary condition that triggers longitudinal fiber organization in the soft tissue.[90–92,180] Mimicking this static mechanical boundary condition has shown organized fiber remodeling from several cell types including fibroblasts,[181–184] MSCs,[185–187] cardiomyocytes,[184] annulus fibrosis chondrocytes,[188] and meniscal fibrochondrocytes.[60,74,86] Mechanical anchoring at the bony ends of a soft tissue-to-bone model system directed longitudinal fiber formation as well as formed interdigitated fibers at the collagen-bone interface (Figure 1.7c).[60] Cell-monolayers mechanically fixed at the end points contracted the cell sheet into a 3D construct. Using this method, the cells organized a highly aligned and integrated enthesis for ACL repair (Figure 1.6b).[68] While mechanically-directed fiber remodeling has been shown in several systems, different cell types have also displayed varying levels of remodeling capability. When tendon and meniscal fibrochondrocytes were embedded in a collagen matrix and clamped, fibrochondrocytes formed significantly larger fibers than tendon cells.[189] MSCs in a tissue engineered meniscus also showed decreased fiber alignment and diameter compared to fibrochondrocytes.[86] These studies indicate that the response to mechanical stimuli is highly dependent on cell type.

Active mechanical loading is applied to enthesis tissues *in vivo*, and these active mechanical signals guide differential tissue formation. While active mechanical loading has not been applied to *in vitro* enthesis tissue engineering yet, other systems have utilized active loading. Bioreactors have been designed to apply uniaxial tensile loads in bulk ligament and tendon tissue engineering (constructs excluding an enthesis).[103,104] After tensile loading of an aligned scaffold seeded with MSCs, type I and III collagen expression increased as did expression of fibroblastic markers including tenascin-C, fibronectin, and integrins α2, α5, and β1.[104] Simultaneous tensile

and compressive stimulation by compressively loading a self-assembled meniscus ring, resulted in significant increases in mechanical and biochemical properties.[190] This effect was further demonstrated by loading mechanically anchored tissue engineered menisci. Dynamic compressive loading of the meniscus enhanced organized collagen fiber formation, mechanical properties, and GAG accumulation. Mimicking native mechanical loads guided heterogeneous tissue development, where tensile loads in the outer meniscus produced a fiber-containing, collagen-rich tissue, and compressive loads on the inner meniscus increased GAG development.[191] The native environment can also serve as a natural load inducer to guide tissue maturation, assuming the construct is robust enough for implantation. A cell self-assembled bone-ligament-bone construct underwent marked increases in collagen content and alignment as well as increases stiffness after implantation, driving biochemical content and mechanical properties towards native ACL.[68] These studies collectively support active mechanical stimulation as a useful tool to the drive structural development of tissue engineered constructs.

Looking Forward

The field of orthopedic interfacial tissue engineering presents a number of exciting opportunities for pushing forward the fields of biomaterials, tissue engineering, and biomechanics. In the coming years, advances are required in our understanding of both the *in vivo* function and generation of entheses, as well as in our capabilities to engineer constructs to replace these complex tissues. Specifically, we have identified three areas of opportunity to inform the design and development of next generation tissue engineered entheses: 1) understanding the development and homeostasis of the native enthesis, 2) development of new materials and bioreactors for enthesis engineering, and 3) mechanical and structural verification of tissue engineering and implant success.

1. Understanding the Development and Homeostasis of Native Entheses
    a. Structure-function relationships, specifically at the length scales critical for the function of this hierarchically structured tissue (Figure 1.3), remain poorly understood in the native enthesis. Improving our understanding of how specific molecular, cellular, and architectural features contribute to the healthy function of entheses, requires correlative compositional and mechanical data collected with micrometer-scale resolution. In addition to high resolution data sets, these measurements need to be performed on hydrated tissue samples under physiologically-relevant conditions. This type of characterization will require the development of creative imaging strategies that correlatively combine multiple techniques capable of providing chemical, structural, and mechanical information on the same piece of tissue.[192]
    b. Various proteins and molecules are present in low concentrations throughout the regions of the enthesis (e.g. non-collagenous proteins in bone, type X collagen in mineralized cartilage, SLRPs in areas with oriented collagen fiber bundles), but the specific functional roles of these macromolecules are largely unknown. For example, the exact function of non-collagenous proteins in bone is unknown given the redundant roles of these proteins in bone formation. Therefore, the cause of irregularities is hard to characterize using knockout models of non-collagenous proteins.[39] Studies examining the roles of these molecules in the formation of these regional structures, either through knockout models or *in vitro* concentration studies, will allow for tissue engineers to target specific results (fibers with controlled diameters, fibrocartilage formation, etc.) to create integrated, biomimetic constructs.

c. Tendon, ligament, cartilage, and bone cell phenotypes have been well characterized independently (Figure 1.4), but the enthesis incorporates these phenotypes in overlapping gradients, which makes specific phenotypic categorization challenging. Spatial characterization of cell phenotypes within the enthesis are needed to define concrete objectives regarding cell seeding and localized stem cell differentiation. While differentiation into bone and cartilage is well studied, less is known about appropriate inputs for fibrochondrocyte and hypertrophic fibrochondrocyte differentiation.

d. Growth factors play an essential role in the development and maintenance of the enthesis, however limited information exists regarding spatial and temporal expression of growth factors in developing and mature entheses. Additionally, growth factors have complex interactions with each other and the extracellular matrix that complicate the study of each one's exact role. Further study should focus on characterizing the spatial and temporal frequencies of expression of growth factors *in vivo*, thereby generating a greater understanding of the time- and length-scales over which growth factors must be applied to drive cellular differentiation in tissue engineered constructs.

2. Develop New Materials and Bioreactors for Entheses Engineering

a. Hierarchical structures within the native tissue give rise to mechanical, cellular, and biochemical cues critical to healthy tissue function. However, generating biomaterials with similar types of hierarchical structuring remains a challenge and requires extensive control over assembly at various length scales. New synthetic approaches need to be developed that can create materials with the critical features of the native tissue (e.g. strategic biomimicry) and that are scalable.[66] This task can

only be accomplished by both understanding the native structures and evaluating which features are critical for a given function. Once key hierarchical structures are identified and synthetic methods have been developed, then new biomaterials can be designed to possess many of the same properties that native tissue benefits from *in vivo*.

b. The range of materials properties (e.g. several orders of magnitude change in stiffness on the order of less than 1 mm) in the enthesis presents unique challenges in creating a graded interface. In order for a tissue engineered construct to be mechanically robust, differing materials must be fully integrated, utilizing concentration gradients, interpenetrating materials, etc., to avoid stress concentrators at the point of material interface. A specific challenge in this regard is the design of structures with partially mineralized collagen fibers or gradients in alignment and fiber diameter to help anchor soft tissue to bone.

c. Current designs of bioreactors for interfacial tissue constructs have been utilized to apply spatially controlled stimuli (Figure 1.7). However, the effects of changing the application profile, e.g. a linear gradient versus a step function, of a chemical stimulus on a tissue engineered construct are not well understood. Moving forward, researchers should focus on finer spatial control. Such experiments will increase understanding of the interactions of different chemical stimuli, leading to more refined systems for controlling local cellular behavior.

3. Improve Mechanical and Structural Verification of Tissue Engineering and Implant Success

a. The baseline mechanical properties (e.g. toughness, stiffness, failure strain) required for enthesis construct implantation have not been identified. Baseline

properties are largely unknown and likely vary significantly with anatomic location. Such mechanical benchmarks would provide engineers with a more concrete goal to work towards when developing constructs. Devices for measuring native load distributions exist,[193] and similar devices should be developed and utilized in these systems to inform design criteria.

b. The mechanical behavior of the enthesis is non-linear and heterogeneous. As such, properties and test protocols used to describe the mechanics of linear elastic materials do not fully describe the behavior of these tissues. For example, cyclic loading would provide information on viscoelastic properties (e.g. storage modulus, loss modulus, hysteresis) and would provide information on the fatigue life of such constructs. Tissue is frequently loaded cyclically *in vivo*, following gait cycles or other repetitive motions. Therefore, the properties of these tissues during cyclic loading need to be explored to validate implant viability.

c. In addition to mechanical characterization, analysis of the structure of the enthesis provides a great opportunity for the development of new techniques. The presence of orientation and heterogeneity necessitates the development or adaptation of techniques to highlight these features. Advances in magnetic resonance imaging of soft tissues includes pulse sequences such as ultrashort T2 echo times that highlight collagen orientation,[194] but these techniques have not been applied to assess the structure or health of entheses. Additionally, while standard histological analyses enable semi-quantitative assessment of spatial patterns of the components of the enthesis, mapping mineral, proteoglycan, and collagen requires different tissue processing methods, distinct stains, and multiple sections. Vibrational microspectroscopy methods enable detection of multiple chemical species at once

through infrared absorption and Raman scattering. These techniques have been more frequently applied to bone, cartilage, tendon, and ligament than the entheses.[12,42,195,196]

As we capitalize on these opportunities and begin to answer these outstanding questions, we will increase our understanding of the native enthesis and, in return, be able to design the next generation of tissue engineered orthopeadic interfaces. Emerging technologies, such as gene therapy and induced pluripotent stem cells (iPSCs),[105] provide new possibilities for engineering complex tissues. iPSCs are a clinically available cell source; however precise control of cell differentiation remains a challenge.[197] Gene therapy potentially allows for more direct control of cell differentiation, which is highly pertinent in systems containing many cell types. Other similar technologies, like CRISPR,[198] have been unexplored in orthopedic systems and may be of great value for spatially guiding local differentiation to achieve desired phenotypic gradients. Additionally, as tissue engineering is a relatively new field, many of the materials processing methods that have been developed for other materials systems (electronic, structural, etc.) have not been applied to biological systems. For example, the electronics industry has demonstrated nanometer-scale control over semiconductor systems using lithography. Some of these technologies have been translated to biological systems,[199] but the requirement of 3D structuring makes application of these techniques difficult. Other cutting edging processing methods, such as 3D printing,[200] have been utilized to develop complex geometries for tissue engineering, but printing resolution needs to be improved in order to gain clinical viability for these constructs. Utilizing materials design principles external to the biological fields could greatly benefit implant production. In the next ten years, we will be able to demonstrate control over the assembly and culture of hierarchically structured living tissues for the repair of orthopedic soft tissue-to-bone interfaces.

References

1. Abraham, A. C. & Haut Donahue, T. L. From meniscus to bone: A quantitative evaluation of structure and function of the human meniscal attachments. *Acta Biomater.* **9,** 6322–6329 (2013).
2. Mente, P. L. & Lewis, J. L. Elastic modulus of calcified cartilage is an order of magnitude less than that of subchondral bone. *J. Orthop. Res.* **12,** 637–647 (1994).
3. Schinagl, R. M., Gurskis, D., Chen, A. C. & Sah, R. L. Depth-Dependent Confined Compression Modulus of Full-Thickness Bovine Articular Cartilage. *J. Orthop. Res.* **15,** 499–506 (1997).
4. Brooks, P. Inflammation as an important feature of osteoarthritis. *Bull. World Health Organ.* **81,** 689–690 (2003).
5. Shelton, W. R. & Dukes, A. D. Meniscus replacement with bone anchors: a surgical technique. *Arthrosc. J. Arthrosc. Relat. Surg.* **10,** 324–327 (1994).
6. Khetia, E. A. & McKeon, B. P. Meniscal allografts: biomechanics and techniques. *Sports Med. Arthrosc.* **15,** 114–20 (2007).
7. Yang, P. J. & Temenoff, J. S. Engineering orthopedic tissue interfaces. *Tissue Eng. Part B. Rev.* **15,** 127–141 (2009).
8. Lu, H. H. & Thomopoulos, S. Functional attachment of soft tissues to bone: development, healing, and tissue engineering. *Annu. Rev. Biomed. Eng.* **15,** 201–26 (2013).
9. Font Tellado, S., Rosado Balmayor, E. & Van Griensven, M. Strategies to engineer tendon/ligament-to-bone interface: Biomaterials, cells and growth factors. *Adv. Drug Deliv. Rev.* 1–15 (2015). doi:10.1016/j.addr.2015.03.004
10. Hammoudi, T. M. & Temenoff, J. S. in *Biomaterials for Tissue Engineering Applications* **11,** 307–341 (2011).

11. Gao, J., Messner, K., Ralphs, J. & Benjamin, M. An immunohistochemical study of enthesis development in the medial collateral ligament of the rat knee joint. *Anat. Embryol. (Berl).* **19,** 399–406 (1996).

12. Spalazzi, J. P., Boskey, A. L., Pleshko, N. & Lu, H. H. Quantitative mapping of matrix content and distribution across the ligament-to-bone insertion. *PLoS One* **8,** e74349 (2013).

13. Thomopoulos, S., Genin, G. M. & Galatz, L. M. The development and morphogenesis of the tendon-to-bone insertion What development can teach us about healing. *J. Musculoskelet. Neuronal Interact.* **10,** 35–45 (2010).

14. Messner, K. & Gao, J. The menisci of the knee joint. Anatomical and functional characteristics, and a rationale for clinical treatment. *J. Anat.* **193,** 161–178 (1998).

15. Gao, J. Immunolocalization of types I, II, and X collagen in the tibial insertion sites of the medial meniscus. *Knee Surgery, Sport. Traumatol. Arthrosc.* **8,** 61–65 (2000).

16. Petersen, W. & Tillmann, B. Structure and vascularization of the cruciate ligaments of the human knee joint. *Anat. Embryol. (Berl).* **200,** 325–334 (1999).

17. Wang, I.-N. E., Mitroo, S., Chen, F. H., Lu, H. H. & Doty, S. B. Age-Dependent Changes in Matrix Composition and Organization at the Ligament-to-Bone Insertion. *J. Orthop. Res.* **24,** 1745–1755 (2006).

18. Benjamin, M. & Ralphs, J. R. The cell and developmental biology of tendons and ligaments. *Int. Rev. Cytol.* **196,** 85–130 (2000).

19. Genin, G. M. *et al.* Functional grading of mineral and collagen in the attachment of tendon to bone. *Biophys. J.* **97,** 976–85 (2009).

20. Buma, P., Ramrattan, N. N., van Tienen, T. G. & Veth, R. P. Tissue engineering of the meniscus. *Biomaterials* **25,** 1523–1532 (2004).

21. Rodrigues, M. T., Reis, R. L. & Gomes, M. E. Engineering tendon and ligament tissues: present developments towards successful clinical products. *J. Tissue Eng. Regen. Med.* **7,** 673–686 (2013).

22. Di Luca, A., Van Blitterswijk, C. A. & Moroni, L. The osteochondral interface as a gradient tissue: From development to the fabrication of gradient scaffolds for regenerative medicine. *Birth Defects Res. Part C* **105,** 34–52 (2015).

23. Vaquette, C. *et al.* A biphasic scaffold design combined with cell sheet technology for simultaneous regeneration of alveolar bone/periodontal ligament complex. *Biomaterials* **33,** 5560–5573 (2012).

24. Waggett, A. D., Ralphs, J. R., Kwan, A. P. L., Woodnutt, D. & Benjamin, M. Characterization of collagens and proteoglycans at the insertion of the human Achilles tendon. *Matrix Biol.* **16,** 457–470 (1998).

25. Fratzl, P. & Weinkamer, R. Nature's hierarchical materials. *Prog. Mater. Sci.* **52,** 1263–1334 (2007).

26. Moffat, K. L. *et al.* Characterization of the structure-function relationship at the ligament-to-bone interface. *Proc. Natl. Acad. Sci.* **105,** 7947–52 (2008).

27. Liu, Y. X., Thomopoulos, S., Birman, V., Li, J. S. & Genin, G. M. Bi-material attachment through a compliant interfacial system at the tendon-to-bone insertion site. *Mech. Mater.* **44,** 83–92 (2012).

28. Shen, G. The role of type X collagen in facilitating and regulating endochondral ossification of articular cartilage. *Orthod. Craniofacial Res.* **8,** 11–17 (2005).

29. Hardingham, T. E. & Fosang, A. J. Proteoglycans: many forms and many function. *FASEB J.* **6,** 861–870 (1992).

30. Benjamin, M. & Ralphs, J. R. Fibrocartilage in tendons and ligaments—an adaptation to

compressive load. *J. Anat.* **193,** 481–494 (1998).

31. Melrose, J., Smith, S., Cake, M., Read, R. & Whitelock, J. Comparative spatial and temporal localisation of perlecan, aggrecan and type I, II and IV collagen in the ovine meniscus: An ageing study. *Histochem. Cell Biol.* **124,** 225–235 (2005).
32. Rossetti, L. *et al.* The microstructure and micromechanics of the tendon–bone insertion. *Nat. Mater.* **16,** 664–670 (2017).
33. Tavakoli Nia, H. *et al.* Aggrecan nanoscale solid-fluid interactions are a primary determinant of cartilage dynamic mechanical properties. *ACS Nano* **9,** 2614–2625 (2015).
34. Garg, A. K., Berg, R. A., Silver, F. H. & Garg, H. G. Effect of proteoglycans on type I collagen fibre formation. *Biomaterials* **10,** 413–419 (1989).
35. Vogel, K. G. & Trotter, J. A. The Effect of Proteoglycans on the Morphology of Collagen Fibrils Formed In Vitro. *Coll. Relat. Res.* **7,** 105–114 (1987).
36. Vogel, K. G., Paulsson, M. & Heinegård, D. Specific inhibition of type I and type II collagen fibrillogenesis by the small proteoglycan of tendon. *Biochem. J.* **223,** 587–97 (1984).
37. Vanderploeg, E. J., Wilson, C. G., Imler, S. M., Ling, C. H. Y. & Levenston, M. E. Regional variations in the distribution and colocalization of extracellular matrix proteins in the juvenile bovine meniscus. *J. Anat.* **221,** 174–186 (2012).
38. Wopenka, B. & Pasteris, J. D. A mineralogical perspective on the apatite in bone. *Mater. Sci. Eng. C* **25,** 131–143 (2005).
39. Nudelman, F., Lausch, A. J., Sommerdijk, N. A. & Sone, E. D. In vitro models of collagen biomineralization. *J. Struct. Biol.* **183,** 258–69 (2013).
40. Weiner, S. & Wagner, H. D. THE MATERIAL BONE: Structure-Mechanical Function Relations. *Annu. Rev. Mater. Sci.* **28,** 271–298 (1998).

41. Reznikov, N., Shahar, R. & Weiner, S. Bone hierarchical structure in three dimensions. *Acta Biomater.* **10,** 3815–3826 (2014).

42. Schwartz, A. G., Pasteris, J. D., Genin, G. M., Daulton, T. L. & Thomopoulos, S. Mineral Distributions at the Developing Tendon Enthesis. *PLoS One* **7,** 1–11 (2012).

43. Keaveny, T. M., Morgan, E. F., Niebur, G. L. & Yeh, O. C. Biomechanics of Trabecular Bone. *Annu. Rev. Biomed. Eng.* **3,** 307–333 (2001).

44. Deymier-Black, A. C., Pasteris, J. D., Genin, G. M. & Thomopoulos, S. Allometry of the Tendon Enthesis: Mechanisms of Load Transfer Between Tendon and Bone. *J. Biomech. Eng.* **137,** 111005 (2015).

45. Allan, K. S., Pilliar, R. M., Wang, J., Grynpas, M. D. & Kandel, R. a. Formation of biphasic constructs containing cartilage with a calcified zone interface. *Tissue Eng.* **13,** 167–177 (2007).

46. Huang, X. *et al.* Osteochondral repair using the combination of fibroblast growth factor and amorphous calcium phosphate/poly(l-lactic acid) hybrid materials. *Biomaterials* **28,** 3091–3100 (2007).

47. Liu, W. *et al.* Nano fiber Scaffolds with Gradients in Mineral Content for Spatial Control of Osteogenesis. *ACS Appl. Mater. Interfaces* **6,** 2842–2849 (2014).

48. Kim, B. S. *et al.* Human collagen-based multilayer scaffolds for tendon-to-bone interface tissue engineering. *J. Biomed. Mater. Res. - Part A* **102,** 4044–4054 (2014).

49. Nyberg, E., Rindone, A., Dorafshar, A. & Grayson, W. L. Comparison of 3D-Printed Poly-ε-caprolactone Scaffolds Functionalized with Tricalcium Phosphate, Hydroxyapatite, Bio-Oss, or Decellularized Bone Matrix. *Tissue Eng. Part A* **00,** ten.TEA.2016.0418 (2016).

50. Tevlek, A., Hosseinian, P., Ogutcu, C., Turk, M. & Aydin, H. M. Bi-layered constructs of

poly(glycerol-sebacate)-β-tricalcium phosphate for bone-soft tissue interface applications. *Mater. Sci. Eng. C* **72,** 316–324 (2017).

51. Spalazzi, J. P., Doty, S. B., Moffat, K. L., Levine, W. N. & Lu, H. H. Development of controlled matrix heterogeneity on a triphasic scaffold for orthopedic interface tissue engineering. *Tissue Eng.* **12,** 3497–3508 (2006).

52. Criscenti, G. *et al.* Triphasic scaffolds for the regeneration of the bone–ligament interface. *Biofabrication* **8,** 015009 (2016).

53. Cooper, J. A., Lu, H. H., Ko, F. K., Freeman, J. W. & Laurencin, C. T. Fiber-based tissue-engineered scaffold for ligament replacement: Design considerations and in vitro evaluation. *Biomaterials* **26,** 1523–1532 (2005).

54. Dormer, N. H. *et al.* Osteochondral interface regeneration of the rabbit knee with macroscopic gradients of bioactive signals. *J. Biomed. Mater. Res.* **100,** 162–170 (2012).

55. Liu, Y. *et al.* Modelling the mechanics of partially mineralized collagen fibrils, fibres and tissue. *J. R. Soc. Interface* **11,** 20130835 (2014).

56. Paxton, J. Z., Donnelly, K., Keatch, R. P. & Baar, K. Engineering the Bone–Ligament Interface Using Polyethylene Glycol Diacrylate Incorporated with Hydroxyapatite. *Tissue Eng. Part A* **15,** 1201–1209 (2009).

57. Altman, G. H. *et al.* Silk matrix for tissue engineered anterior cruciate ligaments. *Biomaterials* **23,** 4131–4141 (2002).

58. Font Tellado, S. *et al.* Fabrication and characterization of biphasic silk fibroin scaffolds for tendon/ligament-to-bone tissue engineering. *Tissue Eng. Part A* **23,** 859–872 (2017).

59. Park, Y.-B., Ha, C.-W., Lee, C.-H. & Park, Y.-G. Restoration of a large osteochondral defect of the knee using a composite of umbilical cord blood-derived mesenchymal stem cells and hyaluronic acid hydrogel: a case report with a 5-year follow-up. *BMC*

Musculoskelet. Disord. **18,** 59 (2017).

60. McCorry, M. C. *et al.* A model system for developing a tissue engineered meniscal enthesis. *Acta Biomater.* **56,** 110–117 (2016).

61. Chang, C. H., Lin, F. H., Lin, C. C., Chou, C. H. & Liu, H. C. Cartilage tissue engineering on the surface of a novel gelatin-calcium- phosphate biphasic scaffold in a double-chamber bioreactor. *J. Biomed. Mater. Res. - Part B Appl. Biomater.* **71,** 313–321 (2004).

62. Wang, I.-N. E. *et al.* Role of osteoblast–fibroblast interactions in the formation of the ligament-to-bone interface. *J. Orthop. Res.* 1609–1620 (2007). doi:10.1002/jor

63. Xu, K. *et al.* Efficient decellularization for tissue engineering of the tendon-bone interface with preservation of biomechanics. *PLoS One* **12,** e0171577 (2017).

64. Sundar, S., Pendegrass, C. J. & Blunn, G. W. Tendon bone healing can be enhanced by demineralized bone matrix: A functional and histological study. *J. Biomed. Mater. Res. - Part B Appl. Biomater.* **88,** 115–122 (2009).

65. Lipner, J. *et al.* In Vivo Evaluation of Adipose-Derived Stromal Cells Delivered with a Nanofiber Scaffold for Tendon-to-Bone Repair. *Tissue Eng. Part A* **21,** 2766–74 (2015).

66. Wegst, U. G., Bai, H., Saiz, E., Tomsia, A. P. & Ritchie, R. O. Bioinspired structural materials. *Nat. Mater.* **14,** 23–36 (2014).

67. Ding, X. *et al.* Integrated Trilayered Silk Fibroin Sca ff old for Osteochondral Di ff erentiation of Adipose-Derived Stem Cells. *ACS Appl. Mater. Interfaces* (2014).

68. Ma, J. *et al.* Three-Dimensional Engineered Bone–Ligament–Bone Constructs for Anterior Cruciate Ligament Replacement. *Tissue Eng. Part A* **18,** 103–116 (2012).

69. Min, H. K., Oh, S. H., Lee, J. M., Im, G. Il & Lee, J. H. Porous membrane with reverse gradients of PDGF-BB and BMP-2 for tendon-to-bone repair: In vitro evaluation on adipose-derived stem cell differentiation. *Acta Biomater.* **10,** 1272–1279 (2014).

70. Baker, B. M. & Mauck, R. L. The effect of nanofiber alignment on the maturation of engineered meniscus constructs. *Biomaterials* **28,** 1967–1977 (2007).

71. Park, J. S. *et al.* Chondrogenic differentiation of mesenchymal stem cells embedded in a scaffold by long-term release of TGF-B3 complexed with chondroitin sulfate. *J. Biomed. Mater. Res. - Part A* **92,** 806–816 (2010).

72. Han, W. M. *et al.* Microstructural heterogeneity directs micromechanics and mechanobiology in native and engineered fibrocartilage. *Nat. Mater.* (2016). doi:10.1038/nmat4520

73. Spalazzi, J. P. *et al.* In vivo evaluation of a multiphased scaffold designed for orthopaedic interface tissue engineering and soft tissue-to-bone integration. *J. Biomed. Mater. Res. - Part A* **86,** 1–12 (2008).

74. Puetzer, J. L., Koo, E. & Bonassar, L. J. Induction of fiber alignment and mechanical anisotropy in tissue engineered menisci with mechanical anchoring. *J. Biomech.* **48,** 1436–1443 (2015).

75. Lian, J. B. & Stein, G. S. Concepts of osteoblast growth and differentiation: basis for modulation of bone cell development and tissue formation. *Crit. Rev. Oral Biol. Med.* **3,** 269–305 (1992).

76. Mackie, E. J., Ahmed, Y. A., Tatarczuch, L., Chen, K. S. & Mirams, M. Endochondral ossification: How cartilage is converted into bone in the developing skeleton. *Int. J. Biochem. Cell Biol.* **40,** 46–62 (2008).

77. Mort, J. S. & Billington, C. J. Articular cartilage and changes in arthritis matrix degradation. *Arthritis Research* **3,** 337–341 (2001).

78. Sanchez-Adams, J. & Athanasiou, K. A. The Knee Meniscus: A Complex Tissue of Diverse Cells. *Cell. Mol. Bioeng.* **2,** 332–340 (2009).

79. Spanoudes, K., Gaspar, D., Pandit, A. & Zeugolis, D. I. The biophysical, biochemical, and biological toolbox for tenogenic phenotype maintenance in vitro. *Trends Biotechnol.* **32,** 474–482 (2014).

80. Hasegawa, A. *et al.* Cellular and extracellular matrix changes in anterior cruciate ligaments during human knee aging and osteoarthritis. *Arthritis Res. Ther.* **15,** R29 (2013).

81. Lee, C. H. *et al.* Protein-releasing polymeric scaffolds induce fibrochondrocytic differentiation of endogenous cells for knee meniscus regeneration in sheep. *Sci. Transl. Med.* **6,** 266ra171 (2014).

82. Monibi, F. A. & Cook, J. L. Tissue-Derived Extracellular Matrix Bioscaffolds: Emerging Applications in Cartilage and Meniscus Repair. *Tissue Eng. Part B Rev.* (2017). doi:10.1089/ten.TEB.2016.0431

83. Zelzer, E., Blitz, E., Killian, M. L. & Thomopoulos, S. Tendon-to-bone attachment: From development to maturity. *Birth Defects Res. Part C* **102,** 101–112 (2014).

84. Jiang, J., Nicoll, S. B. & Lu, H. H. Co-culture of osteoblasts and chondrocytes modulates cellular differentiation in vitro. *Biochem. Biophys. Res. Commun.* **338,** 762–70 (2005).

85. McCorry, M. C., Puetzer, J. L. & Bonassar, L. J. Characterization of mesenchymal stem cells and fibrochondrocytes in three-dimensional co-culture: analysis of cell shape, matrix production, and mechanical performance. *Stem Cell Res. Ther.* **7,** 39 (2016).

86. McCorry, M. C. & Bonassar, L. J. Fiber development and matrix production in tissue-engineered menisci using bovine mesenchymal stem cells and fibrochondrocytes. *Connect. Tissue Res.* **58,** 329–341 (2017).

87. Im, G. Coculture in Musculoskeletal Tissue Regeneration. *Tissue Eng. Part B Rev.* **20,** 545–554 (2014).

88. Bian, L., Zhai, D. Y., Mauck, R. L. & Burdick, J. A. Coculture of Human Mesenchymal

Stem Cells and Enhances Functional Properties of Engineered Cartilage Reverse primer. *Tissue Eng. Part A* **17,** 1137–1145 (2011).

89. Hoben, G. M., Willard, V. P. & Athanasiou, K. A. Fibrochondrogenesis of hESCs: growth factor combinations and cocultures. *Stem Cells Dev.* **18,** 283–92 (2009).

90. Gardner, E. & O'Rahilly, R. The early development of the knee joint in staged human embryos. *J. Anat.* **102,** 289–99 (1968).

91. Gray, D. J. & Gardner, E. Prenatal development of the human knee and superior tibiofibular joints. *Am. J. Anat.* **86,** 235–287 (1950).

92. Mérida-Velasco, J. a *et al.* Development of the human knee joint. *Anat. Rec.* **248,** 269–78 (1997).

93. Caplan, A. I. & Dennis, J. E. Mesenchymal stem cells as trophic mediators. *J. Cell. Biochem.* **98,** 1076–84 (2006).

94. Mackay, A. M. *et al.* Chondrogenic differentiation of cultured human mesenchymal stem cells from marrow. *Tissue Eng.* **4,** 415–28 (1998).

95. Im, G. Il, Shin, Y. W. & Lee, K. B. Do adipose tissue-derived mesenchymal stem cells have the same osteogenic and chondrogenic potential as bone marrow-derived cells? *Osteoarthr. Cartil.* **13,** 845–853 (2005).

96. Spalazzi, J. P. & Lu, H. H. Osteoblast and chondrocyte interactions during cocul- ture on scaffolds. *IEEE Eng. Med. Biol. Mag.* **22,** 27–34 (2003).

97. Gunja, N. J. & Athanasiou, K. a. Passage and reversal effects on gene expression of bovine meniscal fibrochondrocytes. *Arthritis Res. Ther.* **9,** 1–12 (2007).

98. Zeltz, C. & Gullberg, D. The integrin-collagen connection - a glue for tissue repair? *J. Cell Sci.* **129,** 653–664 (2016).

99. Augst, A. D., Kong, H. J. & Mooney, D. J. Alginate hydrogels as biomaterials. *Macromol.*

Biosci. **6,** 623–633 (2006).

100. Baker, B. M., Nathan, A. S., Gee, A. O. & Mauck, R. L. The influence of an aligned nanofibrous topography on human mesenchymal stem cell fibrochondrogenesis. *Biomaterials* **31,** 6190–6200 (2010).

101. Tse, J. R. & Engler, A. J. Stiffness gradients mimicking in vivo tissue variation regulate mesenchymal stem cell fate. *PLoS One* **6,** e15978 (2011).

102. Engler, A. J., Sen, S., Sweeney, H. L. & Discher, D. E. Matrix elasticity directs stem cell lineage specification. *Cell* **126,** 677–89 (2006).

103. Lee, C. H. *et al.* Nanofiber alignment and direction of mechanical strain affect the ECM production of human ACL fibroblast. *Biomaterials* **26,** 1261–70 (2005).

104. Subramony, S. D. *et al.* The guidance of stem cell differentiation by substrate alignment and mechanical stimulation. *Biomaterials* **34,** 1942–1953 (2013).

105. Phillips, J. E., Burns, K. L., Le Doux, J. M., Guldberg, R. E. & García, A. J. Engineering graded tissue interfaces. *Proc. Natl. Acad. Sci. U. S. A.* **105,** 12170–12175 (2008).

106. Urist, M., DeLange, R. & Finerman, G. Bone cell differentiation and growth factors. *Science (80-.).* **220,** 680–686 (1983).

107. Linkhart, T. A., Mohan, S. & Baylink, D. J. Growth factors for bone growth and repair: IGF, TGF and BMP. *Bone* **19,** 1S–12S (1996).

108. Lieberman, J. R., Daluiski, A. & Einhorn, T. a. The Role of Growth Factors in the Repair of Bone. *J. Bone Jt. Surg.* **84,** 1032–1044 (2002).

109. Molloy, T., Wang, Y. & Murrell, G. A. C. The Roles of Growth Factors in Tendon and Ligament Healing. *Sport. Med.* **33,** 381–394 (2003).

110. James, R., Kesturu, G., Balian, G. & Chhabra, A. B. Tendon: Biology, Biomechanics, Repair, Growth Factors, and Evolving Treatment Options. *J. Hand Surg. Am.* **33,** 102–112

(2008).

111. Kakudo, N., Kusumoto, K., Wang, Y. B., Iguchi, Y. & Ogawa, Y. Immunolocalization of vascular endothelial growth factor on intramuscular ectopic osteoinduction by bone morphogenetic protein-2. *Life Sci.* **79,** 1847–1855 (2006).

112. Li, C., Vepari, C., Jin, H.-J., Kim, H. J. & Kaplan, D. L. Electrospun silk-BMP-2 scaffolds for bone tissue engineering. *Biomaterials* **27,** 3115–3124 (2006).

113. Parry, J. A. *et al.* Three-Dimension-Printed Porous Poly(Propylene Fumarate) Scaffolds with Delayed rhBMP-2 Release for Anterior Cruciate Ligament Graft Fixation. *Tissue Eng. Part A* **00,** 1–7 (2017).

114. Patel, Z. S. *et al.* Dual delivery of an angiogenic and an osteogenic growth factor for bone regeneration in a critical size defect model. *Bone* **43,** 931–940 (2008).

115. Indrawattana, N. *et al.* Growth factor combination for chondrogenic induction from human mesenchymal stem cell. *Biochem. Biophys. Res. Commun.* **320,** 914–9 (2004).

116. Yilgor, P., Tuzlakoglu, K., Reis, R. L., Hasirci, N. & Hasirci, V. Incorporation of a sequential BMP-2/BMP-7 delivery system into chitosan-based scaffolds for bone tissue engineering. *Biomaterials* **30,** 3551–3559 (2009).

117. Connelly, J. T., Wilson, C. G. & Levenston, M. E. Characterization of proteoglycan production and processing by chondrocytes and BMSCs in tissue engineered constructs. *Osteoarthr. Cartil.* **16,** 1092–1100 (2008).

118. Johnstone, B., Hering, T. M., Caplan, A. I., Goldberg, V. M. & Yoo, J. U. In vitro chondrogenesis of bone marrow-derived mesenchymal progenitor cells. *Exp Cell Res* **238,** 265–272 (1998).

119. Imler, S. M., Doshi, A. N. & Levenston, M. E. Combined effects of growth factors and static mechanical compression on meniscus explant biosynthesis. *Osteoarthritis Cartilage*

12, 736–44 (2004).

120. Macbarb, R. F., Makris, E. a, Hu, J. C. & Athanasiou, K. a. A chondroitinase-ABC and TGF-β1 treatment regimen for enhancing the mechanical properties of tissue-engineered fibrocartilage. *Acta Biomater.* (2012). doi:10.1016/j.actbio.2012.09.037

121. Marini, R. P., Martin, I., Stevens, M. M., Langer, R. & Shastri, V. P. FGF-2 enhances TGF-B1 induced periosteal chondrogenesis. *J. Orthop. Res.* **22,** 1114–1119 (2004).

122. Augst, A. *et al.* Effects of chondrogenic and osteogenic regulatory factors on composite constructs grown using human mesenchymal stem cells, silk scaffolds and bioreactors. *J. R. Soc. Interface* **5,** 929–939 (2008).

123. Park, H., Temenoff, J. S., Holland, T. A., Tabata, Y. & Mikos, A. G. Delivery of TGF-1 and chondrocytes via injectable, biodegradable hydrogels for cartilage tissue engineering applications. *Biomaterials* **26,** 7095–7103 (2005).

124. Mueller, M. B. *et al.* Hypertrophy in mesenchymal stem cell chondrogenesis: Effect of TGF-β isoforms and chondrogenic conditioning. *Cells Tissues Organs* **192,** 158–166 (2010).

125. Kim, M., Erickson, I. E., Choudhury, M., Pleshko, N. & Mauck, R. L. Transient exposure to TGF-β3 improves the functional chondrogenesis of MSC-laden hyaluronic acid hydrogels. *J. Mech. Behav. Biomed. Mater.* **11,** 92–101 (2012).

126. Farng, E., Bs, A. R. U., Bs, D. B., Bs, S. E. & Mcallister, D. R. The Effects of GDF-5 and Uniaxial Strain on Mesenchymal Stem Cells in 3-D Culture. *Clin. Orthop. Relat. Res.* **466,** 1930–1937 (2008).

127. James, R., Kumbar, S. G., Laurencin, C. T., Balian, G. & Chhabra, A. B. Tendon tissue engineering : adipose-derived stem cell and GDF-5 mediated regeneration using electrospun matrix systems. *Biomed. Mater.* **6,** 025011 (2011).

128. Puetzer, J. L., Brown, B. N., Ballyns, J. J. & Bonassar, L. J. The effect of IGF-I on anatomically shaped tissue-engineered menisci. *Tissue Eng. Part A* **19,** 1443–50 (2013).

129. Aguilar, N. I., Trippel, S., Shi, S. & Bonassar, L. J. Customized Biomaterials to Augment Chondrocyte Gene Therapy. *Acta Biomater.* **53,** 260–267 (2017).

130. Thomopoulos, S., Harwood, F. L., Silva, M. J., Amiel, D. & Gelberman, R. H. Effect of several growth factors on canine flexor tendon fibroblast proliferation and collagen synthesis in vitro. *J. Hand Surg. Am.* **30,** 441–447 (2005).

131. Hee, C. K., Dines, J. S., Solchaga, L. a, Shah, V. R. & Hollinger, J. O. Regenerative tendon and ligament healing: opportunities with recombinant human platelet-derived growth factor BB-homodimer. *Tissue Eng. Part B. Rev.* **18,** 225–34 (2012).

132. Baylink, D. J., Finkelman, R. D. & Mohan, S. Growth factors to stimulate bone formation. *J. Bone Miner. Res.* **8,** S565–S572 (1993).

133. Van der Kraan, P. M., Buma, P., Van Kuppevelt, T. & Van Den Berg, W. B. Interaction of chondrocytes, extracellular matrix and growth factors: Relevance for articular cartilage tissue engineering. *Osteoarthr. Cartil.* **10,** 631–637 (2002).

134. Yoon, B. S. *et al.* BMPs regulate multiple aspects of growth-plate chondrogenesis through opposing actions on FGF pathways. *Development* **133,** 4667–4678 (2006).

135. Minina, E., Kreschel, C., Naski, M. C., Ornitz, D. M. & Vortkamp, A. Interaction of FGF, Ihh/Pthlh, and BMP signaling integrates chondrocyte proliferation and hypertrophic differentiation. *Dev. Cell* **3,** 439–449 (2002).

136. Bessa, P. C., Casal, M. & Reis, R. L. Bone morphogenetic proteins in tissue engineering: the road from laboratory to clinic, part II (BMP delivery). *J. Tissue Eng. Regen. Med.* **2,** 81–96 (2008).

137. Wolfman, N. M. *et al.* Ectopic Induction of Tendon and Ligament in Rats by Growth and

Differentiation Factors 5 , 6 , and 7 , Members of the TGF- ␣ Gene Family. *J. Clin. Invest.* **100,** 321–330 (1997).

138. Chen, D. *et al.* Bone Morphogenetic Proteins. *Growth Factors* **22,** 233–241 (2004).

139. Decker, R. S. *et al.* Cell origin, volume and arrangement are drivers of articular cartilage formation, morphogenesis and response to injury in mouse limbs. *Dev. Biol.* (2017). doi:10.1016/j.ydbio.2017.04.006

140. Heine, U. *et al.* Role of transforming growth factor-beta in the development of the mouse embryo. *J. Cell Biol.* **105,** 2861–76 (1987).

141. Leonard, C. M. *et al.* Role of transforming growth factor-B in chondrogenic pattern formation in the embryonic limb: Stimulation of mesenchymal condensation and fibronectin gene expression by exogenenous TGF-B and evidence for endogenous TGF-B-like activity. *Dev. Biol.* **145,** 99–109 (1991).

142. Kulyk, W. M., Rodgers, B. J., Greer, K. & Kosher, R. A. Promotion of embryonic chick limb cartilage differentiation by transforming growth factor-B. *Dev. Biol.* **135,** 424–430 (1989).

143. Isaksson, O. G. P., Jansson, J.-O. & Gause, I. A. M. Growth Hormone Stimulates Longitudinal Bone Growth. *Science (80-.).* **216,** 1237–1239 (1982).

144. Mohan, S. *et al.* Studies on the mechanisms by which insulin-like growth factor (IGF) binding protein-4 (IGFBP-4) and IGFBP-5 modulate IGF actions in bone cells. *J. Biol. Chem.* **270,** 20424–20431 (1995).

145. Hunziker, E. B., Wagner, J. & Zapf, J. Differential effects of insulin-like growth factor I and growth hormone on developmental stages of rat growth plate chondrocytes in vivo. *J. Clin. Invest.* **93,** 1078–86 (1994).

146. Abrahamsson, S. O. Similar effects of recombinant human insulin-like growth factor-I and

II on cellular activities in flexor tendons of young rabbits: Experimental studies in vitro. *J. Orthop. Res.* **15,** 256–262 (1997).

147. Midy, V. & Plouët, J. Vasculotropin/vascular endothelial growth factor induces differentiation in cultured osteoblasts. *Biochemical and Biophysical Research Communications* **199,** 380–386 (1994).

148. Leung, D. W., Cachianes, G., Kuang, W. J., Goeddel, D. V. & Ferrara, N. Vascular endothelial growth factor is a secreted angiogenic mitogen. *Science (80-.).* **246,** 1306–9 (1989).

149. Keck, P. J. *et al.* Vascular permeability factor, an endothelial cell mitogen related to PDGF. *Science (80-.).* **246,** 1309–1312 (1989).

150. Sundararaj, S. K. C., Cieply, R. D., Gupta, G., Milbrandt, T. A. & Puleo, D. A. Treatment of growth plate injury using IGF-1 loaded PLGA scaffold. *J. Tissue Eng. Regen. Med.* **9,** E202-209 (2015).

151. Gooch, K. J. *et al.* IGF-I and Mechanical Environment Interact to Modulate Engineered Cartilage Development. *Biochem. Biophys. Res. Commun.* **286,** 909–915 (2001).

152. Murphy, W. L., Peters, M. C., Kohn, D. H. & Mooney, D. J. Sustained release of vascular endothelial growth factor from mineralized poly(lactide-co-glycolide) scaffolds for tissue engineering. *Biomaterials* **21,** 2521–2527 (2000).

153. Steinert, A. F. *et al.* Genetically enhanced engineering of meniscus tissue using ex vivo delivery of transforming growth factor-beta 1 complementary deoxyribonucleic acid. *Tissue Eng.* **13,** 2227–37 (2007).

154. Almeida, H. V. *et al.* Controlled release of transforming growth factor-β3 from cartilage-extra-cellular-matrix-derived scaffolds to promote chondrogenesis of human-joint-tissue-derived stem cells. *Acta Biomater.* **10,** 4400–4409 (2014).

155. Hildebrand, A. *et al.* Interaction of the small interstitial proteoglycans biglycan, decorin and fibromodulin with transforming growth factor beta. *Biochem. J.* **302,** 527–34 (1994).

156. Qi, W.-N. & Scully, S. P. Extracellular collagen regulates expression of trasforming growth factor-beta1 gene. *J. Orthop. Res.* **18,** 928–932 (2000).

157. Mongiat, M. *et al.* Fibroblast Growth Factor-binding Protein is a Novel Partner for Perlecan Protein Core. *J. Biol. Chem.* **276,** 10263–10271 (2001).

158. Ruppert, R., Hoffmann, E. & Sebald, W. Human bone morphogenetic protein 2 contains a heparin-binding site which modifies its biological activity. *Eur. J. Biochem* **237,** 295–302 (1996).

159. Zhu, Y., Oganesian, A., Keene, D. R. & Sandell, L. J. Type IIA Procollagen Containing the Cysteine-rich Amino Propeptide is Deposited in the Extracellular Matrix of Prechondrogenic Tissue and Binds to TGF-B1 and BMP-2. *J. Cell Biol.* **144,** 1069–1080 (1999).

160. Kawecki, M. *et al.* A review of decellurization methods caused by an urgent need for quality control of cell-free extracellular matrix' scaffolds and their role in regenerative medicine. *J. Biomed. Mater. Res. Part B Appl. Biomater.* 1–15 (2017). doi:10.1002/jbm.b.33865

161. Farnebo, S., Woon, C. Y., Kim, M., Pham, H. & Chang, J. Reconstruction of the Tendon-Bone Insertion with decellularized tendon-bone composite grafts:comparison with onventional repair. *J. Hand Surg. Am.* **39,** 65–74 (2014).

162. Schwartz, A. G., Lipner, J. H., Pasteris, J. D., Genin, G. M. & Thomopoulos, S. Muscle loading is necessary for the formation of a functional tendon enthesis. *Bone* **55,** 44–51 (2013).

163. Lin, H., Lozito, T. P., Alexander, P. G., Gottardi, R. & Tuan, R. S. Stem Cell-Based

Microphysiological Osteochondral System to Model Tissue Response to Interleukin-1 β. *Mol. Pharm.* **11,** 2203–2212 (2014).

164. Grayson, W. L., Bhumiratana, S., Grace Chao, P. H., Hung, C. T. & Vunjak-Novakovic, G. Spatial regulation of human mesenchymal stem cell differentiation in engineered osteochondral constructs: Effects of pre-differentiation, soluble factors and medium perfusion. *Osteoarthr. Cartil.* **18,** 714–723 (2010).

165. Goldman, S. M. & Barabino, G. A. Spatial Engineering of Osteochondral Tissue Constructs Through Microfluidically Directed Differentiation of Mesenchymal Stem Cells. *Biores. Open Access* **5.1,** 109–117 (2016).

166. Jaiswal, N., Haynesworth, S. E., Caplan, A. I. & Bruder, S. P. Osteogenic Differentiation of Purified , Culture-Expanded Human Mesenchymal Stem Cells In Vitro. *J. Cell. Biochem.* **64,** 295–312 (1997).

167. Grayson, W. L. *et al.* Engineering anatomically shaped human bone grafts. *Proc. Natl. Acad. Sci. U. S. A.* **107,** 3299–3304 (2010).

168. Boskey, A. L. & Roy, R. Cell Culture Systems for Studies of Bone and Tooth Mineralization. *Chem Rev.* **108,** 4716–4733 (2008).

169. Hata, R.-I. & Senoo, H. L-Ascorbic Acid 2-Phosphate Stimulates Collagen Accumulation , Cell Proliferation , and Formation of a Three-Dimensional Tissuelike Substance by Skin Fibroblasts. *J. Cell. Physiol.* **138,** 8–16 (1989).

170. Schwarz, R. I., Kleinman, P. & Owens, N. Ascorbate Can Act as an Inducer of the Collagen Pathway Because Most Steps Are Tightly Coupled ". *Ann. New York Acad. Sci.* (1987).

171. Li, Q. *et al.* Micromechanical Heterogeneity and Anisotropy of the Meniscus Extracellular Matrix. *Acta Biomater.* (2017). doi:10.1016/j.actbio.2017.02.043

172. Goldman, S. M. & Barabino, G. A. Cultivation of agarose-based microfluidic hydrogel promotes the development of large, full-thickness, tissue-engineered articular cartilage constructs. *J. Tissue Eng. Regen. Med.* (2014). doi:10.1002/term

173. Thomopoulos, S., Marquez, J. P., Weinberger, B., Birman, V. & Genin, G. M. Collagen fiber orientation at the tendon to bone insertion and its influence on stress concentrations. *J. Biomech.* **39,** 1842–1851 (2006).

174. Villegas, D. F., Hansen, T. A., Liu, D. F. & Haut Donahue, T. L. A quantitative study of the microstructure and biochemistry of the medial meniscal horn attachments. *Ann. Biomed. Eng.* **36,** 123–131 (2008).

175. Villegas, D. F. & Haut Donahue, T. L. Collagen morphology in human meniscal attachments: a SEM study. *Connect. Tissue Res.* **51,** 327–336 (2010).

176. Villegas, D. F., Maes, J. A., Magee, S. D. & Haut Donahue, T. L. Failure properties and strain distribution analysis of meniscal attachments. *J. Biomech.* **40,** 2655–2662 (2007).

177. Hu, Y. *et al.* Stochastic interdigitation as a toughening mechanism at the interface between tendon and bone. *Biophys. J.* **108,** 431–437 (2015).

178. Kim, H. M., Galatz, L. M., Patel, N., Das, R. & Thomopoulos, S. Recovery Potential After Postnatal Shoulder Paralysis. *J. Bone Jt. Surg.* **91,** 879–891 (2009).

179. Thomopoulos, S., Williams, G. R. & Soslowsky, L. J. Tendon to Bone Healing: Differences in Biomechanical, Structural, and Compositional Properties Due to a Range of Activity Levels. *J. Biomech. Eng.* **125,** 106 (2003).

180. Clark, C. R. & Ogden, J. A. Prenatal and Postnatal Development of Human Knee Joint Mensci. *Iowa Orthop. J.* **1,** 20–27 (1981).

181. Huang, D., Chang, T. R., Aggarwal, A., Lee, R. C. & Ehrlich, H. P. Mechanisms and dynamics of mechanical strengthening in ligament-equivalent fibroblast-populated

collagen matrices. *Ann. Biomed. Eng.* **21,** 289–305 (1993).

182. Thomopoulos, S., Fomovsky, G. M. & Holmes, J. W. The development of structural and mechanical anisotropy in fibroblast populated collagen gels. *J. Biomech. Eng.* **127,** 742–750 (2005).

183. Grinnell, F. Fibroblast-collagen-matrix contraction: growth-factor signalling and mechanical loading. *Trends Cell Biol.* **10,** 362–365 (2000).

184. Costa, K. D., Lee, E. J. & Holmes, J. W. Creating alignment and anisotropy in engineered heart tissue: role of boundary conditions in a model three-dimensional culture system. *Tissue Eng.* **9,** 567–77 (2003).

185. Nirmalanandhan, V. S., Levy, M. S., Huth, A. J. & Butler, D. L. Effects of cell seeding density and collagen concentration on contraction kinetics of mesenchymal stem cell-seeded collagen constructs. *Tissue Eng.* **12,** 1865–72 (2006).

186. Young, R. G. *et al.* Use of mesenchymal stem cells in a collagen matrix for Achilles tendon repair. *J. Orthop. Res.* **16,** 406–413 (1998).

187. Awad, H. A. *et al.* In vitro characterization of mesenchymal stem cell-seeded collagen scaffolds for tendon repair: Effects of initial seeding density on contraction kinetics. *J. Biomed. Mater. Res.* **51,** 233–240 (2000).

188. Bowles, R. D., Williams, R. M., Zipfel, W. R. & Bonassar, L. J. Self-Assembly of Aligned Tissue-Engineered Annulus fibrosus and Intervertebral Disc Composite Via Collagen Gel Contraction. *Tissue Eng. Part A* **16,** (2010).

189. Puetzer, J. L., Sallent, I., Gelmi, A. & Stevens, M. M. Investigating Collagen Fiber Formation for Functional Musculoskeletal Engineering: Going beyond the Fibril. *ORS 2017 Annu. Meet.* (2017).

190. Huey, D. J. & Athanasiou, K. a. Tension-compression loading with chemical stimulation

results in additive increases to functional properties of anatomic meniscal constructs. *PLoS One* **6,** e27857 (2011).

191. Puetzer, J. L. & Bonassar, L. J. Physiologically Distributed Loading Patterns Drive the Formation of Zonally Organized Collagen Structures in Tissue Engineered Meniscus. *Tissue Eng. Part A* **22,** 907–916 (2016).

192. Hendley, C. T., Tao, J., Kunitake, J. A., De Yoreo, J. J. & Estroff, L. A. Microscopy techniques for investigating the control of organic constituents on biomineralization. *MRS Bull.* **40,** 480–489 (2015).

193. Wang, H. *et al.* Bone Plug Versus Suture-Only Fixation of Meniscal Grafts: Effect on Joint Contact Mechanics During Simulated Gait. *Am. J. Sports Med.* **42,** 1682–1689 (2014).

194. Ross, K. A. *et al.* Comparison of Three Methods to Quantify Repair Cartilage Collagen Orientation. *Cartilage* **4,** 111–120 (2013).

195. Khanarian, N. T. *et al.* FTIR-I Compositional Mapping of the Cartilage-to-Bone Interface as a Function of Tissue Region and Age. *J. Bone Miner. Res.* **29,** 1–26 (2014).

196. Mansfield, J. C., Moger, J., Green, E., Moger, C. & Winlove, C. P. Chemically specific imaging and in-situ chemical analysis of articular cartilage with stimulated Raman scattering. *J. Biophotonics* **6,** 803–14 (2013).

197. Yamanaka, S. A Fresh Look at iPS Cells. *Cell* **137,** 13–17 (2009).

198. Lander, E. S. The Heroes of CRISPR. *Cell* **164,** 18–28 (2016).

199. Choi, N. W. *et al.* Microfluidic scaffolds for tissue engineering. *Nat. Mater.* **6,** 908–915 (2007).

200. Jose, R. R., Rodriguez, M. J., Dixon, T. A., Omenetto, F. & Kaplan, D. L. Evolution of Bioinks and Additive Manufacturing Technologies for 3D Bioprinting. *ACS Biomater.*

Sci. Eng. **2,** 1662–1678 (2016).

CHAPTER 2

Understanding the Stiff-to-compliant Transition of the Meniscal Attachments by Spatial Correlation of Composition, Structure, and Mechanics[2]

Abstract

Soft tissue-to-bone interfaces mediate large changes in tissue properties occurring over only a few hundred microns. The meniscus, located within the knee joint, is an excellent example of this system, because it acts as a load redistributor, requiring a mobile soft tissue unit that is anchored to bone. Using Raman microscopy and confocal elastography, we analyzed interfacial regions within the meniscal attachment that arise from changes in composition, structure, and mechanics. We identified how the nano- to meso-scale architecture mediates complex microscale transitional regions across the interface: two regions defined by chemical composition, five distinguished by structural features, and three mechanically distinct regions. We identified three major components that lead to a robust interface between soft tissue and bone: mobile collagen fiber units, a continuous interfacial region, and a local stiffness gradient. This tissue architecture allows for large displacements of collagen fibers in the attachments, enabling meniscal movement without localizing strains to the soft tissue-bone interface. The interplay of these regions reveals a method relying on hierarchical structuring across multiple length scales by which biology minimizes the presence of stress concentrators between highly dissimilar materials. These insights provide design criteria for soft tissue-to-bone attachments and biomimetic material interfaces.

[2] This chapter has been submitted: Boys, A. J., Kunitake, J. A. M. R., Henak, C. R., Cohen, I., Estroff, L. A., Bonassar, L. J.

Introduction

Interfaces between soft tissue and bone provide fascinating examples of biology's solution for integrating two tissues with widely differing material properties over a small distance.[1–4] These interfacial tissue systems, called entheses, are found at the ends of ligaments, tendons, and the meniscus. Entheses anchor these structures to bone, making them essential musculoskeletal junctions that provide motion and stability in the body. Specifically, the meniscus acts as a shock absorber, redistributing high axial loads that develop in the knee into radial strains within the meniscal tissue.[5] It is able to perform this function through its entheses, which mediate a multiple order of magnitude change in stiffness. This large change in stiffness, ~100 kPa in the meniscus to ~20 GPa in bone, is manifest in similarly steep changes in local tissue strains.[6,7] Typical engineered material interfaces, as well as some biological materials, utilize gradual changes in stiffness, on the order of millimeters, to minimize stress concentrations.[2,8] Entheses lack these long-range stiffness gradients, with a multiple order of magnitude change in stiffness occurring over tens of microns, indicating that stress mitigation must occur through a different mechanism in these interfaces.[9]

Structural, compositional, and mechanical characterization with smaller resolution is critical for elucidating this stress mitigation mechanism, as high degrees of morphological heterogeneity exist in the enthesis at this scale. Historically, histological analysis has divided the enthesis into four distinct regions: bone, calcified fibrocartilage, uncalcified fibrocartilage, and ligamentous tissue.[10,11] These regions vary in composition, structure, and mechanics,[1,12–17] but the link between the composition and structure of the tissue and the mechanical behavior of the enthesis is not fully understood.[1,9,14,18,19] In addition, previous literature has shown the presence of different compositional features in other entheses that are not visible through histology, such as a gradient in mineral content at the interface between mineralized and unmineralized tissue.[12,20,21]

Structural features have also been noted, such as the gradients in the degree of misalignment in collagen orientation across the interface and the presence of a splayed fibrillar region in the fibrocartilage of the enthesis, where fibers (~10s of microns) transition to fibrils (~10s – 100s of nanometers).[1,14,22,23] Current theories suggest that movement of individual fibers and fibrils, relating to the different orientations of collagen across these regions, plays a prevalent role in enthesis function.[24] These examples indicate that enthesis composition and structure are more intricate than can be understood through histological analysis and raise the question of the role of composition and structure in the mechanical behavior of the enthesis. Elucidating the mechanism(s) that enables this rapid change in stiffness requires an analysis that can spatially correlate composition, structure, and function at a scale that is relevant to the tissue.

Recent advances in imaging allow for spatial correlation of compositional and mechanical data at the microscale.[3,4,25,26] For example, Raman microscopy provides a means for producing compositional and structural images with micrometer resolution. This technique relies on detecting molecular vibrations to map the distribution of unique chemical species within the sample and is capable of detecting multiple chemical species that are intermixed at the nanoscale.[27] This type of analysis is particularly important for hierarchically structured tissues, such as bone and entheses, as these types of tissue rely on intimate intermixing of dissimilar materials (e.g., apatite crystals and collagen fibrils) at the nanoscale to function mechanically.[6] Further, this technique does not require fixation or dehydration of tissue, allowing for direct comparison to mechanical data.[4,28–32] Confocal elastography, which uses imaging of applied deformations on a material to calculate spatially resolved strains, can probe mechanical behavior of tissue at the same microscale resolution as Raman microscopy.[33–38] Here, we combine these techniques to examine the compositional, structural, and mechanical properties of meniscal entheses and develop a framework for the structure-function relationship in this tissue.

Results and Discussion

Enthesis morphology transitions from porous trabecular bone into large, oriented collagen fibers

At the macroscale, the fibrocartilaginous meniscus transitions to microscale, preferentially-oriented collagen fibers that insert into the tibial plateau over a sloping, sub-surface interface (Figure 2.1a and Figure 2.S1). We explanted this area from neonatal bovids for further analysis of this tibial insertion (Figure 2.1b). A morphological analysis of the enthesis through Picrosirius Red staining for collagen shows a transition from boney trabeculae to large, oriented collagen

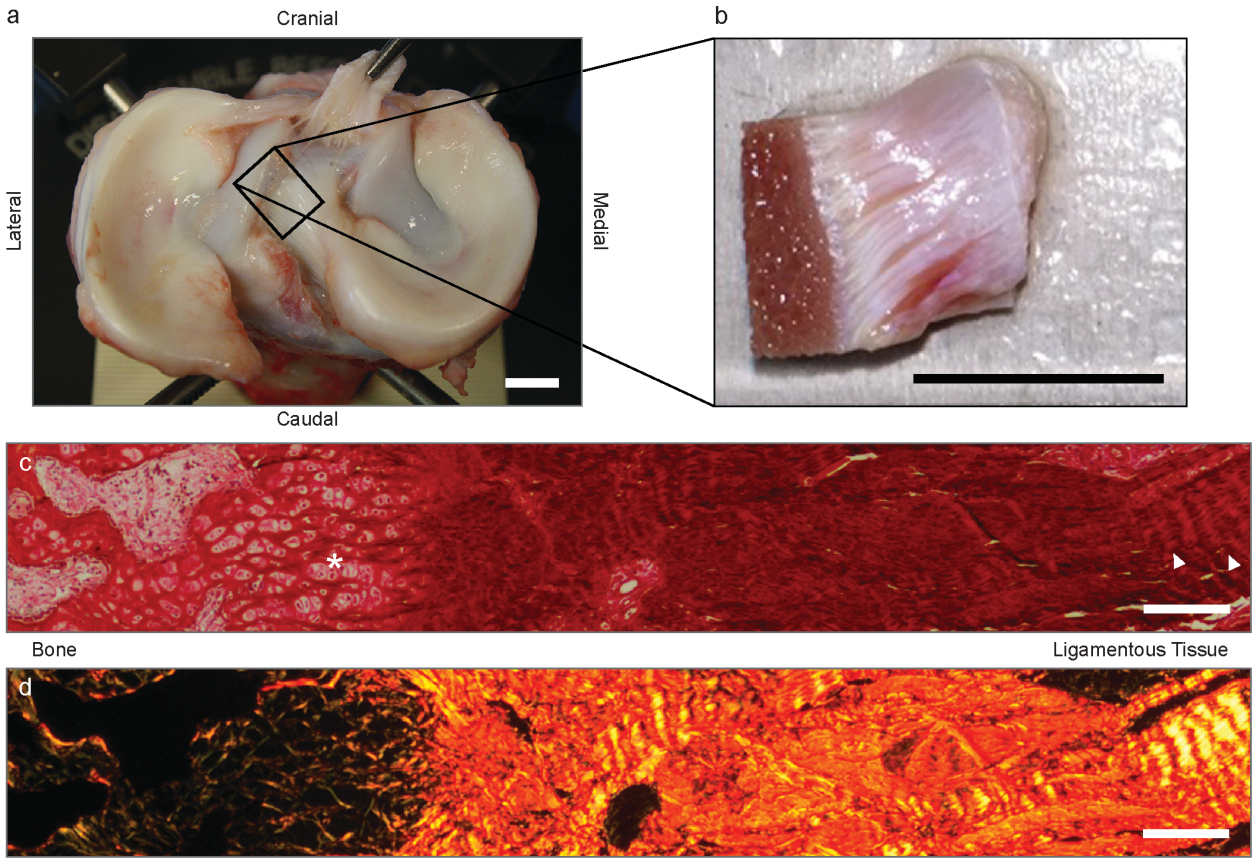

Figure 2.1 Anatomy and structure of the meniscal enthesis. **a** Tibial plateau of a neonatal bovid. The menisci, semi-lunar, fibrocartilaginous discs, situated on the lateral and medial sides of the knee joint, are anchored into the bone through their entheses. Boxed area is approximate location for meniscal enthesis explant. Medial caudal enthesis was used for analysis. This enthesis inserts into the tibial plateau along a sloping interface. The angle of this sloping interface varies, so transverse planes were analyzed as pictured in remaining figures. **b** Meniscal enthesis, flattened using a cryotome thereby generating samples for Raman microscopy and confocal elastography that were square millimeters in cross-sectional area dependent on anatomy. Bone is on the left of

the sample and soft tissue is on the right. **c** Picrosirius Red stain for collagen of demineralized enthesis under white light. Sample shows trabecular structure on the left moving through an intermediate fibrocartilaginous region to a denser collagen region to large collagen fibers on the far right. Star indicates fibrocartilaginous morphology, and arrows point to collagen fibers. **d** Picrosirius Red stain of same area of the enthesis as **c** under cross-polarized light. Color and color intensity are correlated with collagen fiber diameter and degree of orientation.[39,40] Collagen becomes oriented after crossing through the intermediate fibrocartilage. Large, crimped fibers are visible on the far right of the image, consistent with the collagen fibers in **c**. Scale bars for **a** and **b** are 1 cm. Scale bars for **c** and **d** are 200 μm.

fibers, where orientation is evident by color changes in the polarized light image (Figure 2.1c,d). The intermediate area between the trabecular bone and the oriented fibers contains various interfacial regions, visible by changes in the morphology. The trabecular pores of the bone appear to show smaller diameters before transitioning to fibrocartilaginous tissue. The intermediate area between the trabecular bone of the tibial plateau and the oriented fibers in the bulk of the enthesis displays a fibrocartilaginous region followed by microscale transitions in morphology and collagen orientation (Figure 2.1c,d).

To measure changes in composition and structure that occur across this area, Raman microscopy was used to map large areas (~500 μm x 4000 μm) from bone to ligamentous material (Figure 2.2). Explanted entheses were flattened using a cryotome to facilitate optical analysis through Raman microscopy (n = 6). These samples were placed in phosphate buffered saline (PBS) to maintain hydration for all experiments performed in this study. Spectral analysis shows a shift from boney tissue (mineralized collagen), indicated by the presence of the phosphate and carbonate peaks of carbonate-substituted apatite coupled with amide and CH peaks consistent with collagen signatures, to soft collagenous tissue, where the proline/hydroxyproline peaks of collagen are no longer obscured by apatite peaks. The presence of lipidous material was also detected (Figure 2.S2). Composite Raman images (Figure 2.2a) show a transition from mineralized tissue to oriented collagenous material. The mineralized tissue has a typical trabecular structure. Lipidous

material is present in the pores of the trabeculae, likely representing bone marrow.[31] An intermediate region that appears similar in morphology to calcified fibrocartilage is observed near

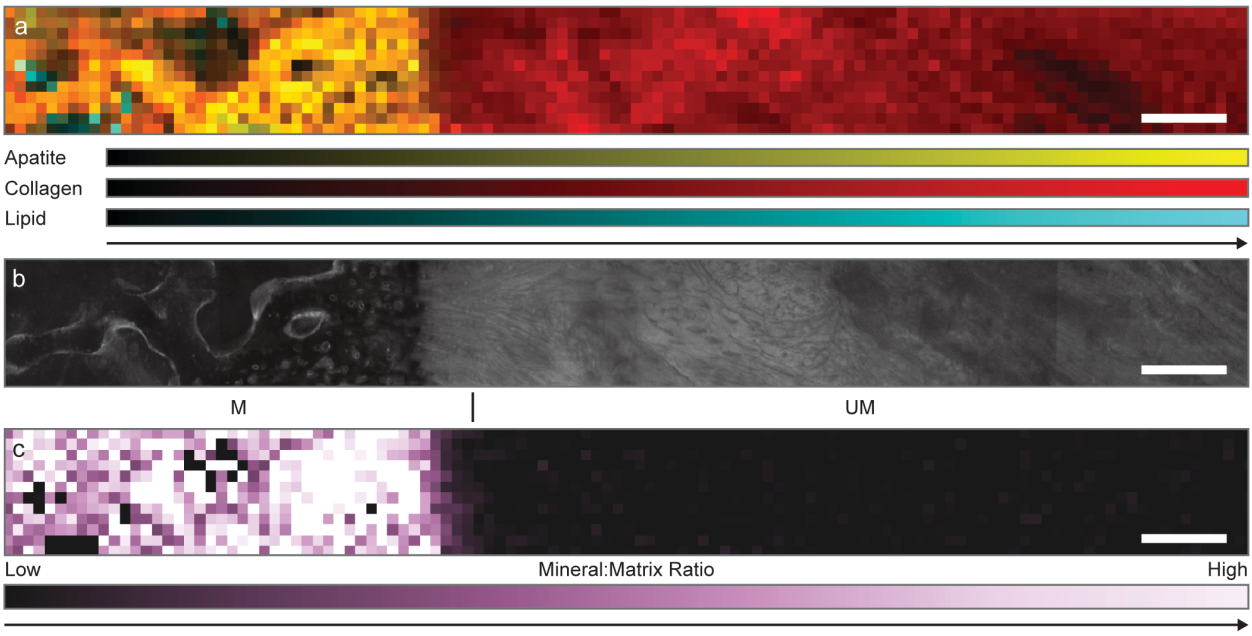

Figure 2.2 Morphological and compositional analysis using Raman microscopy. **a** Representative composite Raman peak area maps of apatite (950 – 980 cm^{-1}), collagen (833 – 905, 1224 – 1296, 1439 – 1484, 2908 – 3028 cm^{-1}), and lipid (1278 – 1326, 1423 – 1468, 2835 – 2870 cm^{-1}).[41,42] Typical trabecular structure can be seen on the left side of the image transitioning to oriented collagen on the right side of the image. Intermediate region contains tissue similar in appearance to calcified fibrocartilage before crossing into soft tissue region. **b** Confocal fluorescence image of same region as **a**. Fluorescence is derived from 5-(4,6-dichlorotriazinyl) aminofluorescein (5-DTAF), a general protein stain. Image is constructed from multiple stitched images. **c** Mineral:matrix image of same region of enthesis as **a** and **b**. Mineral:matrix (950 – 980 cm^{-1} / 1224 – 1296 cm^{-1}) peak area ratio map is plotted for values from 0 to 2. Compositional regions are demarcated: mineralized tissue (M) and unmineralized tissue (UM) with a gradient visible between the regions. Scale bars for all images are 200 μm. See Figure 2.S3 and 2.S4 for n = 2 – 6.

the interface. While the morphology of the enthesis exhibits some sample-to-sample variation, the overall structure remains the same, showing a shift from trabecular bone through intermediate interfacial regions to oriented soft tissue (Figure 2.S3). Structural features in this Raman composite image correlate with a confocal fluorescent image of the same region (Figure 2.2b), providing spatially resolved morphological and compositional measurements.

Transition from mineralized to unmineralized tissue occurs through a gradient

To quantitatively define the compositional changes across the enthesis, mineral:matrix peak area ratio maps were constructed from Raman data (Figure 2.2c and Figure 2.S4).[43,44] The images reveal a shift from mineralized (M) to unmineralized (UM)[3] tissue through an intermediate gradient region, similar to that observed in other entheses.[12,13,21,22] The intermediate gradient region has a length of 188 ± 56 μm (n = 6), where the tissue transitions from mineralized to unmineralized collagenous tissue. The length of this gradient is similar to the size of mineral gradients observed in ligament and tendon entheses[12,13,22] but could appear elongated in this analysis by sub-surface sloping of the interface in the meniscal enthesis (Figure 2.S1). In addition to the gradient region, a band where the mineral:matrix ratio is higher than surrounding tissue is empirically visualized immediately prior to the gradient region, but analysis of secondary apatite-related peaks would be required to test the validity of the presence of this band (Figure 2.S4). Overall, spatial analysis of mineral:matrix ratio images divides the enthesis into two compositionally distinct regions connected through a gradient.

Compositional regions of the enthesis can be further sub-divided into structurally distinct regions

To further understand the structure-function relationship of the enthesis, we developed a method for quantifying details of the microscale collagen architecture. Our analysis indicates the presence of five major structural regions: open trabeculae (M.1), dense trabeculae (M.2), a transitional region (M.3), disorganized bundles (UM.1), and oriented fibers (UM.2) (Figure 2.3). To identify the locations and transitions between these different regions and their relation to the composition, we used Raman images derived from spectral signatures and registered them with our compositional data. In particular, we used maps of the collagen-related portions of the CH peak

[3]Tissue regions are identified parenthetically by number throughout manuscript and in figures for clarity and consistency. Regions numbered (M.1), (M.2), etc. fall within region (M) and so on.

complex, as it shows little polarization dependence and is sensitive to fine changes in tissue morphology and topology due to its high peak intensity (Figure 2.3a and Figure 2.S2). To normalize these data between multiple samples, we divided the distribution of the peak areas of

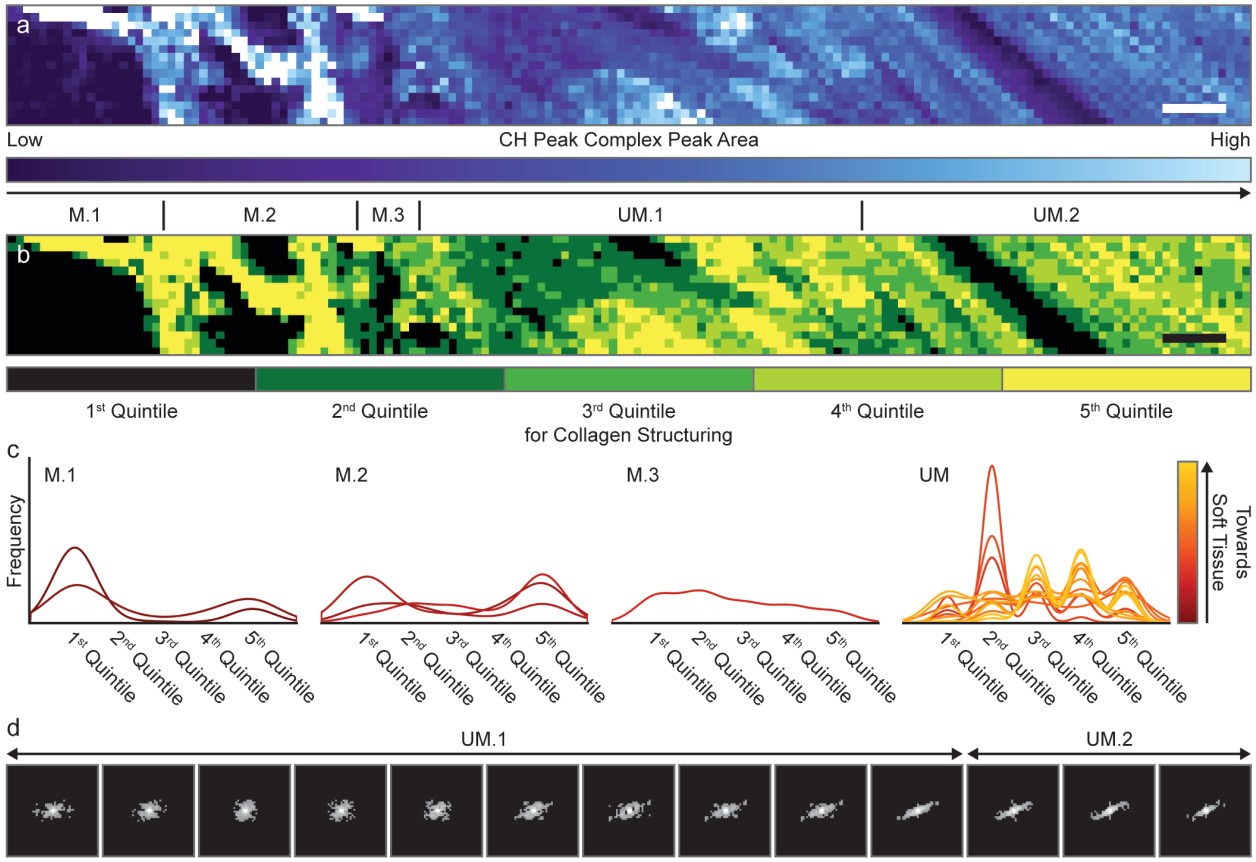

Figure 2.3 Structural analysis using Raman microscopy. **a** Representative Raman image of the collagen-specific portion of the CH peak complex (2908 – 3028 cm^{-1}) area. Color bar is scaled from 0 to 50000. Trabecular structure is visible on left of image and oriented fibers are visible on right. We used collagen specific portions of the CH peak complex to map collagen content, because these are generally the largest spectral signatures in tissue and are sensitive to fine changes in topology and morphology. **b** Quintile-plotted image of the same area for collagen structuring. Structural regions are demarcated: open trabeculae (M.1), dense trabeculae (M.2) (567 ± 266 µm), transitional region (M.3) (200 ± 126 µm), disorganized bundles (UM.1) (200 ± 126 µm), oriented fibers (UM.2). **c** Textural histogram-based analysis of collagen structuring data. For presentation, histograms are shown as continuous lines rather than bars. Histograms are plotted per region: open trabeculae (M.1), dense trabeculae (M.2), transitional region (M.3), remaining tissue, which was found to correspond with unmineralized tissue (UM). **d** FFT-based analysis of orientation for remaining tissue. FFTs are collected on a per pixel sliding window one third the size of the remaining tissue, starting at the end of the transitional region (M.3). Every 6th FFT, including first and last, is plotted to show changes in orientation between disorganized bundles (UM.1) and oriented fibers (UM.2). The demarcation for the last two regions is shown above FFTs and is

determined through calculated orientation index. Scale bars for all images are 200 μm. See Figure 2.S5 and Figure 2.S6 for n = 2 – 6.

the CH peak complex for each sample into five even quintiles and replotted these maps according to quintile distributions (Figure 2.3b). Dividing the data into quintiles both normalizes the images between samples and segments certain structural features. For example, pores were empirically found to fall within the first quintile. Using data from these normalized images, a textural analysis was performed to quantify collagen architecture. The textural analysis spatially binned each sample into 200 μm wide regions and examined histograms of the distribution of pixels within those bins. Using this method (Figures 2.S5, 2.S6, and 2.S7), we identified fingerprints of structural regions based on histogram shapes that were consistently identified across multiple samples: open trabeculae (M.1), dense trabeculae (M.2), a transitional region (M.3), and remaining tissue, which was identified to be spatially consistent with the location of the unmineralized tissue region (UM) (Figure 2.3b,c).

Open trabeculae (M.1) were distinguishable through high frequencies in the first quintile with lower frequencies in the fifth quintile, indicating large porous areas, as the first quintile corresponds to little or no Raman signal. Dense trabeculae (M.2) were distinguishable by low frequencies in the first quintile with high frequencies in the fifth quintile, showing a structure with lower porosity. The tissue structure shifts through a transitional region (M.3) between the trabeculae and the remaining tissue, distinguishable through a broad, flat histogram. Given that these maps are derived from the same spectral data as the compositional analysis, we can spatially register mineralized regions, noting that the trabecular regions and the transitional region are all mineralized, indicating nanoscale apatitic mineral embedded in a collagen matrix. The transitional region demarcates the trabecular structure from the remaining tissue. Thus, our textural analysis reveals that the compositionally-derived mineralized region can be broken up into open trabeculae (M.1), dense trabeculae (M.2), and a transitional region (M.3).

The unmineralized region does not show distinctive trends through textural analysis, but a visual analysis implies a change in overall collagen orientation. To quantify this change, within the unmineralized region, 2D fast Fourier transforms (FFTs) of a sliding window within the normalized Raman images (Figure 2.3b) were collected and filtered for analysis (Figures 2.S6, 2.S8, and Movies 2.1 – 2.6). The onset of oriented tissue was defined through an index related to the orientation of a sliding window FFT. This FFT analysis shows the unmineralized tissue can be divided into two regions: disorganized bundles (UM.1) and oriented fibers (UM.2) (Figure 2.3d).

By combining these two approaches (textural and FFT analyses), five structural regions were identified for n = 6 samples: open trabeculae (M.1), dense trabeculae (M.2) (567 ± 266 μm), a transitional region (M.3) (200 ± 126 μm), disorganized bundles (UM.1) (1008 ± 367 μm), and oriented fibers (UM.2).

Confocal elastography reveals strain gradients across the enthesis

The mechanical behavior of the enthesis was analyzed to understand how the enthesis performs under physiologic loading conditions. To perform this analysis on tissue, deformations were applied with a piezoelectrically-actuated loadframe and imaged on an inverted confocal microscope.[35–38] For analysis, flattened, hydrated samples (n = 6) were pre-stressed and submerged in PBS, a fluid that possesses a similar ionic strength and osmolarity to biological fluids, in a hydration plate. The hydration plate was mounted into a piezoelectrically-actuated loadframe that sits on top of an inverted confocal microscope.[35,38,41] Entheses were loaded at 3% cyclic tension at a physiological strain rate (1 Hz), and videos of loading cycles were recorded for n = 6 samples (Movies 7 – 12). Peak-to-peak strain maps were created from videos using digital image correlation software[15,46] and spatially correlated with data from Raman images using features of mineralized tissue visible in both confocal fluorescence and Raman images (Figure 2.2b,c). Visual analysis of strain maps reveal that strains are highly localized to the soft tissue, consistent with the

fact that the bone has a much higher modulus than soft tissue. Furthermore, we observed the presence of highly localized strains between the fibers in areas situated away from the mineralized interface (Figure 2.4a,b,c). We also observed a multiple order of magnitude increase in peak-to-

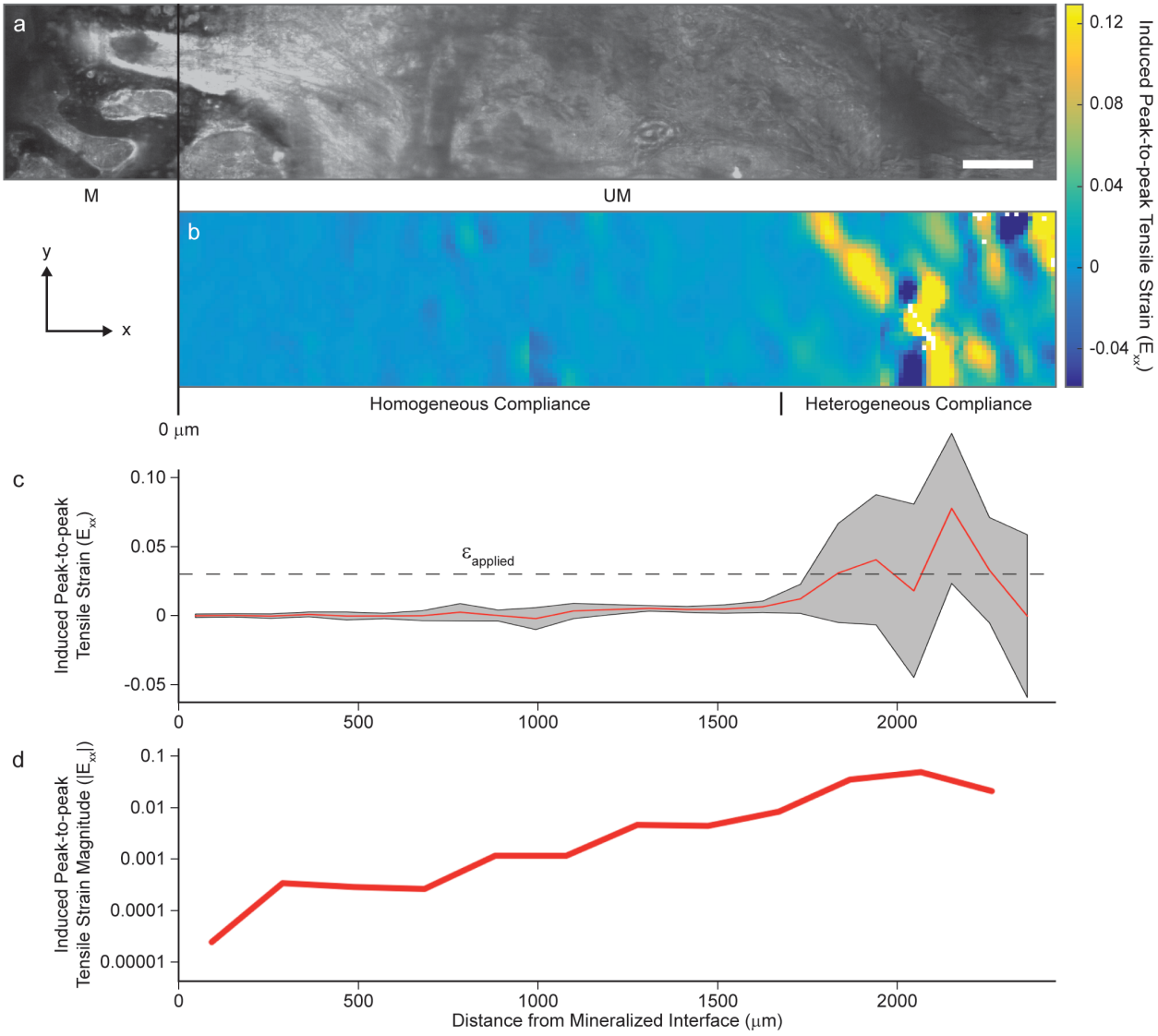

Figure 2.4 Mechanical analysis using confocal fluorescent elastography. **a** Representative confocal fluorescent image of enthesis sample. **b** Peak-to-peak E_{xx} Langrangian finite strain map at frame 10 (peak in loading cycle) starting at mineralized interface with coordinate system corresponding to confocal fluorescent image from **a**. Mineralized tissue (M) and unmineralized tissue (UM) are identified. Additionally, within the unmineralized tissue (UM), the homogeneous compliant region (1310 ± 506 μm) and the heterogeneous compliant regions are identified. **c** Average peak-to-peak E_{xx} Langrangian finite strain as a function of distance from mineralized interface at frame 10. Red line is average strain, and gray region shows standard deviation. Average strains are binned at 100 μm for clarity. **d** Average peak-to-peak E_{xx} Langrangian finite strain

magnitude on a semi-log plot as a function of distance at frame 10. Strains are binned at 200 μm for clarity. **c** and **d** are scaled to match the images in **a** and **b**. Scale bar is 200 μm. See Figure 2.S9 and Figure 2.S10 for n = 2 – 6.

peak strain magnitude moving away from the mineralized interface, evident by a logarithmic trend in strain magnitude (Figure 2.4d). As the compositional variation within this region does not account for this logarithmic increase in strain (Figure 2.2c), structural considerations within the unmineralized region of the enthesis must significantly affect mechanical behavior.

Structural data (Figure 2.3) indicates the collagen in the soft tissue undergoes a change from disorganized bundles to oriented fibers moving away from the mineralized interface. Spatially correlating the mechanical data with the structural data, we observe that the strains in the disorganized bundles region (UM.1) occur at magnitudes similar to the applied strain, meaning that the mineral:matrix gradient can appropriately mediate strains into the mineralized tissue. Qualitative examination of loading movies indicates that, within the oriented fiber region (UM.2), strains originate from fiber movements (Figure 2.4a,b, Figure 2.S9). During loading, fibers can be observed moving with respect to one another, rather than moving as a unit (Movies 7 – 12). This behavior indicates that the fibers are only loosely bound to each other, thereby allowing for them to move individually, as we see deformations within the tissue that do not entirely result from strains within the fibers themselves (Figure 2.4a,b). These observations indicate that the fibers are primarily translating and rotating, rather than stretching, thus allowing for large displacements to occur without localizing strain to the disorganized bundles region (UM.1). Given that strains in the oriented fibers region arise from structural considerations, such as the allowance for fiber translations and rotations, we have termed them “structural strains,” thereby differentiating them from material strains.

To connect the size of these mechanical regions with the structural changes we observed, we analyzed where the structural strains begin to dominate the mechanical behavior of the tissue.

Quantitative measurement of this transition was performed by normalizing strain as a function of distance from the mineralized interface to the average global strain of each sample's strain map. The point at which the average strain increased above the global strain was determined as the transition location (Figure 2.S10). This value was found to occur 1310 ± 506 μm from the mineralized interface, matching closely with the value recorded for the structurally-derived disorganized bundles region (1008 ± 367 μm). The sizes of these regions agree, indicating that the onset of the high structural strains arise from oriented fibers. Further, given that the strain maps were derived from samples under tension, we know that the disorganized bundles region (UM.1) must transfer load. Therefore, we theorize that this region (UM.1) is more homogeneously structured than the heterogeneously organized oriented fibers region (UM.2). These data suggest that the strains in the disorganized bundles region (UM.1) are material strains, while those in the oriented fibers region (UM.2) are primarily structural strains. Given the inverse relationship of strain and stiffness, our mechanical analysis indicates that the mineralized region (M) is much stiffer than the unmineralized region (UM), and that the unmineralized tissue is mechanically comprised of a homogeneous compliant region and a heterogeneous compliant region corresponding to disorganized bundles (UM.1) and oriented fibers (UM.2), respectively.

Enthesis combines structure and composition to provide mobility within the tissue without localizing strain at the interface

Probing the tissue at a length scale that matches the morphological variations observed through histology allowed us to compare and localize composition, structure, and mechanics in the meniscal enthesis (Figure 2.5). We were able to spatially correlate these aspects of the tissue by aligning regions we observed to be present in our Raman and mechanical analyses, namely the interface between mineralized and unmineralized tissue (Figure 2.2b,c). Compositionally, we observed a shift from mineralized (M) to unmineralized (UM) tissue through a gradient in

mineral:matrix ratio, similar to mineral:matrix gradients observed in other entheses found throughout the body.[12,13,21,22] The mineralized portion of the enthesis contains three distinct

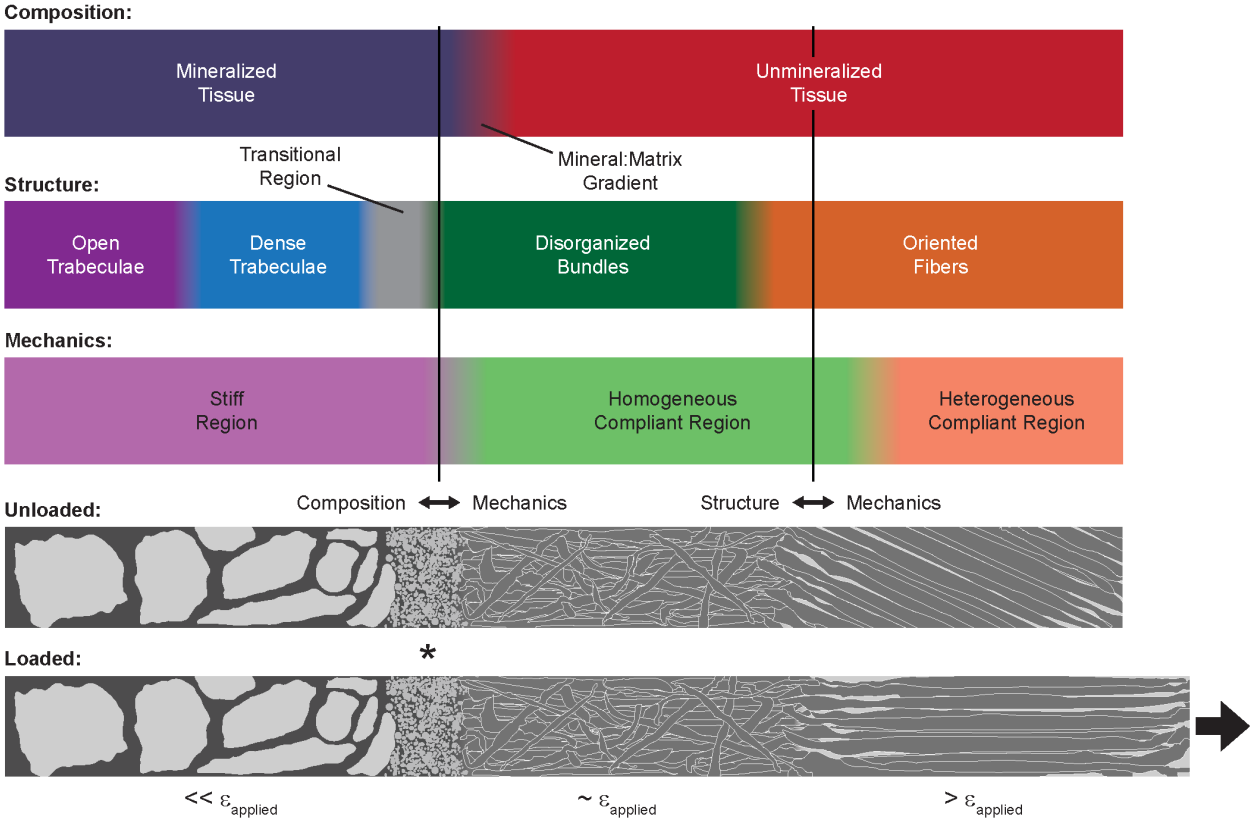

Figure 2.5 Schematic view of the regional changes in the enthesis followed by the resulting mechanics. Regions are plotted to accurately reflect the size and position of regions with respect to one another. Two compositional regions were found: mineralized (M) and unmineralized (UM) tissue, which are separated by a mineral:matrix gradient (188 ± 56 μm). Five structural regions were found: open trabeculae (M.1), dense trabeculae (M.2) (567 ± 266 μm), transitional region (M.3) (200 ± 126 μm), disorganized bundles (UM.1) (1008 ± 367 μm), and oriented fibers (UM.2). Three mechanical regions were found: a stiff region, a homogeneous compliant region (1310 ± 506 μm), and a heterogeneous compliant region. The first mechanical transition is dictated by composition, whereas the second is dictated by structure, as indicated. Schematic of enthesis scaled to regions is shown on bottom in unloaded and loaded configurations. High structural strains develop in the oriented fibers region on the right during loading. Fibrocartilaginous region is indicated by a star in the schematic. Strains are reduced in the mineralized tissue, which gradually transitions into porous tissue that extends through the remainder of the bone in the proximal tibia.

structural regions (M.1, M.2, M.3) that result in a mechanically stiff region, indicating that this mechanical transition is driven by compositional changes at physiologic loads. Hypothetically, structurally changes in the mineralized tissue of the enthesis also relate to local mechanical changes,

as in the mechanical behaviors of porous and dense bone, but further measurements under non-physiologic loading conditions would be required to explicitly measure these changes. The unmineralized portion of the enthesis possesses two structural regions (UM.1, UM.2) that each result in different mechanical behavior, meaning that structure drives the mechanics within the unmineralized tissue (UM) at physiologically relevant loads.[7,47] Previous studies have hypothesized that the mineral:matrix gradient in addition to localized stiffness changes near the interface contribute to the strengthening of the interface between soft tissue and bone at the microscale.[9,14,21,22,48] For the first time, we demonstrate a new mechanical mechanism, fiber sliding within the soft tissue regions of this interface, and spatially correlate it with a full picture of the structuring across the meniscal enthesis.

We further postulate that these structurally defined regions play individual roles pertaining to the bulk mechanics of the enthesis. The oriented fibers (UM.2) of the heterogeneous compliant region permit large displacements to occur within the tissue in the form of structural strains due to fiber sliding. We propose that this sliding phenomenon allows for lateral movement of the meniscus without resulting in the high strains this type of motion would impart into the interface between mineralized and unmineralized tissue. The oriented fibers region transitions into the disorganized bundles (UM.1) of the homogeneous compliant region, which only allows for smaller material strains. This region likely corresponds to the splayed fibers previously identified in tendon entheses. We found the strain magnitude within this region logarithmically decreases prior to the transition into mineralized tissue (M) (Figure 2.4d), which is consistent with previous hypotheses regarding fiber splaying in the enthesis.[1] Within the mineralized tissue, previous mechanical studies on human meniscal entheses using nanoindentation indicate that a logarithmic increase in stiffness occurs within the first few hundred microns moving into mineralized tissue.[9] Extrapolating this information onto our data implies that the logarithmic strain response we

observed would extend into the mineralized tissue. We suggest that the mineral:matrix gradient, marking the beginning of this stiffness increase in the mineralized tissue, is of sufficient length to transition the relatively low strains observed near the interface between mineralized and unmineralized tissues to the further mineralized regions. Subsequently, within the mineralized tissue, the transitional region (M.3) appears to provide a laterally continuous area of attachment for the disorganized bundles (UM.1). The location of the transitional region (M.3) is morphologically consistent with calcified fibrocartilage, as evidenced by the presence of chondrocyte lacunae visible in confocal fluorescent images (Figure 2.2a,b and Figure 2.3a,b). Past the transitional region (M.3), a gradient in porosity from dense trabeculae (M.2) to open trabeculae (M.1) blends the interfacial tissue with subchondral bone (Figure 2.5). The porosity in these regions provides a location for bone marrow to reside but also decreases the bulk tissue stiffness, as bone marrow has a much lower stiffness than bone.

The picture emerges that the oriented fibers (UM.2) of the enthesis provides the meniscus with mobility for its role as a shock absorber, localizing the high displacements required for the meniscus to function to this region (UM.2). The disorganized bundles (UM.1) splay into the mineralized tissue[1] and distribute load through a logarithmic decrease in strain. The transitional region (M.3) marks the onset of mineralized tissue and provides a laterally continuous region of insertion for the disorganized bundles. The start of the transitional region coincides with a local mineral:matrix gradient, interfacing the mineralized and unmineralized tissues before showing a continuing gradient in stiffness extending into the mineralized tissue.[9] The end of the transitional region (M.3) corresponds to the onset of porous tissue, providing a gradual structural transition into subchondral bone, while simultaneously softening the stiffness gradient at a bulk tissue scale. To extend the structures and mechanisms to other engineered systems or mechanical models, we would need to calculate local elastic moduli for each of these regions. Coupling our data with

values from previous works, we can speculate that a change in the stiffness of the oriented fibers (UM.2) (10 – 100 MPa)[9,18] should undergo a logarithmic increase moving through the disorganized bundles (UM.1) within the soft tissue regions. After which the tissue possesses a gradient in mineral:matrix content (1 – 10 GPa),[9,49,50] before reaching the stiffness of calcified cartilage in the transitional region (M.3) and finally to bone (~20 GPa)[6] within the remaining mineralized regions (M.1, M.2). These values represent the local material stiffnesses. While these stiffness values are important with regard to binding soft tissue and bone, we emphasize that structure also plays an important role in enthesis functionality.

This work also provides insight into the nanoscale aspects of the enthesis. As we believe the disorganized bundles region (UM.1) corresponds to the splaying of fibers identified in other entheses,[1] we suggest that the difference in mechanical behavior observed between the disorganized bundles (UM.1) and oriented fibers (UM.2) relates to the nanoscale structuring of the collagen in these regions. Previous studies have found that the fibers of ligaments, tendons, etc. consist of type I collagen, whereas the tissue near the interface between soft tissue and bone is largely type II collagen.[1,11] These collagens self-assemble into fibrils of different sizes based on their type, where type I collagen assembles into fibrils of larger diameters (100s of nanometers) than type II collagen (10s of nanometers).[51,52] The apparent disorganized nature of the disorganized bundles (UM.1) may result from the collagen fibril type within this region, where these structures are organized at the nanoscale but disorganized at the microscale. Conversely the type I collagen results in larger fibrils, generating the microscale organization observed in the oriented fibers region (UM.2). Collagen organization may have further connotations in the location of mineral with respect to collagen across the mineral gradient near the transitional region (M.3). The distribution of the mineral with respect to the collagen fibrils has been shown to be different at the nanoscale, where mineral is largely contained within the interior of collagen fibrils in bone and

exterior to fibrils farther along the gradient.[53] Disorganized collagen bundles may allow for the increased presence of mineral exterior to collagen fibrils. Further, different concentrations of biomolecules associated with collagen cross-linking have been found near the insertion versus the bulk of the enthesis.[1] These data may explain the fiber sliding phenomena we observed within the oriented fibers region (UM.2) versus the disorganized bundles (UM.1), which we found to be necessary for enthesis function. These nanoscale considerations may relate to the overall mechanics of the enthesis, given that we find evidence for a direct relationship between the structure and mechanics of the enthesis within the soft tissue regions.

In addition to the nano- and microscale features we have identified, larger scale features in the lateral directions, including interdigitation between mineralized and unmineralized tissue[54] and between calcified fibrocartilage and bone,[9] also provide further toughening mechanisms by interlocking these tissues and providing an increased surface area.[54] These structural features act in concert to allow for large displacements within the enthesis without localizing strains to the interface between mineralized and unmineralized tissue, thus minimizing the presence of stress concentrators between these mechanically dissimilar materials.

Our analysis of the enthesis was performed on neonatal tissues, which are still developing. While these structures are functional, the size and/or presence of these regions may change as the animals age. While few analyses have approached the construction of the enthesis as it is addressed here, other studies have recognized similar features to the structures we observed. For example, a gradient in collagen organization and alignment was found moving from tendon to bone, likely highlighting similar regions to the two structural regions we termed disorganized bundles (UM.1) and oriented fibers (UM.2).[22] Based on our own observations and those from other studies, we believe these regions will remain present throughout the development of the animals.[11,12,55] However, we speculate that some of these regions, particularly the disorganized bundles (UM.1),

will shrink as the animal ages. In this framework, the oriented fibers (UM.2) will begin to extend closer to the mineral gradient between mineralized and unmineralized tissue during aging, eventually directly representing the splayed fibers previously identified.[1,9] Therefore, the large size of the disorganized bundles region (UM.1) we observed in these samples may be a developmental aspect of the enthesis, possibly indicating its importance when engineering such structures.

Conclusion

Here, we have outlined a full view of the structure of the enthesis, from the bone to oriented fibers in the bulk of the attachment and correlated this structure with the mechanical phenomena that aid in interfacial robustness. Our data indicates a robust soft tissue-to-bone interface requires three components: mobile fiber units, a continuous interfacial region, and a local stiffness gradient. Working in concert, these components gradually dissipate stresses without localizing stresses at the edges of pores, between fibers, etc. These findings elucidate the mechanisms that prevent the buildup of stress concentrators at the soft tissue-to-bone interface while providing extensive mobility within the soft tissue. Implementing these mechanisms in engineered constructs has the potential to inform the production of interfacial tissue implants and biomimetic materials junctions. While a high degree of focus has been placed on generating stiffness gradients for interfacial engineering, our work shows that structural features within the soft portions of the attachment are also necessary for interface function. Specifically, the presence of fibers allows for lateral movement with respect to the interface, which is particularly important to meniscal function. More attention should be paid to the development of hierarchical fiber arrangements in future designs.[56–60] Future work should focus on examining the fibrillar structure of the collagen in the soft tissue regions of the enthesis. Understanding the mechanisms by which the enthesis assembles differently structured but interconnected soft tissue regions would greatly aid in our ability to construct similarly robust interfaces. Further, by comparing the enthesis system to other biological interfaces,

such as the mussel byssus or the sutures of turtle shells,[61–63] we can identify whether nature has converged on similar mechanistic principles for connecting soft and hard materials. Overall, these data can be used to inform the design and fabrication of interfaces between dissimilar materials systems by utilizing the structural framework provided through our analysis of the enthesis and dialing in appropriate moduli for the application. These principles, learned from the construction of the enthesis, constitute a new paradigm for producing robust interfaces in artificial tissues, robotics, prosthetics, and other engineered systems.

Methods

Tissue Acquisition and Preparation: Enthesis samples were explanted from 1 – 3 day old neonatal bovine legs from 12 different animals (6 for Raman analysis and 6 for mechanical analysis) (Gold Medal Packing Inc.). The medial caudal meniscal enthesis was chosen, as it is the most commonly injured enthesis in the human knee joint.[64] Bovine stifle joints were disarticulated, and samples were removed from the center of the enthesis by making cuts parallel to the fibers. These samples were immediately frozen and embedded in Optimum Cutting Temperature (OCT) compound (Tissue-Tek®). Blocks were shaved using a cryostat (Thermo Scientific Mircom HM 550) until bone and ligamentous tissue interface was visible on tissue block. Resulting blocks were unfrozen immediately prior to analysis by Raman microscopy or confocal elastography.

Histology: Enthesis samples were explanted in the same manner as described above. However, instead of cryosectioning, samples were fixed in formalin, decalcified, and embedded in paraffin. Sections were taken at 4 μm thickness and stained with Weigart's hematoxylin (Amresco®) for 10 minutes and Picrosirius Red (Rowley Biochemical Inc.) for 1 hour. Slides were imaged on a microscope (Nikon Eclipse TE2000-S) through an attached camera (Diagnostic Instruments, Inc. RTKE Spot) in white light and under cross-polarized light.

Raman Microscopy: Raman analysis was performed for n = 6 samples. Tissue samples were thawed and glued to a petri dish before submersion in PBS. Raman imaging (Renishaw InVia Confocal Raman microscope) was performed immediately after thawing. Raman spectra were collected using a 532 nm laser (Cobalt Samba 500 DPSS Laser System) through a water immersion objective lens that was also submerged in PBS with the sample. 10x (Leica, NA – 0.30) and 63x (Leica, NA – 0.90) dipping lenses were utilized for mapping and collection of individual spectra, respectively. For mapping, spectra were collected using a ~4 x 0.5 mm grid at a 25 μm step size as laser spot size was determined to be ~25 μm in diameter. Laser power was set to 200 mW, and collected with a 1 second integration time through a 600 l/mm grating on a CCD detector.

Raman images representative of a given biological component were generated using characteristic peak areas that had minimal overlap with other components present in the meniscal enthesis: apatite (950 – 980 cm^{-1}), collagen (833 – 905, 1224 – 1296, 1439 – 1484, 2908 – 3028 cm^{-1}), and lipid (1278 – 1326, 1423 – 1468, 2835 – 2870 cm^{-1}).[41,42] Area maps were converted to text image format and further processed using FIJI.[65] To reduce noise and enhance image quality all peak area images for a given component were summed (with the exception of apatite). Final component images for collagen, apatite, and lipids were stacked and processed as image composites with LUTs assigned to the components (apatite: yellow; collagen: red; lipid: cyan). The minimum was set to zero for each component and maximum intensity values were adjusted to both eliminate saturated pixels and ensure simultaneous visualization of the given components (apatite: 0 – 13900, collagen: 0 – 144000, lipid: 0 – 60600). The final composite image was converted to 24-bit RGB for portability and compatibility (Figure 2.2a and Figure 2.S3).

Peak areas and peak area ratios for compositional and structural analysis were calculated using Renishaw WiRE 4 Software. All negative peak areas were replaced with zeros, since a negative calculated peak area indicates the lack of a peak. The mineral:matrix ratio was calculated

using the ratio of the ν_1 PO_4^{3-} band to the Amide III band and was defined as 950 – 980 cm^{-1} / 1224 – 1296 cm^{-1}. A ratio of these bands was chosen to allow for comparison between samples. Due to the opacity of bone, measurement of composition using a single peak can be challenging.[43,44] Further plotting of maps, averaging of maps, histogram-based analysis, and FFT-based analysis was performed using Mathematica. Maps were plotted and averaged as a function of distance from the interface to measure the length of the mineral:matrix gradient (Figure 2.2c and Figure 2.S4). The gradient start was empirically defined as a mineral:matrix ratio of 2 occurring before the interface, sloping to a value of less than 0.1, which was defined as the end of the gradient region.

Structural collagen maps were produced by mapping the 2908 – 3028 cm^{-1} peak area (Figure 2.S5). The distribution of peak area values for each map was divided into even quintiles, and the maps were replotted using these quintiles in order to normalize data across samples (Figure 2.3a,b and Figure 2.S6). Quantiles were empirically established for distinguishing pores and changes related to topological distribution of fibers. Quintile division was found to follow closest to empirically established quantiles without requiring the division of the distribution using uneven quantiles. Therefore, quintile division of CH peak complex area distribution was used to facilitate analysis of collagen structuring data (Figure 2.S7). Maps were spatially binned into 200 μm (8 pixel) wide columns beginning in the soft tissue regions of the enthesis and extended back to the boney regions. Histograms of the quintile values in these grids were produced and analyzed to determine textural changes in collagen. Fingerprints of different regions were identified from these histograms and used to determine changes in the structure from quintile plots.

Analysis of orientation was performed using FFTs. A region one third of the size of the distance from the transitional region (M.3) to the end of the image was utilized as a sliding window to measure orientation using FFTs. The pixels of this window were first linearly interpolated and a Hann Window function, fitted to the dimensions of the window, was applied to remove artifacts

arising from boundary effects (Figure 2.S8).[66] 2D FFTs were calculated for this window, and 2D FFTs were cropped to only contain the center 50 x 50 pixel area (low frequency area). These images were then thresholded to remove pixels with intensities below 0.5; range of pixel intensities in each 2D FFT is from 0 to 1. Images were rotated in 5 degree increments and center two rows of pixels were averaged. Maximum average pixel intensity was calculated as a function of angle. This value was then divided by the average pixel intensity at the angle orthogonal to the angle with the maximum average pixel intensity and used as an orientation index. These values were plotted, and the peak in the plot was determined as the onset of oriented tissue (Movies 2.1 – 2.6 and Figure 2.S6).

Confocal Fluorescence Elastography: Strain analysis was performed for n = 6 samples. Samples were stained with 5-DTAF (ex / em 492 nm / 516 nm, Invitrogen), a general protein stain, for 60 minutes and pre-stressed at 3 kPa for 30 minutes in PBS, calculated by measuring the cross-sectional area of bony portion of the enthesis tissue block. Samples were mounted into a piezoelectrically-actuated microloadframe with a hydration dish containing PBS.[35,38,45] The microloadframe was placed on an inverted confocal microscope (LSM 5 LIVE, Carl Zeiss Inc.) and imaged using a 10x objective and a 488 nm laser. Samples were cyclically strained in tension at a 3% peak-to-peak amplitude at 1 Hz around the gauge length of the soft tissue of the sample (measured at the conclusion of pre-stressing). Confocal slice thicknesses were ~10 – 20 μm. Videos of loading cycles were recorded at 20 frames per second using a high-speed camera (v7.1, Vision Research). Videos were analyzed using FIJI to determine the start of the loading cycle.[65] Frame 10 was used as peak of sinusoidal loading cycle. Ncorr digital image correlation (DIC) code, run through MATLAB, was used to develop spatially correlated strain maps.[46] A subset radius of 15 with a subset spacing of 5 and a correlation coefficient of 1.2 was used for Ncorr analysis. E_{xx}, E_{yy}, and E_{xy} Langrangian finite strain maps were developed for each sample. These maps were

concatenated into a single, stitched map of the entire enthesis region. These data were loaded into R for analysis. The interface with mineralized tissue was visually identified, and data prior to that interface was removed. Resulting strain maps were collapsed into average strain as a function of distance from the calcified interface. These data were binned in the direction of the interface. Variance and standard deviation were calculated from the initial strain maps and binned in the same manner. To determine the length of the homogeneous compliant region, average strain for the entire map was calculated, and average strains as a function of distance were normalized to this value. The point at which the normalized strain increased above 1 was considered the point at which structural strains dominated the tissue's mechanical behavior. To generate semi-log plots, the absolute value of the average data from above was taken and the log of that value was calculated. These data were plotted as a function of distance from the mineralized interface.

Image Display: To reduce the effects of stitching in confocal fluorescence image (Figure 2.2b), image transparency was decreased to 60%, and stitched images were placed on top of each other. Resulting stitched image transparency was again decreased to 75% and placed over a black background. For remaining confocal fluorescence images, transparency was reduced to 75% and placed over a black background (Figure 2.4a and Figure 2.S9). Brightness and contrast for confocal fluorescent images used in movies (Movies 2.7 – 2.12) were auto-adjusted using FIJI.[65]

Supplemental Information

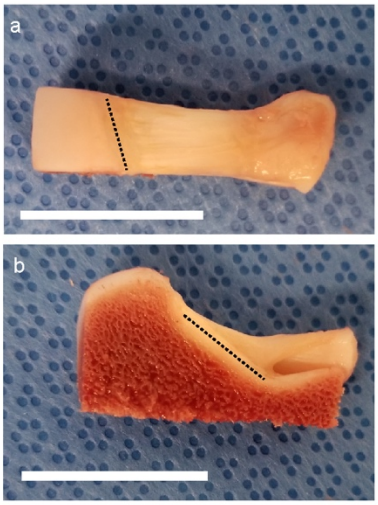

Figure 2.S1 Explant of the medial caudal meniscal enthesis from a neonatal bovid. **a** Transverse view of explanted meniscal enthesis. **b** Sagittal view of explanted meniscal enthesis. Dotted lines show approximate insertion location. We note that bovids can walk at birth, indicating the functionality of this interface. Scale bars are 2 cm.

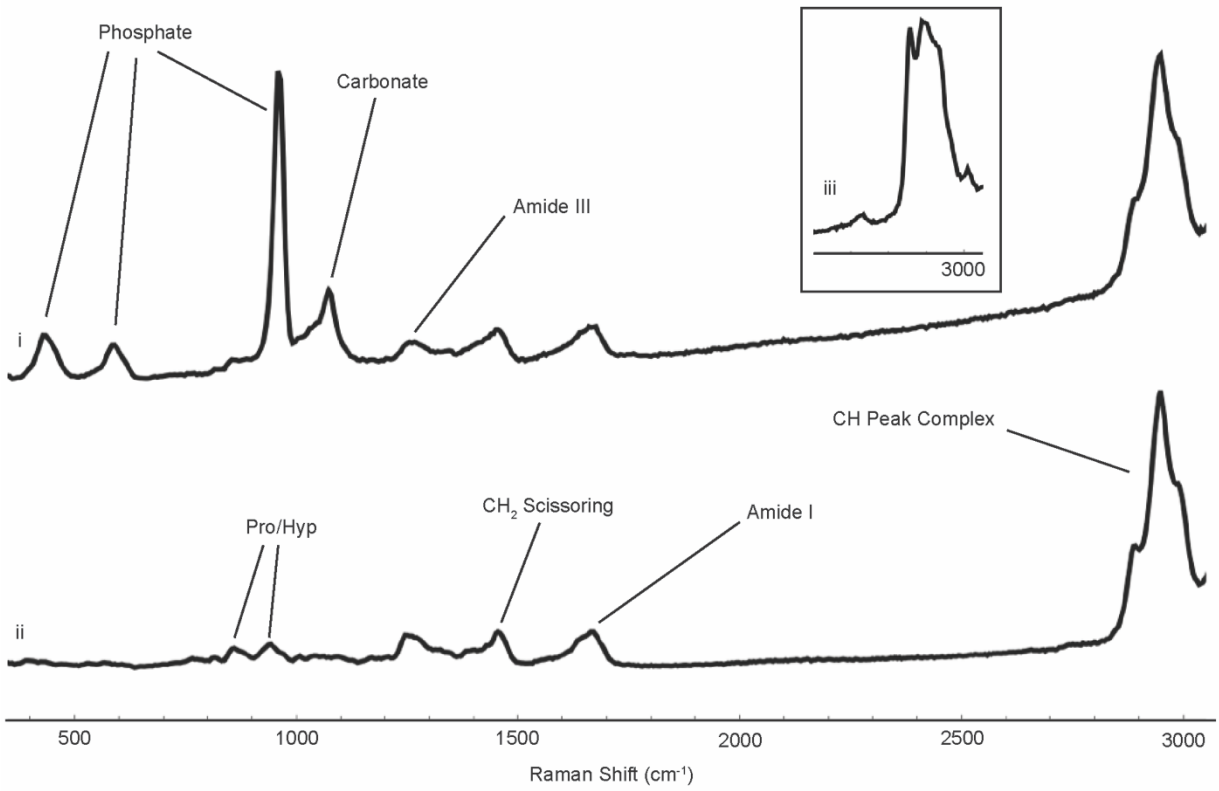

Figure 2.S2 Representative Raman spectra of different regions of the enthesis. Spectrum i is recorded in the boney portion of the enthesis. Spectrum ii is recorded from the soft tissue portion

of the enthesis. Spectrum iii shows only the CH peak complex as recorded from a portion of the enthesis containing lipidous material. Spectra are plotted as standard scores.

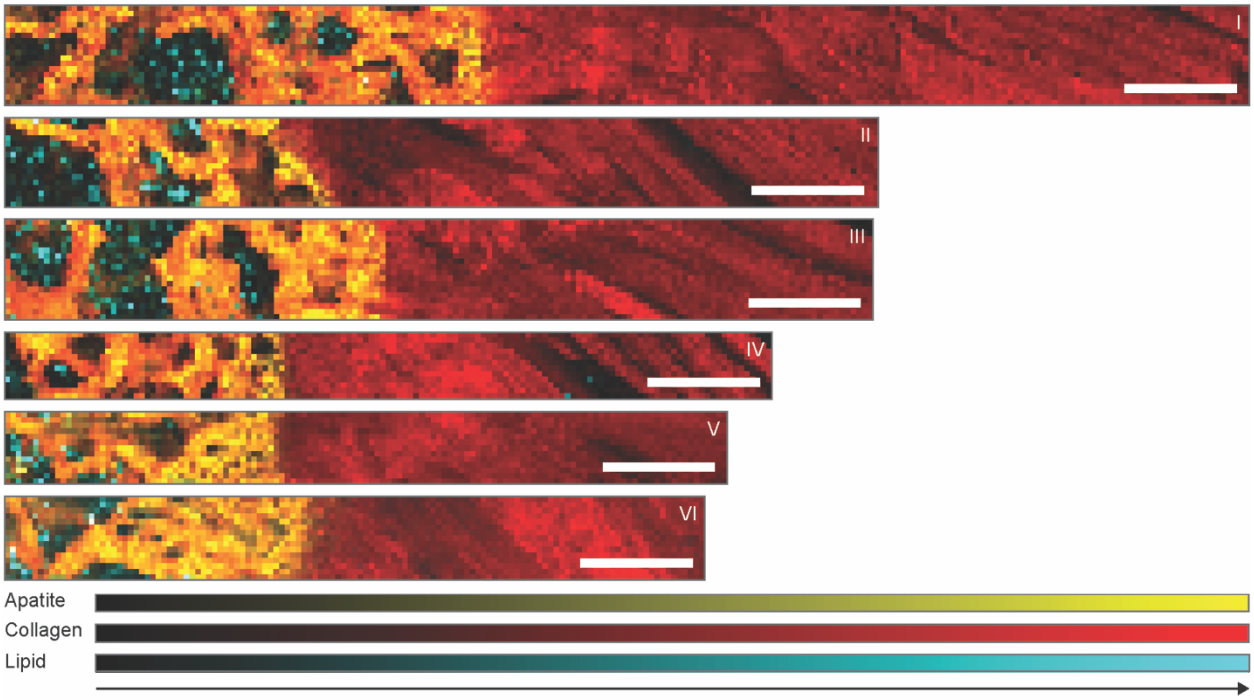

Figure 2.S3 Composite Raman peak area maps for samples, showing apatite (950 – 980 cm^{-1}) in yellow, collagen (833 – 905, 1224 – 1296, 1439 – 1484, 2908 – 3028 cm^{-1}) in red, and lipid (1278 – 1326, 1423 – 1468, 2835 – 2870 cm^{-1}) in cyan. All images show boney tissue on the left and soft tissue on the right. Roman numerals (I–VI) indicate a specific sample and are consistent between figures. Sample II is the representative sample in Figure 3 for structural analysis. Sample V is the representative sample in Figure 2 for compositional analysis. Scale bars are 500 μm.

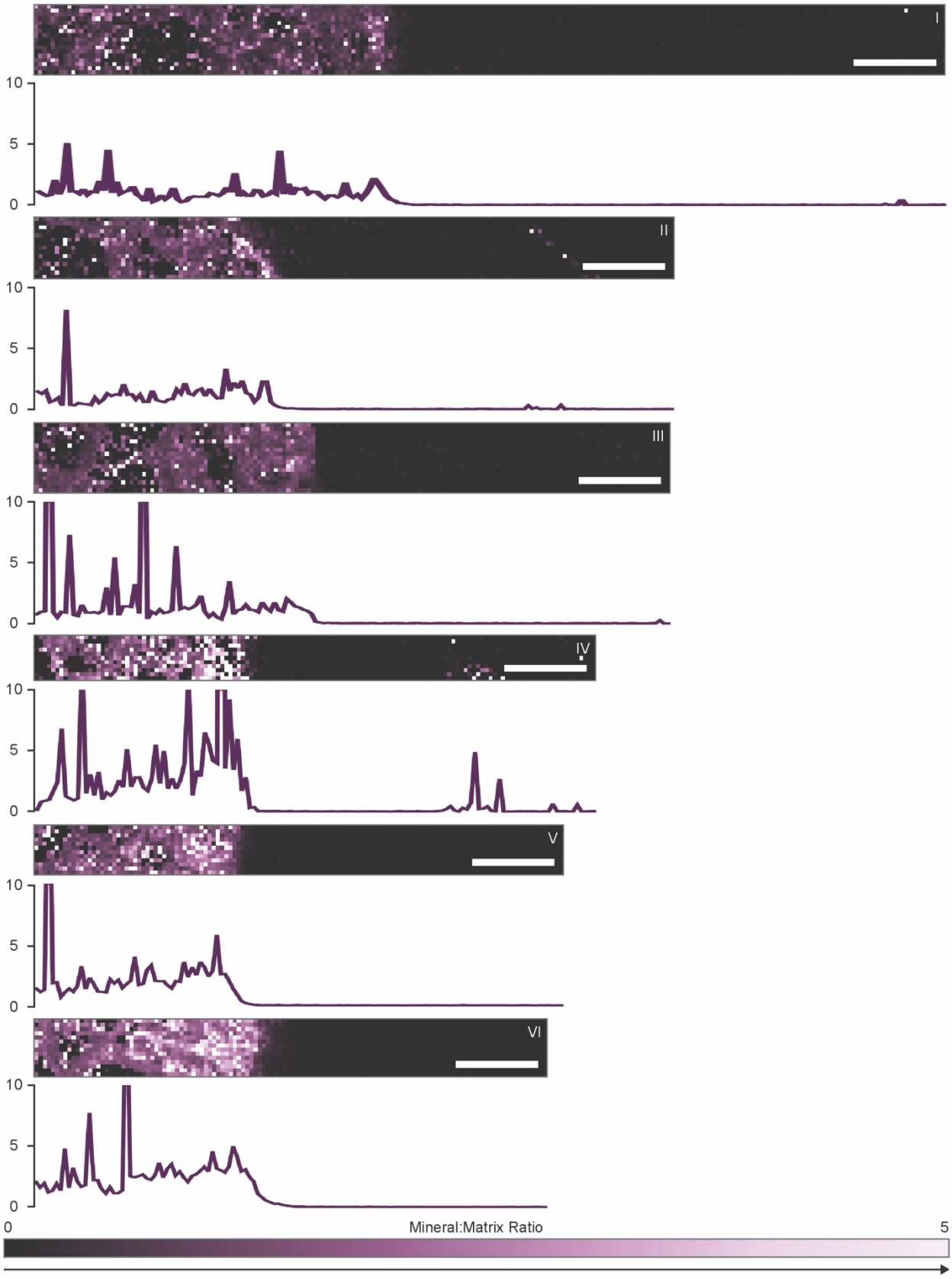
I
II
III
IV
V
VI
10
5
0
0
Mineral:Matrix Ratio
5

Figure 2.S4 Mineral:matrix peak area ratio maps for each sample with accompanying average line scans scaled to image for x axis. Roman numerals (I–VI) indicate a specific sample and are consistent between figures. Sample II is representative sample in Figure 3 for structural analysis. Sample V is representative sample in Figure 2 for compositional analysis. Gradient in mineral:matrix content is visible. Scale bars are 500 μm.

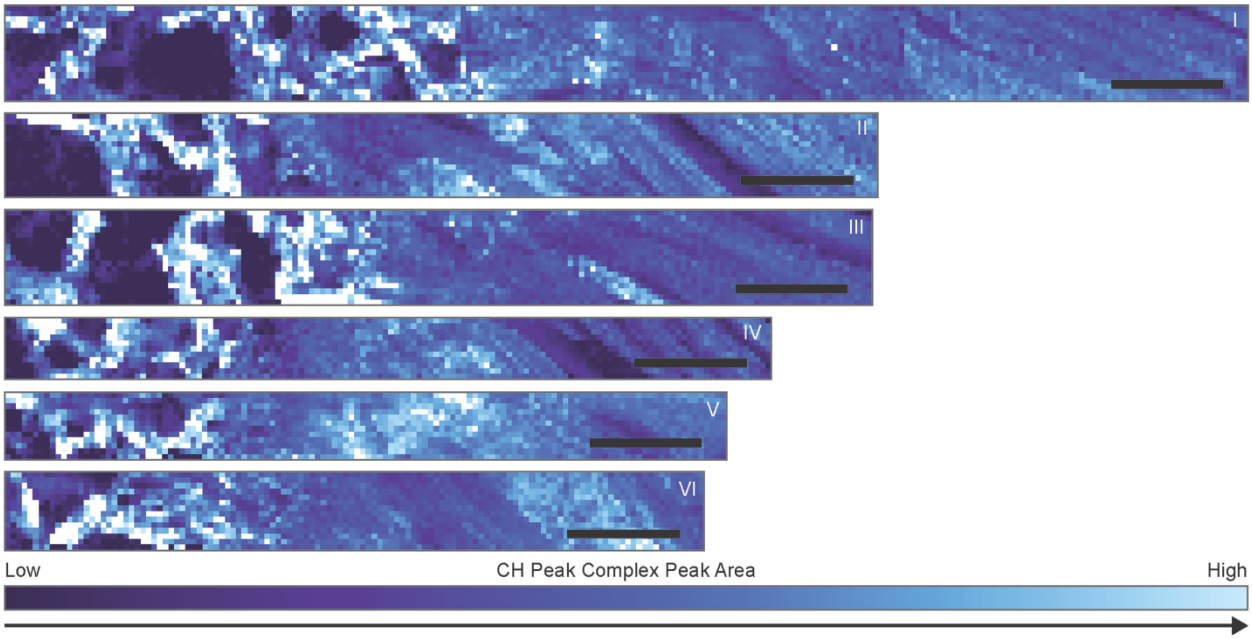

Figure 2.S5 Raw CH peak complex image for each sample. To assess collagen structural changes, we mapped the peak area arising from the collagen-specific portions of the CH peak complex (2908 – 3028 cm^{-1}) to minimize the lipid contribution. The CH peak complex is generally the largest spectral signature for tissue and is sensitive to fine changes in morphology and topology. However, the CH peak complex is also non-specific, in that any components containing CH bonds contribute to the peak shape and area. We know from our data that the enthesis is primarily collagen, but we also detected lipidous content in some areas. Roman numerals (I–VI) indicate a specific sample and are consistent between figures. Sample II is representative sample in Figure 3 for structural analysis. Sample V is representative sample in Figure 2 for compositional analysis. Scale bars are 500 μm.

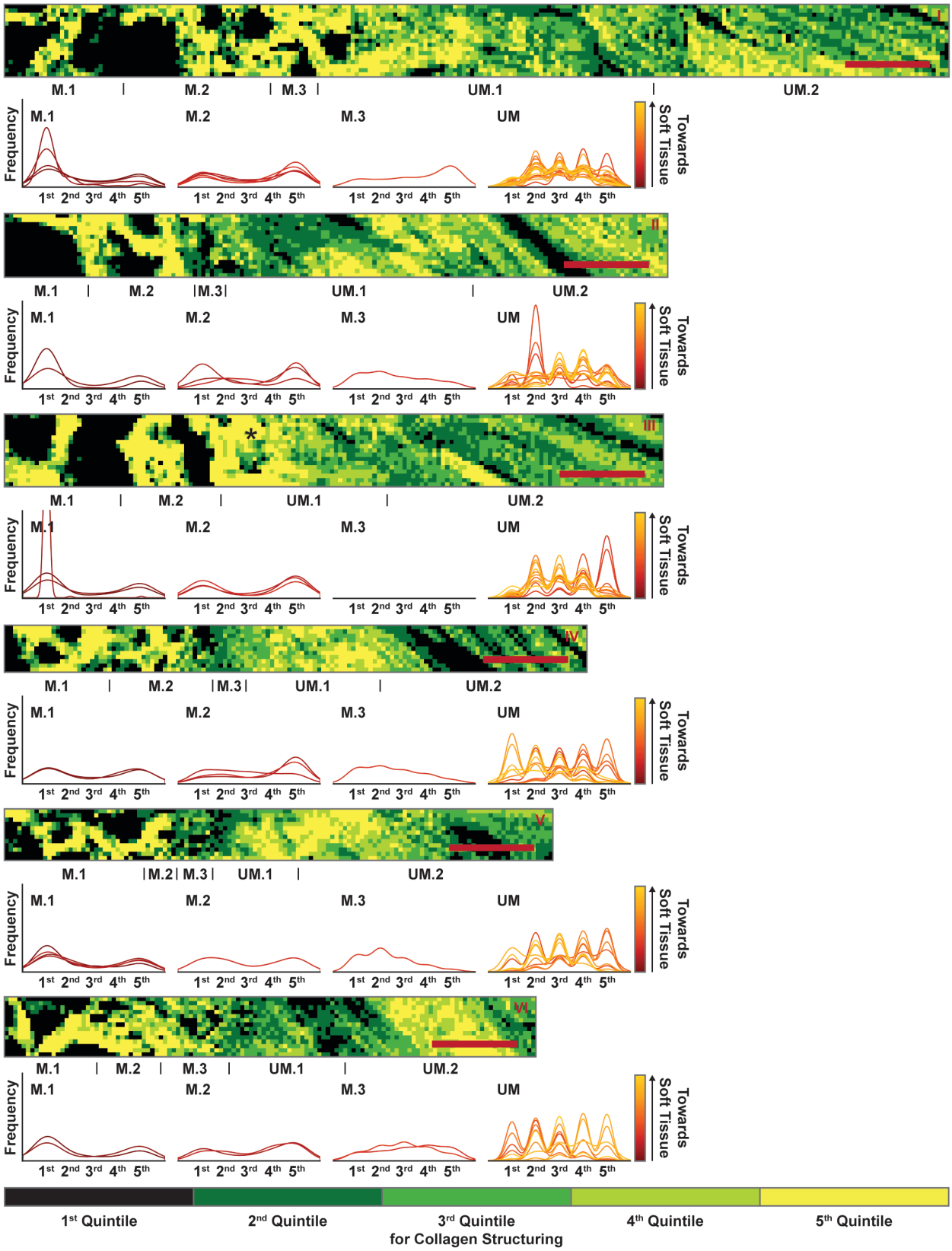
I
M.1
M.2
M.3
UM.1
UM.2
Frequency
M.1
M.2
M.3
UM
1st 2nd 3rd 4th 5th
Towards Soft Tissue
II
III
*
IV
V
VI
1st Quintile
2nd Quintile
3rd Quintile
4th Quintile
5th Quintile
for Collagen Structuring

Figure 2.S6 Quintile images with histogram analysis for each sample. X-axis shows 1st through 5th quintile, labeled as 1st, 2nd, etc. The CH peak area maps from Figure S5, converted into quintile images. See main text for details of this process. Roman numerals indicate the location of each structural region: **M.1** open trabeculae, **M.2** dense trabeculae, **M.3** transitional region, **UM.1** disorganized bundles, **UM.2** oriented fibers. Roman numerals (I–VI) indicate a specific sample and are consistent between figures. Sample II is the representative sample in Figure 3 for structural analysis. Sample V is representative sample in Figure 2 for compositional analysis. The transitional region for sample III was not detectable through the histogram analysis, but a visual inspection of the image would imply that the collagen structuring changes at a resolution below that used for histogram binning. A star indicates this region. The terminology "disorganized bundles" was chosen in that we know that the collagen in this region is oriented based on the Picrosirius Red histological stain under cross-polarizers (Figure 1d), but the orientation is less so than that observed in the oriented fiber region (UM.2) that follows. Scale bars are 500 μm.

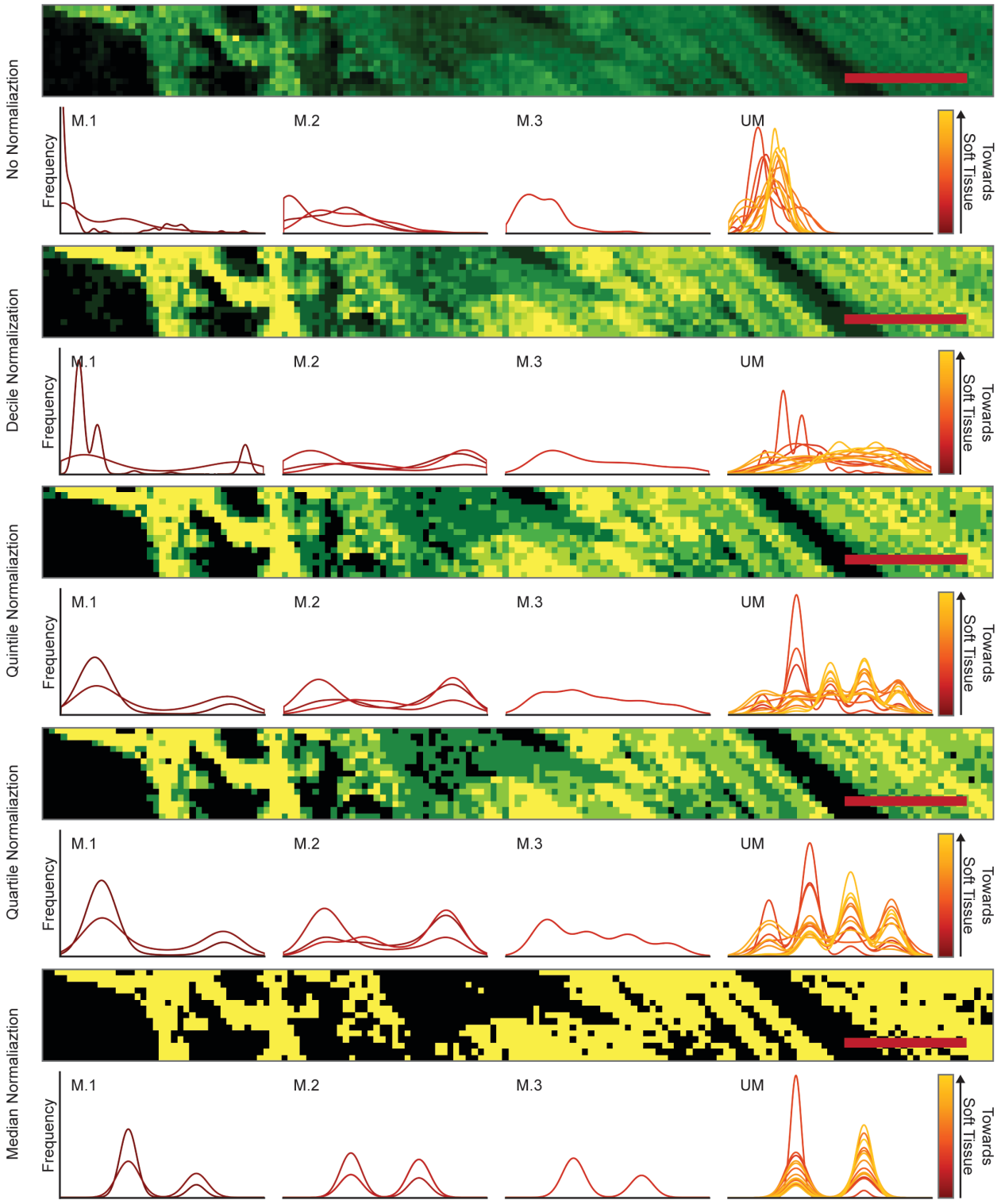

Figure 2.S7 Empirical quantile-based normalization for Raman structuring image. Images of Sample II are replotted for different quantile-based normalization parameters, and resulting quantile histograms are plotted. Top image has no normalization, and the resulting histograms are difficult to interpret. Histogram x-axis is CH peak complex peak area. Decile-based normalization

results in some pixels in the second decile appearing in the pores of the trabeculae, but the histograms begin to show more distinctive regional fingerprints. Histogram x-axis is deciles. Quintile-based normalization results in all porous areas falling within the first quintile with few of the remaining pixels for the soft tissue regions falling into the first quintile. Histograms take on distinctive patterns per region. Histogram x-axis is quintiles. Quartile-based normalized results in scattered first quartile pixels throughout the remainder of the soft tissue, convoluting the histogram-based analysis. Histogram x-axis is quartiles. Median-normalization results in a binary image that is difficult to interpret. Histogram x-axis is medians. Scale bars are 500 μm.

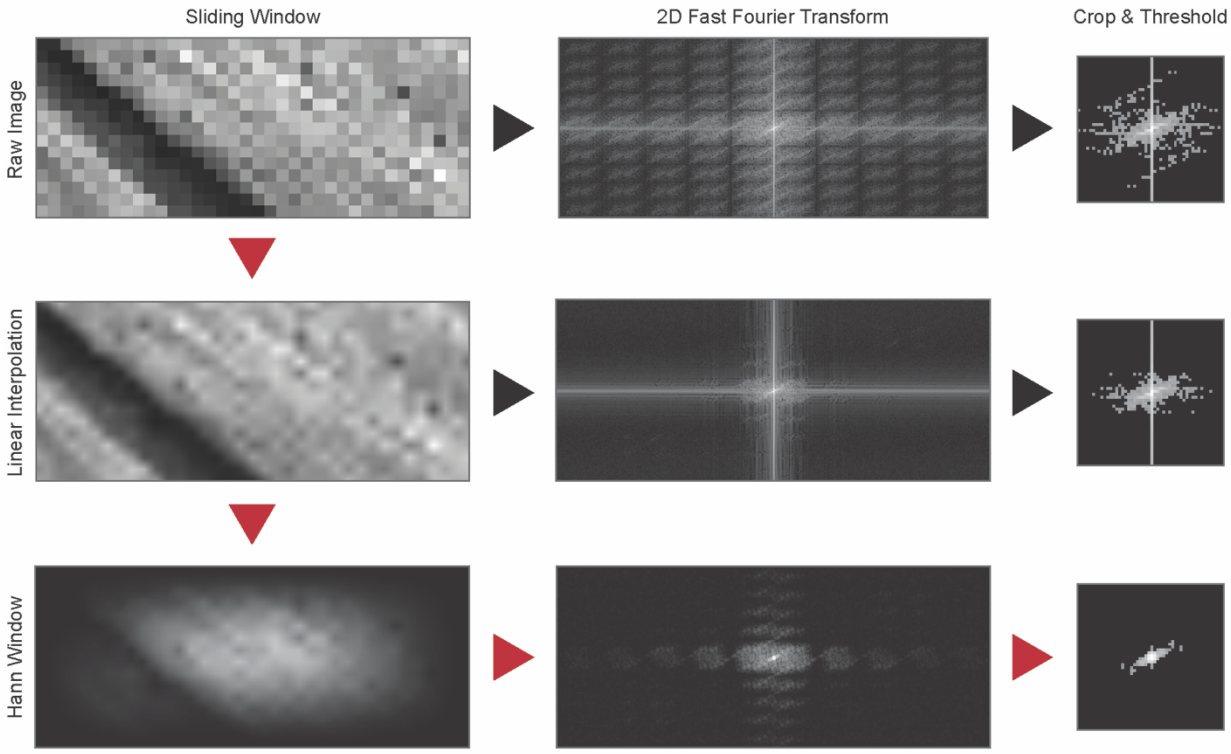

Figure 2.S8 Image filtering for FFT-based orientation analysis. Figure depicts process for production of FFTs from the CH peak area quintile maps. Initial pixelated image is interpolated using a linear function to remove square frequencies. A Hann window function is applied to the image to remove the contribution of edge effects from the resulting FFT, appearing as a cross through the center of the FFT. Resulting FFTs are cropped to show only the low frequency values for the FFTs and thresholded for pixels under an intensity of 0.5 to remove noise. Image filtering path used to produce the FFTs that were used for orientation analysis is shown in red.

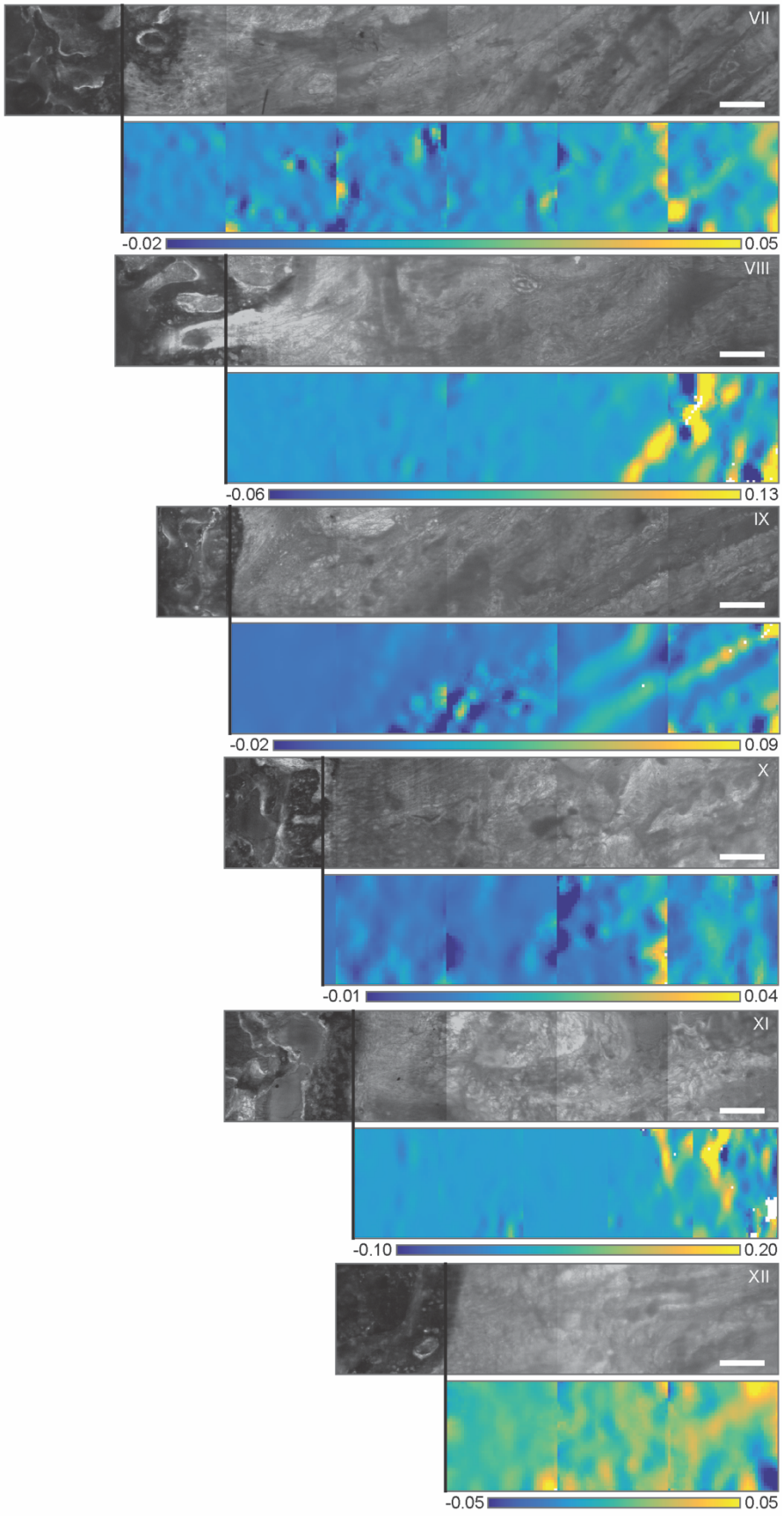
VII
-0.02
0.05
VIII
-0.06
0.13
IX
-0.02
0.09
X
-0.01
0.04
XI
-0.10
0.20
XII
-0.05
0.05

Figure 2.S9 E_{xx} Langrangian finite strain maps for frame 10 for each sample with accompanying confocal fluorescence image. Note that each strain map contains pixels that show strains amplified above the applied strain of 0.03. Roman numerals (VII–XII) indicate individual samples and are consistent between figures. Sample VIII is used as representative sample in Figure 4. Mineralized interface is demarcated at beginning of each strain map and was visually determined based on concurrent features shown in Figure 2b,c.

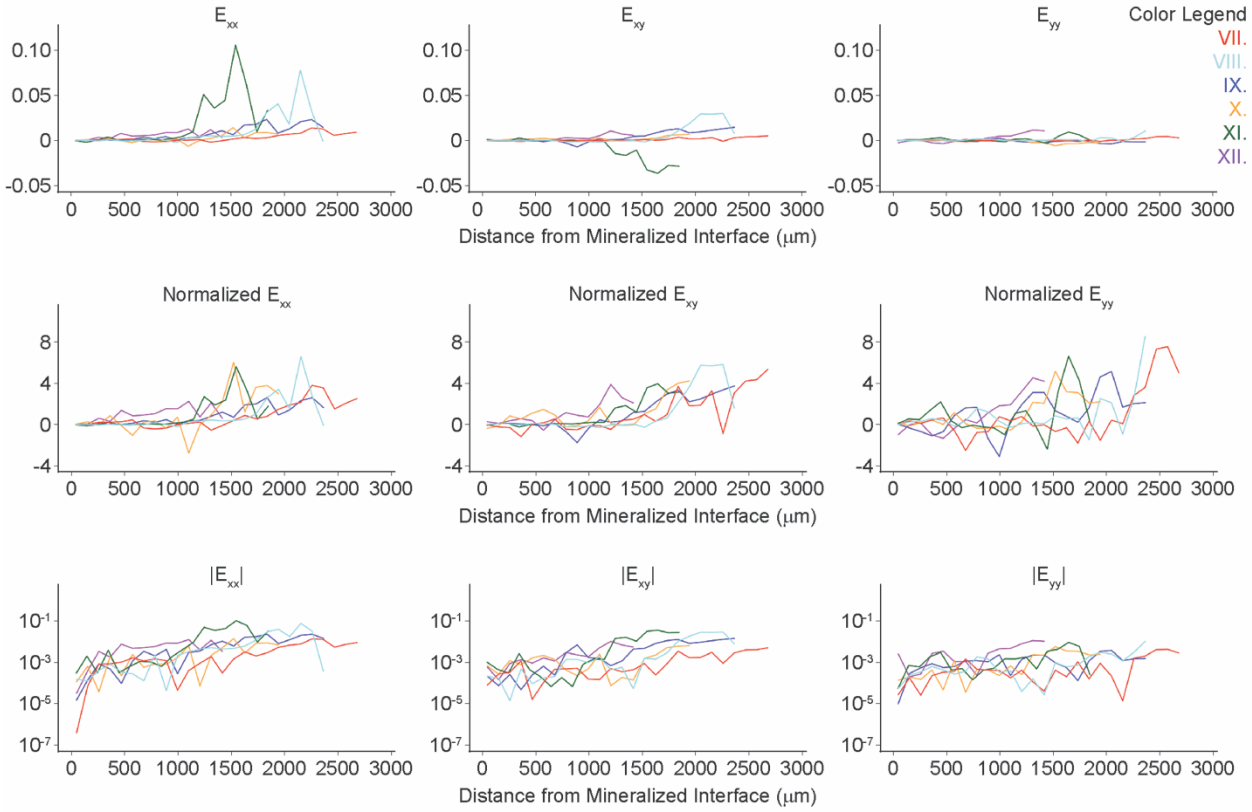

Figure 2.S10 Average strains and normalized strains as a function of distance for each sample. Top row of plots shows average strains as a function of distance, beginning at the mineralized interface for each mechanical sample tested. Middle row of plots shows the average strain as a function of distance normalized to average strain for the entire map for each sample. Bottom row shows magnitude of average strain as a function of distance on a semi-log plot. All data for plots is binned in at 100 μm increments. Color legend in the top right of the figure can be used to identify the individual samples in concordance with Figure S9.

Movie 2.1 – 2.6 Orientation index plot for samples I – VI, respectively, with corresponding FFT stack. Y-axis is orientation index. X-axis is pixel number for first pixel of sliding window beginning at end of transitional region.

Movie 2.7 Load cycle for sample VIII with corresponding E_{xx} tensile strain map. Top image shows loading cycle for sample VIII. Middle image shows E_{xx} Langrangian finite strain map for each frame of loading cycle, referenced to first frame. Plot shows average E_{xx} Langrangian finite strain as a function of distance from the mineralized interface, scaled to the map above. The average

strain for the current frame is highlighted in red with averages strains for other frames shown in gray. Scale bar is 200 μm.

Movie 2.8 – 2.12 Load cycle for samples VII, IX, X, XI, XII, respectively. Scale bars are 200 μm.

References

1. Rossetti, L. *et al.* The microstructure and micromechanics of the tendon–bone insertion. *Nat. Mater.* **16,** 664–670 (2017).
2. Miserez, A., Schneberk, T., Sun, C., Zok, F. W. & Waite, J. H. The Transition from Stiff to Compliant Materials in Squid Beaks. *Science.* **319,** 1816–1819 (2008).
3. Amini, S. *et al.* Textured fluorapatite bonded to calcium sulphate strengthen stomatopod raptorial appendages. *Nat. Commun.* **5,** 3187 (2014).
4. Bergholt, M. S. *et al.* Raman Spectroscopy Reveals New Insights into the Zonal Organization of Native and Tissue-Engineered Articular Cartilage. *ACS Cent. Sci.* **2,** 885–895 (2016).
5. Khetia, E. A. & McKeon, B. P. Meniscal allografts: biomechanics and techniques. *Sports Med. Arthrosc.* **15,** 114–20 (2007).
6. Weiner, S. & Wagner, H. D. THE MATERIAL BONE: Structure-Mechanical Function Relations. *Annu. Rev. Mater. Sci.* **28,** 271–298 (1998).
7. Joshi, M. D., Suh, J. K., Marui, T. & Woo, S. L. Interspecies variation of compressive biomechanical properties of the meniscus. *J. Biomed. Mater. Res.* **29,** 823–8 (1995).
8. Bartlett, N. W. *et al.* A 3D-printed, functionally graded soft robot powered by combustion. *Science.* **349,** 161–165 (2015).
9. Abraham, A. C. & Haut Donahue, T. L. From meniscus to bone: A quantitative evaluation of structure and function of the human meniscal attachments. *Acta Biomater.* **9,** 6322–6329 (2013).
10. Messner, K. & Gao, J. The menisci of the knee joint. Anatomical and functional

characteristics, and a rationale for clinical treatment. *J. Anat.* **193,** 161–178 (1998).

11. Gao, J. Immunolocalization of types I, II, and X collagen in the tibial insertion sites of the medial meniscus. *Knee Surgery, Sport. Traumatol. Arthrosc.* **8,** 61–65 (2000).
12. Spalazzi, J. P., Boskey, A. L., Pleshko, N. & Lu, H. H. Quantitative mapping of matrix content and distribution across the ligament-to-bone insertion. *PLoS One* **8,** e74349 (2013).
13. Schwartz, A. G., Pasteris, J. D., Genin, G. M., Daulton, T. L. & Thomopoulos, S. Mineral Distributions at the Developing Tendon Enthesis. *PLoS One* **7,** 1–11 (2012).
14. Deymier, A. C. *et al.* Micro-mechanical Properties of the Tendon-to-Bone Attachment. *Acta Biomater.* **56,** 25–35 (2017).
15. Spalazzi, J. P., Gallina, J., Fung-Kee-Fung, S. D., Konofagou, E. E. & Lu, H. H. Elastographic imaging of strain distribution in the anterior cruciate ligament and at the ligament–bone insertions. *J. Orthop. Res.* **24,** 2001–2010 (2006).
16. Boys, A. J., McCorry, M. C., Rodeo, S. A., Bonassar, L. J. & Estroff, L. A. Next generation tissue engineering of orthopedic soft tissue-to-bone interfaces. *MRS Commun.* **7,** 289–308 (2017).
17. Bonnevie, E. D. & Mauck, R. L. Physiology and Engineering of the Graded Interfaces of Musculoskeletal Junctions. *Annu. Rev. Biomed. Eng.* **20,** 405–431 (2018).
18. Villegas, D. F., Maes, J. A., Magee, S. D. & Haut Donahue, T. L. Failure properties and strain distribution analysis of meniscal attachments. *J. Biomech.* **40,** 2655–2662 (2007).
19. Hauch, K. N., Villegas, D. F. & Haut Donahue, T. L. Geometry, time-dependent and failure properties of human meniscal attachments. *J. Biomech.* **43,** 463–468 (2010).
20. Wopenka, B., Kent, A., Pasteris, J. D., Yoon, Y. & Thomopoulos, S. The tendon-to-bone transition of the rotator cuff: A preliminary Raman spectroscopic study documenting the

gradual mineralization across the insertion in rat tissue samples. *Appl. Spectrosc.* **62,** 1285–1294 (2008).

21. Deymier-Black, A. C., Pasteris, J. D., Genin, G. M. & Thomopoulos, S. Allometry of the Tendon Enthesis: Mechanisms of Load Transfer Between Tendon and Bone. *J. Biomech. Eng.* **137,** 111005 (2015).
22. Genin, G. M. *et al.* Functional grading of mineral and collagen in the attachment of tendon to bone. *Biophys. J.* **97,** 976–85 (2009).
23. Sherman, V. R., Yang, W. & Meyers, M. A. The materials science of collagen. *J. Mech. Behav. Biomed. Mater.* **52,** 22–50 (2015).
24. Genin, G. M. & Thomopoulos, S. The tendon-to-bone attachment: Unification through disarray. *Nat. Mater.* **16,** 607–608 (2017).
25. Bi, X. *et al.* Raman and mechanical properties correlate at whole bone- and tissue-levels in a genetic mouse model. *J. Biomech.* **44,** 297–303 (2011).
26. Albro, M. B. *et al.* Raman spectroscopic imaging for quantification of depth-dependent and local heterogeneities in native and engineered cartilage. *Regen. Med.* **3,** 1–11 (2018).
27. *Infrared and Raman Spectroscopic Imaging*. (Wiley-VCH, 2014).
28. Zavaleta, C. L. *et al.* Multiplexed imaging of surface enhanced Raman scattering nanotags in living mice using noninvasive Raman spectroscopy. *Proc. Natl. Acad. Sci. U. S. A.* **106,** 13511–13516 (2009).
29. Akiva, A. *et al.* Mineral Formation in the Larval Zebrafish Tail Bone Occurs via an Acidic Disordered Calcium Phosphate Phase. *J. Am. Chem. Soc.* **138,** 14481–14487 (2016).
30. Gamsjaeger, S., Klaushofer, K. & Paschalis, E. P. Raman analysis of proteoglycans simultaneously in bone and cartilage. *J. Raman Spectrosc.* **45,** 794–800 (2014).
31. Mansfield, J. C., Moger, J., Green, E., Moger, C. & Winlove, C. P. Chemically specific

imaging and in-situ chemical analysis of articular cartilage with stimulated Raman scattering. *J. Biophotonics* **6,** 803–14 (2013).

32. Kammer, M. *et al.* Spatially resolved determination of the structure and composition of diatom cell walls by Raman and FTIR imaging. *Anal. Bioanal. Chem.* **398,** 509–517 (2010).

33. Adie, S. G. *et al.* Spectroscopic optical coherence elastography. *Opt. Express* **18,** 25519–34 (2010).

34. Rey-De-Pedraza, V., Cendon, D. A., Sánchez-Gálvez, V. & Gálvez, F. Measurement of fracture properties of concrete at high strain rates. *Philos. Trans. R. Soc. A* **375,** 1–13 (2016).

35. Buckley, M. R., Gleghorn, J. P., Bonassar, L. J. & Cohen, I. Mapping the depth dependence of shear properties in articular cartilage. *J. Biomech.* **41,** 2430–7 (2008).

36. Silverberg, J. L., Dillavou, S., Bonassar, L. J. & Cohen, I. Anatomic variation of depth-dependent mechanical properties in neonatal bovine articular cartilage. *J. Orthop. Res.* **31,** 686–691 (2013).

37. Bartell, L. R., Fortier, L. A., Bonassar, L. J. & Cohen, I. Measuring microscale strain fields in articular cartilage during rapid impact reveals thresholds for chondrocyte death and a protective role for the superficial layer. *J. Biomech.* **48,** 3440–3446 (2015).

38. Sevenler, D. *et al.* Spatial periodicity in growth plate shear mechanical properties is disrupted by vitamin D deficiency. *J. Biomech.* **46,** 1597–1603 (2013).

39. Junqueira, L. C., Bignolas, G. & Brentani, R. R. Picrosirius staining plus polarization microscopy, a specific method for collagen detection in tissue sections. *Histochem. J.* **11,** 447–455 (1979).

40. Dayan, D., Hiss, Y., Hirshberg, A., Bubis, J. J. & Wolman, M. Are the polarization colors

of picrosirius red-stained collagen determined only by the diameter of the fibers? *Histochemistry* **93,** 27–29 (1989).

41. Talari, A. C. S., Zanyar, M., Rehman, S. & Rehman, I. U. Raman spectroscopy of biological tissues. *Appl. Spectrosc. Rev.* **50,** 46–111 (2015).

42. Kazanci, M., Roschger, P., Paschalis, E. P., Klaushofer, K. & Fratzl, P. Bone osteonal tissues by Raman spectral mapping: Orientation-composition. *J. Struct. Biol.* **156,** 489–496 (2006).

43. Taylor, E. A., Lloyd, A. A., Salazar-Lara, C. & Donnelly, E. L. Raman and FT-IR mineral to matrix ratios correlate with physical chemical properties of model compounds and native bone tissue. *Appl. Spectrosc.* **71,** 2404–2410 (2017).

44. Mandair, G. S. & Morris, M. D. Contributions of Raman spectroscopy to the understanding of bone strength. *Bonekey Rep.* **4,** 1–8 (2015).

45. Silverberg, J. L., Barrett, A. R., Das, M., Petersen, P. B. & Bonassar, L. J. Structure-Function Relations and Rigidity Percolation in the Shear Properties of Articular Cartilage. *Biophys. J.* **107,** 1721–1730 (2014).

46. Blaber, J., Adair, B. & Antoniou, A. Ncorr: Open-Source 2D Digital Image Correlation Matlab Software. *Exp. Mech.* **55,** 1105–1122 (2015).

47. Vedi, V. *et al.* Meniscal movement an in-vivo study using dynamic mri. *J. Bone Jt. Surg.* **81B,** 37–41 (1999).

48. Hauch, K. N., Oyen, M. L., Odegard, G. M. & Haut Donahue, T. L. Nanoindentation of the insertional zones of human meniscal attachments into underlying bone. *J. Mech. Behav. Biomed. Mater.* **2,** 339–347 (2009).

49. Ferguson, V. L., Bushby, A. J. & Boyde, A. Nanonmechanical properties and mineral concentration in articular calcified cartilage and subchondral bone. *J. Anat.* **203,** 191–202

(2003).

50. Mente, P. L. & Lewis, J. L. Elastic modulus of calcified cartilage is an order of magnitude less than that of subchondral bone. *J. Orthop. Res.* **12,** 637–647 (1994).

51. Li, Y., Asadi, A., Monroe, M. R. & Douglas, E. P. pH effects on collagen fibrillogenesis in vitro: Electrostatic interactions and phosphate binding. *Mater. Sci. Eng. C* **29,** 1643–1649 (2009).

52. Dong, M., Xu, S., Bünger, M. H., Birkedal, H. & Besenbacher, F. Temporal Assembly of Collagen Type II Studied by Atomic Force Microscopy. *Adv. Eng. Mater.* **9,** 1129–1133 (2007).

53. Deymier, A. C. *et al.* The multiscale structural and mechanical effects of mouse supraspinatus muscle unloading on the mature enthesis. *Acta Biomater.* (2018). doi:10.1016/j.actbio.2018.10.024

54. Hu, Y. *et al.* Stochastic interdigitation as a toughening mechanism at the interface between tendon and bone. *Biophys. J.* **108,** 431–437 (2015).

55. Schwartz, A. G., Long, F. & Thomopoulos, S. Enthesis fibrocartilage cells originate from a population of Hedgehog-responsive cells modulated by the loading environment. *Development* **142,** 196–206 (2015).

56. Font Tellado, S. *et al.* Fabrication and characterization of biphasic silk fibroin scaffolds for tendon/ligament-to-bone tissue engineering. *Tissue Eng. Part A* **23,** 859–872 (2017).

57. Puetzer, J. L., Koo, E. & Bonassar, L. J. Induction of fiber alignment and mechanical anisotropy in tissue engineered menisci with mechanical anchoring. *J. Biomech.* **48,** 1436–1443 (2015).

58. McCorry, M. C. & Bonassar, L. J. Fiber development and matrix production in tissue-engineered menisci using bovine mesenchymal stem cells and fibrochondrocytes.

Connect. Tissue Res. **58,** 329–341 (2017).

59. Ma, J. *et al.* Three-Dimensional Engineered Bone–Ligament–Bone Constructs for Anterior Cruciate Ligament Replacement. *Tissue Eng. Part A* **18,** 103–116 (2012).

60. McCorry, M. C. *et al.* A model system for developing a tissue engineered meniscal enthesis. *Acta Biomater.* **56,** 110–117 (2016).

61. Priemel, T., Degtyar, E., Dean, M. N. & Harrington, M. J. Rapid self-assembly of complex biomolecular architectures during mussel byssus biofabrication. *Nat. Commun.* **8,** 14539 (2017).

62. Lee, B. P., Messersmith, P. B., Israelachvili, J. N. & Waite, J. H. Mussel inspired adhesives and coatings. *Annu. Rev. Mater. Res.* **41,** 99–132 (2011).

63. Liu, L. *et al.* The effects of morphological irregularity on the mechanical behavior of interdigitated biological sutures under tension. *J. Biomech.* **58,** 71–78 (2017).

64. Hwang, B.-Y. *et al.* Risk Factors for Medial Meniscus Posterior Root Tear. *Am. J. Sports Med.* **40,** 1606–1610 (2012).

65. Schindelin, J. *et al.* Fiji : an open-source platform for biological-image analysis. *Nat. Methods* **9,** 676–682 (2012).

66. Hovden, R., Jiang, Y., Xin, H. L. & Kourkoutis, L. F. Periodic Artifact Reduction in Fourier Transforms of Full Field Atomic Resolution Images. *Microsc. Microanal.* **21,** 436–441 (2015).

CHAPTER 3

High Resolution Imaging of Biochemical Concentration in Living Articular Cartilage Using Raman Microscopy[4]

Abstract

Articular cartilage consists of collagen, proteoglycans, and water. Local changes in the concentrations of these components has various implications in both healthy cartilage function and in various disease states, such as osteoarthritis. Raman spectroscopy has the potential to provide a non-destructive means for determining relative local composition. However, these feasibility of such an analysis has yet to be confirmed. Here, we generate a statistical model for calculation of relative local concentrations of the major components in articular cartilage. We confirm the non-destructive capacity of Raman spectroscopy, showing viable living cells after the analysis. Our results match field standards for gauging local concentration and are applied for the analysis of other cartilage features. Overall, we are able to generate high resolution images of the relative local concentrations of the molecular components that make up articular cartilage.

Introduction

Orthopedic injuries are common, often resulting in osteoarthritis.[1] This disease is one of the most prevalent chronic conditions in adults, affecting large portions of the population.[2] Osteoarthritis has debilitating effects on joint health, eroding away articular cartilage, the soft tissue that lines the ends of bones in joints.[3] Throughout the progression of the disease, the relative concentrations of the components found in articular cartilage fluctuate.[3,4] These factors make non-destructive, high resolution analysis of cartilage composition an important area of study in terms of both basic research and clinical diagnosis. Here, we develop a statistical model using Raman spectroscopy

[4] This chapter is in preparation for submission: Boys, A. J., Zhao C. Z., Chan, K. M., Bonassar, L. J., Estroff, L. A.

that non-destructively determines relative local concentrations of the major components of articular cartilage.

Articular cartilage is composed of approximately 70% water, 15% collagen, and 10% proteoglycan.[5,6] Collagen is a triple helical protein, consisting of the repeat amino acid sequence Gly-X-Y, where X and Y are frequently proline and hydroxyproline residues.[7] The proteoglycan content of cartilage is primarily contained within the molecule aggrecan. Aggrecan has a bottle-brush structure, with a series of proteoglycan molecules complexed to the glycosaminoglycan (GAG), hyaluronan. Each proteoglycan consists of a series of sulfated glycosaminoglycan (sGAG) species, including chondroitin sulfate and others, bound to a protein core, which constitute the majority of the mass of the proteoglycans.[8] Cartilage is typically organized zonally as a function of depth, beginning at the surface and extending down to bone. These zones are associated with both cellular phenotypes and collagen organization/concentration. The surface zone is called the superficial zone, where collagen is aligned parallel to the surface. This region typically shows a local maximum in collagen concentration. The superficial zone is followed by the mid zone, where collagen concentration undergoes an increase as a function of depth from a minimum just past the superficial zone to a plateau in concentration, which constitutes the deep zone. Throughout these zones, GAG content linearly increases over the depth of the tissue.[4,9]

Various techniques have been applied for the purpose of determining localized compositional changes in articular cartilage. Currently, magnetic resonance imaging (MRI) is the most commonly used clinical analysis for determining the state of cartilage *in vivo*. This technique measures the relaxation time of, typically, hydrogen atoms, associating this information with local water content. Magnetic resonance imaging can be performed non-invasively and is therefore very useful in diagnosis. However, MRI has a limited resolution and cannot directly measure cartilage concentration, instead relying water relaxation data as a surrogate for local concentration.[6,10–15]

Infrared (IR) spectroscopy has also been used to gauge local composition in cartilaginous tissues. Infrared spectroscopy relies on absorbance of IR light by molecular bonds, based on the polarity of these bonds. As such, resolving IR spectra in the presence of water is difficult, making it less useful in a clinical environment. Near IR spectroscopy has been used as an alternative, as it is somewhat compatible with water, but it does not have well refined signatures for different molecular components, making identification of local composition difficult.[5,16–18]

Recently, Raman spectroscopy has been gaining ground as a useful tool for analysis of orthopedic tissues.[19–26] Raman spectroscopy utilizes a laser to recover detailed information about the local molecular composition of tissue at high resolution by analyzing energy shifts caused by inelastic molecular vibrations. Unlike IR spectroscopy, Raman spectroscopy can be used to retrieve detailed information about the hydration state of a tissue[27,28] without obscuring the protein-related vibrational modes.[29,30] Raman spectroscopy is also non-destructive and can be used on living tissue.[31] Despite these advantages, the measurement of glycosaminoglycans can be difficult, meaning that further advances are necessary to apply this technique in the clinic. Additionally, the feasibility of Raman spectroscopy to produce relative values of local constituents needs to be confirmed. Further, to the best of our knowledge, researchers have yet to perform viability testing on samples that have been analyzed using Raman spectroscopy. To address these challenges, we have designed a statistical model for determining relative concentrations at high resolution and implemented it on living cartilage samples.

This study focuses on applying Raman spectroscopy for the measurement of local compositional changes in living articular cartilage. A statistical model for measuring the relative concentrations of cartilage components was developed and compared to biochemical analyses of hydroxyproline content, as a surrogate for collagen, and GAG content. This method was applied to large regions (millimeters) of tissue to confirm its ability to gauge local concentrations and then

tested on a variety of anatomical locations to analyze for local changes in the composition of cartilage.

Experimental

Tissue Explantation

Articular cartilage samples were explanted from fresh 1 – 3 day old bovids (Gold Medal Packing Inc., Rome, NY). Samples were dissected from four different anatomical locations on the tibial plateau: the outer region of the medial tibial plateau, the inner region of the medial tibial plateau, the outer region of the lateral tibial plateau, and the inner region of the lateral tibial plateau. These samples were cut with a razor blade for analysis in the direction orthogonal to the articular surface (articular surface to osteochondral interface) (Figure 3.S1). After explantation, samples were immediately stored in Dulbecco's phosphate buffered saline (PBS) with protease inhibitors (Thermo Scientific, Waltham, MA) at 4˚C and analyzed within 6 hours of collection.

Collection of Raman Spectral Data from Articular Cartilage Samples

For analysis, samples were glued to a petri and submerged in PBS. Raman analysis was performed with a Renishaw inVia Raman microscope. Prior to spectral data collection, topographical maps of the tissue were constructed using the Renishaw Wire software by rastering the objective in 100 μm steps and collecting a focal point at each step. The software generates an interpolated surface of the sample for analysis. Spectral data were collected using a 532 nm laser at 100 mW through a 40x immersion objective by following the surfaces using a 10 μm step size. Use of the immersion objective simultaneously ensures that the samples remain hydrated and alive throughout the data collection process and prevents issues caused by evaporation during data collection. Data collection format either consisted of a line or map of data points beginning 40 μm off the surface of the articular cartilage and extending into the bony tissue past the osteochondral interface (Figure 3.S1). Line scans were collected for n = 28 samples, and maps were collected for n = 5 samples.

Preparation and Collection of Reference Spectra

Four reference samples were chosen for analysis: rat tail collagen (BioIVT, Westbury, NY), chondroitin sulfate (Shark Cartilage, Sigma Life Sciences, St. Louis, MO), hyaluronan, and deionized water. For collagen reference spectra, collagen was extracted from rat tails as previously described.[32] Briefly, frozen tails were dissected; tendons were removed and placed in 70% ethanol. These tendons were patted dry and placed in 0.1% acetic acid for 48 hrs. The resulting solution was centrifuged at 4500 RPMs, and the supernatant was pipetted into a separate vial. The supernatant was frozen and lyophilized. The resulting lyophilized extract was used as a reference standard. For chondroitin sulfate and hyaluronan references, stock powders were purchased and used. For water reference, deionized water was used. Twenty spectra were collected from each reference using a 532 nm laser at 100 mW through a 50x objective.

Processing of Reference Spectra

The twenty spectra collected from each reference sample were averaged. These spectra were baselined, and the standard scores of the average spectra were calculated. The minimum value for the standard score + 0.01 was added to each value of the spectrum to shift the entire standardized spectrum above zero. The resulting spectra were used to generate the statistical model described below.

Development of Linear Regression Model

A model, consisting of the linear combination of the one, two, three, or four reference spectra (collagen, chondroitin sulfate, hyaluronan, and water) in addition to two baselining terms (slope and vertical shift), was constructed (Table 3.1). A custom MATLAB code was written to minimize the error between the linear model and a sample spectrum for reconstruction of the sample spectrum. To test the validity of the model, a data test was constructed. The data test set consisted

of 11 line scans from 3 different animals collected from articular cartilage samples as described above. A custom MATLAB code was written to choose 100 random spectra from these line scans to generate a representative test set for the analysis. The code applied every permutation of the linear model to the test set and calculated a histogram of the resulting errors for fitting the test set (Figure 3.S2). Using this format, the best linear model was established. The resulting model was applied to all articular cartilage samples that had been analyzed for further analysis. All Raman spectral analyses were performed over the width of 800 to 1800 cm^{-1}.

Viability Testing of Articular Cartilage Samples

To confirm the non-destructive capacity of Raman spectroscopy, samples were collected as above. Synovial fluid was used to lubricate the razor blade during cutting to minimize cell death at the sample surface to be used for analysis. Samples were subjected to Raman line scans as above and then placed in dye solution at 1 mL PBS : 1 µL calcein AM : 1 µL ethidium homodimer (Life Technologies Corporation, ThermoFisher, Waltham, MA) for 30 minutes. Samples were stored in PBS for at least 5 minutes before imaging. Imaging was performed using a Zeiss LSM 710 AxioObserver using a C-Apochromat 10x / 0.45 W objective. Images consisted of 3 channels: the first channel for ethidium homodimer had an excitation wavelength of 561 nm and a detection range of 582 - 741 nm, the second channel for calcein AM had an excitation wavelength of 488 nm and a detection range of 510 - 741 nm, and third channel for reflectance had an excitation wavelength of 488 nm and a detection range of 480 - 497 nm. This analysis was performed for n = 4 samples.

Paired Raman and Biochemical Analyses

A paired biochemical analysis was performed to calibrate Raman data to absolute concentrations. This paired analysis was performed for samples from four animals. The outer regions of the medial and lateral tibial plateau were used for each of the four animals, generating n = 8 total samples.

Immediately following Raman analysis, samples were frozen. Samples were mounted into a sledge microtome and sectioned into 200 μm thick slabs, beginning at the articular surface and extending to the osteochondral interface (Figure 3.S1). These samples were subjected to biochemical analyses for hydroxyproline and sGAG as previously described.[33,34] Briefly, these sections were digested using a papain digest ~16 hours at 60˚C. Assays were performed for sGAG[35] and hydroxyproline[36] content. These data were plotted against the coefficient data from Raman line scans determined through the linear model. Raman data points, collected at 10 μm intervals, were binned at 200 μm for comparison to the biochemical data. These data were plotted against each other for the first 1000 μm of the tissue to determine the exact concentration corresponding to each Raman coefficient value. These data were linearly fitted, and a relationship was determined. Subsequently, this relationship was applied to the previously collected Raman data to determine the local concentration of the major components in articular cartilage.

Histology

Samples were fixed in formalin, decalcified, and embedded in paraffin. Sections were collected at 4 μm thickness. For Picrosirius Red staining, samples were stained with Weigart's hematoxylin for 10 minutes and Picrosirius Red for 1 hour. For Safranin-O staining, samples were stained with Weigart's hematoxylin for 10 minutes, Fast Green for 8 minutes, and Safranin-O for approximately 10 minutes. Slides were imaged on a microscope (Nikon Eclipse TE2000-S) through an attached camera (Diagnostic Instruments, Inc. RTKE Spot) in white light and under cross-polarized light.

Results & Discussion

The goal of this study was to generate a non-destructive means for measuring relative concentrations of local biochemical components, specifically collagen and GAGs, in articular cartilage. Raman spectroscopy was chosen as the modality for collecting this information, as it is sensitive to small changes in molecular composition and can be performed on hydrated tissues. To

produce a consistent and repeatable analysis of cartilage, a linear regression model for reconstructing sample spectra was chosen, given that the measurement of a peak specifically associated with GAG content is difficult.[20] Further, the use of such models has the potential for direct comparison to biochemical assays, which are the current field standards for measuring collagen and GAG content.

Development of a Linear Model Representing the Raman Signature of Cartilage

A statistical model was generated for the non-destructive measurement of the local concentration of collagen and GAG in articular cartilage. This model was designed to consist of a series of spectra added in a linear fashion with two baselining terms to reconstruct the sample spectrum. The relative contributions of the spectra and baselining terms are dictated by a series of coefficients, each associated with a specific term. To choose appropriate terms for the model, we analyzed four components as possible candidates: collagen, chondroitin sulfate, hyaluronan, and water (Figure 3.1). To test for the best linear combination of these four components, all possible permutations were generated, resulting in 15 models (Table 3.1).

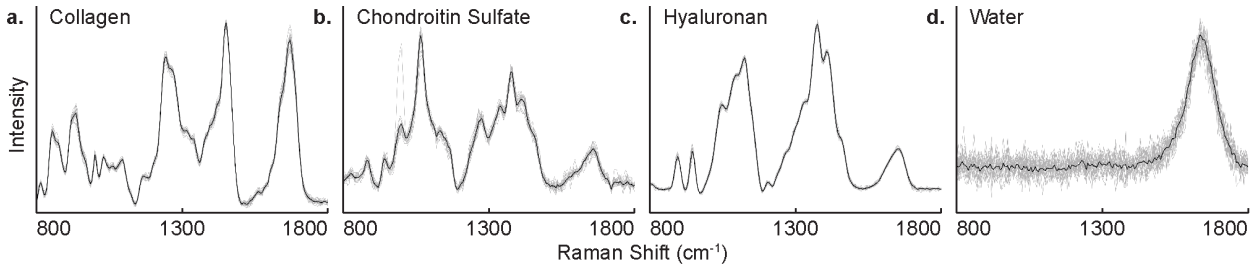

Figure 3.1 Reference spectra for **a** collagen, **b** chondroitin sulfate, **c** hyaluronan, and **d** water. Black lines show average reference spectrum. Gray lines show each individual reference spectrum used to create the average spectrum.

In order to determine the best possible model for the application, a test set consisting of 100 random spectra collected from articular cartilage samples was constructed. Each model was applied to this test set, producing a histogram of the resultant errors in fit (Figure 3.S2). Collagen was found to be a necessary component in the model, as all models containing collagen had lower average errors than those without. Water was also found to be necessary for reconstruction of the

One Component	Two Components	Three Components	Four Components
Collagen	Collagen + HA	Collagen + HA + Water	Collagen + HA + CS + Water
HA	Collagen + CS	Collagen + HA + CS	
CS	Collagen + Water	Collagen + CS + Water	
Water	HA + CS	HA + CS + Water	
	HA + Water		
	CS + Water		

Components:
Collagen
Hyaluronan (HA)
Chondroitin Sulfate (CS)
Water

Table 3.1 Table showing every permutation of the four-component linear regression model.

sample spectra, as the water peak at ~1640 cm^{-1} is present in all spectra, due to the use of hydrated tissue. To represent the GAG content of cartilage, models containing chondroitin sulfate and hyaluronan were analyzed individually (Figure 3.2). For this analysis, models containing only hyaluronan and only chondroitin sulfate were compared, followed by the comparison of hyaluronan and collagen against chondroitin sulfate and collagen, etc. Hyaluronan (Figure 3.2a,b,c)

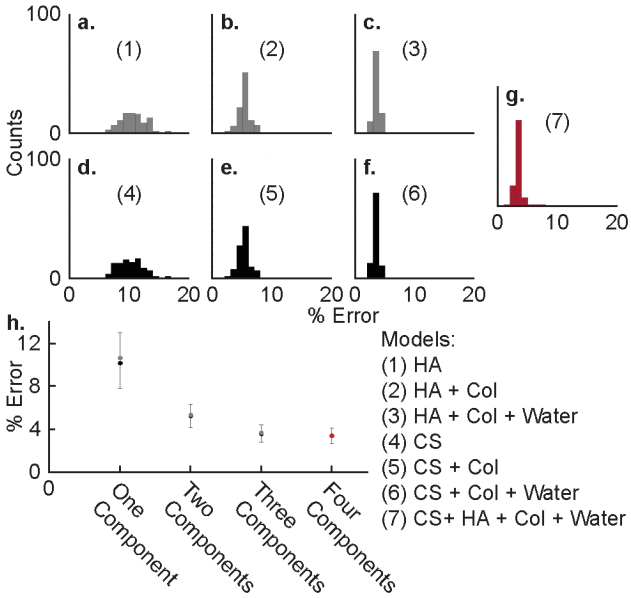

Figure 3.2 Histograms showing the distribution of percent error for different linear models, consisting of collagen (Col), Chondroitin sulfate (CS), hyaluronan (HA), and water. Each model contains between one and four references in addition to two baselining components. Histograms for **a** HA, **b** HA + Col, **c** HA + Col + Water. Histograms for **d** CS, e. CS + Col, **f** CS + Col + Water. **g** Histogram for CS + HA + Col + Water. **h** Plot showing the average error with standard deviation for models containing HA (gray) or CS (black). Model containing all four components (red).

was found to reduce the error by slightly less than chondroitin sulfate (Figure 3.2d,e,f) across models with one, two, and three components. The lowest average error occurred for the model containing all four components (Figure 3.2g). However, as more components are added to the system, the error reduction begins to plateau at three components (Figure 3.2h). Thusly, to avoid overfitting the data, a three-component model was used. As the chondroitin sulfate has a lower average error than hyaluronan across all models and chondroitin sulfate also offers the advantage of a more direct comparison to common biochemical assays, a model containing chondroitin

sulfate, collagen, and water is most advantageous. This model resulted in an average fitting error of 3.56 ± 0.74 % across Raman spectra in the test set, which is only slightly higher than the error for the model containing all four components, 3.39 ± 0.72 %. Thusly, a final model of collagen, chondroitin sulfate, and water was chosen for the remaining analyses (Figure 3.3).

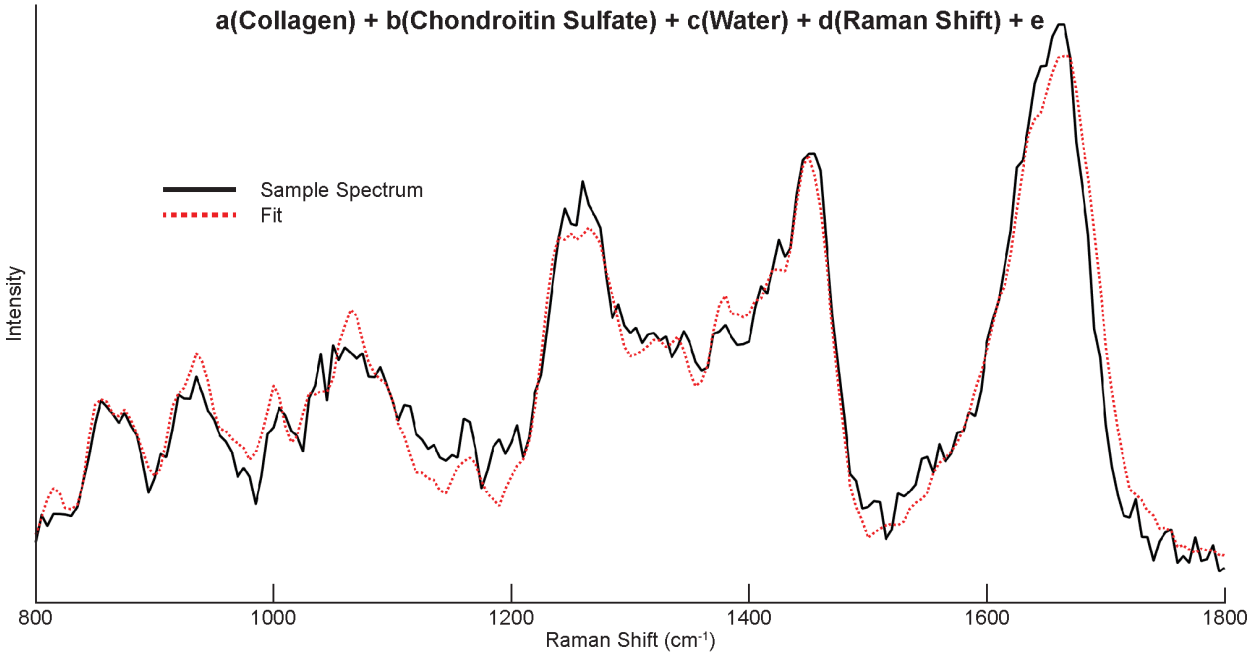

Figure 3.3 Sample spectrum and fit. Fit is generated using linear model as shown above plot.

Paired Raman and Biochemically-derived Concentrations

The results of the model were compared to other analytical techniques by performing paired, spatially resolved Raman spectroscopy and biochemical analyses. This experiment is based on the relationship between hydroxyproline content and collagen and between sGAG content and chondroitin sulfate, both of which should be linear. Samples were collected from the outer regions of the tibial plateau for n = 4 animals, totaling at n = 8 samples. Raman data was collected as a line scan, moving from the articular surface to the osteochondral interface. The linear model was applied to these data resulting in coefficient values for collagen and chondroitin sulfate as a function of depth from the articular surface. After Raman analysis, samples were sectioned into 200 µm thick slabs running from the articular surface to bone. These slabs were individually

subjected to biochemical analyses for hydroxyproline and sGAG content, generating concentrations for each of these components as a function of depth from the surface. These data were correlated to the collagen and chondroitin sulfate coefficients values generated through the model (Figure 3.4).

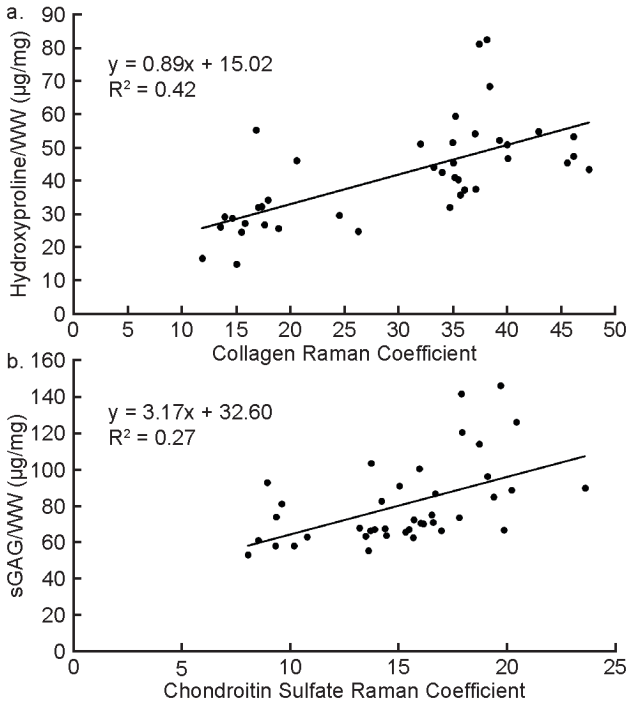

Figure 3.4 a Relationship between hydroxyproline and the collagen coefficient from the linear model. **b** Relationship between sGAG content and chondroitin sulfate coefficient from linear model.

The relationship between the Raman-derived and biochemically-derived datasets was found to be linear for n = 40, with R^2 values of 0.42 and 0.27 for collagen and GAG, respectively. The hydroxyproline curve shows two groupings of data points (Figure 3.4a). These groupings are likely due to small offsets in the location of the mid-zone of cartilage, resulting from the surface curvature of the tibial plateau. This offset means the inflection point in cartilage concentration as a function of depth occurs in a slightly different location for the specific Raman line scan versus the average location of the inflection point for the entire sample as gauged by the biochemical analysis. The sGAG calibration curves is linear with some points showing higher sGAG content than would be predicted by the Raman data. These points, as well those in the collagen analysis, are likely caused by averaging effects, given the small area scanned by Raman versus the much

larger region scanned through the biochemical analysis. Overall, this analysis indicates that the Raman-derived coefficients are good indicators for local collagen and GAG content, thereby non-destructively producing a marker for relative concentration at high resolution.

Comparison of Results to Histology and Confirmation of Non-destructive Analysis

To confirm the accuracy of this technique, the linear model was applied to Raman data collected

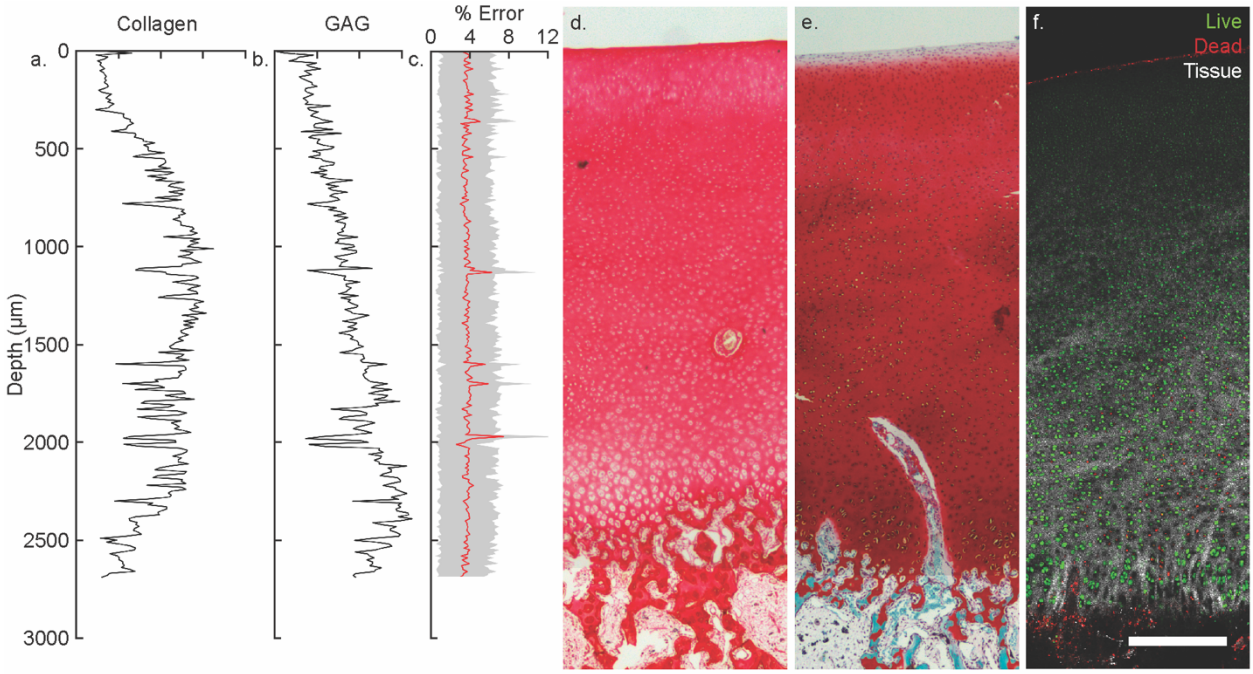

Figure 3.5 Representative line scans from inner region of medial tibial plateau showing **a** collagen content, **b** GAG content, and **c** error for each Raman fit as a function of depth from the articular surface. The line scans extend from the surface at 0 μm to the first evidence of mineralized tissue at the end of the line scan. **d** Picrosirius Red counterstained with hematoxylin for collagen (red) and cells (purple) of cross-section of articular cartilage from surface to the osteochondral interface. **e** Safranin-O stain for negatively charged glycosaminoglycans (red), counterstained with Fast Green, a general protein stain (green), and hematoxylin for cells (purple). **f** Live/Dead stain of sample subjected to Raman analysis showing live cells (green), dead cells (red), and the tissue through confocal reflectance (white).

on n = 37 articular cartilage samples. The samples all show similar trends, corresponding to the zonal organization of collagen (Figure 3.5a,b). These results also agree with data from the literature.[3,4,9] The line scans show small fluctuations in the data, likely corresponding to the presence of cells, as the data was collected with a 10 μm resolution. These fluctuations appear larger in deeper regions of the tissue, which is consistent with the larger cell size of hypertrophic

chondrocytes in the deep zone.[37] The fitting error from the linear model remains consistently low throughout the scan, indicating that the model is applicable over multiple compositions within articular cartilage samples (Figure 3.5c). The coefficients associated with water were not analyzed due to the excessive presence of water in this analytical setup (hydrated, submerged samples). These scans were also compared to histology taken from similar samples, again revealing similar trends for collagen and GAG content (Figure 3.5d,e). Further, samples that had been subjected to Raman microscopy showed no signs of damage, which was confirmed with a Live/Dead stain, showing living cells throughout the depth of the tissue (Figure 3.5f).

The data collection format can also be extended into large scale maps of the depth of articular cartilage, showing similar trends to those revealed through histology (Figure 3.6). We emphasize that this analysis is performed non-destructively and simultaneously, resulting in maps of the relative concentration of collagen and GAG in living tissue. Further, the resolution of Raman spectroscopy is dictated by the objective lens used, in this case 40x, meaning that much higher resolutions are theoretically possible. In this case a 40x objective was determined ideal, as higher magnifications result in more noise due to the size of the chondrocyte cells in cartilage.

Application to Anatomical Locations across the Tibial Plateau

To measure local differences in cartilage composition, this technique was applied to different locations across the tibial plateau to gauge overall composition trends as a function of anatomy (Figure 3.7). We compared the inner and outer locations of the medial and lateral tibial plateau (Figure 3.S1). These regions are subjected to different stresses based on the anatomy of the knee joint,[38] meaning that these areas may have different compositional trends. All locations showed an average zonal organization with respect to collagen concentration. However, comparison of these data reveals a much steeper incline in collagen content through the mid zone of the cartilage from outer region of the medial tibial plateau than in other locations (Figure 3.7a,b,c,d).

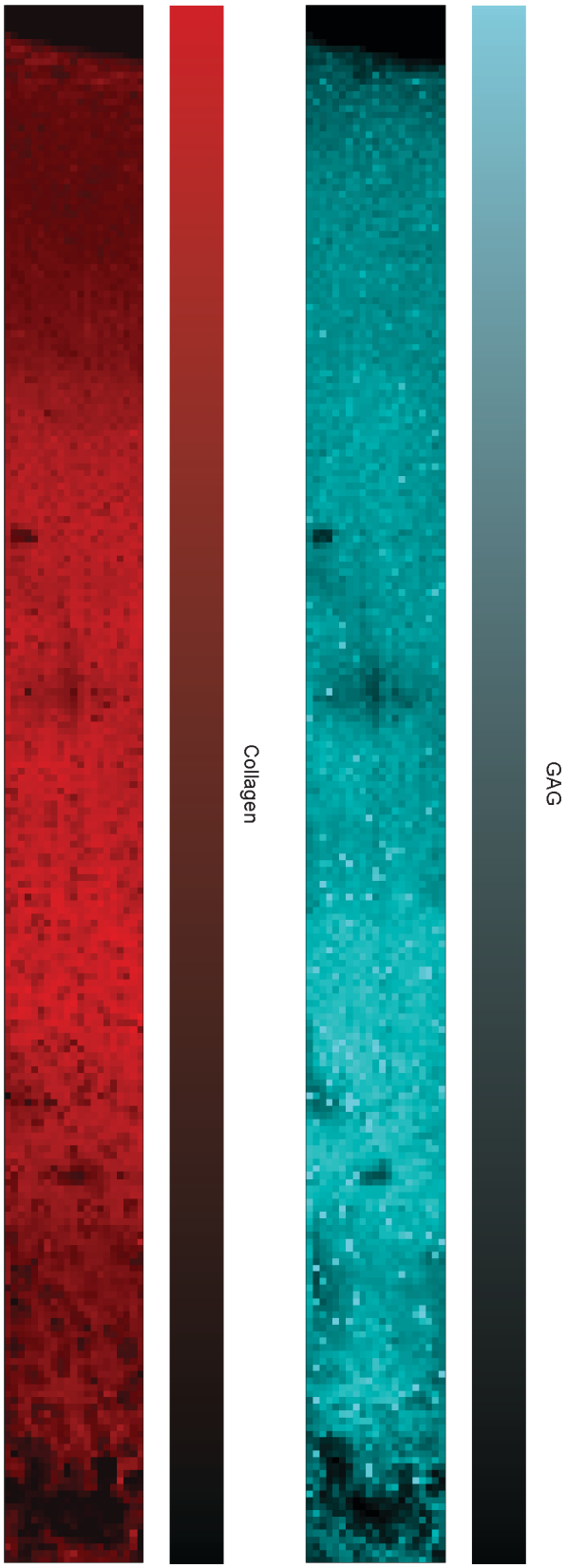

Figure 3.6 Raman-derived image showing **a** collagen content and **b** GAG content on a sample from the inner region of the medial tibial plateau.

This area of the tibial plateau is subjected to higher stresses than any of the surrounding locations, possibly indicating the origin of this result. The GAG content shows an average linear increase throughout the depth for all locations (Figure 3.7e,f,g,h). However, the tissue samples taken from the inner regions of the tibial plateau show higher variances in GAG content in deeper regions of the sample. These results may be due to the immaturity of the tissue analyzed, possibly indicating an earlier stage of maturity for the cartilage in the inner regions of the tibial plateau.

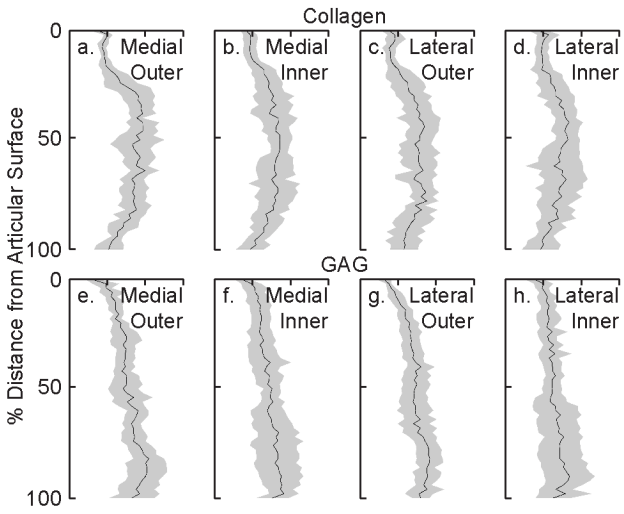

Figure 3.7 Average line scans for collagen content as a function of depth (a,b,c,d). Gray areas represent standard deviation. Line scan for the **a** outer region of the medial tibial plateau, **b** inner region of the medial tibial plateau, **c** outer region of the lateral tibial plateau, **d** inner region of the lateral tibial plateau. Average line scans for GAG content as a function of depth (e,f,g,h). Gray areas represent standard deviation. Line scan for the **e** outer region of the medial tibial plateau, **f** inner region of the medial tibial plateau, **g** outer region of the lateral tibial plateau, **h** inner region of the lateral tibial plateau.

Conclusions

This study shows the successful implementation of a non-destructive technique for collecting local concentrations of the major components of articular cartilage from living tissue. A statistical model was applied for reconstructing Raman spectra collected from cartilage samples. This model was compared to a biochemical analysis, showing that the values produced by the linear model represent relative changes in the local collagen and GAG content. Further work should be performed on the analysis of osteoarthritic tissue, to determine the feasibility of detecting early-stage osteoarthritis through the local loss of GAG content. This technique, given its applicability to hydrated living tissues, can be applied to the surfaces of cartilage to detect these early stage changes. This methodology can also be applied in the laboratory for gauging the health of tissues

during orthopedic studies. Lastly, this type of analysis can be applied to other tissue systems, potentially producing similarly high resolution compositional imaging for these systems. Overall, this study shows promise for future spectroscopic analytical techniques in the clinic, potentially providing increased diagnostic capabilities.

Supplemental Information

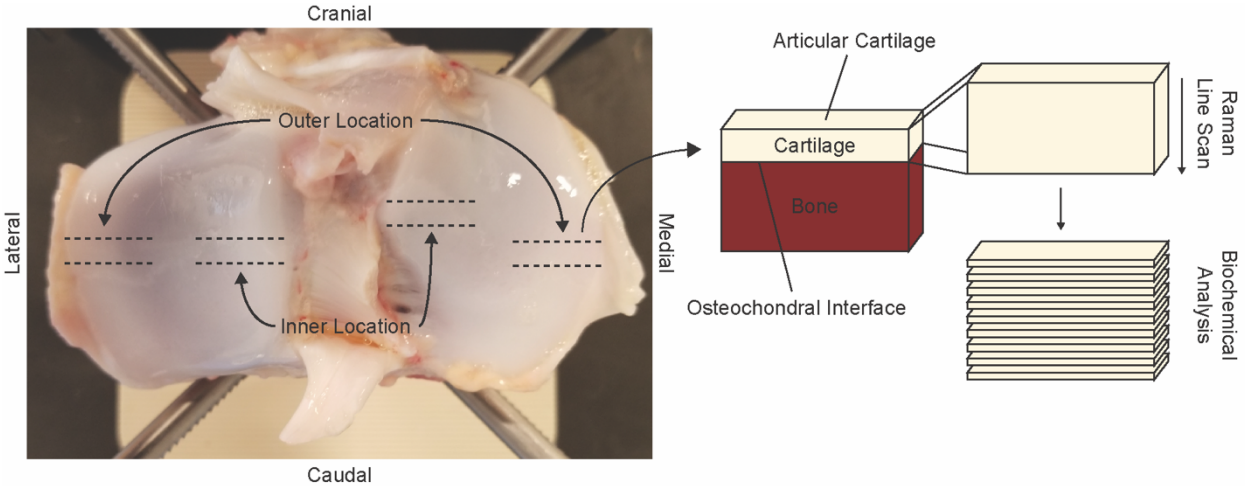

Figure 3.S1. Image of a neonatal bovine tibial plateau. Sample collection areas are highlighted. Schematic shows extraction and analysis procedure for Raman line scans and spatially resolved biochemical analysis.

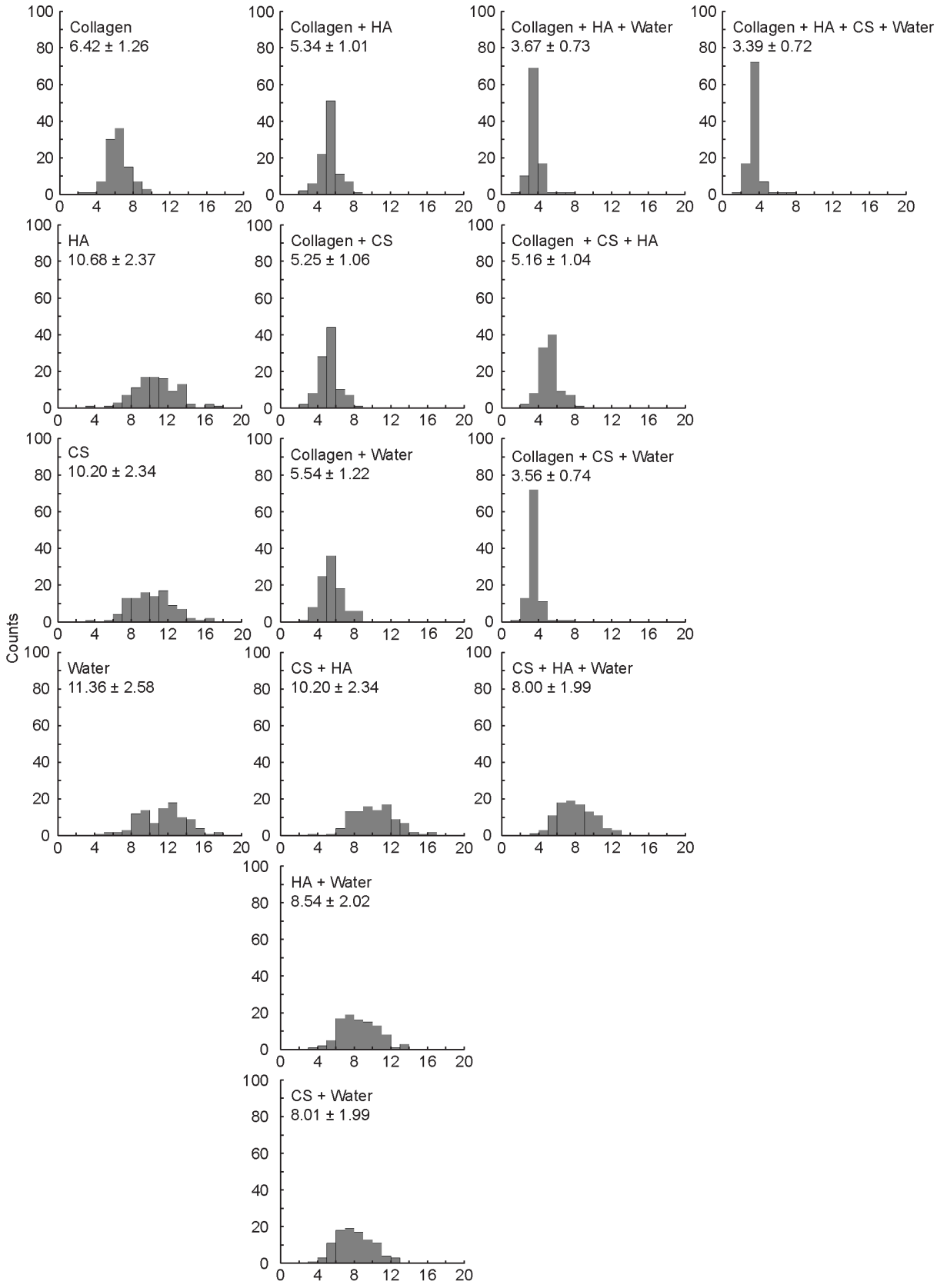
Collagen
6.42 ± 1.26
Collagen + HA
5.34 ± 1.01
Collagen + HA + Water
3.67 ± 0.73
Collagen + HA + CS + Water
3.39 ± 0.72
HA
10.68 ± 2.37
Collagen + CS
5.25 ± 1.06
Collagen + CS + HA
5.16 ± 1.04
CS
10.20 ± 2.34
Collagen + Water
5.54 ± 1.22
Collagen + CS + Water
3.56 ± 0.74
Water
11.36 ± 2.58
CS + HA
10.20 ± 2.34
CS + HA + Water
8.00 ± 1.99
HA + Water
8.54 ± 2.02
CS + Water
8.01 ± 1.99
Counts

Figure 3.S2. Histograms of error for the test set for each model per every permutations of a linear regression model based on the components: collagen, hyaluronan (HA), chondroitin sulfate (CS), and water.

References

1. Ortved, K. F., Begum, L., Mohammed, H. O. & Nixon, A. J. Implantation of rAAV5-IGF-I Transduced Autologous Chondrocytes Improves Cartilage Repair in Full-thickness Defects in the Equine Model. *Mol. Ther.* **23,** 363–373 (2015).
2. Allen, K. D. & Golightly, Y. M. Epidemiology of osteoarthritis: state of the evidence. *Curr. Opin. Rheumatol.* **27,** 276–283 (2015).
3. Pritzker, K. P. H. *et al.* Osteoarthritis cartilage histopathology: Grading and staging. *Osteoarthr. Cartil.* **14,** 13–29 (2006).
4. Klein, T. J., Chaudhry, M., Bae, W. C. & Sah, R. L. Depth-dependent biomechanical and biochemical properties of fetal, newborn, and tissue-engineered articular cartilage. *J. Biomech.* **40,** 182–190 (2007).
5. Palukuru, U. P., McGoverin, C. M. & Pleshko, N. Assessment of hyaline cartilage matrix composition using near infrared spectroscopy. *Matrix Biol.* **38,** 3–11 (2014).
6. Nelson, B. B. *et al.* Recent advances in articular cartilage evaluation using computed tomography and magnetic resonance imaging. *Equine Vet. J.* **50,** 564–579 (2018).
7. Sarkar, B., O'Leary, L. E. & Hartgerink, J. D. Self-Assembly of Fiber-Forming Collagen Mimetic Peptides Controlled by Triple-Helical Nucleation. *J. Am. Chem. Soc.* **136,** 14417–14424 (2014).
8. Kiani, C., Chen, L., Wu, Y. J., Yee, A. J. & Yang, B. B. Structure and function of aggrecan. *Cell Res.* **12,** 19–32 (2002).
9. Silverberg, J. L., Barrett, A. R., Das, M., Petersen, P. B. & Bonassar, L. J. Structure-Function Relations and Rigidity Percolation in the Shear Properties of Articular Cartilage. *Biophys. J.* **107,** 1721–1730 (2014).
10. Boesen, M. *et al.* Osteoarthritis year in review 2016: imaging. *Osteoarthr. Cartil.* **25,** 216–

226 (2017).

11. Wang, Y., Teichtahl, A. J. & Cicuttini, F. M. Osteoarthritis year in review 2015: imaging. *Osteoarthr. Cartil.* **24,** 49–57 (2016).

12. Pedoia, V., Li, X., Su, F., Calixto, N. & Majumdar, S. Fully automatic analysis of the knee articular cartilage T1ρ relaxation time using voxel-based relaxometry. *J. Magn. Reson. Imaging* **43,** 970–980 (2016).

13. Goebel, L., Müller, A., Bücker, A. & Madry, H. High resolution MRI imaging at 9.4 Tesla of the osteochondral unit in a translational model of articular cartilage repair. *BMC Musculoskelet. Disord.* **16,** 1–12 (2015).

14. Novakofski, K. D. *et al.* High-Resolution Methods for Diagnosing Cartilage Damage In Vivo. *Cartilage* **7,** 39–51 (2016).

15. Sewerin, P., Schleich, C., Vordenbäumen, S. & Ostendorf, B. Update on imaging in rheumatic diseases: cartilage. *Clin. Exp. Rheumatol.* **36,** 139–144 (2018).

16. Khanarian, N. T. *et al.* FTIR-I Compositional Mapping of the Cartilage-to-Bone Interface as a Function of Tissue Region and Age. *J. Bone Miner. Res.* **29,** 1–26 (2014).

17. Spalazzi, J. P., Boskey, A. L., Pleshko, N. & Lu, H. H. Quantitative mapping of matrix content and distribution across the ligament-to-bone insertion. *PLoS One* **8,** e74349 (2013).

18. McGoverin, C. M., Lewis, K., Yang, X., Bostrom, M. P. G. & Pleshko, N. The contribution of bone and cartilage to the near-infrared spectrum of osteochondral tissue. *Appl. Spectrosc.* **68,** 1168–75 (2014).

19. Bonifacio, A. *et al.* Chemical imaging of articular cartilage sections with Raman mapping, employing uni- and multi-variate methods for data analysis. *Analyst* **135,** 3193 (2010).

20. Bergholt, M. S. *et al.* Raman Spectroscopy Reveals New Insights into the Zonal

Organization of Native and Tissue-Engineered Articular Cartilage. *ACS Cent. Sci.* **2,** 885–895 (2016).

21. Albro, M. B. *et al.* Raman spectroscopic imaging for quantification of depth-dependent and local heterogeneities in native and engineered cartilage. *Regen. Med.* **3,** 1–11 (2018).
22. Ellis, R., Green, E. & Winlove, C. P. Structural analysis of glycosaminoglycans and proteoglycans by means of Raman microspectrometry. *Connect. Tissue Res.* **50,** 29–36 (2009).
23. Gamsjaeger, S., Klaushofer, K. & Paschalis, E. P. Raman analysis of proteoglycans simultaneously in bone and cartilage. *J. Raman Spectrosc.* **45,** 794–800 (2014).
24. Esmonde-White, K. A. *et al.* Raman spectroscopy of synovial fluid as a tool for diagnosing osteoarthritis. *J. Biomed. Opt.* **14,** 034013 (2009).
25. Taylor, E. A., Lloyd, A. A., Salazar-Lara, C. & Donnelly, E. L. Raman and FT-IR mineral to matrix ratios correlate with physical chemical properties of model compounds and native bone tissue. *Appl. Spectrosc.* **71,** 2404–2410 (2017).
26. Takahashi, Y. *et al.* Raman spectroscopy investigation of load-assisted microstructural alterations in human knee cartilage: Preliminary study into diagnostic potential for osteoarthritis. *J. Mech. Behav. Biomed. Mater.* **31,** 77–85 (2014).
27. Unal, M., Yang, S. & Akkus, O. Molecular spectroscopic identification of the water compartments in bone. *Bone* **67,** 228–236 (2014).
28. Unal, M. & Akkus, O. Raman spectral classification of mineral- and collagen-bound water's associations to elastic and post-yield mechanical properties of cortical bone. *Bone* **81,** 315–326 (2015).
29. Rygula, A. *et al.* Raman spectroscopy of proteins: a review. *J. Raman Spectrosc.* **44,** 1061–1076 (2013).

30. Talari, A. C. S., Zanyar, M., Rehman, S. & Rehman, I. U. Raman spectroscopy of biological tissues. *Appl. Spectrosc. Rev.* **50,** 46–111 (2015).

31. Akiva, A. *et al.* Mineral Formation in the Larval Zebrafish Tail Bone Occurs via an Acidic Disordered Calcium Phosphate Phase. *J. Am. Chem. Soc.* **138,** 14481–14487 (2016).

32. Iannucci, L. E., Boys, A. J., McCorry, M. C., Estroff, L. A. & Bonassar, L. J. Cellular and Chemical Gradients to Engineer the Meniscus-to-Bone Insertion. *Adv. Healthc. Mater.* **1800806,** 1800806 (2018).

33. Ballyns, J. J. *et al.* Image-Guided Tissue Engineering of Anatomically Shaped Implants via MRI and Micro-CT Using Injection Molding. *Tissue Eng. Part A* **14,** 1195–1202 (2008).

34. DiDomenico, C. D., Kaghazchi, A. & Bonassar, L. J. Measurement of local diffusion and composition in degraded articular cartilage reveals the unique role of surface structure in controlling macromolecular transport. *J. Biomech.* **82,** 38–45 (2018).

35. Enobakhare, B. O., Bader, D. L. & Lee, D. A. Quantification of Sulfated Glycosaminoglycans in Chondrocyte/Alginate Cultures, by Use of 1,9-Dimethylmethylene Blue. *Anal. Biochem.* **243,** 189–191 (1996).

36. Neuman, R. E. & Logan, M. A. The determination of hydroxyproline. *J. Biol. Chem.* **184,** 299–306 (1950).

37. Buckwalter, J. A., Mankin, H. J. & Grodzinsky, A. J. Articular cartilage and osteoarthritis. *AAOS Instructional course lectures* **54,** 465–480 (2005).

38. Wang, H., Chen, T., Torzilli, P., Warren, R. & Maher, S. Dynamic contact stress patterns on the tibial plateaus during simulated gait: A novel application of normalized cross correlation. *J. Biomech.* **47,** 568–574 (2014).

CHAPTER 4

Top-down Fabrication of Spatially Controlled Mineral Gradient Scaffolds for Interfacial Tissue Engineering[5]

Abstract

Materials engineering can generally be divided into "bottom-up" and "top-down" approaches, where current state-of-the-art methodologies are bottom-up, relying on the advent of atomic-scale technologies. Applying bottom-up approaches to biological tissues is challenging due to the inherent complexity of these systems. Top-down methodologies provide many advantages over bottom-up approaches for biological tissues, given that some of the complexity is already built into the system. Here, we generate interfacial scaffolds by the spatially controlled removal of mineral content from trabecular bone using a chelating solution. We controlled the degree and location of the mineral interface, producing scaffolds that support cell growth, while maintaining the hierarchical structure of these tissues. We characterized the structural and compositional gradients across the scaffold using X-ray diffraction, microcomputed tomography (μCT), and Raman microscopy, revealing the presence of mineral gradients on the scale of 20 – 40 μm. Using these data, we generated a model showing the dependence of mineral removal as function of time in the chelating solution and initial bone morphology, specifically trabecular density. These scaffolds will be useful for interfacial tissue engineering, with application in the fields of orthopedics, developmental biology, and cancer metastasis to bone.

[5] This chapter has been submitted: Boys, A. J., Zhou, H., Harrod, J. B.,McCorry, M. C., Estroff, L. A., Bonassar, L. J.

Introduction

Methodologies for engineering complex materials systems are often divided into "top-down" and "bottom-up" approaches. Bottom-up approaches, involving the synthesis of a material beginning at the molecular or even atomic scale, provide a high degree of control over the final system. Current efforts in materials science and biomedical engineering generally focus on bottom-up approaches, given recent advances in materials fabrication, polymer synthesis, and other nanoscale systems.[1–3] Despite the advantages to these bottom-up systems, generating the hierarchy necessary for recapitulating tissue structure and function can be challenging. Currently, no biological scaffolds produced from a bottom-up approach have successfully recapitulated the complex structure of bone, let alone the soft tissue-to-bone interfaces. Top-down approaches have been utilized throughout human history and in biomedical engineering. For example, decellularized tissue, like the intestinal submucosa, has been utilized as a tissue graft in various applications,[4–7] and demineralized bone has been used as a void filler and as a biomaterial in other applications.[8,9] Here, we develop a method for spatially controlled demineralization of decellularized bone to generate soft tissue-to-bone interfaces for tissue engineering.

Understanding the hierarchical structure of soft tissue-to-bone interfaces is critical for engineering complex, multiscale materials to match the physical and chemical properties of native tissue interfaces.[10–12] These interfaces link soft tissue with trabecular bone through multiple interfacial regions. Trabecular bone is a hierarchically structured tissue consisting at the nanoscale of oriented collagen fibrils intercalated with platelets of mineral oriented along the axis of the fibril.[13–15] This mineral is primarily poorly crystalline carbonated hydroxyapatite. At a larger scale these fibrils are arranged into lamellar sheets that are wrapped circumferentially around a network of struts that make up the bulk of trabecular bone.[13,14] The organization of the soft tissue of these regions varies depending on the particular interface but generally consists of oriented collagen.

The interface between soft tissue and bone consists of a series of intermediate regions, typically unmineralized cartilage/fibrocartilage, mineralized cartilage/fibrocartilage, and a thin layer of dense bone, that are centrally coupled by a mineral gradient.[10–12,16,17] This gradient dictates the interface between these hard and soft tissues.

Soft tissue-to-bone interfaces exist throughout the human body. Most notably, these interfaces are present at the ends of ligaments and tendons and between cartilage and bone. In all these cases, the interface mechanically mediates a multiple order of magnitude transition in stiffness.[16,18,19] For ligaments and tendons, the function of the interface is primarily mechanical, transitioning the tensile strains experienced in the ligament into the bone to allow for stabilization and movement. The function of the interface between cartilage and bone varies depending on the location. The osteochondral interface plays a mechanical role, linking cartilage to bone and providing an anchor for articulation within the knee joint. Other cartilage-to-bone interfaces are relevant to development, such as the growth plate and the interface present during endochondral ossification.[10,11,20] These interfaces can also act as loci for cancer metastasis to bone.[21] The pervasiveness of interfacial tissue systems throughout biological fields highlights the need for a generalizable scaffold system.

Development of interfacial tissue engineered scaffolds is important for the production of implants as well as the study of different native interfaces,[10–12,16,17] as a native-like scaffold would provide access to studying the effects of scaffold composition on cell behavior, in both healthy and pathological models.[22] Recent reviews have described the fabrication of interfacial scaffolds, which can typically be classified as graded scaffolds, consisting of multiple delineated regions, and gradient scaffolds, utilizing a continuous change in composition and/or structure.[10,11,17] Graded scaffolds[23] can precisely reproduce the relative mechanical properties across soft tissue-to-bone interfaces but may suffer from a lack of continuity between regions. Cell-based, tissue engineering

approaches have shown success in generating morphologically accurate interfacial constructs.[24] However, as with many cell-based approaches, careful timing would be ultimately required to implant these scaffolds due to long culture times. Production of interfacial scaffolds using materials-based fabrication methods has generated constructs that appear morphologically similar to soft tissue-to-bone interfaces,[25] but these scaffolds do not possess the regional composition observed in native interfaces as of yet. Other bottom-up approaches have resulted in scaffolds lacking hierarchical structure or proper compositional aspects (low mineral concentration).[26,27] Gradient scaffolds have typically been produced using a bottom-up approach by growing mineral inside of a soft scaffold or mixing mineral into a soft material.[26,28] For example, a mineral gradient was formed on a polymer nanofiber scaffold by partially submerging a portion of the scaffold in a solution containing the precursor ions for apatitic mineral.[26] The top point of contact between the solution and the scaffold was continually increased over the mineral growth period, thereby generating a mineral gradient. Such scaffolds, however, lack the hierarchical structure of bone, consisting of calcium phosphate mineral grown on the exterior of polymer fibers. Other scaffolds with mineral gradients have been fabricated using complex diffusion systems, but these scaffolds also lack the hierarchical structure of bone.[27,29] Although these approaches are encouraging, collectively they point to the need for methods to produce hierarchical scaffolds with graded structure and composition to more accurately mimic those seen in native interfaces.

We have chosen to approach this problem of generating a mineral gradient using spatially controlled mineral *removal* from bone. Demineralization is commonly used in biology and biomedical engineering to prepare samples for histological analysis. Further, powdered, demineralized bone has been used as a void filler during surgery.[8,9] For these applications, demineralization is often accomplished using strong demineralizing agents like hydrochloric acid or formic acid. These agents risk damaging the underlying protein matrix during demineralization,

thereby eliminating the hierarchical structuring inherent to tissue. Demineralization using a chelator, ethylenediaminetetraacetic acid (EDTA), has been shown to leave the protein matrix intact.[30] To the best of our knowledge, no studies have examined methods for spatially controlled demineralization, regardless of demineralization agent.

In this study, we demonstrate the fabrication of a cell-seedable scaffold with an apatitic mineral gradient possessing the inherent hierarchical structure of trabecular bone. These scaffolds were generated using a top-down approach, by removing the mineral content from decellularized bone. The resulting scaffold was demonstrated to contain structural and compositional gradients and an intact fibrillar collagen structure. Such scaffolds are useful for generating tissue engineered interfaces with application in orthopedics, developmental studies, and cancer research.

Materials and Methods

Bone Plug Decellularization

Trabecular bone biopsies were extracted and decellularized as previously described.[31,32] Briefly, bone biopsies were explanted from 1 – 3 day old neonatal bovine distal femurs (Gold Medal Packing, Inc., Rome, NY) using a 6 mm diameter coring bit and sectioned into 10 mm long cylinders. Cellular debris and bone marrow was removed from biopsies by rinsing them with high velocity stream of deionized water (~140 mL/s through a 5 mm diameter nozzle), followed by sequential soaks of 0.1 w/v% ethylenediaminetetraacetic acid (EDTA) (TCI, Tokyo, Japan) in phosphate buffered saline (PBS) (Corning, Manassas, VA) for 1 hour, hypotonic buffer (10 mM Trizma base (TCI, Tokyo, Japan), 0.1 w/v% EDTA in PBS) at 4°C for 24 hours, and detergent (10 mM Trizma base, 0.5 w/v% sodium dodecyl sulfate (SDS) (Sigma, St. Louis, MO) in PBS) at 4°C for 24 hours. Following washes, biopsies were rinsed 7 times with PBS and frozen.

Partial Demineralization

Bone biopsies were skewered on a 20 gauge surgical needle and partially suspended in a bath containing 9.5 w/v% EDTA in PBS solution (pH = 7.4) for demineralization.[30] The EDTA solution was gently stirred, avoiding the formation of a vortex. The bone plugs were collected at time points of 3, 4, 4.5, 5, 6, and 12 hours. The partially demineralized bone plugs were washed with deionized water 5 times and frozen (Figure 4.1, Figure 4.S1).

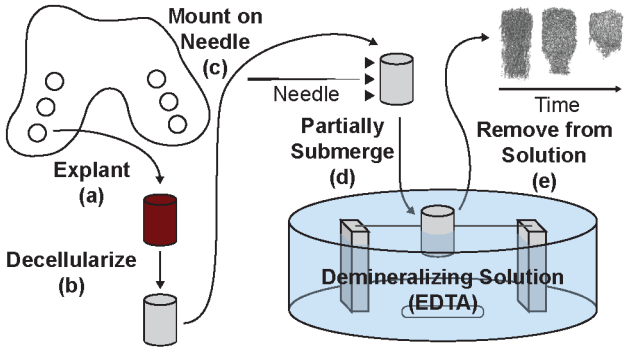

Figure 4.1. Schematic of process for forming mineral gradient in bone scaffolds. (a) Bone biopsies are explanted from bovine condyles using a coring bit. (b) Cartilage and bone marrow are removed from biopsies and biopsies are decellularized. (c) Biopsies are mounted on a needle. Mounting location determines location of demineralization front. (d) Bone biopsies are partially submerged in a demineralizing solution to immediately below mounting location. (e) Biopsies are removed from demineralizing solution, where time in the solution dictates the morphology of the resulting interfacial scaffold.

X-ray Computed Tomographic Analysis

Mineral content in bone scaffolds was analyzed using microscale X-ray computed tomography (μCT) at either a ~15 μm voxel resolution (Xradia Zeiss VersaXRM-520, Zeiss, Oberkochen, Germany), or a 50 μm voxel resolution (GE eXplore CT-120 microCT, GE Healthcare, Chicago, Illinois). Higher resolution data was processed using Avizo Fire software (Version 8.1.1) to visualize the mineral profile and the microstructure of the trabecular bone. Lower resolution μCT data were processed using FIJI[33] to examine the demineralization process. To analyze these data, μCT stacks containing interfacial scaffolds were converted in 8-bit images. These stacks were normalized to the sample holder, a gridded paper box. To eliminate variations in the sample holder

material, 30 randomly chosen voxels were averaged, and each voxel in the stack was divided by this number. The normalized data was thresholded using an empirically derived value of 16 (from an 8-bit image), resulting in a binary image of mineralized tissue and other contents of the stack. Each scaffold was segmented from this stack by cropping around the individual scaffold and in all three dimensions. The trabecular density was determined by taking the average number of mineralized voxels from the first 10 full slices of the mineralized end of the scaffold. The number of mineral voxels was counted for the whole stack. The length of each scaffold was determined (Supplemental Information, Figure 4.S2). The fractional demineralized content was calculated by dividing the number of mineral voxels within the whole stack by the length of the scaffold. These data were processed in MATLAB to find the relationship between the fractional demineralized content, trabecular density, and time. A first order surface was fitted to the data points using the Curve Fitting Tool (cftool) package.

Powder X-ray Diffraction

X-ray diffraction (pXRD) was used to determine the relative mineral portion per quarter moving axially along the bone plug. Four partially demineralized bone scaffolds were lyophilized and quartered perpendicular to the axis, moving from mineralized to demineralized portions of the scaffold. Corresponding quarters from the four bone scaffolds were ground under liquid nitrogen using a mortar and pestle. The four powders were analyzed with pXRD using a Bruker D8 Advance ECO Powder Diffractometer (Bruker, Billerica, MA). The X-ray exposure were taken at a distance of 250 mm, 40 kV and 25 mA with Cu K-α radiation with a detector slit opening of 9 mm. The XRD data were processed using MATLAB and Microsoft Excel. This experiment was performed four times to determine consistency.

Histology

Partially demineralized bone scaffolds were fixed, dehydrated, embedded in poly methyl methacrylate (PMMA), sectioned to a 10 μm thickness, and stained with Von Kossa and methyl green pyronin to visualize mineral gradient. Other bone scaffolds were fixed, decalcified, dehydrated, embedded in paraffin, sectioned to a 4 μm thickness, and stained. Hematoxylin and Eosin (H&E) and Picrosirius Red with Hematoxylin were used to show collagenous matrix in trabecular bone and the result of decellularization. Sections imaged using an Aperio Scanscope slide scanner (Aperio Technologies, Inc., Vista, CA) under brightfield. Picrosirius Red stained slides were also imaged under cross-polarizers with a Nikon Eclipse TE2000-S microscope (Nikon Instruments, Melville, NY) and a SPOT RT camera (Diagnostic Instruments, Steriling Heights, MI) to view the alignment of collagen fibrils after demineralization.

Raman Microscopy

Raman microscopy was performed on a PMMA embedded sample using a WiTec Alpha300R Confocal Raman Microscope. Data were collected using a 532 nm laser at 30 mW of power through a 50x objective (Zeiss LD EC Epiplan-Neofluor Dic 40x / 0.55). Spectra were collected in 10 μm increments as line scans across the interface between mineralized and demineralized tissue within individual trabeculae in the transition zone between the fully mineralized and fully demineralized ends of the bone plug. Each spectrum is an average of 3 accumulations with an integration time of 8 seconds. For analysis, data were analyzed in MATLAB, using the ratio of peak intensities for 957:1673 cm^{-1} to determine the mineral:matrix ratio.[34] The results at this peak ratio were also compared to the ratio of the peak intensities for 428:1673 cm^{-1}.

Mesenchymal Stem Cell (MSC) Seeding

To assess the ability of scaffolds to support cells, partially demineralized scaffolds were seeded with mesenchymal stem cells (MSCs). MSCs were isolated from trabecular bone marrow of 1 – 3

day old neonatal bovine distal femurs. Briefly, the trabecular region of the femur was washed with heparin supplemented media, and the extract solution was centrifuged at 300 x$\bar{g}$. Pelleted cells were plated on culture flasks and the non-adherent cell population was washed off after 48 hours. Isolated MSCs were plated at a cellular density of 2000 cells/cm^3 and expanded to passage 2 in an expansion media including Dulbecco's modified Eagle's medium without sodium pyruvate (DMEM) (Corning, Manassas, VA), 10% fetal bovine serum (FBS) (Gemini Bio-Products, West Sacramento, CA, 1 ng/mL basic fibroblast growth factor (bfGF) (BD Biosciences, Franklin Lakes, NJ) and 100 IU/mL penicillin.

Bone biopsies used for viability testing were cut in half along the axis prior to demineralization. These samples were skewered halfway along the axis of the sample and submerged in the demineralizing solution for 4.5 hours. After partial demineralization, bone scaffolds were soaked in 70% ethanol for 1.5 hours, washed in PBS, and soaked in an osteogenic media containing Minimum Essential Medium-α (MEM-α) (ThermoFisher, Waltham, MA), 10% FBS, 100 IU/mL penicillin, 2 mM L-glutamine (VWR, Brooklyn, NY), 0.1 μM beta-glycerolphosphate (MP, Santa Ana, CA), 50 μM ascorbic acid, 0.1 μM dexamethasone. Bone scaffolds were seeded as previously described.[32] Briefly, bone scaffolds were skewered and suspended in a spinner flask. The flask was supplied filled with 150 mL of osteogenic media containing 500,000 cells/bone scaffold and stored in an incubator for 48 hours. Following seeding, scaffolds were transferred into osteogenic media for 3 days of static culture.

To determine the viability of cellular populations after seeding, Live/Dead stains were performed on bone. Briefly, seeded bone scaffolds were transferred from culture media to dye solution at 1 mL PBS : 1 μL calcein AM : 1 μL ethidium homodimer (Life Technologies Corporation, ThermoFisher, Waltham, MA), and left for 30 minutes. Samples were stored in PBS for at least 5 minutes before imaging. Imaging was performed using a Zeiss LSM 710

AxioObserver using a C-Apochromat 10x / 0.45 W objective. Images consisted of 3 channels: the first channel for ethidium homodimer had an excitation wavelength of 561 nm and a detection range of 582 - 741 nm, the second channel for calcein AM had an excitation wavelength of 488 nm and a detection range of 510 - 741 nm, and third channel for reflectance had an excitation wavelength of 488 nm and a detection range of 480 - 497 nm. Images were collected every 750 μm moving across the bone plugs, beginning approximately ~1 mm from the beginning and ending ~1 mm from the end of the bone plug. Slice thicknesses were ~250 μm. Live/dead counting was performed in FIJI.[33] Data were analyzed using Microsoft Excel. Confocal z-stacks were also collected. The z-stacks taken from the ends of the bone plugs consist of 25 slices over 193.2 μm. The z-stack collected from the center of the bone plug consisted of 80 slices over 478.0 μm. Images were compiled using Zeiss ZEN 2.3 (blue edition).

Additional samples were cultured for 4 days after seeding to image the MSC-deposited matrix. These samples were prepared for sectioning and stained with H&E, as above.

Results

A spatial gradient in mineral was generated in bone scaffolds through half submersion in an EDTA solution (Figure 4.1, Figure 4.S1). Analysis using μCT confirmed the removal of mineral as a function of time (Figure 4.2, Figure 4.S3, Movie 4.1). In accordance with typical diffusion patterns, mineral removal progressed from the end and sides of the scaffold that were exposed to solution. Minimal demineralization was observed at 3 hours, while at 4 hours, the sides and end of scaffolds began to show the presence of demineralized collagen (Figure 4.S3). After 4.5 hours, this exposure pattern generated a conical mineral profile (Figure 4.2b, d-h, Movie 4.1). The portion of the scaffold exposed to EDTA appeared entirely demineralized at 5 hours, and the demineralization front began to progress into the portion of the bone scaffold that was not submerged at 6 hours (Figure 4.3a). By 12 hours, the bone scaffolds were generally observed to be entirely demineralized,

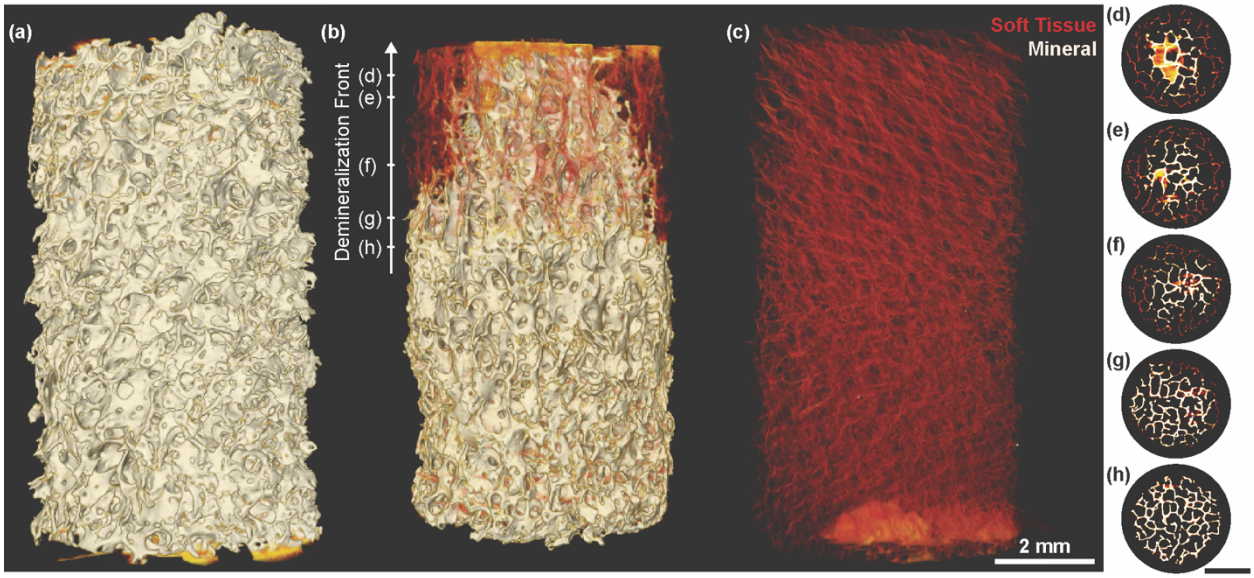

Figure 4.2. X-ray μCT of interfacial scaffolds showing demineralization front morphology. High densities are shown in white (mineral), and lower densities are shown in yellow and red (collagen). (a) Fully mineralized bone biopsy prior to submersion in demineralization solution. (b) Interfacial scaffold after half submersion for 4.5 hours in demineralization solution. Demineralization front forms conical profile as demineralization progresses. (c) Fully demineralized bone biopsy. (d – h) Single slices from μCT of (b). Hash mark on Demineralization Front arrow in (b) indicates approximate location of each slice.

some containing a small core in the un-submerged portion of the scaffold (Figure 4.S3). To confirm the degree of control over the demineralization front location, scaffolds were also submerged up to a quarter and up to three quarters of the scaffold, finding that the demineralization front progressed in a similar manner (Figure 4.S4).

Variation in the demineralization progression was qualitatively observed to be dependent on the porosity, or, inversely, on the trabecular volume of the scaffolds, through analysis of μCT data. To confirm this speculation, the average trabecular density was calculated from the mineralized portion of each scaffold. This density was calculated as the average number of mineralized voxels over the first 10 slices from the mineralized end of the scaffold. The total mineral volume per unit length or fractional demineralized content was plotted as a function of trabecular volume and time. A first order surface was fitted to these data, finding an adjusted R^2 value of 0.68 (Figure 4.3b,c,d, Figure 4.S5, Figure 4.S6). One sample that had been demineralized

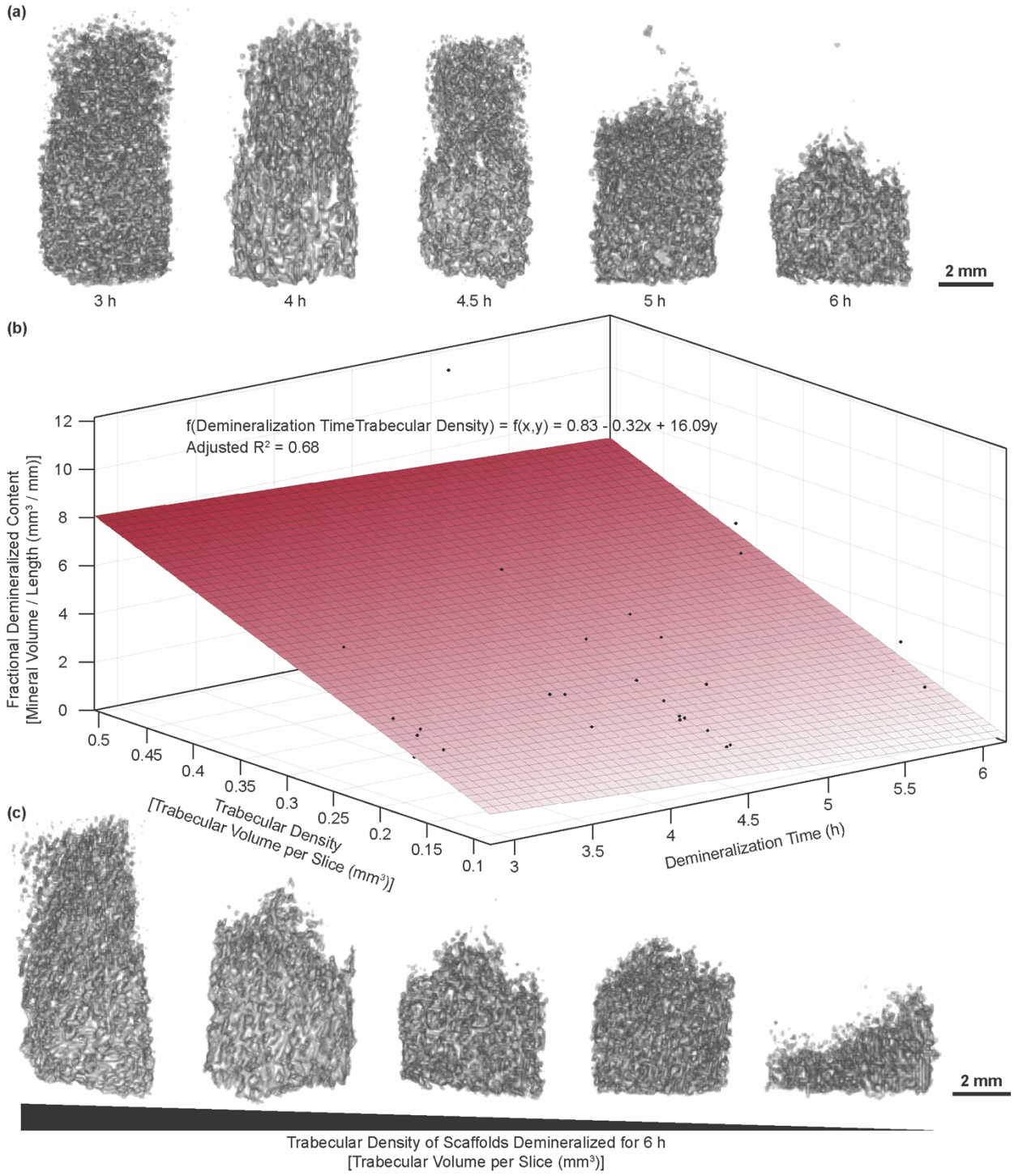

Figure 4.3. (a) Demineralization morphology progression for time points at a trabecular density between 0.2 and 0.25 mm^3. (b) Plot showing relationship of fractional demineralized content to time to trabecular density with accompanying fitted surface. (c) Resulting morphology of demineralizing bone scaffolds at 6 hours, shown as a function of trabecular density.

for 4.5 hours became fully demineralized over this time period. This sample was not included in the analysis, as the trabecular volume could not be reliably calculated due to the lack of mineral. While the bone biopsies follow the same general trend in demineralization, the trabecular volume dictates the state the sample reaches after a given time point (Figure 4.3e,f). Of the 8 partially demineralized scaffolds at the 6 hour time point, 6 show the expected trend in morphology, following the adjusted R^2 value of 0.68 from the fitted surface (Figure 4.3b).

To confirm the mineral distribution across the scaffold, pXRD was performed. For this analysis, four bone scaffolds were divided axially into quarters, and the corresponding quarters of these scaffolds were cryo-fractured and mixed together. Powder X-ray diffraction showed a decrease in the intensity of characteristic carbonated apatite peaks (~26˚ and ~32˚) progressing from the mineralized end of the bone scaffold to the demineralized end (Figure 4.4). Further, this

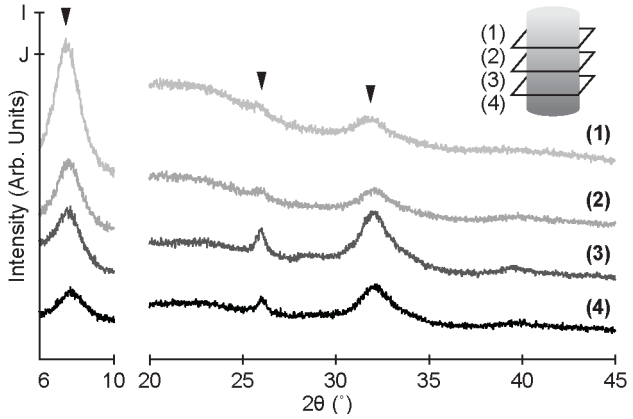

Figure 4.4. Representative diffraction patterns from pXRD analysis of quartered mineral scaffolds (n=4). (1 – 4) Patterns moving from demineralized (1) to mineralized (4) end of scaffold. Patterns from 6° to 10° and from 20° to 45° are scaled to I and J, respectively.

analysis confirms that the EDTA does not affect the mineral type, maintaining mineral within the scaffold as carbonated apatite.[35] A peak with increasing intensity moving from the mineralized to demineralized end of the scaffold was also observed at a 2θ of 8˚ (Figure 4.4). This peak is associated with triple helical structure of collagen.[35]

Histological analysis was used to assess changes in the microstructure of the bone matrix in the scaffold as a function of demineralization. Hematoxylin and eosin staining shows successful decellularization and maintenance of the protein content in the scaffolds (Figure 4.5a). Analysis of scaffolds through Von Kossa staining demonstrates that demineralization occurs from the outside of the trabecular struts into the interior. Phosphate staining, relating the mineral content,

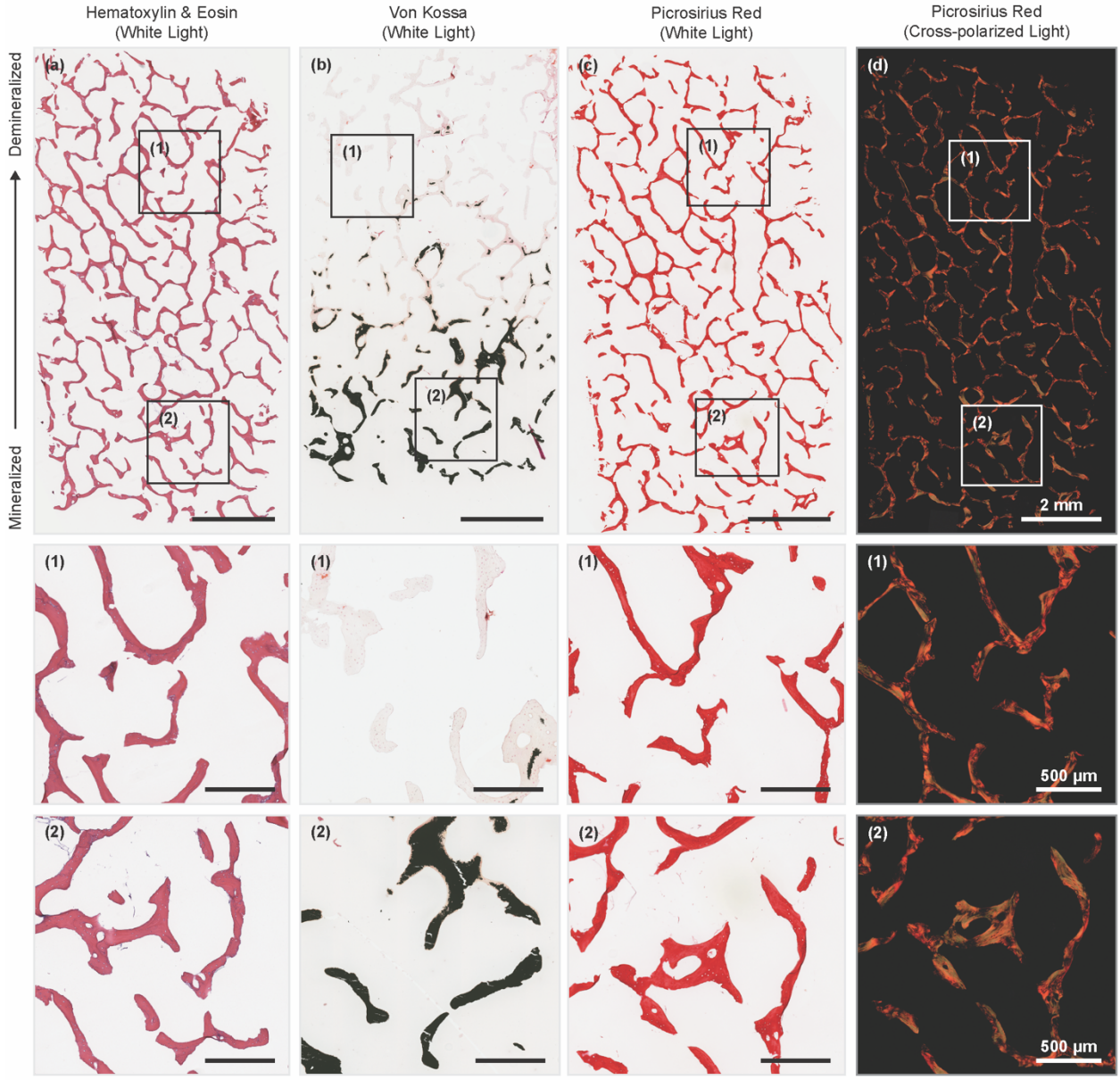

Figure 4.5. Histological stains for interfacial scaffolds, where (a – d) show whole scaffold and (1) and (2) show insets from (a – d). (a) Hematoxylin and eosin stain of section. (b) Von Kossa stain

of section. (c) Picrosirius Red stain of section under white light. (d) Same Picrosirius Red section under cross-polarizers.

can be observed in the cores of individual trabeculae located within the transition zone from the mineralized to demineralized ends of the bone plug. (Figure 4.5b). Picrosirius Red staining confirms that the fibrillar structure of the collagen is not altered by the demineralization protocol (Figure 4.5c). Picrosirius Red stain through cross-polarizers reveals differences in coloration between the mineralized and demineralized ends of the scaffold (Figure 4.5d). Changes in color and intensity of Picrosirius Red stains under cross-polarizers have been shown to relate to changes collagen fibril orientation and diameter.[36–38] Collagen appeared redder in demineralized regions of the scaffolds (Figure 4.5d, (1)) and greener in mineralized areas (Figure 4.5d, (2)).

The µCT, pXRD, and histology data confirm a structural gradient, on the order of 100's to 1000's of microns, moving from the mineralized to demineralized ends of the bone plugs. From the Von Kossa staining, we noted a transitional zone between the two regions in which individual trabeculae possess apparent mineral gradients on a much smaller length scale (Figure 4.6a). To semi-quantitatively measure these compositional gradients, we used Raman microscopy on PMMA embedded tissue. This analysis revealed a ~20 – 40 µm gradient in the mineral:matrix ratio ($\nu_1PO_4^{3-}$: Amide I) within individual trabecular located within the immediate transitional zone (Figure 4.6b,c, Figure 4.S7). The size of this gradient was also confirmed by comparing these

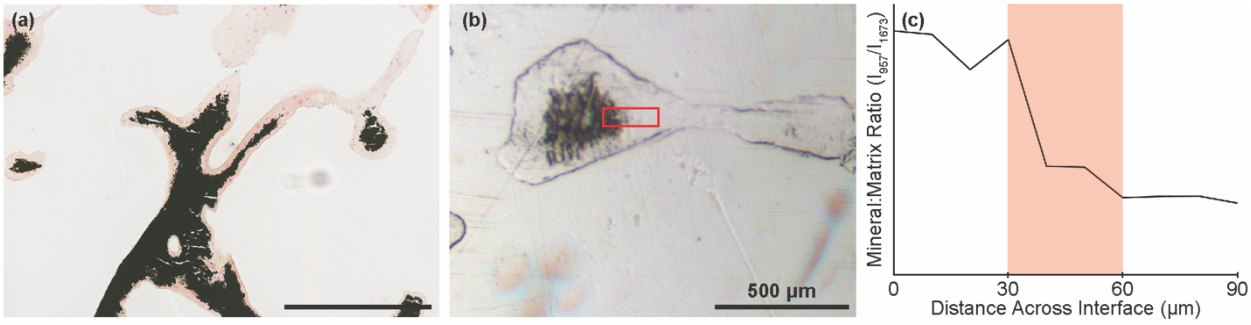

Figure 4.6. Images and Raman-derived line scan showing local compositional gradient within transitional zone between mineralized and demineralized tissue. (a) Von Kossa stain of transitional zone near middle of a bone plug. (b) White light image showing a partially demineralized

individual trabeculae. Red box indicates region from which a Raman line scan was collected. (c) Representative line scan of mineral:matrix ratio, derived from peak intensity ratio of 957 cm^{-1} : 1673 cm^{-1} from Raman spectroscopy.

results to other mineral:matrix ratios (e.g., $\nu_2PO_4^{3-}$: Amide I) as function of distance. Finally, partially demineralized scaffolds were seeded with MSCs to confirm the applicability of these scaffolds for supporting cellular adhesion and growth. Live/Dead staining (n = 6) of scaffolds found an average viability of 91% with no differences observed between the mineralized and demineralized ends of the scaffold (Figure 4.S8). Cells were found to actively bind to the scaffold, spreading along the exterior of the trabeculae (Figure 4.7a, Figure 4.S9). Qualitative differences

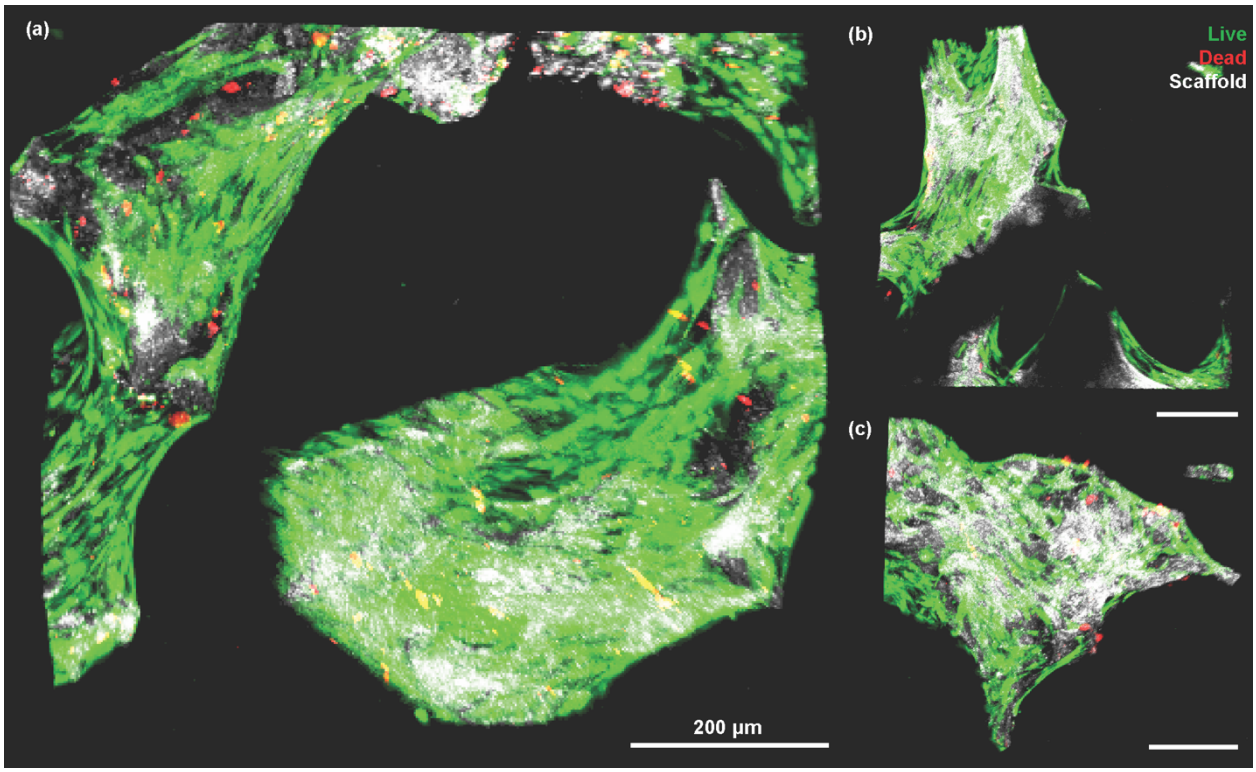

Figure 4.7. Live/Dead stain of MSCs seeded onto interfacial scaffolds. Green indicates live cells, red indicates dead cells, and white shows the scaffold through confocal reflectance. (a) Z-stack recorded from the center of the scaffold. (b) Z-stack recorded from demineralized end of scaffold. (c) Z-stack recorded from mineralized end of scaffold.

in cell spreading were observed between the mineralized and demineralized portions of the scaffold (Figure 4.7b,c). To confirm this observation, samples were cultured for 4 days after seeding to determine the extent of this observation, and differences in cell spreading behavior on

the demineralized portions of the scaffold versus the mineralized portions of the scaffold were observed (Figure 4.S10). Cells appeared more elongated along the exterior of the trabeculae in the mineralized sections of the scaffold. Cells in the demineralized regions showed rounder phenotypes, grouping together in a matrix that the cells deposit around the scaffold (Figure 4.S10).

Discussion

We have demonstrated the fabrication of a native-like interfacial scaffold containing structural and compositional gradients of apatitic mineral using a spatially controlled, top-down approach. Studies have shown the feasibility of using decellularized scaffolds as implants,[4,5,7–9,31,39–41] but to the best of our knowledge, this study is the first to apply top-down approaches to biological systems in a spatially controlled manner. Given the inherent complexity of biological systems, top-down approaches are a useful mechanism for creating relevant systems for a variety of applications. The main challenge for this approach is identifying factors that vary within an animal population that affect the resulting scaffold. We used neonatal bovine bone as a source of tissue, which provides a consistent source of tissue, but these explants show variation in the trabecular density. We were able to measure the trabecular density from our gradient scaffolds, finding that this factor is relevant to the overall demineralization of the scaffold (Figure 4.3). By measuring this property prior to beginning the demineralization process, a predictable gradient can be generated. Use of other tissues for top-down generation of tissue engineered scaffolds could be useful for a variety of applications, provided that the main variables are identified. For example, one could treat tendons using an enzymatic degradation to produce an oriented collagen scaffold that has a low enough density for cells to penetrate into the interior of the scaffold during seeding. These approaches will open up a new direction for future tissue engineering initiatives.

For generating a gradient in mineral content, we chose to use EDTA as demineralizing agent due to its chelating properties. Unlike harsher demineralizing agents such as HCl or formic

acid, EDTA leaves the underlying protein matrix intact, allowing for a native-like scaffold.[30] Utilization of EDTA likely results in longer demineralization times than stronger acids, but these longer times provide more control over the demineralization process. Despite this factor, care still needs to be taken when applying the demineralizing fluid to the scaffolds. Any areas that are in contact with EDTA will demineralize, and improper application of the solution is likely to result in a fully demineralized scaffold. However, utilizing this detail means that the location of the mineral front can be easily controlled by modulating the point of contact between the scaffold and the demineralizing fluid (Figure 4.S4). Utilization of this aspect allows the process to be modified for a multitude of applications.

We used pXRD to verify that the mineral type was not changed during demineralization of the scaffold. We observed peaks typically associated with the carbonated apatite found in bone (Figure 4.4). We also observed a peak at a 2θ of 8˚, which is associated with triple helical structure of collagen.[35] Interestingly, areas of the scaffold with a higher degree of demineralization also presented a higher intensity of the collagen helix peak versus mineralized areas of the scaffold. This increase in peak intensity may be related to a stress relaxation of the collagen in the scaffold as the intrafibrillar mineral platelets are removed from the collagen fibrils. A similar observation was found upon examination of Picrosirius Red stains of the collagen under cross-polarizers. Mineralized areas of the scaffold were found to have a green color, whereas demineralized areas of the scaffold were red. This green to red color change is related to an increase in the diameter and/or orientation of collagen.[36–38] As the demineralization process does not add any collagen to scaffold, the diameter of the fibrils is unlikely to change. As such, this color change may be attributed to an increase in orientation, possibly related to the removal of internal stresses generated by the apatite platelets.

Our scaffolds contain a structural gradient extending across their length, continuously progressing from mineralized to demineralized tissue. If we focus on the transitional zone, we also observe a local compositional gradient across individual trabeculae (Figure 4.6a). Using Raman microscopy, we determined this gradient to be approximately 20 – 40 μm in length (Figure 4.6b,c and Figure 4.S7), on the same order of magnitude as mineral:matrix gradients in native tissues.[42–44] Due to the presence of mineralized cores we observed in some trabeculae, we wanted to confirm that the gradient in the scaffolds is compositional, rather than a geometrical artifact resulting from this cored structure. As we observe a gradient that is longer than the thickness of the sections from which we collected the data, we believe this gradient is compositional. Further, as removal of mineral in our system progresses in a manner typical of any diffusion process, a compositional gradient at the scale of that found in native tissue is to be expected at the interface between mineralized and demineralized tissue. This gradient size makes these scaffolds ideal for examining cellular behavior at interfaces *in vitro*.

To examine the feasibility of using these scaffolds for tissue engineering applications, we seeded MSCs onto the scaffolds (Figure 4.7, Figure 4.S9). We found high viability across the scaffold, with no observable difference in viability per location (mineralized or demineralized) (Figure 4.S8). While the viability did not change as a function of location, the morphology as the cells did change from more elongated on the mineralized sections to more rounded on the demineralized sections. These morphological differences are most likely in response to changes in material properties, such as stiffness, between these areas.[45,46] More analysis, however, needs to be performed to confirm that these observations relate to scaffold-driven differentiation of the seeded cells.

Our synthetic approach results in a scaffold possessing compositional and hierarchical structuring similar to that observed in native tissues. Significantly, a key feature of the scaffolds

prepared using this top down approach is that the collagen network remains continuous throughout the entire length of the scaffold. This feature is critical for ensuring a mechanically robust scaffold. Our scaffolds, however, do not possess the interfacial regions present in the osteochondral interface, enthesis, or growth plate. Despite the lack of native morphology, our scaffolds are porous and thus can be easily integrated with injectable materials, such as collagen gels, with and without cells. Previous experiments from our labs using fully mineralized bone biopsies has shown promise for direct interaction between reconstituted collagen gels and the cell-deposited matrix surrounding the bone scaffold.[32]

These scaffolds have application in a variety of fields that target the construction of interfacial biological systems through tissue engineering. Orthopedic tissue interfaces, such as the enthesis or the osteochondral interface, require the presence of a mineral gradient to function.[10–12] For example, these scaffolds could be applied to systems that use similar tissues to generate seamless interfacial structures.[32] These scaffolds would also be useful for analyzing cellular behavior in developmental systems. For example, seeding chondrocytes or other musculoskeletal cells onto interfacial scaffolds would allow for the *in vitro* study of cellular behavior during endochondral ossification or long bone growth directed from the growth plate. Our partially mineralized scaffolds are also useful for examining cellular behavior in pathological systems. For example, the growth plate has been implicated as a possible "metastatic niche" for cancer cell localization.[21] Interfacial scaffolds allow for the direct study of these systems without requiring complex animal models. Further, scaffolds containing both mineralized and unmineralized regions allow for studying cell behaviors as a function of material composition, which can be useful when determining the reasoning for particular cancer cells to metastasize to bone.

In conclusion, we successfully fabricated a hierarchically structured scaffold containing a structural and composition mineral gradients for use in tissue engineering. This scaffold was

created using a top-down approach that has not previously been applied to biological systems. These scaffolds were shown to contain a gradient in mineral content using a combination of μCT, pXRD, histology, and Raman microscopy, and the resulting scaffolds were found to be compatible with typical cell seeding methodologies. The scaffolds will be useful for a variety of tissue engineering applications, targeting the complex interfacial systems found in biology. Further, the top-down approach to tissue engineering provides access to a wider range of tissue morphologies and hierarchies than previously accessible.

Supplemental Information

Supplemental Methods

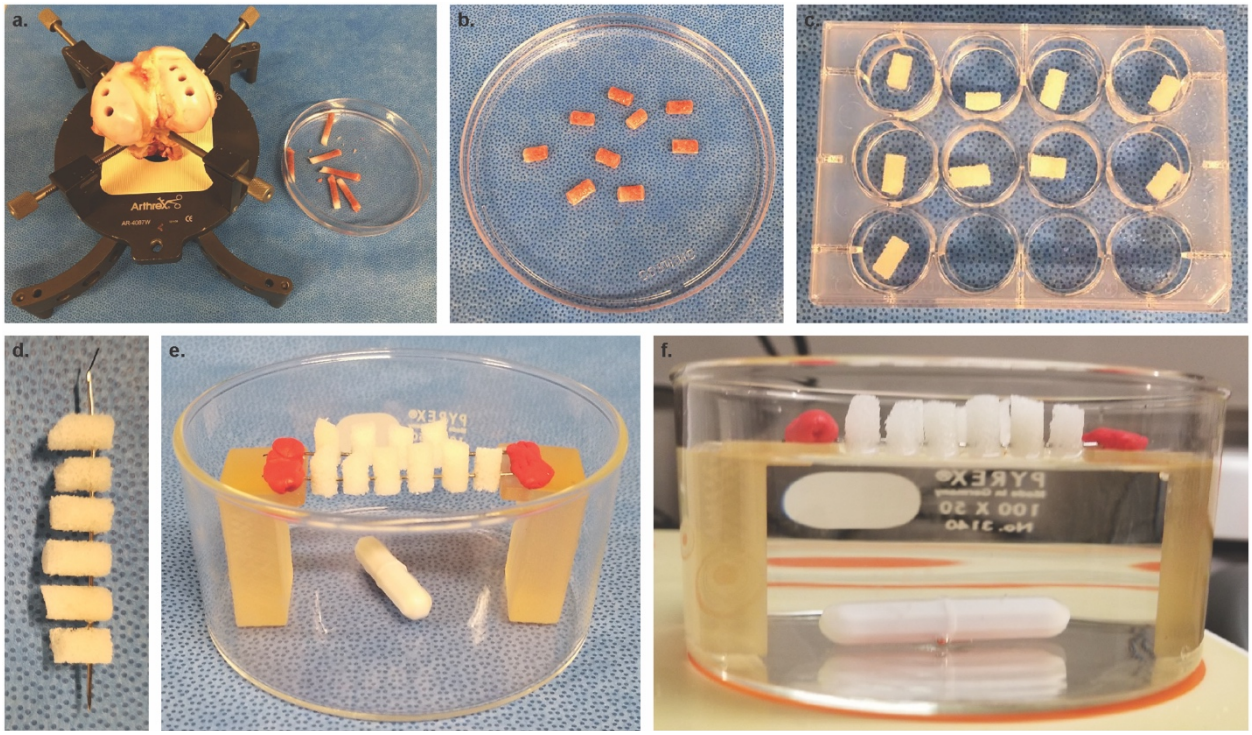

Figure 4.S1. Demineralization procedure: a. explantation from bovine femur, b. explanted biopsies, c. decellularized biopsies, d. skewered biopsies, e. biopsies in demineralization setup, f. fluid level for demineralization front halfway along scaffold axis.

Determination of Length of Scaffolds

Each sample subjected to a μCT scan was angled within the sample holder. To determine the length of each scaffold, the first and last z-slice containing an 'full' elliptical slice of the scaffold was found. A circle was drawn around these slices, determining the x, y, and z coordinates of the first and last 'full' z-slice and used to determine the length of the scaffold with the following equations:

$$d = \sqrt{(x_1 - x_2)^2 + (y_1 - y_2)^2 + (z_1 - z_2)^2}$$

$$h = \sqrt{(z_1 - z_2)^2}$$

$$\theta = arcsin(h/d)$$

$$w = \frac{r}{tan(\theta)}$$

$$l = d + 2w$$

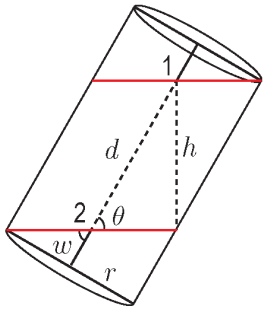

Figure 4.S2. Equations and schematic to calculate length of scaffold oriented at an angle.

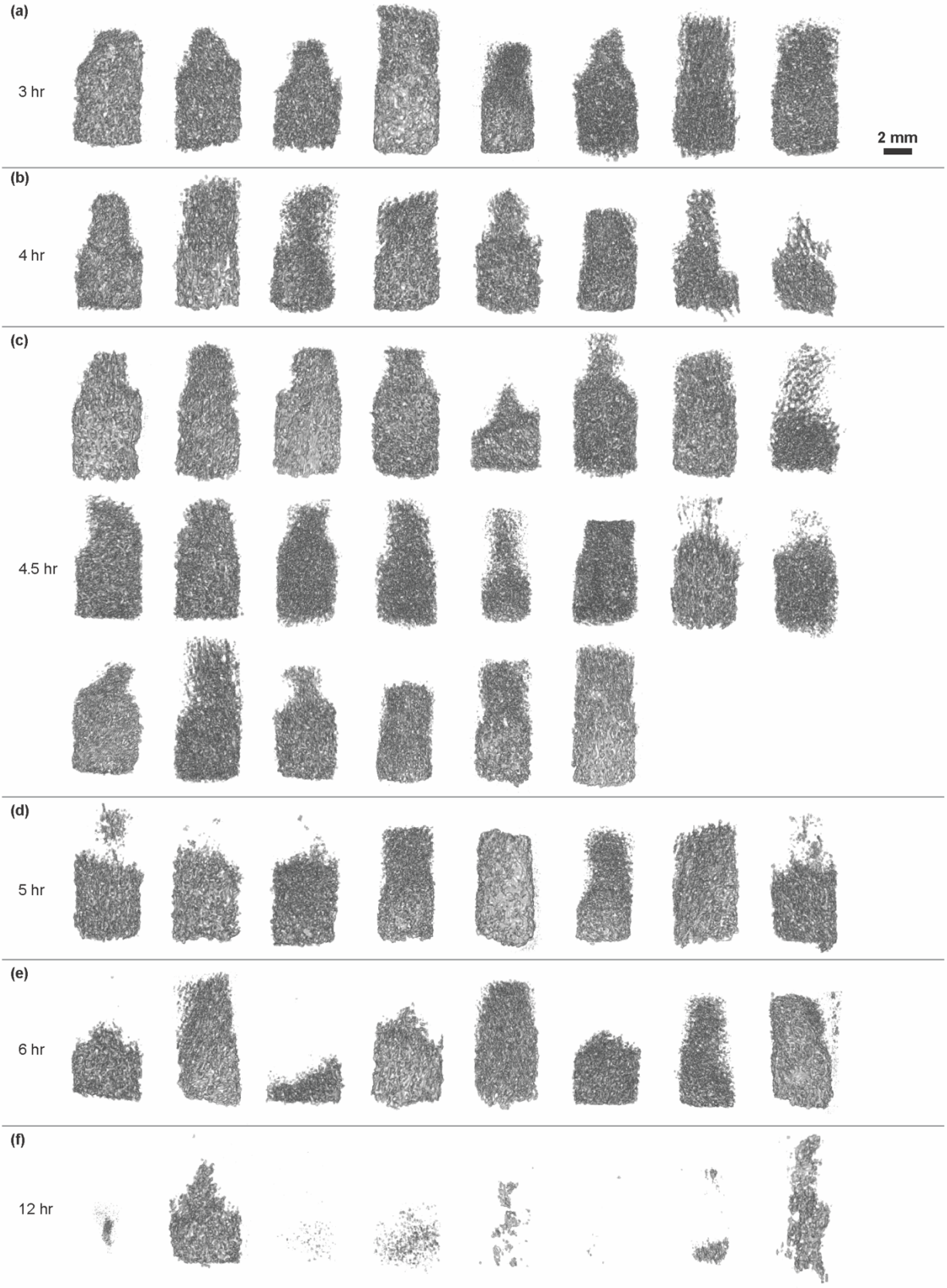
(a)
3 hr
2 mm
(b)
4 hr
(c)
4.5 hr
(d)
5 hr
(e)
6 hr
(f)
12 hr

Figure 4.S3. µCT renderings of all fabricated interfacial scaffolds at (a) 3 hour time point, (b) 4 hour time point, (c) 4.5 hour time point, (d) 5 hour time point, (e) 6 hour time point, and (f) 12 hour time point.

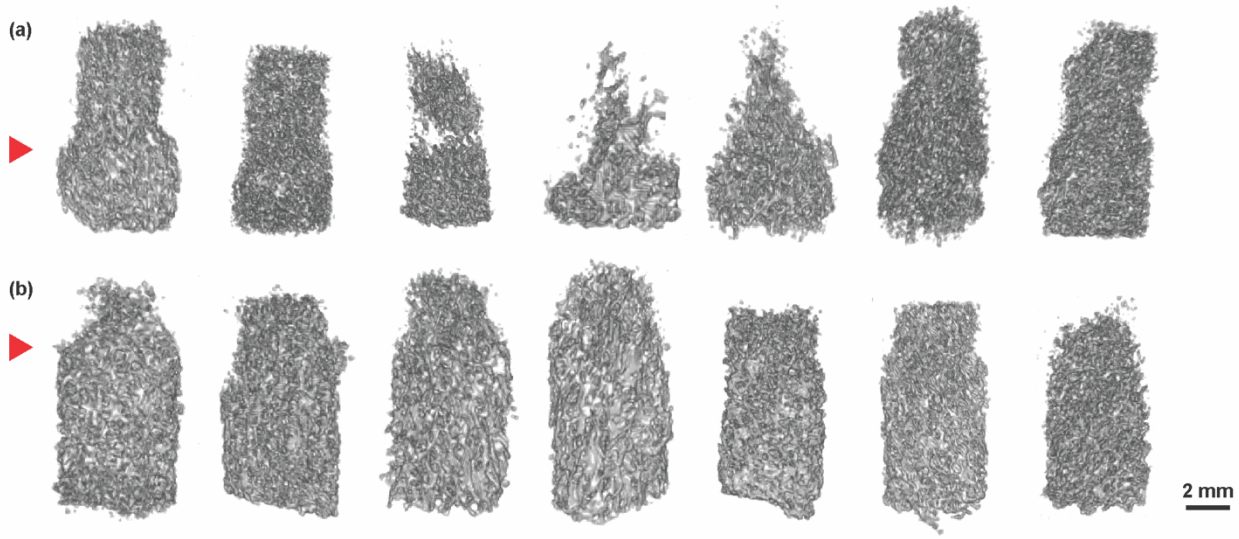

Figure 4.S4. Rendered µCT images of interfacial scaffolds demineralized for 4.5 hours at different skewering locations. Red arrow indicates skewering location.

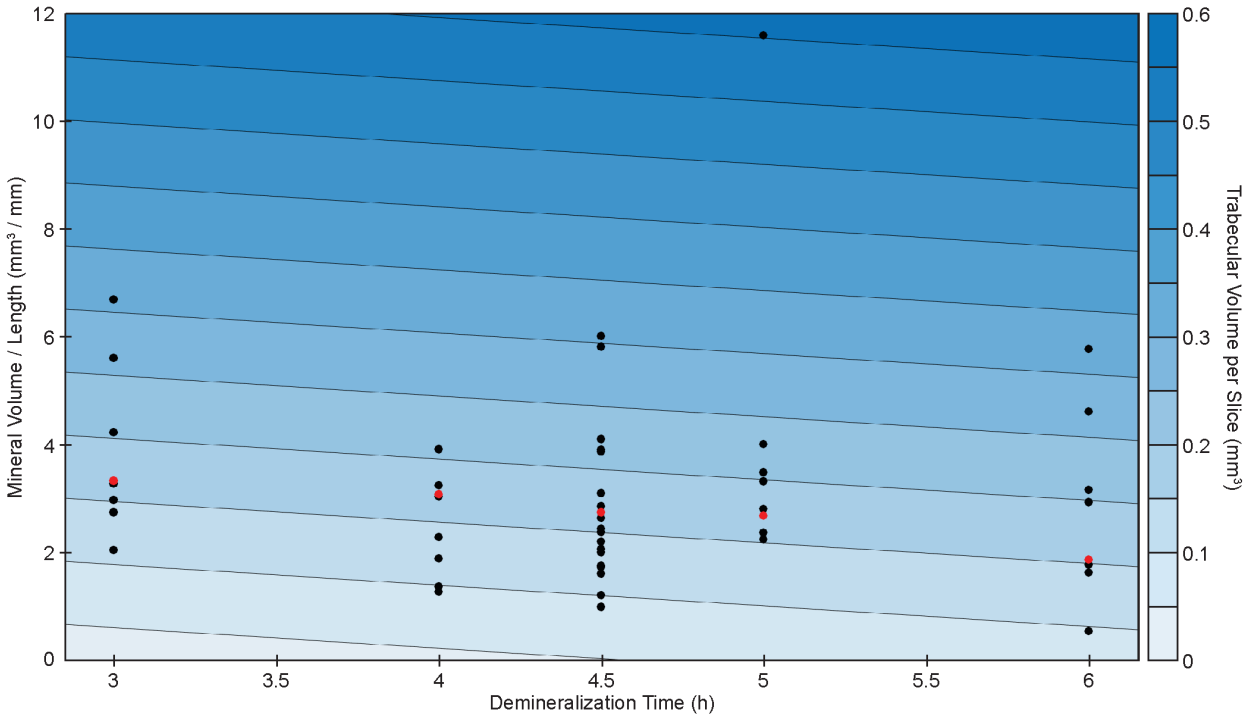

Figure 4.S5. Alternate view of fitted surface for relationship of mineral volume / length to time to trabecular volume per slice from Figure 4.3b. Red dots show the chosen interfacial scaffolds in Figure 4.3a.

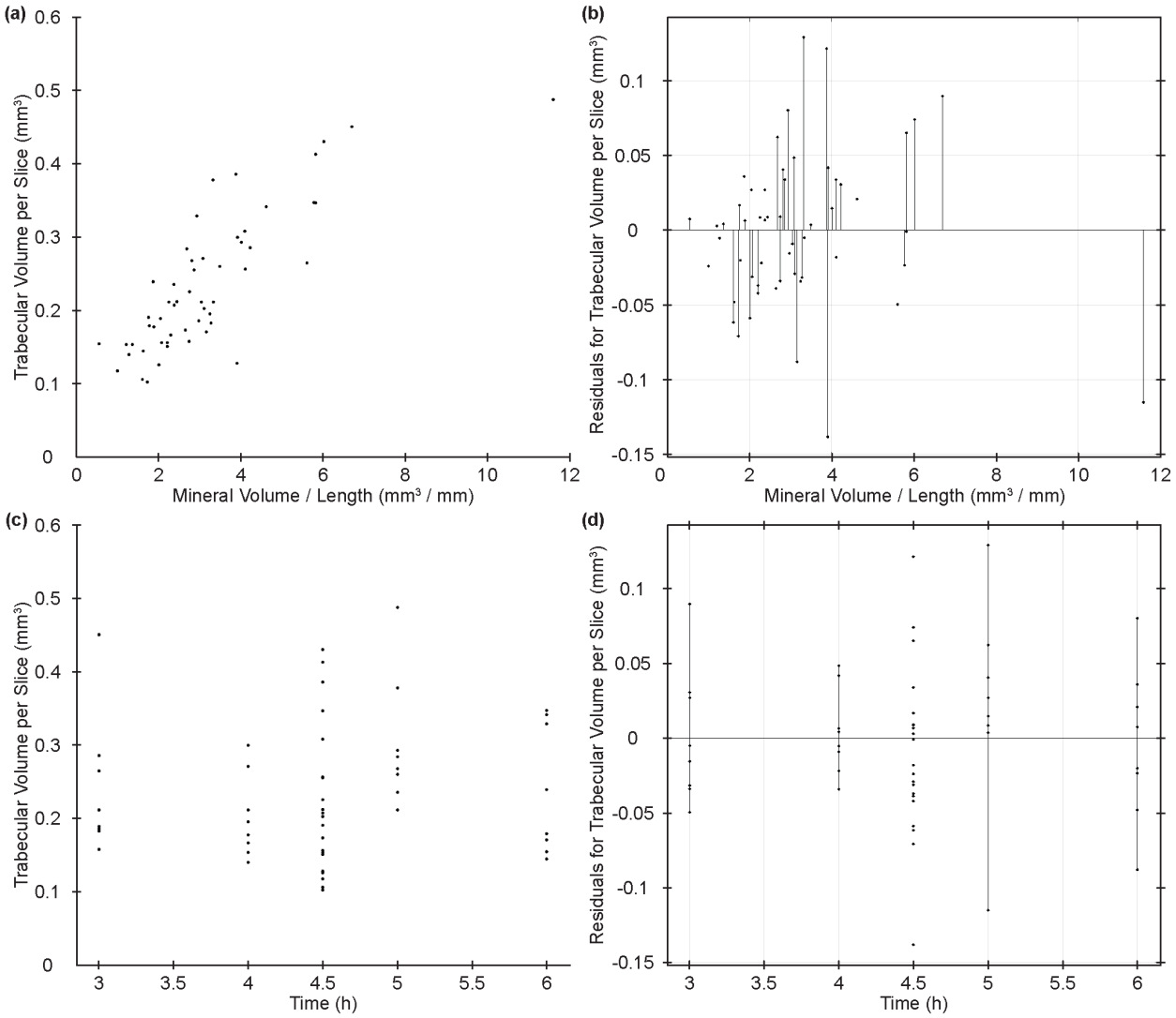

Figure 4.S6. (a) Plot of trabecular volume per slice versus mineral volume / length with labeled axes. (b) Plot showing residuals for surface fit for mineral volume / length. (c) Plot of trabecular volume per slice versus time with labeled axes. (d) Plot of residuals for surface fit for time.

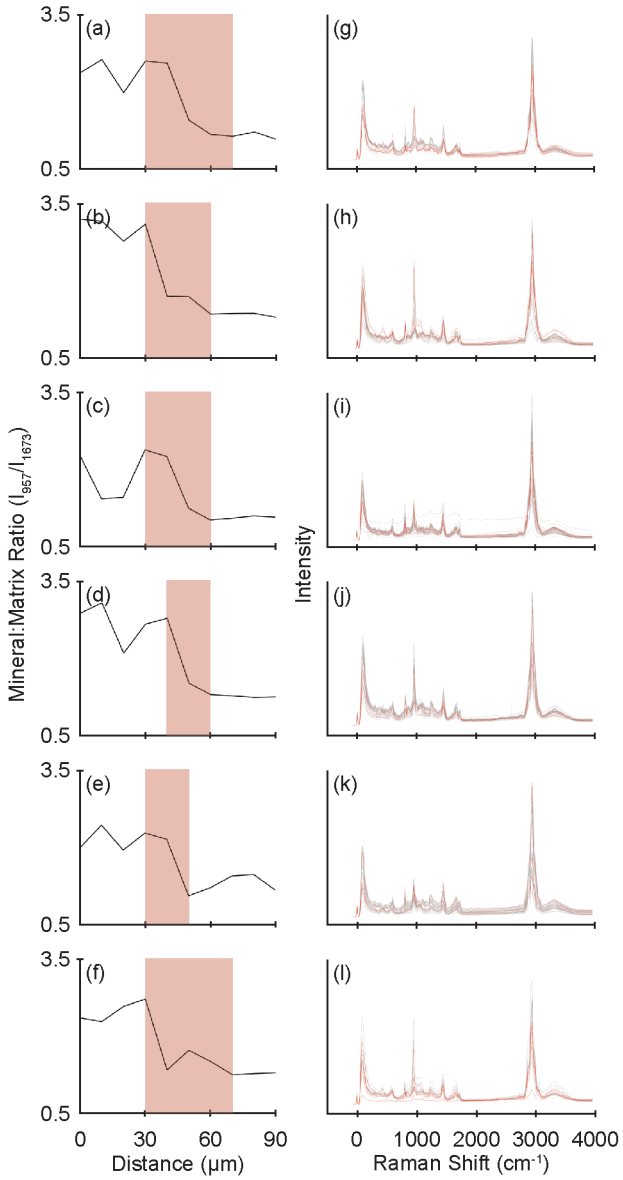

Figure 4.S7. (a – f) Mineral:matrix gradient as a function of distance at the immediate interface between mineralized and demineralized tissue paired with (g – l) Raman spectra across line scan used to calculate mineral : matrix ratio (957 : 1673 cm^{-1}). Red shaded regions indicate gradient, and red spectra are within gradient region. Gray spectra are from region extending around gradient.

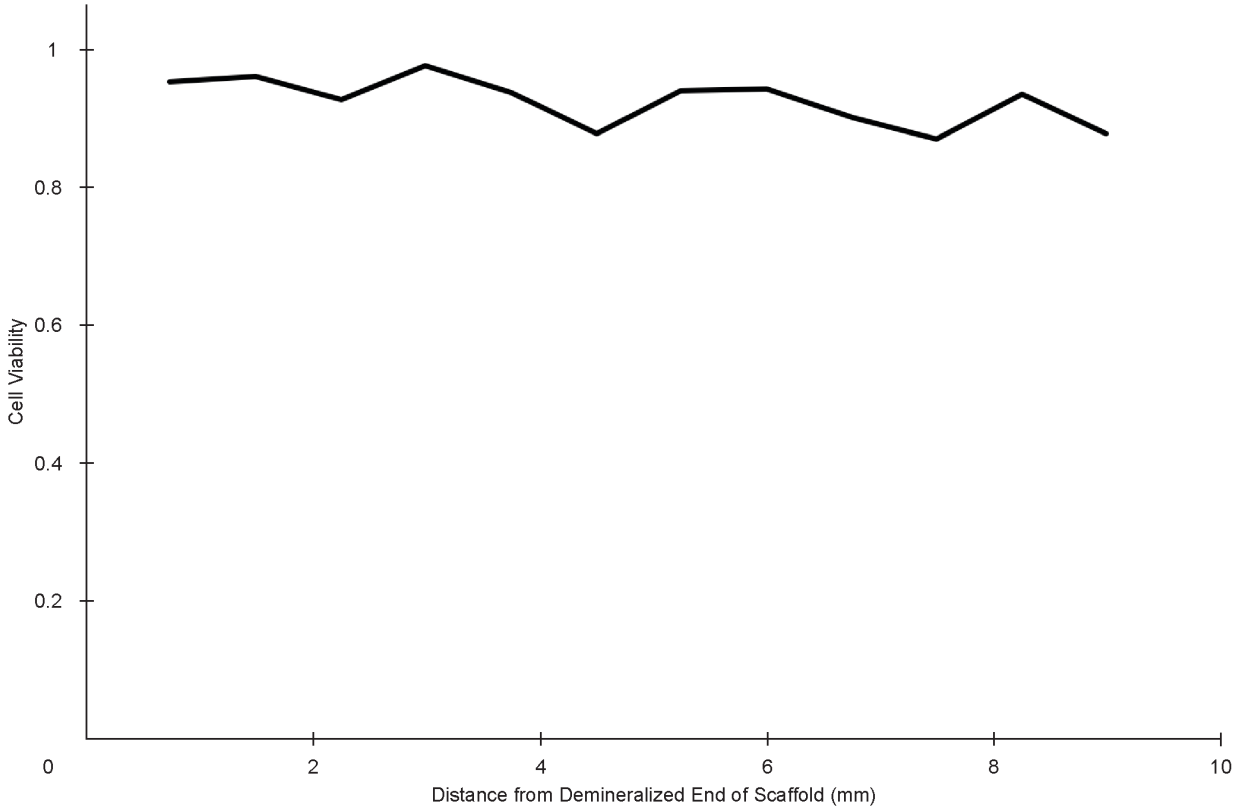

Figure 4.S8. Representative plot of cell viability, from Live/Dead assay after seeding, as a function of distance across partially demineralized scaffold. The line represents the fraction of live cells versus total cells with data collected at 750 μm increments from demineralized end of scaffold to mineralized end of scaffold.

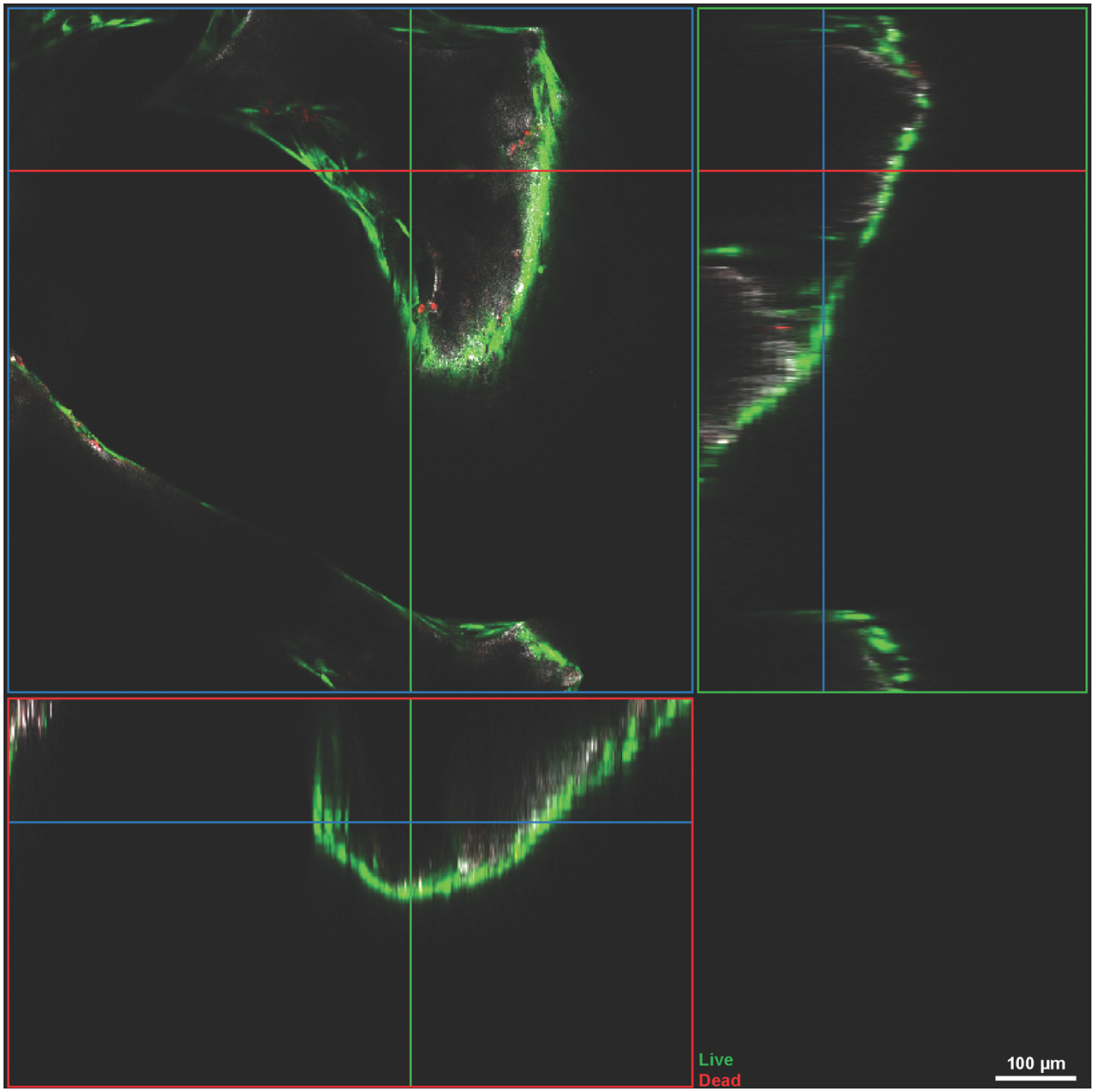

Figure 4.S9. Confocal image of Live/Dead stain from z-stack in Figure 4.7a showing different slices of z-stack. Images show that cells are adhered to the exterior of the trabeculae.

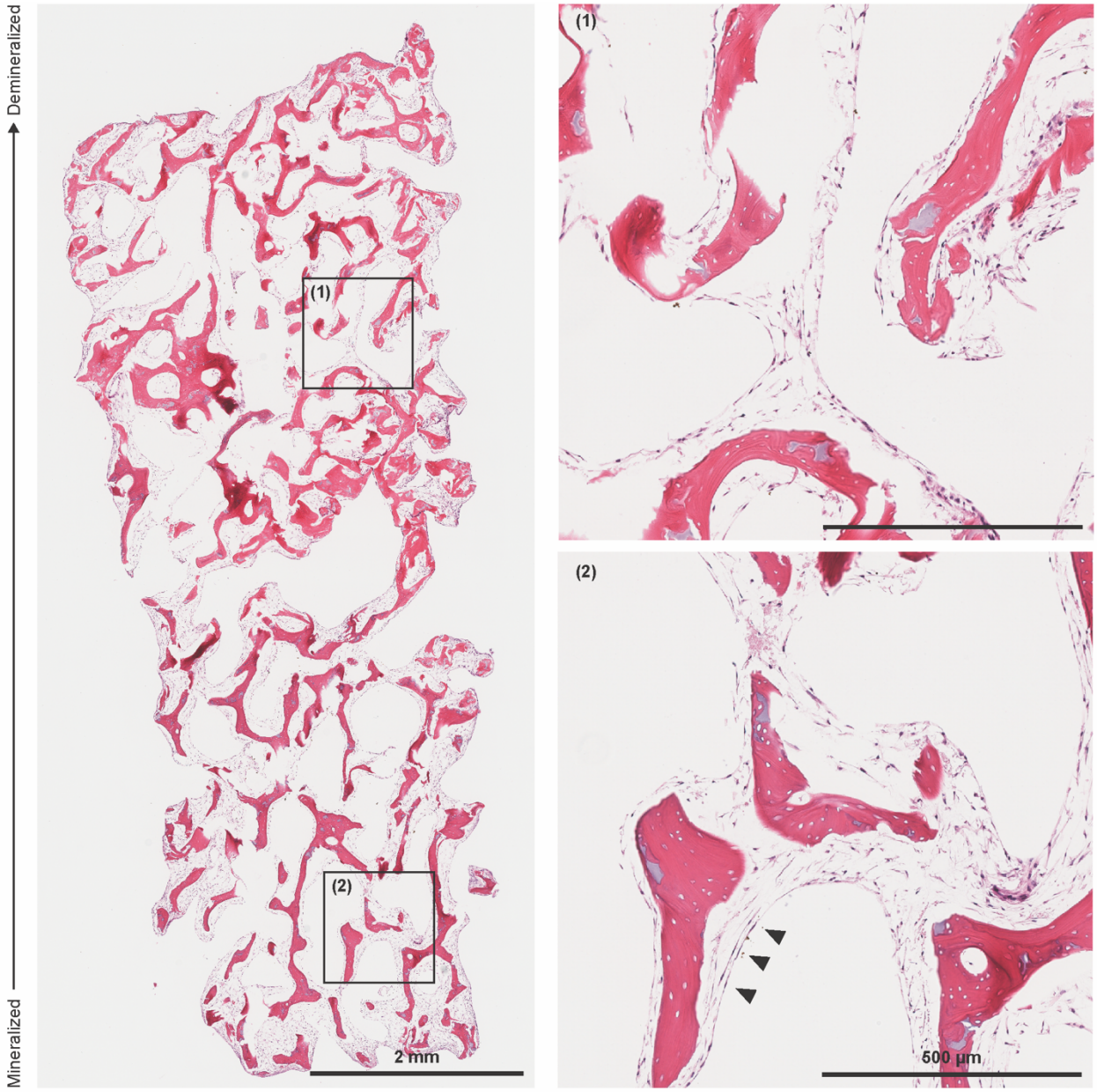

Figure 4.S10. Hematoxylin and eosin stain of scaffold seeded with MSCs and cultured for 4 days. (1) Demineralized region of scaffold, showing MSCs with rounded phenotypes. (2) Mineralized region of scaffold, showing MSCs elongated along edges of scaffold. Arrows indicate elongated cells in mineralized region of scaffold.

Movie 4.1. Movie of µCT scan, showing mineralization front using data shown in Figure 2.

References

(1) Kataoka, K.; Harada, A.; Nagasaki, Y. Block Copolymer Micelles for Drug Delivery: Design, Characterization and Biological Significance. *Adv. Drug Deliv. Rev.* **2012**, *64*

(SUPPL.), 37–48.

(2) Murphy, S. V.; Atala, A. 3D Bioprinting of Tissues and Organs. *Nat. Biotechnol.* **2014**, *32* (8), 773–785.

(3) Pham, Q. P.; Sharma, U.; Mikos, A. G. Electrospinning of Polymeric Nanofibers for Tissue Engineering Applications: A Review. *Tissue Eng.* **2006**, *12* (5), 1197–1211.

(4) Voytik-Harbin, S. L.; Brightman, A. O.; Kraine, M. R.; Waisner, B.; Badylak, S. F. Identification of Extractable Growth Factors from Small Intestinal Submucosa. *J. Cell. Biochem.* **1997**, *67* (4), 478–491.

(5) Badylak, S. F.; Tullius, R.; Kokini, K.; Shelbourne, K. D.; Klootwyk, T.; Voytik, S. L.; Kraine, M. R.; Simmons, C. The Use of Xenogeneic Small Intestinal Submucosa as a Biomaterial for Achille's Tendon Repair in a Dog Model. *J. Biomed. Mater. Res.* **1995**, *29* (8), 977–985.

(6) Badylak, S.; Kokini, K.; Tullius, B.; Simmons-Byrd, A.; Morff, R. Morphologic Study of Small Intestinal Submucosa as a Body Wall Repair Device. *J. Surg. Res.* **2002**, *103* (2), 190–202.

(7) Badylak, S. F.; Lantz, G. C.; Coffey, A.; Geddes, L. A. Small Intestinal Submucosa as a Large Diameter Vascular Graft in the Dog. *J. Surg. Res.* **1989**, *47* (1), 74–80.

(8) Gruskin, E.; Doll, B. A.; Futrell, F. W.; Schmitz, J. P.; Hollinger, J. O. Demineralized Bone Matrix in Bone Repair: History and Use. *Adv. Drug Deliv. Rev.* **2012**, *64* (12), 1063–1077.

(9) Finkemeier, C. G. Bone-Grafting and Bone-Graft Substitutes. *J. Bone Jt. Surg.* **2002**, *84–A* (3), 454–464.

(10) Boys, A. J.; McCorry, M. C.; Rodeo, S. A.; Bonassar, L. J.; Estroff, L. A. Next Generation Tissue Engineering of Orthopedic Soft Tissue-to-Bone Interfaces. *MRS Commun.* **2017**, *7*

(3), 289–308.

(11) Bonnevie, E. D.; Mauck, R. L. Physiology and Engineering of the Graded Interfaces of Musculoskeletal Junctions. *Annu. Rev. Biomed. Eng.* **2018**, *20*, 405–431.

(12) Lu, H. H.; Thomopoulos, S. Functional Attachment of Soft Tissues to Bone: Development, Healing, and Tissue Engineering. *Annu. Rev. Biomed. Eng.* **2013**, *15*, 201–226.

(13) Weiner, S.; Wagner, H. D. THE MATERIAL BONE: Structure-Mechanical Function Relations. *Annu. Rev. Mater. Sci.* **1998**, *28*, 271–298.

(14) Reznikov, N.; Shahar, R.; Weiner, S. Bone Hierarchical Structure in Three Dimensions. *Acta Biomater.* **2014**, *10*, 3815–3826.

(15) Reznikov, N.; Bilton, M.; Lari, L.; Stevens, M. M.; Kröger, R. Fractal-like Hierarchical Organization of Bone Begins at the Nanoscale. *Science (80-.).* **2018**, *360* (6388), eaao2189.

(16) Yang, P. J.; Temenoff, J. S. Engineering Orthopedic Tissue Interfaces. *Tissue Eng. Part B. Rev.* **2009**, *15* (2), 127–141.

(17) Font Tellado, S.; Rosado Balmayor, E.; Van Griensven, M. Strategies to Engineer Tendon/Ligament-to-Bone Interface: Biomaterials, Cells and Growth Factors. *Adv. Drug Deliv. Rev.* **2015**, 1–15.

(18) Mente, P. L.; Lewis, J. L. Elastic Modulus of Calcified Cartilage Is an Order of Magnitude Less than That of Subchondral Bone. *J. Orthop. Res.* **1994**, *12* (5), 637–647.

(19) Abraham, A. C.; Haut Donahue, T. L. From Meniscus to Bone: A Quantitative Evaluation of Structure and Function of the Human Meniscal Attachments. *Acta Biomater.* **2013**, *9* (5), 6322–6329.

(20) Goldring, M. B.; Tsuchimochi, K.; Ijiri, K. The Control of Chondrogenesis. *J. Cell.*

Biochem. **2006**, *97* (1), 33–44.

(21) He, F.; Chiou, A. E.; Loh, H. C.; Lynch, M.; Seo, B. R.; Song, Y. H.; Lee, M. J.; Hoerth, R.; Bortel, E. L.; Willie, B. M.; et al. Multiscale Characterization of the Mineral Phase at Skeletal Sites of Breast Cancer Metastasis. *Proc. Natl. Acad. Sci.* **2017**, 201708161.

(22) Choi, S.; Friedrichs, J.; Hye, Y.; Werner, C.; Estroff, L. A.; Fischbach, C. Intrafibrillar, Bone-Mimetic Collagen Mineralization Regulates Breast Cancer Cell Adhesion and Migration. *Biomaterials* **2018**, *10*, 1–12.

(23) Spalazzi, J. P.; Doty, S. B.; Moffat, K. L.; Levine, W. N.; Lu, H. H. Development of Controlled Matrix Heterogeneity on a Triphasic Scaffold for Orthopedic Interface Tissue Engineering. *Tissue Eng.* **2006**, *12* (12), 3497–3508.

(24) Ma, J.; Smietana, M. J.; Kostrominova, T. Y.; Wojtys, E. M.; Larkin, L. M.; Arruda, E. M. Three-Dimensional Engineered Bone–Ligament–Bone Constructs for Anterior Cruciate Ligament Replacement. *Tissue Eng. Part A* **2012**, *18* (1–2), 103–116.

(25) Font Tellado, S.; Bonani, W.; Rosado Balmayor, E.; Föhr, P.; Motta, A.; Migliaresi, C.; van Griensven, M. Fabrication and Characterization of Biphasic Silk Fibroin Scaffolds for Tendon/Ligament-to-Bone Tissue Engineering. *Tissue Eng. Part A* **2017**, *23* (15–16), 859–872.

(26) Liu, W.; Lipner, J.; Xie, J.; Manning, C. N.; Thomopoulos, S.; Xia, Y. Nano Fiber Scaffolds with Gradients in Mineral Content for Spatial Control of Osteogenesis. *ACS Appl. Mater. Interfaces* **2014**, *6*, 2842–2849.

(27) Lin, H.; Lozito, T. P.; Alexander, P. G.; Gottardi, R.; Tuan, R. S. Stem Cell-Based Microphysiological Osteochondral System to Model Tissue Response to Interleukin-1 β. *Mol. Pharm.* **2014**, *11*, 2203–2212.

(28) Lipner, J.; Liu, W.; Liu, Y. X.; Boyle, J.; Genin, G. M.; Xia, Y.; Thomopoulos, S. The

Mechanics of PLGA Nanofiber Scaffolds with Biomimetic Gradients in Mineral for Tendon-to-Bone Repair. *J. Mech. Behav. Biomed. Mater.* **2014**, *40*, 59–68.

(29) Zhu, C.; Qiu, J.; Pongkitwitoon, S.; Thomopoulos, S.; Xia, Y. Inverse Opal Scaffolds with Gradations in Mineral Content for Spatial Control of Osteogenesis. *Adv. Mater.* **2018**, *30* (1706706), 1–7.

(30) Quan, B. D.; Sone, E. D. Structural Changes in Collagen Fibrils across a Mineralized Interface Revealed by Cryo-TEM. *Bone* **2015**, *77*, 42–49.

(31) McCorry, M. C.; Mansfield, M. M.; Sha, X.; Coppola, D. J.; Lee, J. W.; Bonassar, L. J. A Model System for Developing a Tissue Engineered Meniscal Enthesis. *Acta Biomater.* **2016**, *56*, 110–117.

(32) Iannucci, L. E.; Boys, A. J.; McCorry, M. C.; Estroff, L. A.; Bonassar, L. J. Cellular and Chemical Gradients to Engineer the Meniscus-to-Bone Insertion. *Adv. Healthc. Mater.* **2018**, *1800806*, 1–10.

(33) Schindelin, J.; Arganda-carreras, I.; Frise, E.; Kaynig, V.; Longair, M.; Pietzsch, T.; Preibisch, S.; Rueden, C.; Saalfeld, S.; Schmid, B.; et al. Fiji : An Open-Source Platform for Biological-Image Analysis. *Nat. Methods* **2012**, *9* (7), 676–682.

(34) Talari, A. C. S.; Zanyar, M.; Rehman, S.; Rehman, I. U. Raman Spectroscopy of Biological Tissues. *Appl. Spectrosc. Rev.* **2015**, *50*, 46–111.

(35) Nicoletti, A.; Torricelli, P.; Bigi, A.; Fornasari, P.; Fini, M.; Moroni, L. Incorporation of Nanostructured Hydroxyapatite and Poly(N -Isopropylacrylamide) in Demineralized Bone Matrix Enhances Osteoblast and Human Mesenchymal Stem Cell Activity. *Biointerphases* **2015**, *10* (4), 041001.

(36) Junqueira, L. C.; Bignolas, G.; Brentani, R. R. Picrosirius Staining plus Polarization Microscopy, a Specific Method for Collagen Detection in Tissue Sections. *Histochem. J.*

1979, *11*, 447–455.

(37) Rich, L.; Whittaker, P. Collagen and Picrosirius Red Staining: A Polarized Light Assessment of Fibrillar Hue and Spatial Distribution. *Brazilian J. Morphol. Sci.* **2005**, *22* (2), 97–104.

(38) Dayan, D.; Hiss, Y.; Hirshberg, A.; Bubis, J. J.; Wolman, M. Are the Polarization Colors of Picrosirius Red-Stained Collagen Determined Only by the Diameter of the Fibers? *Histochemistry* **1989**, *93*, 27–29.

(39) Grayson, W. L.; Fröhlich, M.; Yeager, K.; Bhumiratana, S.; Chan, M. E.; Cannizzaro, C.; Wan, L. Q.; Liu, X. S.; Guo, X. E.; Vunjak-Novakovic, G. Engineering Anatomically Shaped Human Bone Grafts. *Proc. Natl. Acad. Sci. U. S. A.* **2010**, *107* (8), 3299–3304.

(40) Grayson, W. L.; Bhumiratana, S.; Grace Chao, P. H.; Hung, C. T.; Vunjak-Novakovic, G. Spatial Regulation of Human Mesenchymal Stem Cell Differentiation in Engineered Osteochondral Constructs: Effects of Pre-Differentiation, Soluble Factors and Medium Perfusion. *Osteoarthr. Cartil.* **2010**, *18* (5), 714–723.

(41) Grayson, W. L.; Bhumiratana, S.; Cannizzaro, C.; Chao, P. G.; Lennon, D. P.; Caplan, A. I.; Vunjak-Novakovic, G. Effects of Initial Seeding Density and Fluid Perfusion Rate on Formation of Tissue-Engineered Bone. *Tissue Eng. Part A* **2008**, *14* (11), 1809–1820.

(42) Schwartz, A. G.; Pasteris, J. D.; Genin, G. M.; Daulton, T. L.; Thomopoulos, S. Mineral Distributions at the Developing Tendon Enthesis. *PLoS One* **2012**, *7* (11), 1–11.

(43) Deymier-Black, A. C.; Pasteris, J. D.; Genin, G. M.; Thomopoulos, S. Allometry of the Tendon Enthesis: Mechanisms of Load Transfer Between Tendon and Bone. *J. Biomech. Eng.* **2015**, *137* (11), 111005.

(44) Deymier, A. C.; An, Y.; Boyle, J. J.; Schwartz, A. G.; Birman, V.; Genin, G. M.; Thomopoulos, S.; Barber, A. H. Micro-Mechanical Properties of the Tendon-to-Bone

Attachment. *Acta Biomater.* **2017**, *56*, 25–35.

(45) Mao, A. S.; Shin, J. W.; Mooney, D. J. Effects of Substrate Stiffness and Cell-Cell Contact on Mesenchymal Stem Cell Differentiation. *Biomaterials* **2016**, *98*, 184–191.

(46) Chaudhuri, O.; Gu, L.; Klumpers, D.; Darnell, M.; Bencherif, S. A.; Weaver, J. C.; Huebsch, N.; Lee, H. P.; Lippens, E.; Duda, G. N.; et al. Hydrogels with Tunable Stress Relaxation Regulate Stem Cell Fate and Activity. *Nat. Mater.* **2016**, *15* (3), 326–334.

CHAPTER 5

Introducing Engineering Design and Materials Science at an Earlier Age through Ceramic Cold Casting[6]

Abstract

Elementary and middle school science curriculums typically focus on generating an interest in science and engineering through the use of hands-on activities that demonstrate specific concepts. Laboratory activities designed in this manner often circumvent some of the main challenges that engineers and scientists face, namely balancing advantages and disadvantages for a variety of potential solutions to solve a specific problem. This activity was designed to show students that different solutions for a given problem can exist, and engineers must manage priorities when choosing the best solution. This laboratory involves cold casting ceramics slurries with varying viscosities into a mold. The resulting casts have a varying final density, controlled by the initial viscosity. Students are presented with different outcome measures regarding the objects they cast: ease of manufacturing, cost, aesthetics, and mechanical properties. Based on the laboratory design, no single cast will perform the best in any of these categories. The students are then asked to choose the best mold, and justify their answers based on the initial problem presented to them by balancing which outcome measures they consider to be important for solving this specific problem. This laboratory teaches basic science concepts like viscosity and density, while addressing common industrial manufacturing issues, such as cost and ease of manufacturing. Through a combination of these features, this laboratory introduces engineering and design concepts using the scientific method to students at an earlier age.

[6] This chapter has been published: Boys, A. J., Walsh, M. C., *J. Chem. Educ.*, **96** 1, 104-109 (2019).

Introduction

Engineers and scientists are often presented with multiple solutions when approaching specific design and engineering problems. Part of the process for solving such problems is understanding the specifics and appropriately balancing advantages and disadvantages for particular solutions. Despite being one of the main obstacles that engineers and scientists face and a necessity for the implementation and application of any scientific principle, the balancing of solutions is typically only lightly addressed in primary and middle school science, technology, engineering, and mathematics (STEM) education.[1,2] Due to the importance of this concept, various organizations have committed to integrating engineering design into the structure of science education.[3–5] To directly address the application of design principles in the classroom, we have developed a laboratory activity using an inquiry-based learning approach where students are presented with a series of possible solutions to a given problem, each with conflicting advantages and disadvantages, requiring students to choose factors they think are most important for a specified application.

Our laboratory introduces manufacturing processes and uses this framework to place students into the mindset of industrial engineers and scientists. Manufacturing processes, while an incredibly important part of science and engineering, are not typically addressed in early-stage curricula. While various experiments use inquiry-based learning to examine scientific and engineering concepts,[6–15] a dearth of classroom activities exist that focus on manufacturing, particularly for early stage students.[6,16] The laboratory experiment presented here utilizes casting, one of the oldest methods of materials manufacturing, dating back to 4000 BCE.[17] Casting is also a common industrial technique for producing a wide variety of objects from jewelry to engine blocks. Given all these factors, casting provides an effective means for introducing students to materials science, design, and engineering.

Casting is typically performed by melting a given material and pouring that material into a mold to reform it in a specific shape. To avoid the use of the high temperatures required for casting materials such as metals, this experiment uses cold or evaporative casting, a technique often used for casting ceramic materials, such as coffee mugs or other ceramics. Cold casting relies on a colloid or slurry, where small particles are suspended in a liquid. The slurry is poured into a mold, where the liquid component of the slurry evaporates. As evaporation occurs, the particles are pulled towards each other through surface tension, resulting in a densification of the particles into a solid object. The resulting cast is often heated or fired to promote further densification through sintering. Certain materials, such as Plaster of Paris, will result in a somewhat robust object without requiring the firing step of the casting process. Plaster of Paris, calcium sulfate hemihydrate ($CaSO_4 \bullet ½H_2O$), will form into gypsum ($CaSO_4 \bullet 2H_2O$), a hard, ceramic material, when mixed with water.[18] Plaster of Paris, usage of which dates back to the Ancient Egyptians,[19] is also non-toxic and inexpensive, making it ideal for use in a classroom. The wide usage of casting as an industrial process and its ease of implementation in a classroom, make casting an ideal manufacturing process to target for introducing engineering concepts to students at an earlier age.

Various factors affect the overall outcome of any manufacturing process. Specifically, the ability of a given material to be cast relies on the viscosity of the material prior to casting, in this case the viscosity of the slurry. Lower viscosity slurries are more likely to fill the mold that they are poured into but have a lower final density as a result of the increased volume of water, causing lessened densification. High viscosity slurries will result in a denser, stronger object but are less likely to adequately take the shape of the mold. Slurry viscosity can be controlled by varying the amount of water that is added to a specific mass of ceramic powder. Beyond viscosity, other factors that are necessary to address in any industrial setting are the cost of the manufacturing process and the quality of the resulting object.

In this experiment, students cast three Plaster of Paris stars using cookie cutters placed on aluminum foil as molds. The three stars have different densities controlled by varying the volume of water mixed with a specific mass of Plaster of Paris. Given that the initial mass of the Plaster of Paris remains the same for each star, the resulting density of the star is only controlled by the volume of water added to produce the slurry. These varying densities provide each star with different properties. Students will learn about viscosity, they will directly calculate the density of each object they make, and they will balance a variety of other outcomes measures, such as strength, cost, and ease of manufacturing or processability, to choose which star they think is the best based on the specified design problem.

Experimental Overview

This laboratory was targeted at introducing engineering and design concepts to younger students. Initially, to identify which age groups were appropriate for this laboratory, we examined Next Generation Science Standards (NGSS), a set of K-12 science content standards widely recognized across the United States, determining that students in grades 3 through 12 would be the most appropriate group for demonstrating these concepts.[3,20] This laboratory primarily covers standards focusing on engineering design. Additionally, this activity involves the physical sciences, emphasizing the difference between a chemical and physical change. Specifically, this laboratory fits the following NGSS standards: 3-5-ETS1-1, 3-5-ETS1-2, 3-5-ETS1-3, 5-PS1-4, MS-ETS1-2, HS-ETS1-1 (text for standards can be found in Supplemental Information).[3]

Laboratory Design

The casting laboratory was designed and tested to determine appropriate material, volume, and mass for casting objects with varying densities (Box 1). Laboratory testing determined that the low density star had the best aesthetic qualities, was easiest to manufacture, but was also the most likely to break at lower drop heights. The high density star was the strongest, but had the poorest

aesthetics and was difficult to manufacture. The medium density star fell between the other two stars in all categories. The results vary based on the students' ability to make the stars, thus emphasizing processability. Based on these results, documentation for this laboratory was written, including a module for explaining the activity to teachers, a laboratory sheet to guide students through the activity, and an analysis sheet for students to assess their findings and record their final recommendation from the activity. An alternative analysis sheet was also written for students to perform density calculations (Supplemental Information). This sheet was not implemented in the classroom during our study. Using this documentation, the laboratory was demonstrated by the authors at a local middle school in Ithaca, NY and at a STEM teacher workshop in New York City to assess the feasibility of performing this laboratory in a classroom setting and to receive verbal feedback from teachers and students to improve the laboratory.

Box 1. Summary of Casting Laboratory

Preparing Casts: Students measure 50 g of Plaster of Paris into three beakers. Varying amounts of water (35 mL, 30 mL, and 25 mL) generate three groups: low density, medium density, and high density, respectively. The students create three slurries and pour the mixtures into the molds. They record observations regarding the processability for each slurry (difficulty in pouring, ability of slurry to fill the mold, amount of material lost, etc.) and record the thickness of the slurry in the mold. Casts are left at room temperature for at least 24 hours to dry.

Poured Casts for each group:

Low Density | Medium Density | High Density

Sample Testing: Students remove casts from molds and measure the thickness and mass for each sample. Using the change in thickness and the mass, students can calculate the density for each sample and hypothesize which star will be the strongest. Then, students drop the samples from increasing heights, beginning at 5 cm, to determine the strength of each sample group. Sample failure is considered the loss of at least one point of the star.

Failed samples for each group:

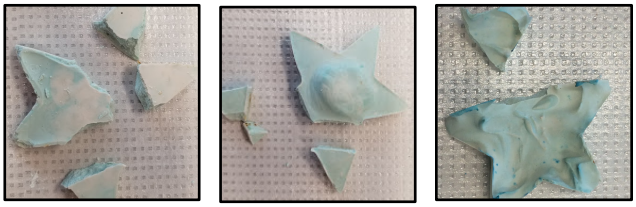

Low Density | Medium Density | High Density

Analysis: Students record observations with regard to the different groups (ease of removal from mold, aesthetic quality, relative strength, etc.). Then, they calculate the cost for producing samples for each group, using a provided cost per mL of water and cost per gram of Plaster of Paris. Lastly, the students make a recommendation for the most appropriate group by analyzing the following factors: cost, strength, ease of production, appearance, and amount of material lost during production.

Data Analysis

Responses from the student surveys were recorded and analyzed in MATLAB and IBM SPSS software. Ambiguous responses or incomplete responses were not included in results (n = 3 at School 2 and n = 1 at School 3). Cronbach's alpha was calculated for the responses with regard to each school to determine the reliability of the student survey responses.

Hazards

Plaster of Paris is a powder and therefore can be an inhalation concern. Additionally, students should avoid placing body parts inside of the plaster mixture, as mixing of Plaster of Paris and water is exothermic. General laboratory safety practices should be observed, as in any laboratory setting. Plaster of Paris should not be disposed of in a drain, as the plaster may solidify and clog the drain.

Results

The student survey responses were quantified (1 - Disagree, 2 - Somewhat Disagree, 3 - Neither Agree nor Disagree, 4 - Somewhat Agree, 5 - Agree) and used to determine the success of the laboratory. 'Somewhat Agree' and 'Agree' were considered a success for each question. Overall response was successful, with 95.4 % of students saying they enjoyed the activity, 87.0 % of students saying that they understand what viscosity is, 82.4 % of students saying that they have a better understanding of how engineers design products, and 85.2 % of students saying that they understand what casting is and how it would be used (Figure 5.1). The mean of the average response from the student survey was found to be 4.4 +/- 0.5 (Figure 5.2), indicating an overall positive response from the students to the laboratory. We performed a Cronbach's alpha to test the reliability of the survey questions. Our reliability for the 5 questions was 0.731, which is acceptable. The teacher survey responses were also recorded (Figure 5.3). Two of the three teachers found the

activity to be positive for all categories, whereas the third teacher's response varied depending on the question.

Discussion

We implemented a laboratory activity for introducing engineering design concepts through materials science to middle school students. Students were required to assess which cast they believed to be best for the posed application according to a set of criteria. The laboratory was

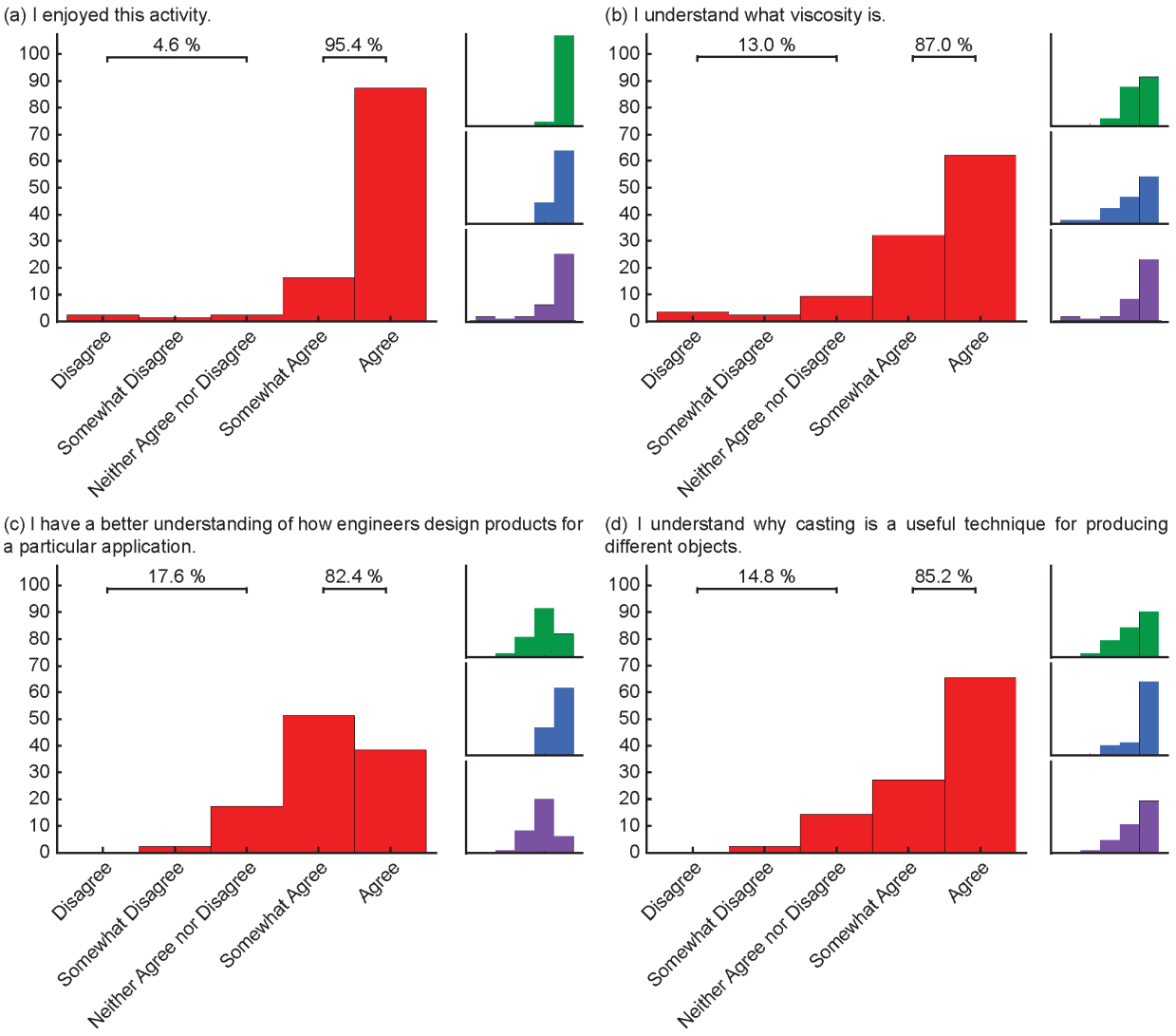

Figure 5.1 Student survey questions with accompanying histograms of responses **a – d**. Overall response (red, n = 108), School 1 response (green, n = 29), School 2 response (blue, n = 32), School 3 response (purple, n = 47). Brackets indicate percent positive and percent negative responses for each question, where Agree and Somewhat Agree were considered positive and Neither Agree nor Disagree, Somewhat Disagree, and Disagree were considered negative.

designed such that none of the possible sample groups performed best for all criteria. The purpose of this design was meant to cause students to decide which categories they considered most important for the provided application. Such an analysis is more representative of that which would be used by an engineer or scientist in a research lab or company. We included realistic evaluative categories such as cost and ease of manufacturing to introduce some engineering concepts that are not typically considered in a science curriculum. The students also gauged strength, thus providing a functional measurement for their evaluative analysis. We grounded these parameters in scientific concepts such as density and viscosity to show the students the usefulness of applying these concepts to product development and design.

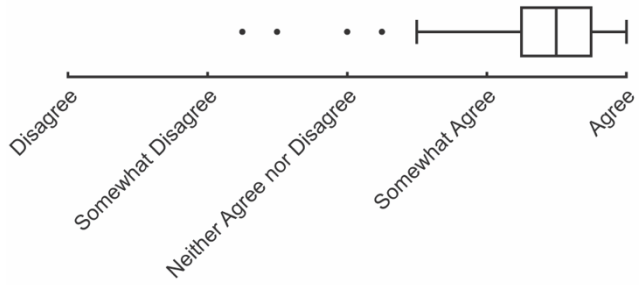

Figure 5.2 Box plot of mean response of all questions for students from student survey. Values were collected per student as an average of each student's response to all questions in the survey (1 - Disagree, 2 - Somewhat Disagree, 3 - Neither Agree nor Disagree, 4 - Somewhat Agree, 5 - Agree).

Using casting as a template, students were guided through a realistic engineering design problem, which generates an effective inquiry-based learning activity. Inquiry-based learning necessitates activities that require students to think through problems,[21] which was effectively implemented in this casting laboratory. Various educational organizations emphasize critical thinking and communication skills as essential for postsecondary success and citizenship.[3,5] The concepts and skills introduced in this laboratory act to strengthen student's understanding of inquiry-based science, which has been shown to enhance students' understanding and retention of content.[22] This activity presents a scenario for the students with an open-ended question, where they have to conduct an experiment, collect various pieces of qualitative and quantitative information, and dictate a judgement based on the data they collected. Students were able to recognize the different qualities of the casts based on their experience in the manufacturing portion

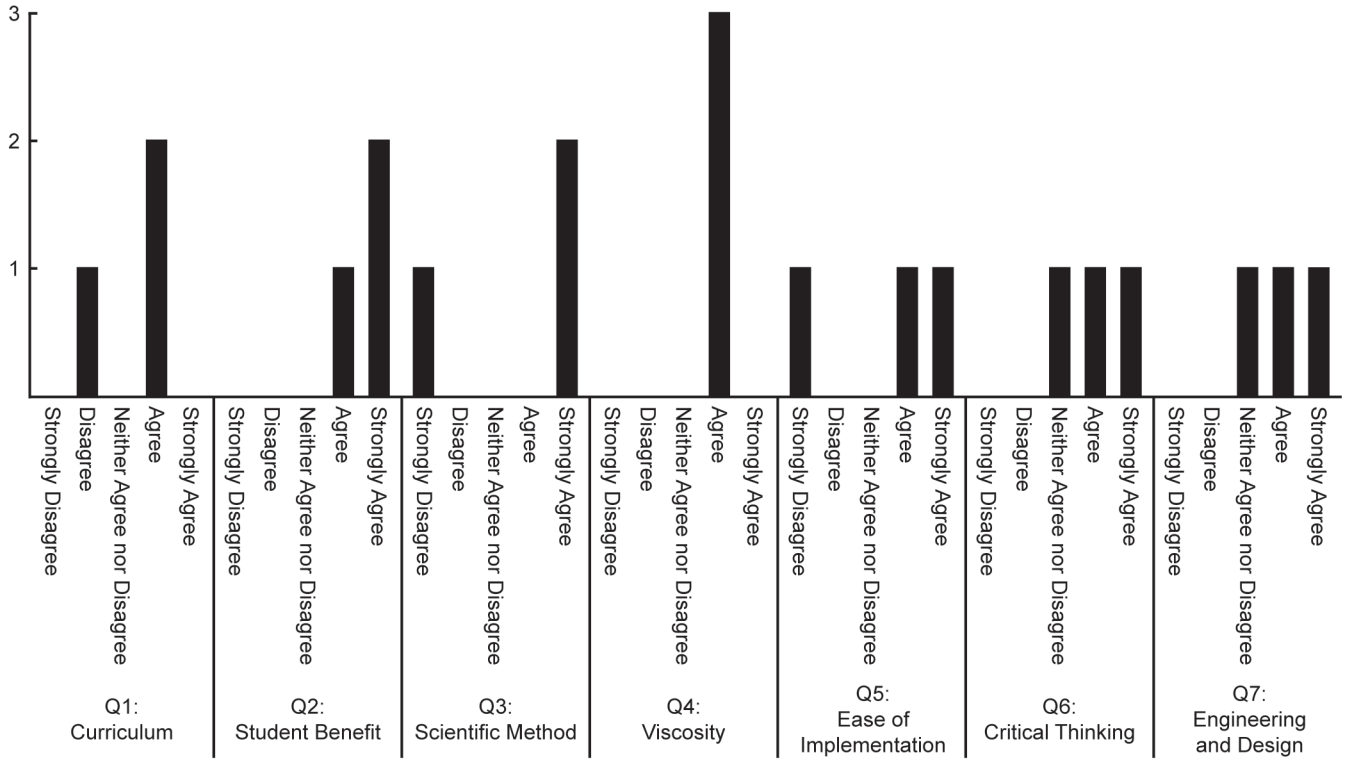

Figure 5.3 Teacher survey responses (n = 3, one per school).

of the laboratory. Teachers received a variety of different responses based on what the students felt was important, indicating that students thought through their design solutions. For example, one student recommended the medium density star stating, "I would recommend [the medium density star] because it's almost the strongest and it was quite easy to make. Also it wasn't the most expensive." Students are asked to use critical thinking skills to determine which evidence is most important for the given problem and to communicate their conclusion based on this evidence. These skills are crucial to prepare students for successful careers.

Based on the results of our survey, the students enjoyed the activity, which will ideally encourage their pursuit of scientific and engineering career paths throughout the remainder of their education. The survey also assessed the students' understanding of viscosity, design, and casting as a manufacturing process, all of which had positive results (Figure 5.1 and Figure 5.2). Teacher feedback was also generally positive, with two of the three teachers responding positively to all

questions (Figure 5.3). One teacher commented, “Very cool lab. The students loved making casts and testing them.” The last teacher was less satisfied with the laboratory and found the lab difficult to clean up given that it was implemented in four back-to-back classes. In the future, pre-measuring of the Plaster of Paris prior to the lab may reduce any difficulty associated with students measuring the Plaster of Paris, providing more time to focus on preparation and other concepts in the activity. The laboratory was written with two possible assessments for the students, one targeted at classrooms with more advanced mathematical backgrounds. The challenging assessment included the density calculation referenced in the procedure (Box 1). While the addition of density as a concept greatly benefits the students’ ability to understand the cold casting process and predict the results of the mechanical testing, the density calculation also requires more advanced calculations. For this reason, the challenging assessment was not implemented at the three schools involved in the survey. We feel that teachers may feel more comfortable implementing these equations after having performed the activity at least once.

Conclusion

We designed and implemented a laboratory that introduces engineering and design using materials engineering. Based on student response, the laboratory was successful at introducing these concepts through an enjoyable lab with scientific value. We provide teachers with a hands-on, inquiry-based laboratory emphasizing concepts that extend into professional engineering and scientific fields. Through use of this laboratory, we hope to instill in students a greater understanding of engineering and science and to promote these fields to students who are interested in pursuing scientific careers.

Supplemental Information

Supplemental information includes the Casting Laboratory Module, Casting Laboratory, Casting Laboratory Student Analysis, and Casting Laboratory Student Analysis – Challenging.

Casting

Author(s): Alexander Boys & Mark Walsh

Date Created: 2015

Subject: Physics

Grade Level: Upper Elementary/Middle School/High School

Standards: Next Generation Science Standards (www.nextgenscience.org)

3-5-ETS1-1 Define a simple design problem reflecting a need or a want that includes specified criteria for success and constraints on materials, time, or cost.

3-5-ETS1-2 Generate and compare multiple possible solutions to a problem based on how well each is likely to meet the criteria and constraints of the problem.

3-5-ETS1-3 Plan and carry out fair tests in which variables are controlled and failure points are considered to identify aspects of a model or prototype that can be improved.

5-PS1-4 Conduct an investigation to determine whether the mixing of two or more substances results in new substances.

MS-ETS1-2 Evaluate competing design solutions using a systematic process to determine how well they meet the criteria and constraints of the problem.

HS-ETS1-1 Analyze a major global challenge to specify qualitative and quantitative criteria and constraints for solutions that account for societal needs and wants.

Schedule: 2 - 1 hour classes

CCMR Lending Library Connected Activities:

Objectives:	**Vocabulary:**
Students will learn about the manufacturing process of casting. They will create their own casts, test them for strength, and analyze different factors to see which is most practical. They will learn some concepts associated with casting and the various ways this process is used. Students will also reconcile competing design and engineering principles to understand that the majority of engineering problems require an assessment of tradeoffs.	Casting Mold Density Viscosity Flow Friction
Students Will: * Learn the basics of casting and see some examples of what it is used for. * Understand and define the concepts of density and viscosity. * Cast Plaster of Paris into molds. * Take measurements to calculate the density of the mold. * Demonstrate their findings in writing. * Analyze different variables to see which mold is the most practical to use. * Perform an assessment of design tradeoffs to choose the best casting procedure.	**Materials:** **For Each Group (2-4 students)** Popsicle Stick Measuring Cylinder 3 Cookie Cutters Aluminum Foil **For Class** Plaster of Paris Balance Scale **For Teacher** SDS for Plaster of Paris ***Provided by Teacher*** Rulers Meter sticks Beakers or Cups
Safety	Please refer to SDS sheet for Plaster of Paris before using. Be sure to throw away any excess plaster in the garbage. Do not pour down sink as it will solidify in drain.

Science Content for the Teacher:

Casting is a common industrial method used for producing objects for many different industries. Casting is a processing technique where the desired material is melted or suspended in liquid, then poured into a mold and allowed to solidify. Casting is used to produce many different objects including jewelry, candy, mugs, and even engine blocks in cars. Metals, are often cast by melt casting, which requires very high temperatures, ~1000-3000˚F, much higher temperatures than many materials can be exposed to (ovens can only reach temperatures of ~900˚F). Ceramics are also frequently cast but usually by cold casting (the process that will be used in this lab). This technique involves suspending a powder of the ceramic material in a liquid (usually water) and pouring it into the mold. As the suspension sits in the mold, water evaporates out, and the ceramic particles are pulled together. Once the cast has dried, it is often heated to allow the particles to fuse together into a stronger structure. However, some materials, such as Plaster of Paris, do not require this heating step and will produce a strong structure at room temperature. The ability of a material to be cast, is largely based on its viscosity. Viscosity is a measure of a liquid's ability to "flow." In the case of ceramic suspensions, the viscosity is related to the ratio of solid:liquid in the mixture. If too little water is added to the mixture, the suspension will be too viscous to fill the mold it is poured into. If too much water is added to the mixture, the ceramic particles have farther to move as they are pulled together during the evaporation of the water, resulting in a structure with a lower density. Density is measured in terms of mass per unit volume. Often, we think of the density of a material as the weight of the atoms in material divided by the area they take up. However, at larger scales, an object's density can be a function of the amount of empty space contained within the structure as pores. In this lab, the second definition describes the density we have control over. In particular, the density can affect the strength of the object in question.

This laboratory is targeted at introducing engineering and design concepts to students at an earlier age. Introductory science curriculums often involve determining a concrete answer to a scientific question. However, engineering problems rarely have a single solution and frequently require the engineer or scientist to balance a number of positive and negative qualities to produce the best solution. In this activity, the students will cast different mixes of Plaster of Paris into a cookie cutter mold as a small-scale example of casting. The resulting casts will have a variety of properties, none of which are solely the best for the specified parameters. The students will need to determine which properties they think are most important to produce the best cast given the design criteria. Through this activity, the students will learn to balance competing design solutions, providing insight into engineering and design principles.

Another key component in manufacturing is the cost of materials. This lab involves the calculation of the cost for each of the casts that are produced. The costs of water and Plaster of Paris are typically a fraction of a cent for the amounts being used. This lab has been designed using inflated costs to make calculations easier for students. However, current costs can be used to make the lab more realistic.

Preparation:

Set out materials for groups to prepare casts.
Choose which analysis you want to use with your class ('challenging' analysis requires your students to calculate the density of the casts).

Classroom Procedure:

Engage
Explain casting to students and show video of slip casting, which is similar to what they will be doing (https://www.youtube.com/watch?v=FZzOTX9Ihqs or https://www.youtube.com/watch?v=eEWIuyeNp2k). Explain the concept of density if this is new to the students. Be sure to differentiate between material density and object density. Perform a demonstration using liquids of different viscosities (honey, syrup, and water), and time how long they move down a ramp or measure the distance each traveled after a certain time. Explain the concept of viscosity.
Discuss engineering as a concept (problem solving-based science). **(Time: 15 mins)**

Explore
Hand out lab sheet and have students review it. Students will prepare their 3 mixtures and pour into the molds. They will let the molds sit for 2 or more days before taking them out and testing them. NOTE: The 25 mL mixture will be very hard to pour. It may need to be scooped in, tapped down, etc. **(Time: 45 mins)**

Perform drop testing after molds have dried. Record results. Perform calculations and make conclusions using analysis sheet. **(Time: 45 mins)**

Explain
Allow students time to discuss casting and viscosity concepts at end of class. Students must also demonstrate their understanding of the presented concepts on the activity sheet. You can show a video on metal casting that shows other applications. **(Time: 15 mins)**

Resources:

"How it's made: Ceramic Slip Casting - YouTube." 2013. 3 Nov. 2015 <https://www.youtube.com/watch?v=FZzOTX9Ihqs>

"Liquid Fire" to Metal Sword in minutes! - A ... - YouTube." 2011. 3 Nov. 2015 <https://www.youtube.com/watch?v=eEWIuyeNp2k>

Assessment:

The following rubric can be used to assess students during each part of the activity. The term "expectations" here refers to the content, process and attitudinal goals for this activity. Evidence for understanding may be in the form of oral as well as written communication, both with the teacher as well as observed communication with other students. Specifics are listed in the table below.

4= exceeds expectations
3= meets expectations consistently
2= meets expectations occasionally
1= not meeting expectations

	Engage	Explore	Explain
4	Shows leadership in the discussion and an understanding of casting and viscosity.	Completes work accurately while providing an explanation for what is observed. Works very well with group.	Provides an in depth explanation of findings. Fills out worksheet clearly.
3	Participates in the discussion and shows an understanding of casting and viscosity.	Completes work accurately and works cooperatively with group.	Provides clear explanation of findings. Fills out worksheet clearly.
2	Contributes to the discussion, but shows little understanding of casting or viscosity.	Works cooperatively with partner, but makes some mistakes with the procedure.	Provides a limited explanation of findings. Fills out some of the worksheet.
1	Does not participate in discussion. Shows no understanding of casting or viscosity.	Has trouble working with partner. Does little to complete the procedure.	Is not clear in explanation of findings. Does not fill out worksheet.

Acknowledgements:

Cornell Center for Materials Research
Lehigh University's Materials Science and Engineering Program
Cornell University's Materials Science and Engineering Program

Which Mixture Produces the Best Cast?

Background Info:
You are a casting technician for a company (Casts 'R Us). Your boss has asked you to find out what mixture of Plaster of Paris and water will produce a cast that not only looks good but that can also survive falls from large distances.

Objective:
Find out which of the 3 mixtures of Plaster of Paris and water gives the best results in terms of aesthetics, endurance, and cost.

Vocabulary:

Viscosity -

_____

_____

Materials:

Plaster of Paris	3 Plastic beakers	Measuring cylinder
Stirring stick	3 Star molds	Aluminum foil
Ruler		

Procedure:
Preparing the Mixtures & Molds:

____ 1) Measure out 60 mL of Plaster of Paris in a beaker.

____ 2) Pour 35 mL of water into the beaker with the Plaster of Paris.

____ 3) Stir the mixture until all of the powder is dissolved in the water.

____ 4) Measure the ***volume*** of your mixture and record this in the table.

____ 5) Place the star mold on a sheet of aluminum foil and pour the mixture into the star mold. Try to get as much of the mixture into the mold as possible. The more you get in, the better your results will be!

____ 6) Measure the ***height/thickness*** of the mixture, using a ruler. Record this in your data table as cast A.

____ 7) Repeat steps 1-6, using 30 mL of water. Record data as cast B.

____ 8) Repeat steps 1-6, using 25 mL of water. Record data as cast C.

____ 9) Look at each star mold and make observations about each mold below.

____ 10) Let the molds sit for two or more days.

Observations:

Which mixture was the hardest to pour?	
Which mixture was the easiest to pour?	
Did all of the mixtures completely fill the mold?	
Did any of the mixtures spill out of the mold?	
Other observations?	

Data Table:

Cast Properties						
Cast	Water (mL)	Mixture Volume (mL)	Mixture Height (cm)	Cast Height (cm)	Cast Mass (g)	Cost ($)
A	35					
B	30					
C	25					

Testing the Castings:

____ 1) Remove the casts from each of the molds. Be sure to keep track of which is which!

____ 2) Measure the ***height*** of each cast. Record in your table.

____ 3) Measure the ***mass*** of each cast. Record in your table.

____ 4) Drop each of the casts from a height of 5 cm. If the star breaks (loses at least one arm), then record the height that you dropped it from. If not, then increase the height by 5 cm and continue dropping the stars increasing heights until they break. Record in the ***Cast Strength*** data table.

____ 5) Get results from 2 other groups and calculate the average break height. Record in table.

____ 6) Record observations you made during the experiment.

____ 7) Calculate the cost for making each cast. Record in cast properties table.

____ 8) Answer the questions in the ***Evaluation*** section in the ***Casting Analysis***.

Data Table:

Cast Strength				
	Break Height (cm)			
Sample	Test 1	Test 2	Test 3	Average
35 mL				
30 mL				
25 mL				

Observations:

Which cast was the easiest to get out of the mold?	
Which cast was the hardest to get out of the mold?	
Which cast looked the best?	
Did any of the mixtures spill out of the mold?	
Other observations?	

Calculate Cost of Each Cast:

If water costs $0.03/mL and the Plaster of Paris cost $0.05/mL, what is the production cost of each star?

formula: cost = (volume of water x 0.03) + (volume of plaster x 0.05)
eg: cost = (50mL x $0.03/mL) + (100 mL x $0.05/mL)
cost = ($1.50) + ($5.00)
cost = $6.50

Cast A	*Cast B*	*Cast C*

Casting Analysis

Evaluation:

Look at the following factors		
Cost of making the cast	Ease of pouring the mixture into the mold	How well the mixture filled the mold
Strength of the cast	Appearance of the cast	Amount of cast waste

Based on what you observed, answer the following questions:

Which star was easiest to make?

_____

Which star lost the least amount of material during casting?

_____

Which star was the best looking?

_____

Which star was the strongest?

_____

Which star is the least expensive?

_____

Which star would you recommend? Why?

_____

_____

What are the most important factors you considered in coming to this conclusion? State and explain the three most important factors.

_____

_____

What is viscosity? Why would a casting engineer be interested in viscosity?

_____

_____

Casting Analysis

Use the data from your results table to make the following calculations. Be sure to show your work and record your answers in the result table. (Remember that 1 mL = 1 cm^3)

Before Casting:

Calculate area of mold (A):

formula: $A = \frac{Vi}{hi}$ *Vi = mixture volume*

hi = mixture height

Cast A	***Cast B***	***Cast C***
Average area (A):		

After Casting:

Calculate volume of cast (Vf):

formula: $Vf = A \times hf$ *A = average area of mold*

hf = cast height

Cast A	***Cast B***	***Cast C***

Calculate density of cast (ρ):

formula: $\rho = \frac{m}{Vf}$ *m = mass of cast*

Vf = volume of cast

Cast A	***Cast B***	***Cast C***

Evaluation:

Look at the following factors		
Cost of making the cast	Ease of pouring the mixture into the mold	How well the mixture filled the mold
Strength of the cast	Appearance of the cast	Amount of cast waste
Density of each cast		

Based on what you observed, answer the following questions:

Which star was easiest to make?

_____

Which star lost the least amount of material during casting?

_____

Which star was the best looking?

_____

Which star was the strongest?

_____

Which star is the least expensive?

_____

Which star would you recommend? Why?

_____

_____

What are the most important factors you considered in coming to this conclusion? State and explain the three most important factors.

_____

_____

Does density correlate with strength? Explain using your results.

_____

_____

What is viscosity? Why would a casting engineer be interested in viscosity?

_____

_____

References

1. Carr, R. L., Bennett IV, L. D. & Strobel, J. Engineering in the K-12 STEM standards of the 50 U.S. States: An analysis of presence and extent. *J. Eng. Educ.* **101,** 539–564 (2012).
2. Schroeder, C. M., Scott, T. P., Tolson, H., Huang, T. & Lee, Y. A Meta-Analysis of National Research : Effects of Teaching Strategies on Student Achievement in Science in the United States. *J. Res. Sci. Teach.* **44,** 1436–1460 (2007).
3. Next Generation Science Standards.
4. Cooper, M. M. Chemistry and the Next Generation Science Standards. *J. Chem. Educ.* **90,** 679–680 (2013).
5. Commission, E. Science With And For Society (Swafs). *Science Education* at <http://ec.europa.eu/research/swafs/index.cfm?pg= policy&lib=education>
6. Mc Ilrath, S. P., Robertson, N. J. & Kuchta, R. J. Bustin' bunnies: An adaptable inquiry-based approach introducing molecular weight and polymer properties. *J. Chem. Educ.* **89,** 928–932 (2012).
7. Marle, P. D. *et al.* CSI-chocolate science investigation and the case of the recipe rip-off: Using an extended problem-based scenario to enhance high school students' science engagement. *J. Chem. Educ.* **91,** 345–350 (2014).
8. Fakayode, S. O., King, A. G., Yakubu, M., Mohammed, A. K. & Pollard, D. A. Determination of Fe content of some food items by Flame Atomic Absorption Spectroscopy (FAAS): A guided-inquiry learning experience in instrumental analysis laboratory. *J. Chem. Educ.* **89,** 109–113 (2012).
9. Koga, N., Kimura, T. & Shigedomi, K. Laboratory inquiry for determining the chemical composition of a component in a daily use detergent: Sodium sesquicarbonate. *J. Chem.*

Educ. **88,** 1309–1313 (2011).

10. Wada, T. & Koga, N. Chemical composition of sodium percarbonate: An inquiry-based laboratory exercise. *J. Chem. Educ.* **90,** 1048–1052 (2013).
11. Prilliman, S. G. An inquiry-based density laboratory for teaching experimental error. *J. Chem. Educ.* **89,** 1305–1307 (2012).
12. Senkbeil, E. G. Inquiry-Based Approach to a Carbohydrate Analysis Experiment. *J. Chem. Educ.* **76,** 80 (1999).
13. Bennett, J. & Forster, T. IR Cards: Inquiry-based introduction to infrared spectroscopy. *J. Chem. Educ.* **87,** 73–77 (2010).
14. Stout, R. P. CO2 Investigations: An Open Inquiry Experiment for General Chemistry. *J. Chem. Educ.* **93,** 713–717 (2016).
15. Hooker, P. D., Deutschman, W. A. & Avery, B. J. The Biology and Chemistry of Brewing: An Interdisciplinary Course. *J. Chem. Educ.* **91,** 336–339 (2014).
16. Hudson, R., Glaisher, S., Bishop, A. & Katz, J. L. From Lobster Shells to Plastic Objects: A Bioplastics Activity. *J. Chem. Educ.* **92,** 1882–1885 (2015).
17. Kalpakjian, S. & Schmid, S. R. *Manufacturing Processes for Engineering Materials*. (Pearson Eduction Inc., 2008).
18. Sirokman, G. Synthesis, Dehydration, and Rehydration of Calcium Sulfate (Gypsum, Plaster of Paris). *J. Chem. Educ.* **91,** 557–559 (2014).
19. Warren, L. E. Chemistry and chemical arts in ancient egypt. II. *J. Chem. Educ.* **1,** 297–302 (1934).
20. National Research Council. *A Framework for K-12 Science Education: Practices, Crosscutting Concepts, and Core Ideas*. (The National Academies Press, 2012).
21. Fortus, D., Reddy, S. & Dershimer, R. C. Design-based science. *Sci. Teach.* **70,** 38–41

(2003).

22. Minner, D. D., Levy, A. J. & Century, J. Inquiry-based science instruction-what is it and does it matter? Results from a research synthesis years 1984 to 2002. *J. Res. Sci. Teach.* **47,** 474–496 (2010).

GENERAL CONCLUSIONS

Overview

Chapter 1 begins with a review of interfacial systems and the methods by which researchers have attempted to reconstruct these systems. This chapter highlights the instances in the human body, where interfacial structures are located, specifically the entheses, which link tendons, ligaments, and the menisci to bone. These structures are of general interest from a materials perspective, as they typically mediate multiple order of magnitude changes in stiffness. In linking these structures to bone, the enthesis directly allows for the actuation and stabilization of the human body, making them of the utmost importance for basic movement. Further, these structures hold significant clinical relevance, as they are involved in the repair and replacement of damaged orthopedic tissues. Due to their ideal functional properties and their clinical relevance, the entheses are of great interest to clinicians, engineers, and scientists.

Historically, the enthesis has been found to consist of four major regions: bone, calcified and uncalcified fibrocartilage, and the associated ligamentous structure. These regions are constructed *in vivo* through a variety of cell phenotypes, extending from osteoclasts and osteogenic cell types in the bone to fibroblasts in the ligamentous tissue. The calcified and uncalcified fibrocartilaginous tissues are linked through a gradient in mineral content. However, these regions do not fully explain the system, as a mimic of this layout does not result in the inherent properties of the enthesis.

As such, previous work to engineer an enthesis has typically focused tissue engineering as a means of recreating the complex structure that is the enthesis, relying on cells to generate some of the features that are not yet fully understood. In the context of the review, the tissue engineering approach was divided into four major areas: materials selection, cellular contributions, biochemical factors, and construct maturation. For interfacial tissue engineering, these four areas

need to be applied in tandem to the adjacent regions of the interface with a linking of the regions through a gradient. The most successful enthesis engineering attempts have typically used this format, generating a multi-region structure possessing gradients in tissue type between regions. In some cases, studies have resulted in morphologies that resemble the enthesis, but the actual recreation of the entire structure has yet to be achieved. Additionally, the overall structures are still largely derived by cellular maturation, indicating a lack of knowledge in the inherent mechanisms that allow the enthesis to function. This chapter culminates with a list of factors necessary for advancing the field of biological interfacial engineering.

Chapter 2 focuses on the characterization of the native enthesis found at the end of the meniscus. The goal of this chapter was to discover the exact spatial distribution of composition, structure, and mechanics to develop a working structure-function relationship for enthesis engineering. To develop this relationship, Raman microscopy was coupled with confocal elastography to explore these factors at the microscale in a spatially resolved manner.

Raman microscopy provides a means for determining the local composition of a material non-destructively. This type of analysis is beneficial, in that the results can be directly compared to local mechanics, as no alterations need be made to the tissue for analysis. Raman spectra can also be collected in a grid format, providing spatially resolved compositional information. The resulting image from this type of analysis can be further analyzed to develop information about the local structuring of the tissue, thereby providing simultaneous information on the composition and structure of the tissue. These data can be compared to local mechanical information collected through confocal elastography techniques, where a tissue is cyclically strained under a confocal microscope. Videos of the loading cycle can be collected and analyzed to develop spatially resolved maps of the local mechanics of the tissue. As the preparation for both Raman microscopy

and confocal elastography are the same, these data can be compared to develop a structure-function relationship.

Analysis of these data found two compositional regions, five structural regions, and three mechanically-derived regions. The compositional regions show that the enthesis mainly consists of mineralized and unmineralized tissue linked through a mineral gradient. The mineralized tissue possesses three major structures: open trabeculae, consisting of a porous bony region, closed trabeculae consisting of a bony region with smaller pore sizes, and a transitional region, where a continuous mineralized area links the mineralized tissue to the unmineralized tissue. These regions are contained within the mechanically stiff region of the enthesis, where minimal strain is evident during physiological loading. The unmineralized tissue consists of two structural regions: a region consisting of disorganized bundles near the mineralized interface, moving to organized fibers, farther away from the interface. The organized fibers were found to move individually, allowing for large displacements within the soft tissue of the enthesis without localizing strains to the interface between mineralized and unmineralized tissue, resulting in a heterogeneously complaint mechanical region. These fibers unravel within the disorganized bundles region before connecting into the mineralized tissue. The disorganized bundles were found to logarithmically decrease the strain magnitude across this area, resulting in the third and final mechanical region.

Overall, this analysis provided a complete layout of the composition, structure, and mechanics of the enthesis, generating a spatially resolved structure-function relationship. This study also revealed the presence of further mechanical regions within the soft tissue of the enthesis, an area that has not been explored mechanically at the microscale. Further, the generation of this structure-function relationship required the development of a suite of Raman image analysis tools that can be applied to other tissue systems for the development of simultaneous compositional and structural information.

Chapter 3 extends the usage of Raman microscopy for tissue analytics to other orthopedic systems, specifically articular cartilage. Articular cartilage is the soft tissue found lining the ends of long bones within joints. Degeneration of this tissue is heavily associated with the development of diseases like osteoarthritis. The early stages of osteoarthritis are associated with local compositional changes, which often remain undetected clinically due to a lack of a means for detecting these changes without explanting tissue samples for histological analysis. This inability to detect early-stage osteoarthritis reveals the need for a non-destructive, high resolution assessment of cartilage for local composition.

Raman microscopy proved ideal for this type of analysis in the spatially resolved assessment of the enthesis in Chapter 2. However, to apply this technique in the clinic, generalizable composition, such as mineralized or unmineralized, is insufficient to determine the state of the tissue. A value associated the local concentrations of the biomolecules that constitute cartilage is necessary. As such, we developed a method for producing relative measures of the collagen and GAG content in cartilage that trend with standard biochemical assays that also analyze for these components.

To generate measures for collagen and GAG content in cartilage, a linear model was developed and tested using data collected from the cross-section of articular cartilage samples. This area of analysis, the cross-section of articular cartilage, has known concentration trends and was therefore considered an ideal sample for the analysis of local concentration changes. The resulting linear model consisted of reference spectra for collagen, chondroitin sulfate, and water, along with two baselining components to reconstruct sample spectra from cartilage. The coefficients from the collagen and chondroitin sulfate portions of the model were compared to biochemical assays for hydroxyproline and sGAG, respectively, finding a linear relationship. This correlation indicates that the linear model produces indicators for the relative concentrations of

collagen and GAGs. These techniques were further applied to different anatomical locations containing articular cartilage, finding variations as function of anatomical location. Overall, this study shows the successful implementation of Raman microscopy techniques to clinically relevant systems.

Chapter 4 discusses the use of information discovered in Chapter 2 for the development of interfacial scaffolds for tissue engineering. As previously discussed, native interfacial systems possess a continuous gradient in tissue composition and structure; one of the major factors that makes interfacial engineering challenging. Previous attempts to engineer enthesis structures in the Bonassar and Estroff groups have utilized decellularized bone coupled to collagen gels as means of recreating the bone and soft tissue portions of the enthesis, respectively. While the resulting constructs have shown similar morphologies to the native enthesis, the transition between the two regions is still very distinct, generating stress concentrations at the interface, resulting in an overall weakening of the structure. A solution to this issue is the spatially resolved removal of mineral content from the decellularized bone. This approach generates the desired interface without the need to reconstruct the complex structure of bone within a collagen gel.

Demineralization of bone is often practiced as histological preparation as well as for the use of demineralized bone in clinical applications, such as void filling. This study revolves around performing this demineralization in a spatially controlled manner to develop a structure that can be applied for tissue engineering purposes. To accomplish this goal, we chose EDTA as a demineralization agent, as it is known to remove mineral without damaging the underlying collagen matrix. Bone biopsies, removed from bovine femurs, were partially suspended in an EDTA solution, subsequently removing mineral from the regions of the biopsy in contact with the demineralizing solution. The resulting morphologies of the bone biopsies were analyzed using μCT to determine the spatial layout of mineral in the partially demineralized bone scaffold. The

mineral removal was determined to be affected significantly by the trabecular density of the initial bone scaffold. This relationship was determined using a multivariable fit of trabecular density, resulting mineral content, and demineralization time, finding that demineralization can be controlled for when accounting for these variables. Analysis of mineral content through histology and pXRD found that the scaffolds remained intact, and the mineral was distributed in a gradient fashion throughout the scaffold. Cell viability after seeding scaffolds with MSCs was analyzed, finding that mineral removal did not affect viability.

This procedure results in a multi-region, interfacial scaffold, connected through a gradient in mineral content that can be used for tissue engineering or other applications requiring a scaffold with mineralized and unmineralized regions. This scaffold can be applied to the enthesis engineering application discussed earlier, for the purpose of including the necessary structural regions of the enthesis that were found during the analysis in Chapter 2. Overall, this chapter highlights the advent of spatially resolved top-down materials engineering in a biomedical context for the development of interfacial tissue engineered scaffolds.

Lastly, Chapter 5 discusses the development and implementation of a laboratory for introducing engineering and design concepts to early-stage students, considering engineering as a career path. While this chapter takes a different direction from the proceeding chapters, the introduction of science and engineering at an earlier age is extremely important for the continued advancement of science and technology. This study developed a laboratory based on cold casting ceramics to confront students with a multifaceted design problem possessing numerous possible outcomes. This type of problem is much more realistic to engineering and science than the typical lab practical format of many early-stage science courses.

This laboratory consisted of the construction of ceramic casts that each perform best in different prescribed real-world categories, including aesthetics, ease of manufacturing, mechanics,

cost, etc. Students are asked to produce and analyze casts with varying material properties, finally providing a recommendation for which cast best suits a provided application. As no cast performs best in all categories, students are required to determine which categories they think are most important for the application and justify their recommendation. Further, through the production of these casts, students learn about different scientific concepts like viscosity and density and the effect of these concepts on functional properties. This activity was implemented in classroom environments to determine if the goals of the laboratory were reached, finding general success with both teachers and students. Overall, this chapter highlights the necessity for outreach in science and the need to introduce concepts that are necessary for science and engineering to students at an earlier age.

Future Directions

This dissertation discusses the characterization and synthesis of interfacial tissue systems, as well as the extension of characterization techniques to other tissues.

The enthesis is a complex tissue that has been examined in various studies, especially in recent times. Various factors have been discovered that increase the strength and toughness of the enthesis. Key among these factors is the mineral:matrix gradient that exists between mineralized and unmineralized tissues. Other factors, such as the interdigitation between different regions of the enthesis and the splaying of fibers from the ligamentous tissue to the fibrocartilage have been theorized as important factors in enthesis function. Despite these discoveries, the exact layout of the structure and composition of the enthesis has never explored, and a mechanical understanding of how the enthesis mediates large strains has never been fully developed. Further, most studies have focused on analyzing the mechanics of the tissue at the nanoscale or millimeter-scale, leaving a lack of information at the microscale, which is the size of many of the features that exist in this tissue. This dissertation sought to fulfill these deficiencies by directly mapping the microscale

composition and structure using novel methodologies derived from Raman spectroscopy and directly comparing these results to mechanical data collected at the same resolution.

Image analysis techniques were applied to Raman-derived data to find fingerprints for regional differences across the enthesis. This type of approach has never been applied to spectroscopic data collected from tissues and has application in a variety of systems. As Raman spectroscopy allows for the production of images of different compositional aspects of tissue, one can examine these different aspects for structural features. For example, in this case, collagen content alone is used to analyze for structural features that exist in the bone. These data are not convoluted by other features that may cause issue in other techniques, such as the presence of mineral. This type of analysis can be performed using fluorescent stains, but in addition to requiring more complicated preparation (preparation for Raman spectroscopy is minimal), fluorescent analysis is limited in the number of components that can be resolved. Raman spectroscopy allows for the simultaneous collection of all compositional data from the tissue, meaning that not only can the same image analyses be performed, but these types of analyses can be spatially compared to each other. This methodology is quite powerful in complex, multi-component systems and will prove useful, specifically in biological cases, where numerous compositional aspects contribute to the overall function of the material.

Regarding the characterization of the enthesis, further work should be performed on the disorganized bundles region of this structure. Mechanically, a region was identified that links the large collagen fibers that constitute the bulk of the enthesis to mineralized tissue in the bone by logarithmically reducing the strain magnitude throughout this area. However, the exact mechanism by which this logarithmic decrease occurs was not discovered. Further characterization of this region through higher resolution techniques would likely reveal this mechanism. For example, confocal elastography, performed at higher resolution, may show further structural means of stain

reduction, indicated through either microscopic fiber structure or small fiber movements. These data can be confirmed using higher resolution microscopic techniques, like scanning electron microscopy to examine local fiber structure. Approximate regional distinctions can be determined using Raman microscopy and marked prior to performing higher resolution analytical techniques. Using this experimental layout, the resulting regions can still be correlated with the mechanical data, thusly discovering the mechanisms by which this strain reduction occurs.

The enthesis is a three-dimensional structure, consisting of an angled insertion into bone. The study detailed in Chapter 2 does not discuss structuring along this third axis, focusing on analysis only across the interface. To address the three-dimensional aspects of the tissue, μCT analysis, should be performed on the interface of the enthesis to examine the overall interface morphology. While, the data would indicate that the enthesis possesses a similar structure, when compared as a function of depth from the proximal portion of the enthesis, analysis has not been performed to determine if any type of layered structure is present. An analysis through μCT has the potential to not only determine the exact morphology of the interface but also if the fibers that extend out of the mineralized tissue have an overall ordered structure in the directions orthogonal to the analysis performed in Chapter 2.

Lastly, further work should analyze the viscoelastic properties of the enthesis, particularly in the disorganized bundles region. Histological analysis would indicate that parts of this region possess GAG content, which would likely contribute to the viscoelastic properties of the interface. Determination of the extent of this viscoelasticity and its relevance at physiological loads has not been explored.

Chapter 3 discusses the non-destructive determination of the relative concentrations of collagen and GAG content. Prior to this work, Raman analysis had been performed on articular cartilage, but the feasibility of using Raman analysis to gauge local biochemical concentrations

had never been confirmed. Additionally, gauging local GAG content using Raman spectroscopy has proven difficult in previous studies. The non-destructive capacity had also never been directly analyzed, with the only previous studies directed at maintaining tissue viability focusing on visual cues rather than analyzing directly for cell viability. This study addresses these shortcomings, showing that a linear model can produce relative values for local collagen and GAG content that trend similarly to biochemically-derived concentrations of these constituents. Further, samples were confirmed alive with no defects in cell viability after Raman analysis. These advancements are necessary to support Raman spectroscopy as a potential diagnostic tool.

The major application of the technique outlined in Chapter 3 lies in a clinically relevant analysis for early-stage osteoarthritis in cartilage. To determine if this technique is applicable for such an analysis, the methodology outlined here should be applied to map local compositional changes across a cartilage surface. To create a controlled experiment, localized degradation can be generated through the application of degradative enzymes, such as trypsin or collagenase. These enzymes can be applied locally by adhering a container to the surface of the cartilage. Raman imaging can then be performed on the surface of the cartilage to search for these degraded areas. This type of analysis would prove, in a controlled manner, that detection of local concentration changes is feasible on intact cartilage surfaces. These analyses have already begun, showing promise for gauging cartilage defects. The next steps for this procedure are to apply this technique to the analysis of actual osteoarthritic tissue, analyzing for osteoarthritic lesions. If these steps all prove successful, the ultimate application of this technique to an arthroscopic Raman probe is still necessary for clinical application.

The construction of a synthetic enthesis has proven difficult to accomplish given the complex, hierarchical structure of collagen coupled to the spatially distinct layout of the mineral content. Many studies have approached this issue by growing mineral on a biocompatible scaffold

or by mixing mineral with an organic component to simulate the properties of bone. These approaches are unlikely to result in a scaffold that is truly biomimetic, as they do not meet the required composition, in the case of mineral-grown scaffolds, or the hierarchical structure, in the case of mixture-based scaffolds. To avoid these issues, Chapter 4 shows an approach to this problem using explanted tissue that was subsequently treated to generate a mineral gradient, thereby fulfilling both the compositional requirements and the hierarchical aspects for an interfacial scaffold. This type of approach, the spatial engineering of explant tissue, has not been previously utilized and opens up a new type of implant preparation for complex, biological systems.

Generally, the interfacial structures developed in Chapter 4 show great promise for application to tissue engineering. However, the exact effects of the local mineral content on cell behavior, specifically the behavior of MSCs, needs to be explored. Some of this analysis has already been performed, showing that the mineral content does affect MSC behavior. However, this subject also needs to be addressed in the context of an entire enthesis construct, possessing the addition of a cell-seeded collagen gel. Further, these constructs would still likely benefit from the addition of mineral deposition at the interface between the mineralized and unmineralized portions of the structure. This mineralized region, corresponding to the transitional region from Chapter 2, does not necessarily need to exactly mimic bone, as this region likely bears a closer resemblance to calcified cartilage. Thusly, this mineralization could be achieved through simple mineral growth using appropriate concentrations of calcium and phosphate salts. The presence of such a region, providing a stiff, continuous linkage prior to the presence of a mineral gradient, is likely more important than the structure of this region.

Lastly, regarding the classroom laboratory developed in Chapter 5, any application discovered in current research that can be suitably applied to early-stage students should be instituted. At the very least, these types of activities provide students with critical-thinking skills

through inquiry-based learning that will benefit the students regardless of a chosen career path. These types of activities place young students on the cutting edge of research, showing them why the careers of engineers and scientists are important for the continued advancement of society. This type of research is necessary to produce new generations of engineers and scientists to carry on the work that we strive to accomplish.

This dissertation highlights a series of novel techniques based on Raman microscopy for the non-destructive, high resolution analysis of different tissue systems. In the case of interfacial tissues, these techniques were coupled with local mechanical analyses to determine a spatially resolved structure-function relationship. Raman microscopy methodologies were extended for the imaging of concentrations of biomolecules in articular cartilage. Information learned from analysis of the enthesis was then applied for the creation of interfacial scaffolds for tissue engineering. Lastly, the dissertation highlights the development of a materials science laboratory for introducing engineering to early-stage students. Overall, this work lays a foundation for advanced characterization and materials synthesis techniques for application to complex tissue systems.